Ligand Design for Metal-Organic Frameworks and Single-Molecule Magnets

Jeffery R. Regier

Submitted in partial fulfilment

of the requirements for the Degree of Master of Science

Supervised by:

Prof. Melanie Pilkington

Brock University

St. Catharines Ontario, Canada

Abstract

This thesis describes two projects in which ligand design has been employed for the synthesis of coordination compounds exhibiting interesting structural and magnetic properties.

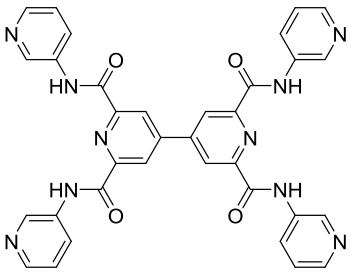

$\mathbf{L_I}$

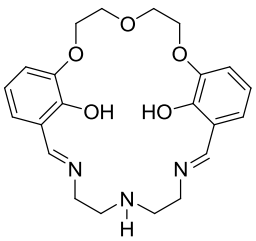

$\mathbf{L_{II}}$

In Project 1 a flexible, polydentate 4,4'-bipyridine ligand ($\mathbf{L_I}$) was prepared and fully characterized. Its coordination chemistry with $Cu_2(OAc)_4$ afforded a new complex with stoichiometry $[Cu_4(\mathbf{L_I})_{1.5}(OAc)_2(py)_2(OH_2)]_n$ (**III**). Single crystal X-ray diffraction experiments revealed that (**III**) crystallized as a porous, 3-D MOF with a structurally unique trinodal 4,4,5-c net topology. Variable temperature powder X-ray diffraction and TGA experiments revealed that (**III**) became amorphous upon desolvation, but that the crystallinity of the complex was fully restored after resolvation, rendering it a new addition to the family of breathable MOFs.

Project 2 presents a joint synthetic, experimental and theoretical approach towards the discovery of Ln-based SMMs. The synthesis and characterization of a new dual-compartmental macrocycle ($\mathbf{L_{II}}$), with an N_3O_2 cavity suitable for the preparation of seven-coordinate lanthanide complexes was achieved. Reaction of ($\mathbf{L_{II}}$) with $LnCl_3 \cdot 6H_2O$, (where Ln^{3+} = Dy, Tb and Er), in the presence of NaOH afforded three novel complexes with stoichiometry $[Ln_2Na_2(\mathbf{L_{II}})_2(Cl)_4(MeOH)] \cdot xH_2O$ (**IVa-c**).

X-ray diffraction studies revealed that the complexes were isostructural, comprising two coordinated macrocycles linked *via* a bridging μ_2 chloride to afford a dimer. Both macrocycles of each dimer contained a Ln^{3+} ion with pseudo D_{5h} geometry that is coordinated equatorially by the five donor atoms in the N_3O_2 pocket together with two axial chloride ligands, as well as a 6-coordinate Na^+ ion, residing in the $O_3O_2^{2-}$ pocket. All three complexes have been magnetically characterized. A frequency dependence to the out of phase component of the ac susceptibility data was observed for the Dy^{3+}complex (**IVa**), consistent with SMM behaviour. The ac data was successfully modelled to a single component Debye equation and a fit of the temperature dependence of τ_c to the Arrhenius equation afforded an effective energy barrier (U_{eff}) of 12.6 cm^{-1} and a pre-exponential factor, τ_0 of 2.91 x 10^{-7} s for this complex. Unfortunately, no slow relaxation of the magnetization was observed for the Tb^{3+} and Er^{3+} derivatives (**IVb**) and (**IVc**). Comprehensive *ab initio* studies carried out on (**IVa-c**) shed important light on the relaxation dynamics in all three complexes, revealing that deviation from idealised D_{5h} geometry results in less well isolated ground states and active quantum tunnelling mechanisms, further supporting the experimental observations of predominantly field induced SMM behaviour for (**IVa**), but no SMM properties for complexes (**IVb** and **c**).

Table of Contents

List of Figures

List of Tables

List of Schemes

List of Abbreviations

ANO: Atomic Natural Orbital.

BDC: benzene dicarboxylate.

bipy: Bipyridine.

bpa: 1,2-bi(4-pyridyl)ethane.

bpac: Bis(4-pyridyl)acetylene.

bpeb: 1,4-bis[2-(4-pyridyl)ethenyl]benzene.

CAC: Crystal-to-Amorphous-to-Crystal.

CASPT2: Complete Active Space Second Order Perturbation Theory.

CASSCF: Complete Active Space Self-Consistent Field Theory.

CC: Coupled Cluster Theory.

CI: Configuration Interaction.

CPF: Coupled Pair Functional Theory.

CSF: Configuration State Function.

dabco: 1,4-diazabicyclo[2,2,2]octane.

dc: Direct Current.

DCM: Dichloromethane.

DFT: Density Functional Theory.

DKH: Douglas-Kroll-Hess.

dmen: N,N′-dimethylethylenediamine. ,

DMF: N,N'-Dimethylformamide.

dobpdc: 4,4′-dioxidobiphenyl-3,3′-dicarboxylate.

DOTA: 1,4,7,10-tetraazacyclododecane-N,N',N'',N'''-tetraacetic acid, 54

epda: 5-ethyl-pyridine-2,3-dicarboxylate.

etbipy: 1,2-bis-(4-pyridyl)ethane.

FAB: Fast Atom Bombardment.

FT: Fourier Transform.

h: hour.

H_5DPMT: hexamethylenediamine-N,N,N′,N′-tetrakis(methylene)-phosphonic acid.

HF: Hartree-Fock.

HS: High Spin.

IR: Infrared.

IRMOF: Isoreticular Metal Organic Framework.

lp: Large Pore. ,

LS: Low Spin.

MC: Multiconfigurational.

Me-ip: 5-methylisophthalate.

MHz: MegaHertz.

MIL: Materials from Institut Lavoisier.

MO: Molecular Orbital.

MOF: Metal Organic Framework.

MP2: Second Order Moller Plesset Theory.

MRI: Magnetic Resonance Imaging.

MS: Mass Spectrometry.

np: Narrow Pore. ,

PXRD: Powder X-ray Diffraction.

py: Pyridine.

pz: Pyrazine. ,

RASSCF: Restricted Active Space SCF.

RASSI: Restricted Active Space State Interaction.

RCSR: Reticular Chemistry Structural Resource.

SBU: Secondary Building Unit.

SCF: Self-Consistent Field Theory.

SCXRD: Single Crystal X-ray Diffraction.

SMMs: Single Molecule Magnet.

SPC: Soft Porous Crystals.

SQUID: Superconducting Quantum Interference Device.

TCB: 1,3,5-tricyanobenzene.

TEB: 1,3,5-tris(4-ethynylbenzonitrile)benzene.

TGA: Thermogravimetric Analysis.

THF: tetrahydrofuran. ; Tetrahydrofuran.

TM: Transition Metal.

TPDC: terphenyldicarboxylate.

UV: Ultra violet.

Vis: Visible.

ZIF: Zeolitic Imidizolate Framework.

Acknowledgments

Firstly, I would like to thank my supervisor, Prof. M. Pilkington, for all of her assistance and guidance throughout my time at Brock University. The opportunities presented to me, working in her research group have facilitated my development into a competent research chemist. Furthermore, the transferable skillset I have acquired should guarantee my success as a researcher long after I graduate. I am also particularly grateful for the time Prof. Pilkington puts aside to ensure that my written and oral presentations are always of the highest quality. I would also like to acknowledge my peers in the Pilkington group, both past and present, for making all of my years at Brock very enjoyable.

I would like to acknowledge the efforts and expertise of our collaborators. In particular, Prof. J.M. Rawson at the University of Windsor whose knowledge of specialised laboratory techniques has impacted significantly on the quality of my research results and has been crucial to my success as a researcher. The experience of working in his laboratory at the University of Windsor was enjoyable and provided me with a complementary skillset which has in turn helped advance my research progress. I would also like to thank Prof. F.S. Razavi at Brock for magnetic susceptibility data. Thanks also go out to Prof. G. Kostakis at the University of Sussex, for help with interpreting the MOF topology, to Prof. M. MacLachlan at UBC for gas adsorption studies and to Prof. M.R. Ferreira André at the University of Aveiro, for solid state photoluminescence measurements.

In addition, I would like to thank the members of my committee, Prof. P. Zelisko and Prof. T.C. Stamatatos for all of their guidance throughout my MSc

studies. Their ability to challenge my results and ideas has helped me grow as a scientific researcher. Finally, I would like to acknowledge all of the people who have supported me outside of my research. Most importantly, I would like to thank my parents for all of their support, as well as the financial assistance that has made my MSc degree financially feasible. In addition, I would like to thank my brothers, sister and girlfriend for their patience and understanding while I finished my formal education. These people have kept me going always with their abundant encouragement.

Chapter 1 : Introduction

1.0: Preface

The main focus of research in the Pilkington group is centered on the design and synthesis of organic ligands for the development of a diverse range of magnetically interesting coordination compounds that include single molecule magnets (SMMs), spin crossover compounds, magnetic conductors and MRI contrast agents. Within the context of this research, this thesis is comprised of two projects: **Project 1** describes the structural and physical properties of a new breathable Cu^{2+} MOF, assembled from a flexible polydentate 4,4'-bipyridine ligand and in **Project 2,** a joint synthetic and *ab initio* approach is employed for the discovery of a new family of Ln-SMMs. In order to introduce both topics to the reader, the first section of this chapter contains a brief overview of the field of metal-organic frameworks (MOFs). This is followed by a short review of the basic concepts of magnetism, molecular magnetism and an introduction to the field of single molecule magnets (SMMs). Finally, in the final section of this chapter, the quantum computational methodology required for the *ab initio* studies described in Chapter 3 is introduced.

1.1: Metal Organic Frameworks

A metal-organic framework (MOF) is *a coordination network with organic ligands containing potential voids*.[1] This is the universally accepted definition and is

deliberately vague to account for a diverse range of structural topologies that include both rigid and flexible frameworks. As the definition suggests, MOFs may also have discrete void spaces when solvent/guest molecules are evacuated from within the material. In dynamic frameworks, evacuation of the guest molecules can lead to dramatic changes in their porosity.[2] Furthermore, it is not a requirement for a MOF to be crystalline; however, amorphous MOFs are rarely reported in the literature, since they are difficult to characterise. To date, many sub-groups of MOFs exist with their own terminology, which for different classes of MOFs, will be explained within the body of this thesis as they are encountered.

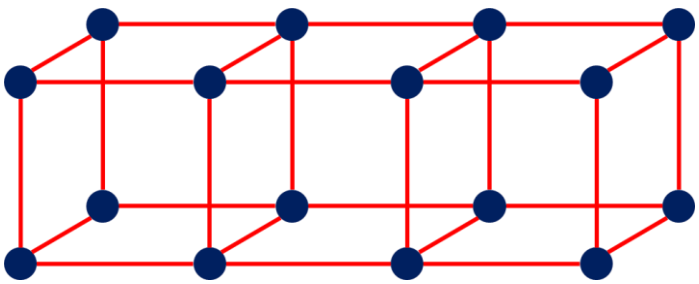

Figure 1.1 Depiction of a finite fragment of a MOF, where the linkers and connectors are represented as red lines and blue circles, respectively.

The structure of a MOF consists of two fundamental components: linkers and connectors (or nodes).[3] A linker is an organic molecule with two or more discrete coordination modes acting as a spacer between metal ions. Traditionally, linkers were exclusively rigid by lacking translational and rotational modes of freedom, however, MOFs are now synthesised from both rigid and flexible linkers, which has led to new generations of MOFs and will be reviewed in the first section of this chapter. Pyridyl

N-[4] and carboxylate O-donors are typically employed as the metal binding sites in organic linkers,[5] although a few examples of MOFs assembled from S-donors are also reported in the literature.[6] A selection of some of the most common classes of organic linkers employed for the preparation of MOFs is presented in Figure 1.2.

Connectors are the metal ions that coordinate to two or more linkers. Transition metals are the most abundant type of connectors utilized due to their natural lability, which facilitates the rearrangement of initially formed kinetic products into a uniform thermodynamic product.[7] Lanthanide-based MOFs do exist, but due to their high coordination numbers and lack of preference for a specific geometry, it is very challenging to predict with confidence how they will behave as connectors and therefore in comparison to the TM-based systems, they are much less well explored to date.[8]

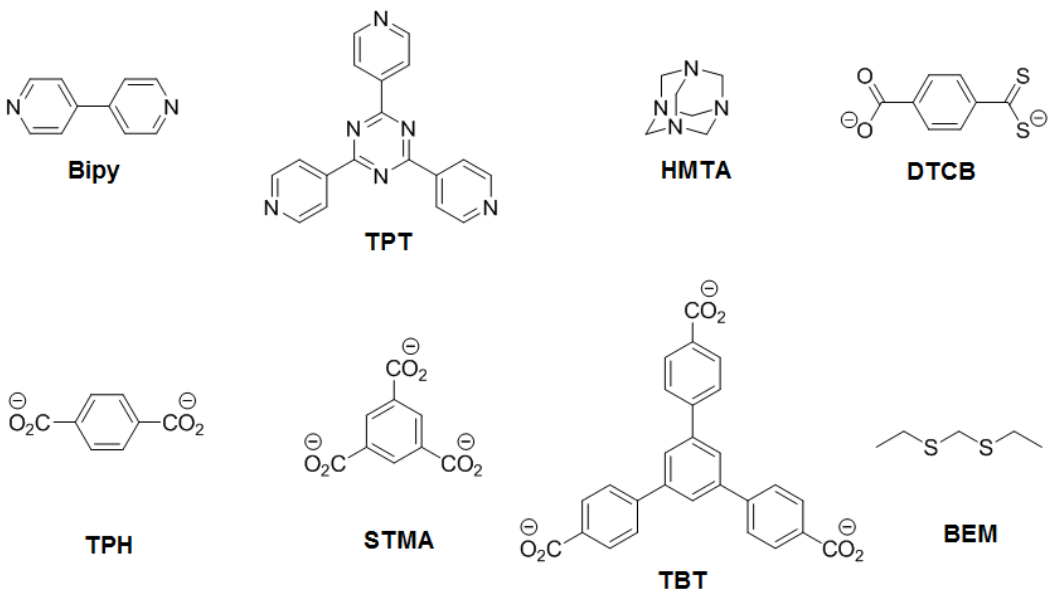

Figure 1.2: Selected examples of the most commonly used organic linkers in MOF chemistry.[7]

Due to the synthetic versatility of the organic linkers, MOFs can be tailored for a wide range of applications that include gas storage,[9] catalysis,[10] molecular magnetism,[11] drug delivery[12] and optics[13]. As a result, research in MOF chemistry has experienced a rapid growth over the past two decades, with the number of papers published per year increasing exponentially since 1991.[7] Out of the above applications, hydrogen storage has been the dominant accelerator of research in the field of MOFs due to the promise of H_2 as a clean fuel that could replace petroleum.[14] However, H_2 gas is too volatile under ambient conditions for practical applications. In regard to this challenge, MOFs have shown exceptional promise as low weight materials that can store H_2 at a density close to liquid H_2 near ambient conditions. In addition to the practicality of MOFs, their low temperature syntheses, ease of fine-tuning and remarkable versatility makes them more appealing over their aluminophosphate and aluminosilicate predecessors.[14]

In this context, tailoring a MOF for a specific application can in some cases be easily achieved by applying the concept of rational design, which involves the careful choice of metal ions and organic units. For example, paramagnetic ions can be incorporated into the MOF for applications in molecular magnetism[15] and/or chiral ligands may be employed, targeting the enantioselective binding of specific substrates.[16] The vast majority of successful synthetic strategies currently employed for the discovery of new MOF topologies rely on serendipity.[17] However, rational design approaches have been successfully employed for the preparation of a select few families of MOFs, but the rational design of new structural topologies remains one of the biggest challenges in the field of MOF chemistry to-date.

The remainder of this section describes the development of the field of microporous materials, highlighting the main achievements in MOF chemistry from the perspective of both synthetic design and novel applications.

1.1.1: Historical Perspectives

Research into microporous materials was established well before MOFs appeared in the literature. The first prominent predecessor to MOFs is the class of porous systems termed zeolites, described as silicate structures having the general formula $x[(M^{1+},M^{2+}_{1/2})\cdot AlO_2]\cdot ySiO_2\cdot zH_2O$ where M^{1+} = Li, Na, K, M^{2+} = Mg, Ca, Sr, Ba and *x*, *y*, *z* represent the various composition ratios for the different types of zeolites.[18] Minerals belonging to the zeolite family vary in natural abundance with some found in large deposits, for example, Analcite, Erionite, Erdenite, and Phillipsite[19] and others that are less common, such as, Faujasite and Offretitet.[18]

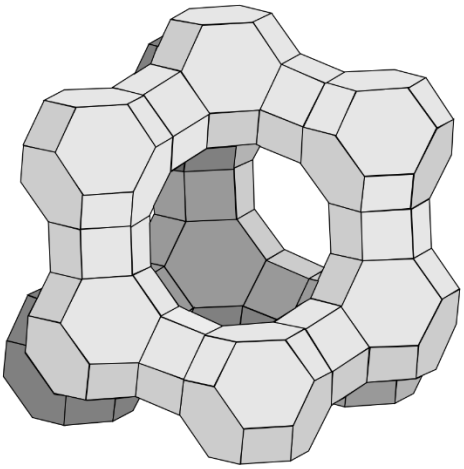

Figure 1.3: Crystal structure of Faujasite taken from Wikimedia Commons.

Zeolites were first studied and identified in 1756 by the Swedish mineralogist, Cronstedt (1722-1765)[18] and they soon became ubiquitous in industrial processes due

to their rich surface properties.[20,21,22] It was not until the 1940s, however, that systematic studies into the preparation and properties of these materials commenced. Early pioneers of this research included the New Zealand born chemist Richard Barrer[23] and the Union Carbide Corporation in the United States.[18]

The next major advancement in the field of microporous materials occurred in the 1980s with the introduction of atypical non-Si containing zeolites.[24] These materials were, and still are, fabricated entirely in laboratories, in contrast to Si-containing zeolites, which are both found in nature and synthetically prepared in the laboratory.[25] The replacement of silicon with phosphorous (aluminophosphates), sulfides, oxides, borates, germinates, and titanates offers advantages over traditional aluminosilicates, affording novel frameworks and structural topologies that can be optimized for a particular application. Since the introduction of this second family of microporous materials, the term "*zeolite"* is now applied to both natural aluminosilicates and their isomorphous derivatives.[24] Research into the isomorphous replacement of ions in zeolite structures remains a fertile field that is propelled by the demand for porous materials for applications in industrial waste water purification[26] and thermal petroleum cracking.[27] Even though these materials have proven to be effective for a number of domestic and industrial applications, their synthesis is non-trivial, typically requiring high temperatures and pressures.[28]

As a response to this challenge, MOFs began to appear in the early 1990s through the pioneering work of Robson,[29] Yaghi,[30] Moore[31] and Zaworotko.[32] Early work in this field revealed the promise of MOFs as functional porous materials capable of catalysis, ion-exchange, hydrogen gas adsorption, and selective substrate

adsorption.[33] In addition to demonstrating these functions, MOFs also yielded novel topologies, offering alternative strategies for varying the pore size and composition of a microporous material.

As previously mentioned, many of the crucial discoveries in MOF chemistry were initially observed via trial-and-error experiments.[5,30] This has afforded three distinct generations of MOFs, each improving on the limitations of its predecessors.[34] It should be noted that each generation does not define a quantified era in MOF chemistry, and that there is a substantial chronological overlap between the three generations, *vide infra.*

1.1.2: First Generation MOFs

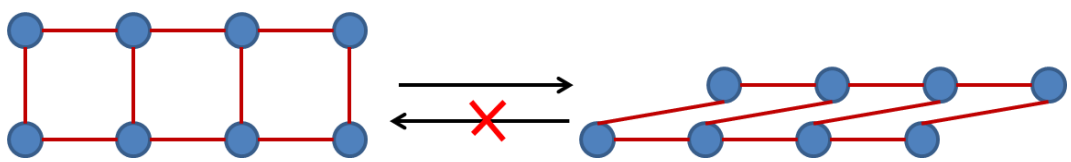

Figure 1.4: Ball and Stick representation of an arbitrary first generation MOF depicting the characteristic feature of an irreversible collapse.

First generation MOFs are characterised by the observation of an irreversible collapse to an amorphous solid upon the removal of solvent from the pores of the framework (Figure 1.4).[34] This early class of MOFs dominated the pioneering era of this field and served as a 'proof of principle' to show that porous coordination networks could be prepared from organic linkers and metal connectors. Due to the collapse of the structure, first generation MOFs do not have accessible inner surfaces and are therefore incapable of facilitating the interesting applications found in the

subsequent generations of MOFs.[34] Despite the instability of these materials, they made noticeable advances in addressing the challenge of structural design and prediction, which eventually led to a systematic approach for analysing networks.[35] Early examples showed that by using organic spacers and transition metal nodes, chemists could semi-rationally reproduce some of the obscure topologies found in inorganic porous materials using low temperature solution-based chemistry, instead of the high temperature and pressure strategies previously employed.

An early milestone in the development of first generation MOFs was the synthesis of [Ag(TCB)(CF_3SO_3)] (**1.1**), where TCB is 1,3,5-tricyanobenzene, Figure 1.5.[36] At this time, chemists were interested in reproducing the topologies of the 3D-networks of AlB_2 and $ThSi_2$, since it was predicted that these compounds display unusual mechanical, thermal and electrical properties.[37] There was success in the synthesis of 2D three-connected nets,[38] but the 3D networks of this type remained elusive. Moore approached this problem rationally by proposing that the desired framework could be synthesized by replacing the Al nodes and B spacers with metals and organic ligands that favoured trigonal planar geometries. By considering the exact analogues of AlB_2 and $ThSi_2$, namely CaCuP[39] and LaPtSi,[40] respectively, Moore proposed that Cu^{2+} and Pt^{2+} could be replaced by the three-coordinate Ag^{+} while P and Si could be replaced by the symmetric, tritopic, 1,3,5-tricyanobenzene (TCB) ligand. The Ca^{2+} and La^{3+} cations were replaced by weakly coordinating $CF_3SO_3^{-}$ counter-anions to balance the change, without affecting the topology of the structure. Using this methodology, Moore successfully prepared the desired 3D network

generated via offset π- π stacking interactions between neighbouring honeycomb sheets.[35]

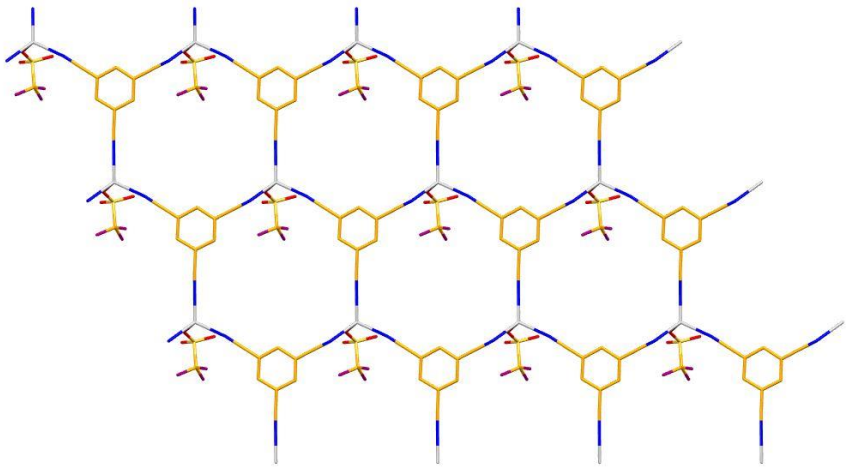

Figure 1.5: Molecular structure of [Ag(TCB)(CF_3SO_3)] (**1.1**) showing the hexagonal pores containing the $CF_3SO_3^-$ counter anions. Hydrogen atoms are omitted for clarity.[36]

Unfortunately, the triflate anions in this structure reside within the hexagonal pores of the planes, thus blocking guest molecules from accessing the inner surface of the MOF. To overcome this problem, Moore replaced the TCB linker with 1,3,5-tris(4-ethynylbenzonitrile)benzene (TEB) to enlarge the pores from 10 Å to 15 Å, thus providing additional space for solvent molecules to reside within the cavities.[36] In addition to this structural feat, [Ag(TEB)(CF_3SO_3)] (**1.2**) (Figure 1.6) also garnered appreciation as a pioneering example of a MOF that endures solvent exchange without a collapse in its structural topology. This was demonstrated by exchanging the benzene guest molecules with deuterated benzene by suspending the MOF in C_6D_6.[36]

For the preparation of simple frameworks, Moore's approach can be very successful. However, when considering other 3D regular frameworks assembled from

higher coordinate metal ions, the greater number of coordination possibilities results in an intrinsic lack of control over the extended assembly of the MOF. In the late 1990s and early 2000s, Yaghi *et al.* focused on developing monomeric coordination units in order to assemble extended networks with targeted topologies. These fundamental building blocks of MOFs are now referred to as secondary building units (SBUs).[7]

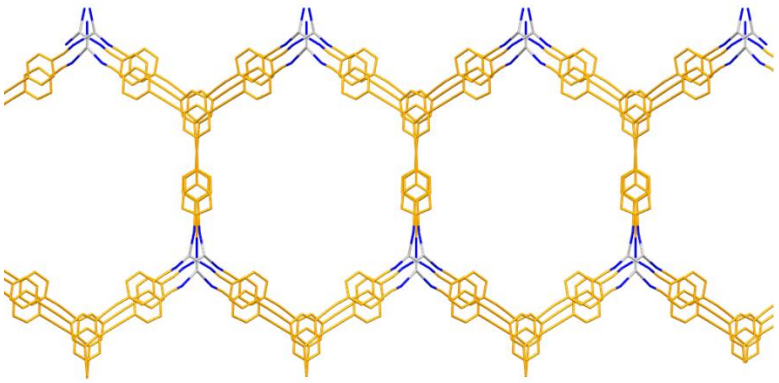

Figure 1.6: Molecular structure of [Ag(TEB)(CF_3SO_3)] (**1.2**) showing the extended hexagonal pores viewed along the *a*-axis. Nitrogen atoms are blue and the silver atoms are silver. Hydrogen atoms, solvent molecules and counter anions are omitted for clarity.[36]

Further establishing the usefulness of this approach Yaghi showed that metal carboxylate clusters could be used to lock the metal ions in their positions. This idea led to the synthesis of SBUs with rigid paddle wheel conformations of the $M_2(O_2CR)_4$ type, where M^{2+} = Cu or Zn[41,42,43] In this work, benzene dicarboxylate (BDC) derivatives were employed for the preparation of the SBUs since the restricted angles of the coordination modes can be further exploited to direct the self-assembly of the paddle wheel clusters. By exploring the *meta*- and *para*- substitution sites of BDC, Yaghi prepared two completely different compounds: a truncated cuboctahedron

$[Cu_{24}(m\text{-BDC})_{24}(DMF)_{14}(H_2O)_{10}]\cdot(H_2O)_{50}\cdot(DMF)_6\cdot(C_2H_5OH)_6$ (**1.3**),[41] and a 2D extended grid, $[Zn(p\text{-BDC})\cdot(DMF)(H_2O)]$ (**1.4**).[42] To apply the success of these results to 3D MOFs, Yaghi tailored the carboxylate linker to afford a 90° link by substituting a bromine atom into the *ortho*-position of *p*-BDC. Subsequent reaction of *p*-BDC together with Cu(II) afforded the 3D-MOF, $[Cu_2(o\text{-Br-}p\text{-BDC})]_2(H_2O)_2\cdot(DMF)_8(H_2O)_2$,[43] (**1.5**). As expected from Yaghi`s previous work, the MOF exhibits the cubic topology that is observed in NbO extended networks (Figure 1.7). Although this cubic topology was targeted for its interior void space, the solvent in the pores serve to template the assembly of the framework and unfortunately, their subsequent removal resulted in the loss of the structural topology of the MOF.

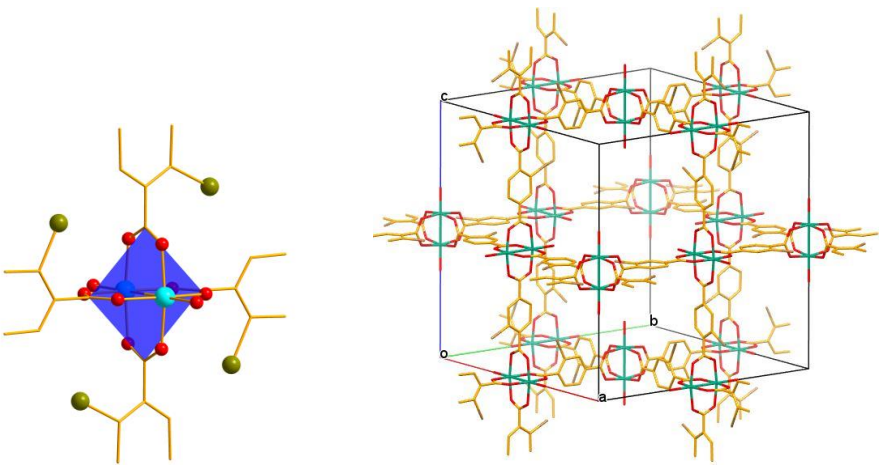

Figure 1.7: Molecular structure of $Cu_2[o\text{-Br-}p\text{-BDC}]_2(H_2O)_2\cdot(DMF)_8(H_2O)_2$ (**1.5**). Left: the truncated SBU used for the assembly of the MOF where Cu(II) ions and Br are represented as teal and brown spheres respectively. The blue plane outlines the paddle-wheel conformation of the cluster. Right: The unit cell of the MOF, highlighting its cubic topology.[43]

In spite of their limited applications, first generation MOFs resulted in crucial advances toward the preparation and design of extended coordination networks from

organic linkers. However, while propelling MOFs into the spotlight of research, these early examples also revealed some inherent challenges. The issue of stability quickly rose to prominence since it was clear that in order for porous coordination networks to be used in industrial processes they must be chemically and thermally robust. The solution to these challenges brought about research into a new, second generation of MOFs.

1.1.3: Second Generation MOFs

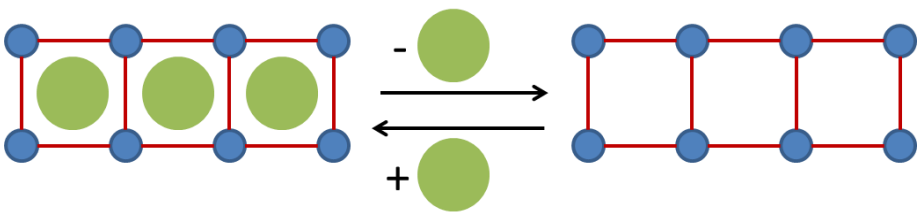

Figure 1.8: Ball and stick representation of an arbitrary second generation MOF showing the characteristic structural rigidity of the MOF as it withstands guest (green) removal and adsorption.

Second generation MOFs began to appear in the literature in the mid- to late-1990s from the groups of Yaghi[44,45] and Kitigawa.[46] The characterising feature of second generation MOFs is that they retain their structural topology when solvent/guest molecules are removed from the pores of the framework.[47] This has led to the synthesis of porous materials with some of the lowest densities and highest surface areas reported to date.[46] With access to the inner surface, MOFs were shown to behave like zeolites in that they can perform a wide variety of functions from selective gas[48] and substrate adsorption, to facilitating catalytic and ion exchange reactions.[49] Due to the endless possibilities for the realisation of the organic linkers,

second generation MOFs now have applications in nearly every field of chemistry, that includes environmental,[50] physical and[51] organic/inorganic synthesis[52] and are now also finding applications in biology, such as with the immobilisation of enzymes for the development of biocatalysts.[53]

Some of the earliest and most important advancements of second generation MOFs were made by Yaghi *et al.,* who addressed the challenges of stability and rational design. Of these research achievements, the most well-known is the discovery of $[Zn_4O(BDC)_3{\cdot}(DMF)_8(C_6H_5Cl)]$ (**1.7**), known as MOF-5,[54] whose rational design led to a porous 3-D framework with high thermal stability. Yaghi *et al.,* rationalized that a thermally robust SBU could be synthesised from a stable oxide-centered tetranuclear supertetrahedral cluster of Zn^{2+} carboxylates with fixed-angle coordination sites (Figure 1.9). Expanding on his earlier work with carboxylate linkers, Yaghi chose *p*-BDC as a linear linker between the Zn^{2+} clusters, which resulted in the isolation of a cubic six-connected net. The stability of MOF-5 was first evident through solvent exchange reactions where DMF and chlorobenzene were exchanged with chloroform without any deformations in the MOF topology. To further this study, the chloroform molecules were evacuated from MOF-5 at room temperature under reduced pressure. Single crystal X-ray diffraction studies on the evacuated MOF confirmed that after desolvation, it maintained its porous framework. Looking to test the limits of this MOF, Yaghi *et al.* heated it to 300 °C for 24 h, which had no effect on the morphology or crystallinity of the material. This impressive stability allowed for porosity studies using N_2 gas adsorption, which revealed that the MOF has a pore volume of 0.54-0.61 cm^3 per millilitre of sample compared to 0.47

cm^3mL^{-3} for the porous *zeolite A*. MOF-5 also has a calculated density of 0.59 $g \cdot cm^{-3}$, making it one of the least dense porous materials reported at the time.

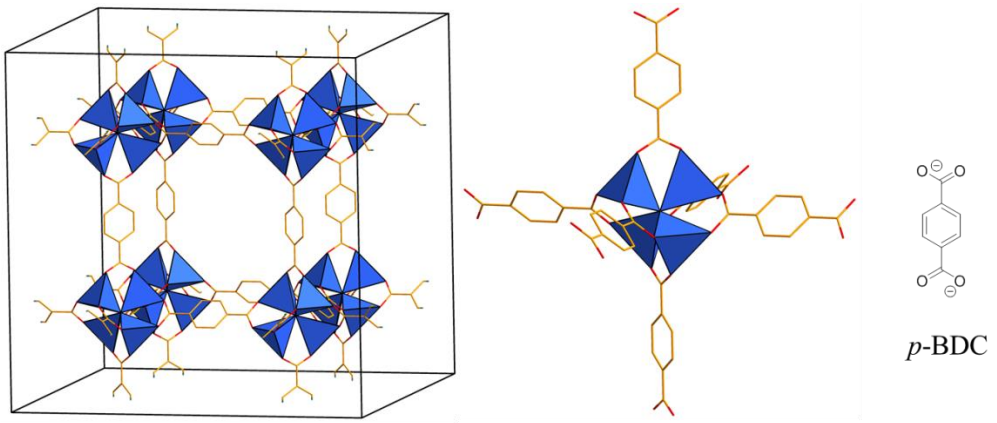

MOF-5 SBU for MOF-5

Figure 1.9: Left, crystal structure of MOF-5 (**1.7**). The Zn^{2+} ion coordination spheres are shown as polyhedrons and the H-atoms are omitted for clarity; middle, tetranuclear supertetrahedron SBU; right, molecular structure of the *p*-benzenedicarboxylate linker.[54]

Following the superior properties of MOF-5, Yaghi *et al*. synthesised an entire family of MOF-5 derivatives which were assembled from the same tetranuclear Zn^{2+} cluster. The objectives of this study were to increase the pore volume while retaining the stability of the framework by systematically employing longer dicarboxylate linkers. This work resulted in the isolation of fifteen unique isoreticular MOF derivatives (IRMOF) of MOF-5 reported in the journal *Science* [55] the largest of which is IRMOF-16 (**1.8**), Figure 1.10. In this context, IRMOF-16 was prepared from a terphenyldicarboxylate (TPDC) linker and has an accessible pore volume making up 91 % of the total MOF volume. This has led to a record low density of 0.21 g/cm^3 for a porous coordination network. Of this series, IRMOF-6 (**1.9**) was also shown to be an

excellent material for methane adsorption, where studies revealed an uptake of 155 cm^3mL^{-3} on a volume/volume basis of methane per sample at 298 K and 36 atm; a considerable improvement over 87 cm^3/cm^3 for one of the leaders in gas adsorption, *zeolite 5A.*

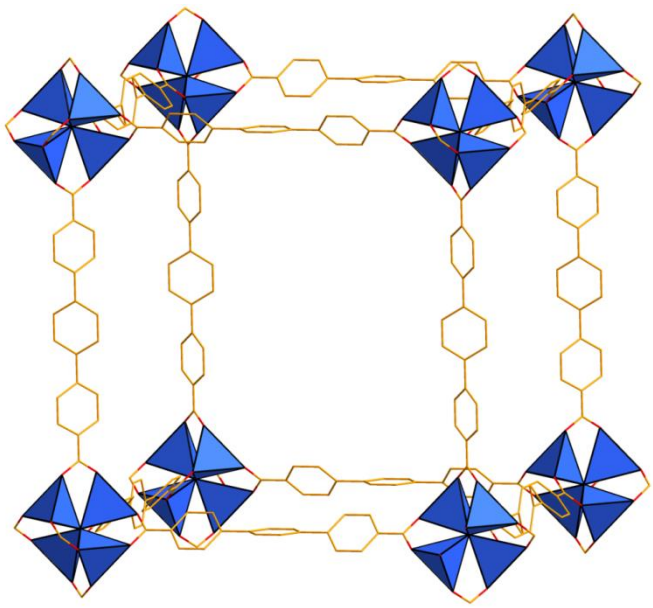

Figure 1.10: Molecular structure of IRMOF-16 (**1.8**). The Zn^{2+} coordination spheres are represented as blue polyhedrons.[54]

In the decade following this research, thousands of second generation MOFs were synthesised, although only a select few have resulted in significant advancements in the field. Some of the most popular and well-studied MOF families, include HKUST-1 (Hong-Kong University of Science and Technology),[56] MOF-74,[57] PCN-14 (Porous Coordination Network),[58] NJU-Bai (Nanjing University),[59] NU (Northwestern University),[60] NOTT (University of Nottingham)[61] and UTSA-20 (University of Texas at San Antonio).[62] Each of these families contains several isoreticular frameworks which may differ in the metal ion employed, or possibly

slight modifications to the organic linker resulting in different physical properties or pore size and shape. It is becoming increasingly less common for established groups to focus on synthesising new families of MOFs, as research objectives are currently focused towards fine-tuning the chemical and physical properties of the most promising MOFs for a particular commercial application. One impressive example is HKUST-1, which is among one of the leading examples of MOFs exploited for methane delivery, with a working capacity of 150 cm^3/cm^3 and a respectable uptake of 227 cm^3/cm^3 at 298 K and 35 atm.[63] More recently, ZJNU-50 (Zhejiang Normal University) has demonstrated one of the highest methane working capacities of 184 cm^3/cm^{-3} at standard temperature and pressure.[64] Regarding hydrogen gas storage, NU-100 achieved the highest working capacity of 99.5 mg/g (H_2/NU-100) at 56 atm and 77 K[65], and MOF-210 currently has the highest total H_2 gas capacity of 176 mg/g at 80 atm and 77 K.[66] This is an appreciable improvement over the initial H_2 adsorption reports using MOF-5 (45 mg/g) in 2003.[67]

Another trend in the literature involves 'decorating' established MOFs with substrates that coordinate within the pores of the framework.[68] The goal of this research is to tailor the MOF towards a specific application. An example of this approach is the functionalization of the well-studied MOF-74 derivative, M_2(dobpdc)[69] (**1.10**), (where dobpdc = 4,4′-dioxidobiphenyl-3,3′-dicarboxylate and M^{2+} = Mg (**1.10a**), Mn (**1.10b**), Fe (**1.10c**), Co (**1.10d**) and Zn (**1.10e**)). In this MOF, *N*,*N*′-dimethylethylenediamine (dmen) coordinates to the metal ions within the framework and cooperatively inserts CO_2 into the pores (Scheme 1.1). Remarkably, the MOF was shown to endure ten cycles without any loss of capacity in CO_2

adsorption (12 g CO_2/100 g MOF). This recent example demonstrates the versatility of a MOF, which combines catalysis with gas storage, both of which are fields that have garnered immense interest over recent years.[70,71]

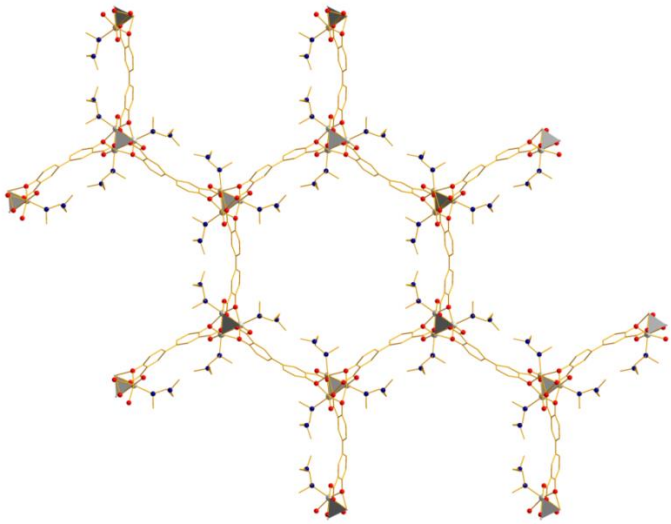

Figure 1.11: Crystal structure of Mn_2(dobpdc) (**1.10**) decorated with N,N′-dimethylethylenediamine (dmen) in the hexagonal pores of the MOF. Mn^{2+} clusters are depicted as grey triangles and the dmen ligands are shown coordinated to Mn^{2+} in the pores.[69]

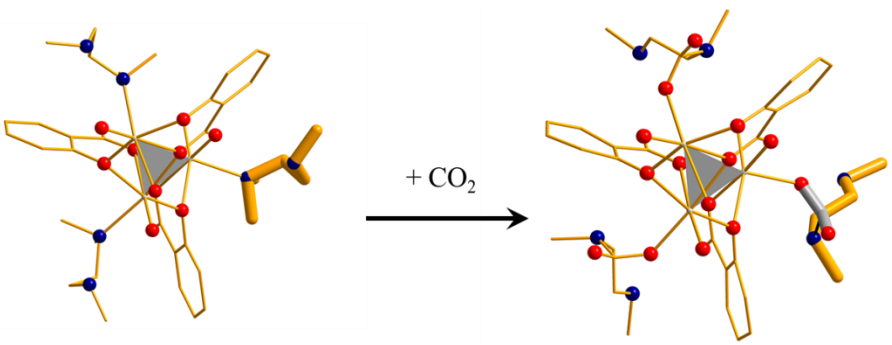

Scheme 1.1: Cooperative insertion of CO_2 into the pores of M_2(dobpdc). N,N′-dimethylethylenediamine is enlarged for clarity and the C-atom from CO_2 is coloured grey in the carboxamide product after insertion. H-atoms are omitted.[69]

It is clear from these examples that the chemical rigidity and thermal stability of MOFs have made it possible for them to perform important industrial processes in a field where zeolites dominate. However, over the past decade, chemists began to look into the potential applications of MOFs that go beyond the capabilities of zeolites. In this regard, chemists targeted the realisation of dynamic frameworks, that is, frameworks that can undergo discrete phase transitions. The results from this research have afforded what are referred to as *third generation* MOFs.

1.1.4: Third Generation MOFs

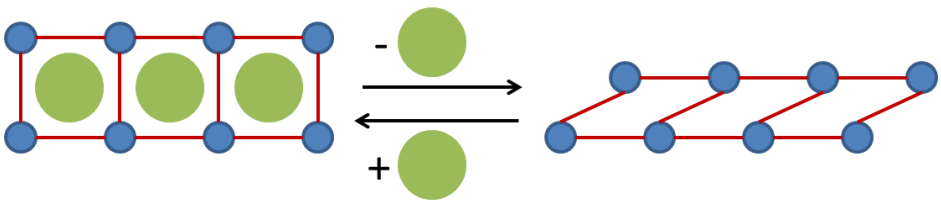

Figure 1.12: Ball and stick representation of an idealized third generation MOF showing the characteristic feature of a substantial change in potential pore volume in response to external stimuli such as removal and adsorption of guests.

Third generation MOFs have a dynamic framework that undergoes a reversible phase transition in response to external stimuli such as temperature, pressure, light, and guest adsorption/desorption.[2] The concept of a dynamic framework was first proposed in 1998[72] by Kitigawa[3] with major contributions from the work of Férey *et al.*[73] Due to their flexible frameworks, these MOFs are more formally referred to as *soft-porous crystals* (SPCs) or *flexible-MOFs*.[2] To distinguish SPCs from other generations of MOFs, Horike defines SPCs as "*porous solids that possess both a highly ordered network and structural transformability. They are*

bistable or multistable crystalline materials with long range structural ordering, a reversible transformability between states, and permanent porosity. The term porosity means that at least one crystal phase possesses space that can be occupied by guest molecules, so that the framework exhibits reproducible guest adsorption.''[74] This definition refers to materials that undergo structural transitions of the crystal-to-crystal, or crystal-to-amorphous-to-crystal (CAC) types. The most common type of SPC is the breathing MOF which undergoes a substantial pore-size transition, such as, narrow-pore to large-pore (np → lp).[2] However, out of the tens of thousands of MOFs reported in the literature, only approximately 100 are characterized as breathing MOFs.[2]

Early examples of SPCs proved to be significantly more challenging to prepare and study when compared to previous generations of MOFs due to the lack of understanding regarding how the MOF will behave. Jenkins *et al.* approached this issue by categorising SPCs based on a concept of dimensional rigidity, where the framework is analysed by considering which parts are rigid and which parts are flexible.[75] In this concept, SPCs are split into four categories based on their dimensional rigidity within a breathing mechanism (0D to 3D).

Zero Dimensional Breathing SPC

Figure 1.13: Depiction of an SPC showing that there are no rigid dimensions in this material which leads to zero-dimensional breathing.

Zero dimensional breathing (0DB) SPCs are three dimensional coordination networks with zero rigid dimensions indicating that they are flexible in three dimensions.[75] For this reason, they are inherently rare since it is difficult to obtain crystalline materials with structural freedom in all three dimensions. There are, however, two known design features that are used to assemble 0DB-SPCs. The first is rigid linker twisting, where a linker is capable of rotating about an axis in response to guest desorption/adsorption, or a change in pressure; and the second is by using the phenomenon of spin-crossover.[75]

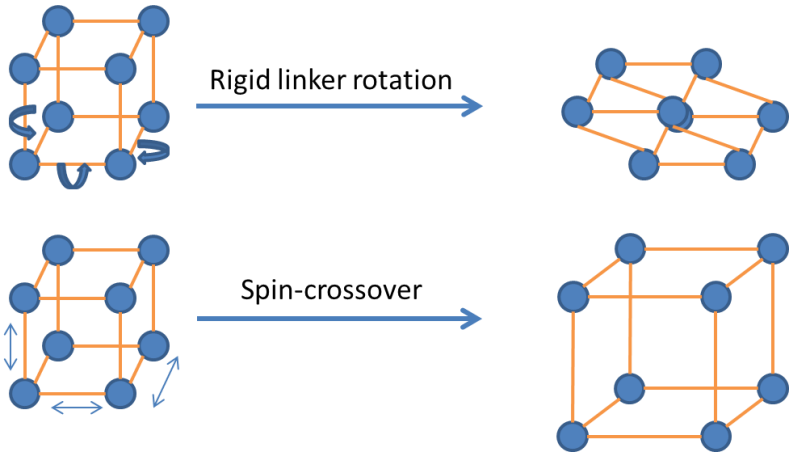

Figure 1.14: Depiction of the breathing mechanisms in 0DB-SPCs.

Rigid linker twisting was employed in ZIF-8 (zeolitic imidazole framework)[76] which, at ambient pressure, exists as a rigid framework with a Sodalite topology, but at extreme pressure (1.47 GPa) the MOF is flexible and a new phase is obtained comprising of rotated imidazole ligands.[77] However, using high pressure to induce a structural transformation is less desirable than guest exchange which has been popularised by the MIL-88 (Materials from Institut Lavoisier) series. MIL-88 is a porous framework with the formula $[M_3(\mu_3\text{-}O)(H_2O)_2X(\text{dicarboxylate})_3]\cdot\text{guest}$ (**1.11**), where M^{3+} is Fe or Cr, X^- is F, Cl or acetate and the dicarboxylate linkers are fumarate, terephthalate, 2,6-naphthalenedicarboxylate, or 4,4′-biphenyldicarboxylate.[78] MIL-88 is comprised of trigonal bipyramidal cavities formed by trigonal-prismatic $M_3(\mu_3\text{-}O)(H_2O)_3(\text{dicarboxylate})_6$ clusters at the vertices, bridged by a dicarboxylate linker. The combination of the rotational freedom of the trimer with the twisting of the dicarboxylate linker leads to atom displacements greater than 10 Å and a volume expansion of 230% (Figure 1.15).

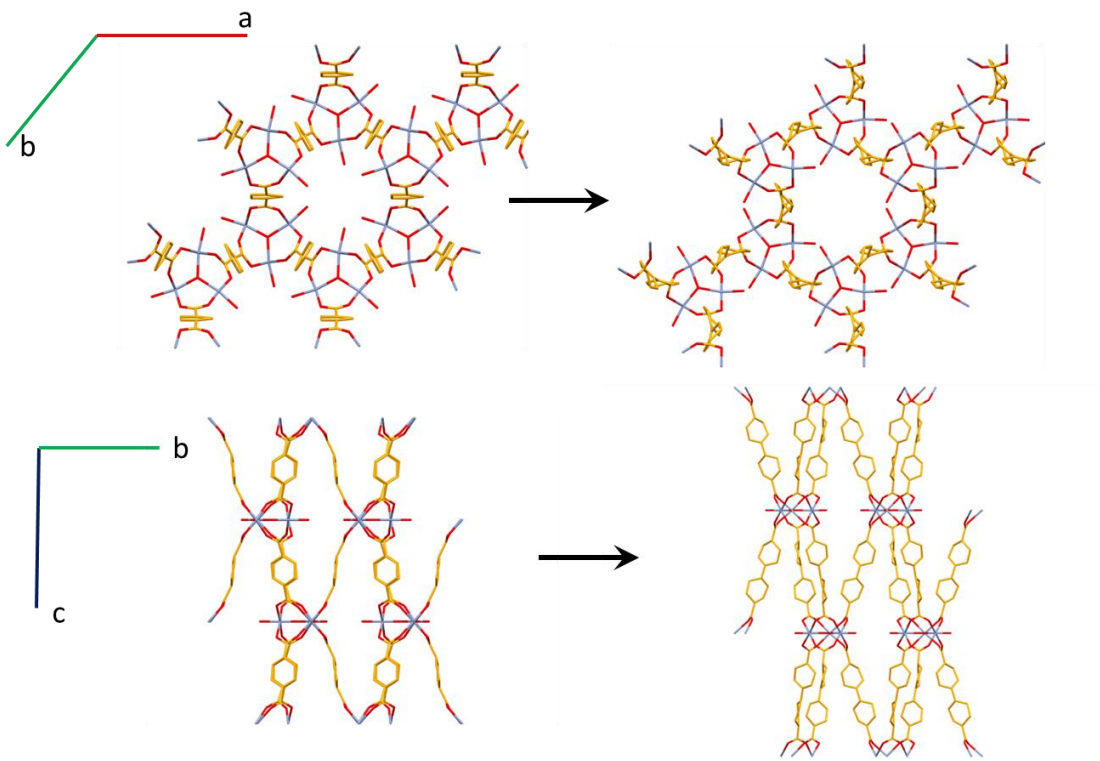

Figure 1.15: Molecular structures of the two discrete phase-transitions as a result of rigid linker twisting in 3-dimensions observed in MIL-88 (**1.11**). Top: Structural transformation as viewed down the *a*-axis; Bottom: Phase transition as viewed down the *c*-axis.[78]

Aside from rigid linker twisting, 0DB has been induced through spin-crossover. The $Fe(pz)[M^{II}(CN)_4]$ MOF (**1.12**), where M^{II} = Ni, Pd, Pt; pz = pyrazine, studied by both Kitagawa[79] and Kepert[80] undergoes a spin transition near room temperature induced by either light or temperature (Figure 1.16). In this MOF, a spin transition causes the percent volume of the pore to increase from 18.1 % for the LS state to 22.4 % for the HS state, resulting in a total increase in the void space volume of 54 $Å^3$. This research was further investigated by Real *et al.*,[81] who exchanged the pyrazine for the extended linker bis(4-pyridyl)acetylene (bpac) (**1.13**). The bpac linker

not only maintained the near room temperature spin-transition, but also nearly doubled the void space of the MOF.

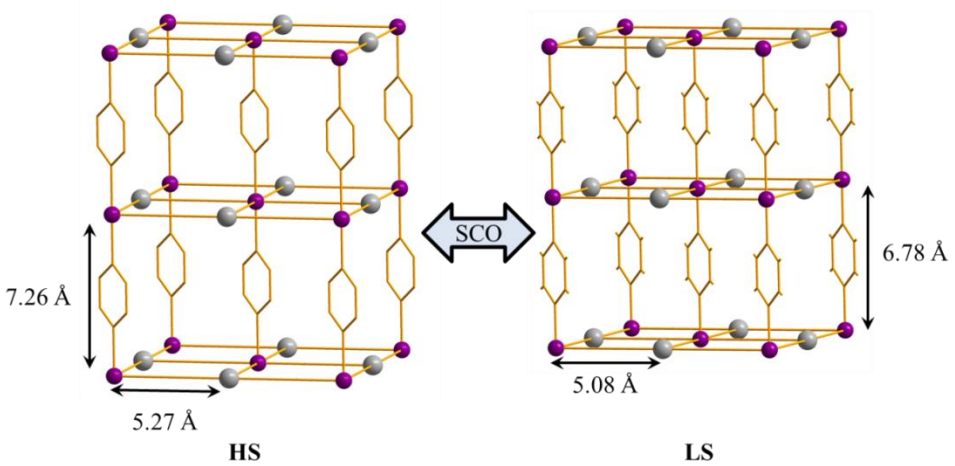

Figure 1.16: Molecular structures of the HS and LS states of Fe(pz)[$Pt^{II}(CN)_4$] (**1.12**).[79]

One Dimensional Breathing (1DB) SPCs

Figure 1.17: Representation of a 1DB-SPC, showing one rigid dimension.

SPCs with one dimension of rigidity, for the most part, share a common facial rhombohedral topology. The most popular 1DB-SPC, as well as, the most widely recognised SPC of any dimension, is MIL-53 (**1.14**) which was first synthesised by Férey in 2002.[82] MIL-53's popularity is a result of its trivial synthesis and predictable breathing behaviour. In this MOF, the linkers are rigid with torsional freedom and the structural transformation results in a distortion of the linker-metal-linker angle. This

deformation ultimately leads to a ‘pinching’ of the rhombohedral face, referred to as ‘kneecap’ bending due to the linker-metal-linker SBU distorting in a manor analogous to a leg. The framework responds to the presence and absence of guest molecules where it transitions from np to lp, respectively.

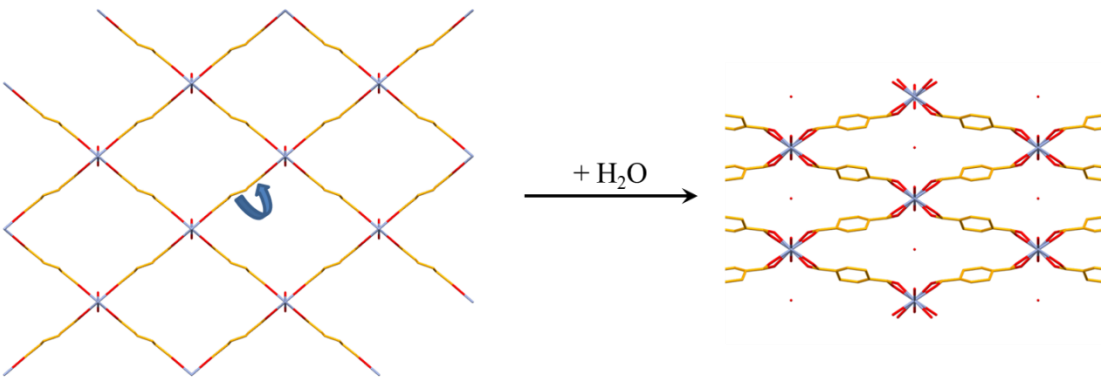

Figure 1.18: Molecular structures of the two phases of MIL-53 (**1.14**). The lp → np transition is shown here as a response to the uptake of water guest molecules. In the lp state, the phenyl ring is perpendicular to the rhombohedral face of the pore, but in the np state, the phenyl ring is rotated to a conformation that makes it nearly parallel with the rhombohedral face.[82]

Alternatively, 1DB-SPCs can be prepared through rigid linker bending which has been successfully achieved following two strategies. The first is to employ two different linkers, where the first rigid linear linker is used to assemble 1D-chains and the second connects the chains together forming a flexible rhombohedral face perpendicular to the chains. The second approach is to use a single ditopic ligand to first assemble 1D-chains, which then crystallize in a 3D topology that is stabilized via linkers between the systems.[75]

Regarding the first approach, Kim *et al.* prepared the 1DB-SPC [Zn_2(1,4-bdc)$_2$(dabco)]·4DMF·½H_2O (**1.15**), where dabco is 1,4-diazabicyclo[2,2,2]octane to

form the rigid dimension as chains which are linked together by *p*-bipyridinedicarboxylate (1,4-bdc) linkers to form the other two flexible dimensions.[83] The flexibility of this framework is a result of the bending of the rigid 1,4-bdc linkers which exhibit different breathing effects depending on the type of encapsulated guest molecules. In the original MOF, DMF molecules reside within the lattice and the carboxylates of the bdc linker are bent out of the plane of the benzene ring which forces a strong deviation from linearity. However, when the DMF is removed, the Zn-(1,4-bdc) linkages become collinear resulting in a cubic topology. Furthermore, when benzene is introduced into the lattice, the MOF breathes to a np conformation since the carboxylates distort out of the plane of the benzene ring on opposite sides. The groups Cohen and Fisher showed that applying this approach, the breathing effects can be tuned *via* linker replacement of 1,4-dbc. This resulted in the realization of a series of new derivatives, each displaying 1D breathing effects to various extents.[84]

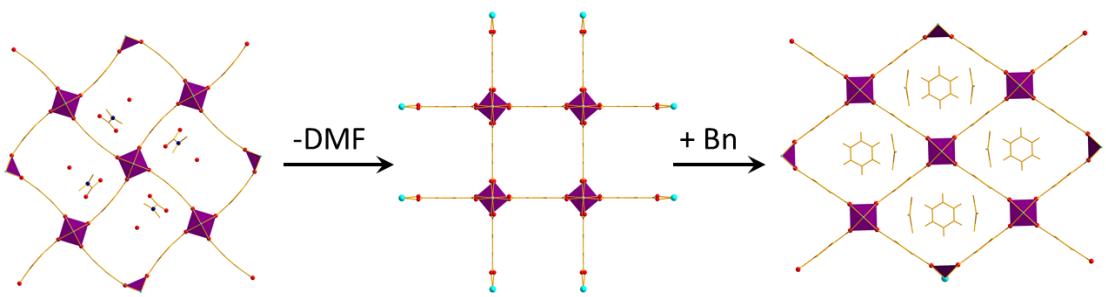

Figure 1.19: Crystal structure of $[Zn_2(1,4\text{-bdc})_2(dabco)]\cdot 4DMF\cdot \frac{1}{2}H_2O$ (**1.15**) and its subsequent structural transformations due to the loss of DMF guest molecules and the adsorption of benzene (Bn) solvent molecules. The rigid 1D-chain axis is represented as purple polyhedrons.[83]

To explore the single linker approach, Long *et al.* employed a ditriazole linker for the preparation of $[Cu(BDTri)(DMF)]\cdot 1.2H_2O$ (**1.16**) which consists of 1D-chains

of octahedral Cu^{2+} ions bridged together by triazole groups with DMF molecules residing in the 1D channels (Figure 1.20).[85] When the DMF molecules are removed from the pores, the rhombohedral face flattens to a NP structural phase with coordinating DMF molecules acting as pillars perpendicular to the face formed by the triazole linkers. There are two bending modes of the linker, first at the triazolate rings, which are bent on opposite sides of the benzene plane yielding an α-angle and second at the metal-linker interface affording a β-angle, Figure 1.20.

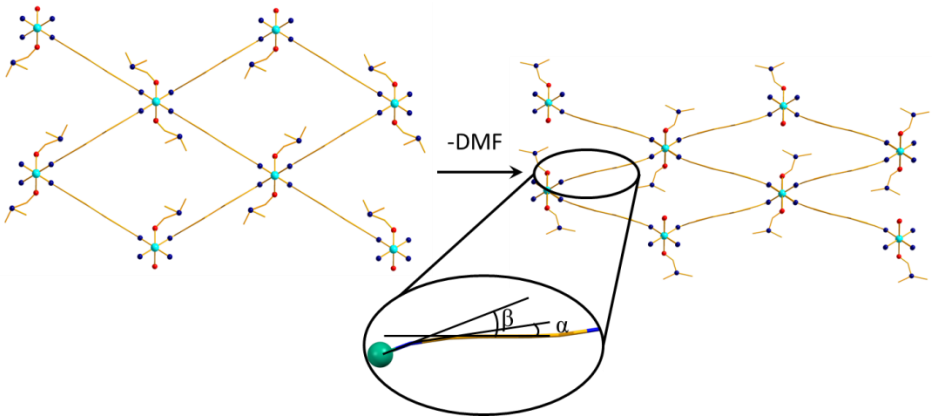

Figure 1.20: Molecular structure of the 1DB-SPC, Cu(BDTri)(DMF)·1.2H_2O (**1.16**) showing the structural transformation due to rigid linker bending. Coordination of BDTri results in flexible 1D-chains that form the rhombohedral face of the MOF. The rhombohedral planes are linked together by DMF linkers which results in a rigid axis along the Zn(II) ions (teal) perpendicular to the faces.[85]

Additionally 1DB-SPCs can be prepared by introducing flexible linker twisting in the plane of the rhombohedral face. This approach was applied by Costantino *et al.* for the preparation of $Cu_3(L)(etbipy)_2$ (**1.17**), which uses two flexible linkers where etbipy is 1,2-bis-(4-pyridyl)ethane and L is the linker phosphonate (N,N,N′,N′-tetrakis(phosphonomethyl) hexamethylenediamine).[86] This 1DB-SPC

displays a reversible lp to np transition resulting in a corresponding 26% volume difference due to the twisting of both linkers (Figure 1.21). This was proven by replacing each of the linkers with their rigid analogue leading to MOFs displaying either no breathing, or an irreversible lp to np transition.

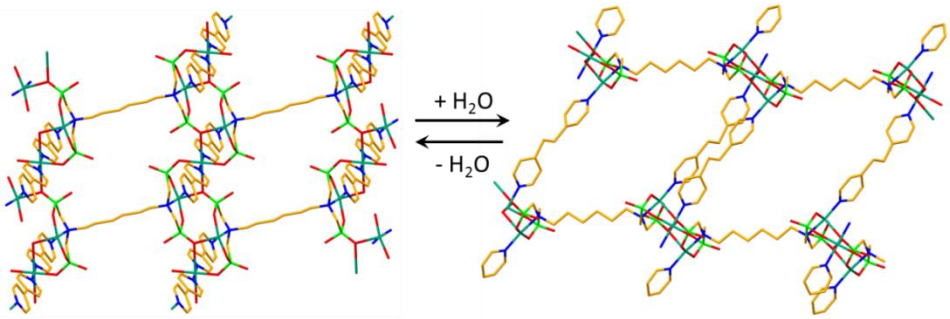

Figure 1.21: Molecular structure of the 1DB SPC, $Cu_3(L)(etbipy)_2$ (**1.17**) showing the reversible structural transformation between np and lp upon hydration and dehydration.[86]

Two Dimensional Breathing (2DB) SPC

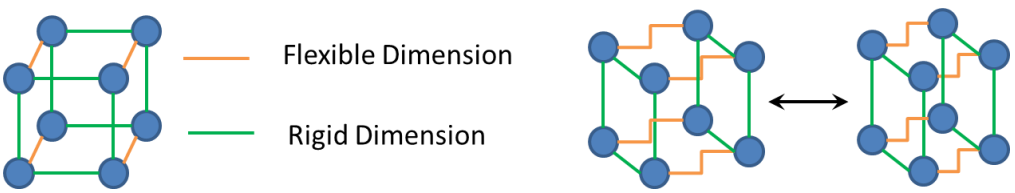

Figure 1.22: Depiction of a 2DB-SPC showing 'accordion-like' breathing.

Two dimensional SPCs have two rigid sheets bridged by flexible pillars leading to a breathing mechanism analogous to the expansion and contraction of an accordion. The breathing mechanisms in 2D-SPCs have so far been accomplished by implementing fully flexible linkers, double-hinged linker twisting and rigid linker tilting. Using the fully flexible linker method Alberti *et al*. prepared several MOFs of

the type $ZrPO_4[O_2P(OH)_2]_{1-x}(O_2POH\text{-}(CH_2)_n\text{-}HOPO_2)_{x/2}\cdot mH_2O$ (**1.18**).[87] The Zr derivative is comprised of rigid faces formed by $ZrPO_4$ and phosphoric acid and the faces are bridged together by flexible alkanediphosphonic acid to induce an accordion-like breathing mechanism. A similar methodology was also adopted by Cabeza *et al.* for the realization of a breathing lanthanum MOF, $La(H_5DPMT)\cdot H_2O$ (**1.19**), where H_5DPMT is the flexible linker hexamethylenediamine-N,N,N′,N′-tetrakis(methylene)-phosphonic acid.[88]

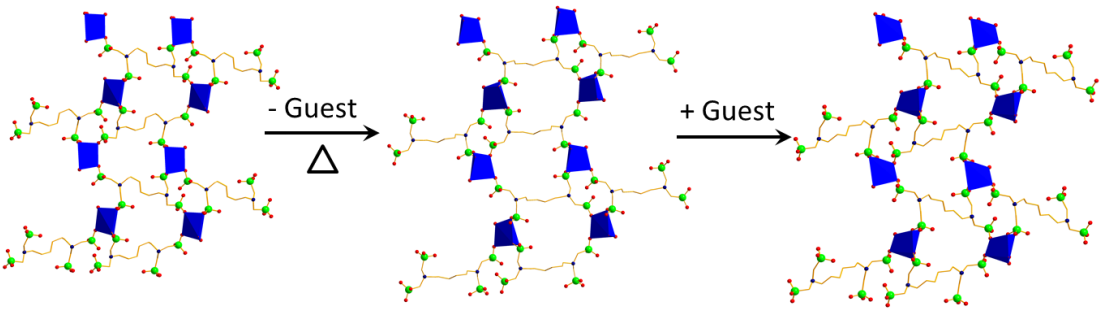

Figure 1.23: Depiction of the transitions observed for $La(H_5DPMT)\cdot H_2O$ (**1.19**). The lanthanide units are represented as blue polyhedrons. Throughout the breathing mechanism, the Ln-P-chain is unchanged. Structural changes occur in the alkane unit, only.[88]

Using fully flexible ligands is clearly a useful strategy for preparing 2DB-SPCs, but they typically result in substantial volume changes. Wang *et al*. showed that including double-hinge linker rotations into the flexible axis of the MOF results in small pore volume changes.[89] This is particularly evident in $[Co_2(epda)_2(bpa)(H_2O)_2]\cdot 3H_2O$ (**1.20**), where epda is the rigid linker 5-ethyl-pyridine-2,3-dicarboxylate and bpa is the flexible linker 1,2-bi(4-pyridyl)ethane, where a double-hinged rotation occurs along both pyridyl-alkane bonds. Exploiting this methodology in **1.20** yielded a relatively small volume change of 9 %. Vittal

expanded this strategy by using the flexible unsaturated linker 1,4-bis[2-(4-pyridyl)ethenyl]benzene (bpeb), which undergoes *cis-trans* rearrangements leading to a deformation of the MOF, Figure 1.24.[90]

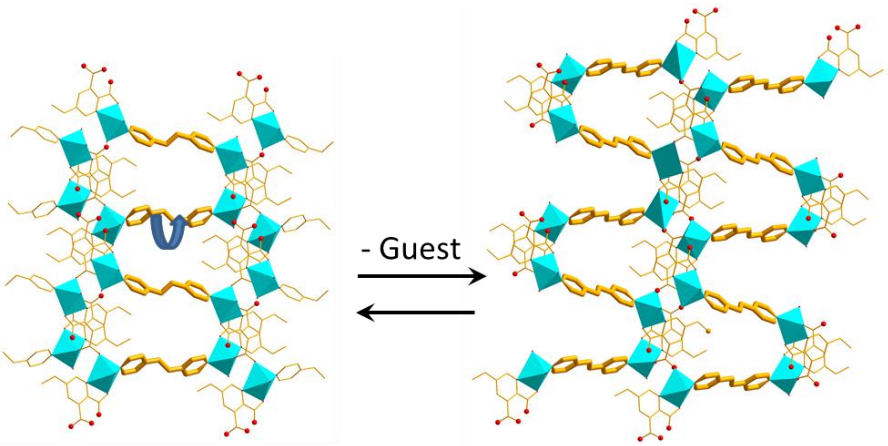

Figure 1.24: Depiction of the structural transition in $[Co_2(epda)_2(bpa)(H_2O)_2]\cdot 3H_2O$ (**1.20**) in response to guest removal and adsorption. Hydrogen atoms and solvent molecules are omitted for clarity. The coordination units are depicted as blue polyhedra.[89]

In contrast to the typical accordion breathing mechanism, 2DB-SPCs can also breathe by a sliding of rigid 2D planes due to rigid linker tilting. In this context, Zeng *et al*. prepared $[Co(5\text{-}NH_2\text{-}bdc)(bipy)_{0.5}(H_2O)]\cdot 2H_2O$ (**1.21**), where the rigid linker 5-NH_2-bdc forms 2D planes and bipy bridges them together.[91] After removing the solvent, the coordination geometry of the Co^{II} ion changes from octahedral to distorted square pyramidal leading to an induced shift of the bipy linkers, Figure 1.25. Reintroduction of the solvent into the lattice leads to the reformation of the as-synthesised MOF.

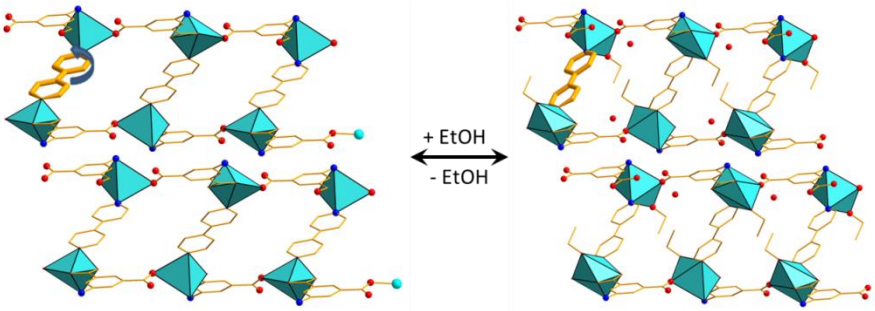

Figure 1.25: Rigid linker tilting of $[Co(5\text{-}NH_2\text{-}bdc)(bipy)_{0.5}(H_2O)]\cdot 2H_2O$ (**1.21**), where the coordination geometry around the Co(II) ions is represented by blue polyhedra.[91]

Three Dimensional Breathing (3DB) SPCs

Figure 1.26: Depiction of a 3DB-SPC showing no flexible dimensions.

MOFs that are rigid in 3D are the most common in the chemical literature and have for the most part, been covered in the discussion of second generation MOFs. However, it is possible for some of these MOFs to exhibit breathing mechanisms that differ from the previously described 0-2DB SPCs. Breathing of 3DB-SPCs occurs exclusively in interpenetrating systems, where two or more distinct frameworks are intertwined. Intermolecular rearrangements lead to changes in the solvent accessible pore volume such as with $[Cu(CN)_3L^1]\cdot H_2O\cdot CH_3CH_2OH$ (**1.22**), where L^1 is 2,6-bis-((3,5-dimethyl-1H-pyrazol-4-yl)methyl)pyridine.[92] This doubly interpenetrated network undergoes a breathing transformation in response to the adsorption of benzene, cyclohexane, acetonitrile and tetrahydrofuran (THF) molecules, whereby the

two interlocking networks effectively slide relative to one another leading to a change in the accessible pore volume.

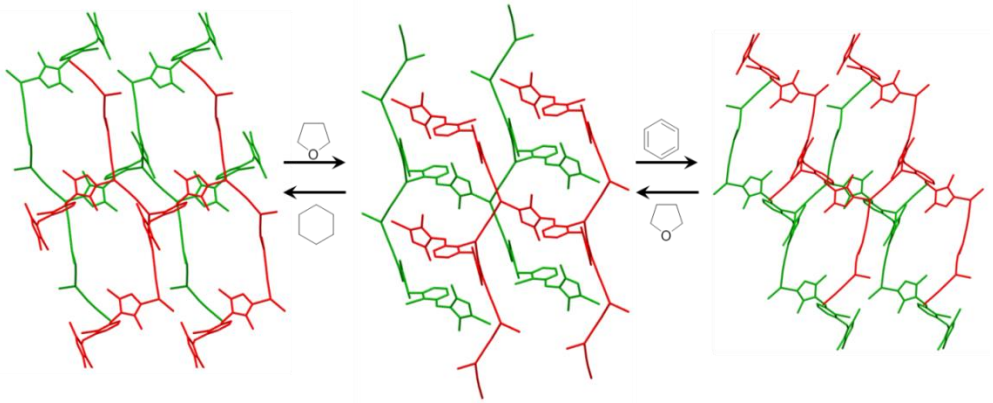

Figure 1.27: Structural transformations of $[Cu(CN)_3L]\cdot H_2O\cdot CH_3CH_2OH$ (**1.22**). Each constituent MOF is uniquely coloured and the transformations occur in response to solvent exchange as indicated by the arrows.[92]

3DB-SPCs have further been shown to breathe as a function of gas uptake. Recently, Schröder *et al.*[93] studied the interpenetrated framework $(Me_2NH_2)_{1.75}[In(L)]_{1.75}(DMF)_{12}(H_2O)_{10,}$ NOTT-202, where L is biphenyl-3,3′,5,5′-tetra(phenyl-4-carboxylic acid). This system of interpenetrating networks expands upon removal of the guest molecules to form a new interpenetrating net $[Me_2NH_2]_{1.75}[In(L)]_{1.75}$, NOTT-202a which expands as the temperature is increased. Gas adsorption results on NOTT-202a showed additional flexibility in response to CO_2 adsorption and desorption.[93]

Applications of SPCs

The versatility of breathing MOFs opens up a novel field of research unattainable in zeolitic materials. In addition to performing many of the applications

found in second generation MOFs, the flexible frameworks offer new opportunities for applications. One of the innovative applications of breathing MOFs is in the field of molecular magnetism, where structural transitions may change the interactions between paramagnetic ions from antiferro- to ferro-magnetic such as in Dunbar's $[Cu(tzc)(dpp)]_n \cdot 2H_2O$ (**1.23**), a MOF assembled from 1D chains.[94] The copper ions in this MOF switch from being antiferromagnetically coupled in its dehydrated phase to ferromagnetically coupled when hydrated, acting like a magnetic sponge for applications in small molecule sensing.

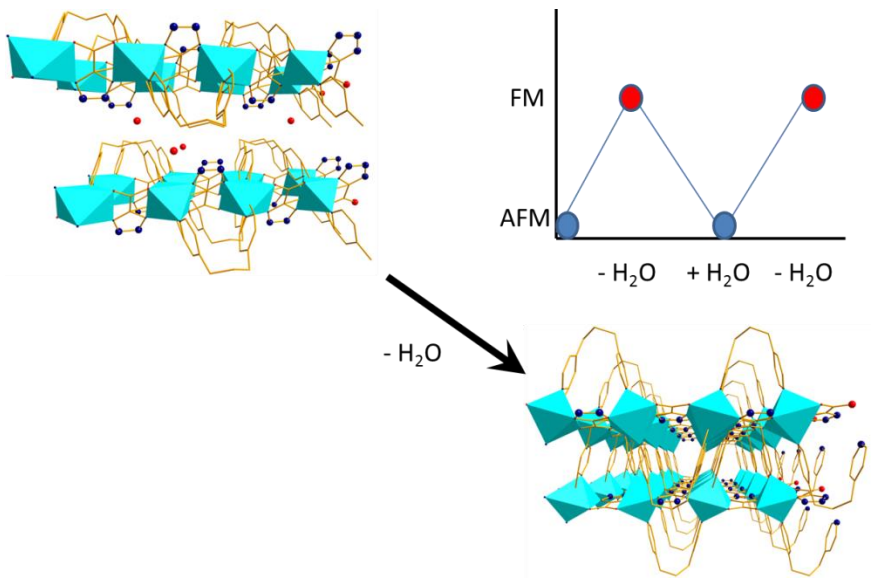

Figure 1.28: Transformation of the SPC, $[Cu(tzc)(dpp)]_n \cdot 2H_2O$ (**1.23**) leading to a change in magnetic long-range ordering upon dehydration and rehydration. The Cu(II) coordination spheres are shown as teal polyhedra.[94]

Additionally, SPCs comprising paramagnetic ions have been exploited as potential refrigerants by utilising the magnetocaloric effect.[95] The magnetocaloric effect is an observable physical phenomenon where the temperature of a material

increases or decreases in response to a changing external magnetic field.[95] Du *et al.* prepared $[Mn(Me\text{-}ip)(DMF)]_n$ (**1.24**), where Me-ip = 5-methylisophthalate, which undergoes a CAC phase transition upon the removal and uptake of DMF guest molecules within the lattice. The crystal phase exhibits the highest magnetocaloric effect for a Mn^{2+}-based material to-date and the amorphous phase is capable of acting as a DMF sensor due to the change in magnetic response as it adsorbs and desorbs DMF molecules.

Compounds such as Dunbar's single chain magnetic switch (**1.23**)[91] and Du's flexible MOF **1.24**[95] are multidisciplinary, lying at the interface of supramolecular chemistry and molecular magnetism. Therefore, these materials are inherently challenging as they require a broad knowledge of both research fields. This multidisciplinary approach is frequently employed in the Pilkington research group which gives rise to remarkable diversity in the individual projects within the group. The next section of the introduction reflects this diversity and reviews the field of magnetochemistry that is relevant for Project 2 presented in Chapter 3 of this thesis.

1.2: Molecular Magnetism

Molecular magnetism is an area of research that investigates the magnetic behaviour of materials comprised of discrete molecules.[96] Given the breadth of systems studied in this field, for practical reasons, only the field of single molecule magnets is briefly reviewed in this section.

1.2.1: Traditional *vs* Molecule-based Magnets

Throughout history, what we refer to as "magnets" are bulk materials of micrometer or larger dimensions in which each paramagnetic ion in the material contributes to the bulk magnetic behaviour through co-operative spin-spin interactions. The theory and synthesis of such traditional magnets is now well-established affording a number of important materials over the centuries that include the magnetic compass.[97] In present-day technology, conventional magnetic materials are inorganic metals, their oxides or alloys (e.g. Fe, Fe_2O_3, Cr_2O_3, $SmCo_5$ and $Nd_2Fe_{14}B$), which are typically formed *via* high temperature and pressure or metallurgical processes.[98] The synthetic strategy employed for the preparation of these compounds is therefore limited to elemental doping. Furthermore, the high temperatures and pressures required for their preparation offers little opportunity for chemical tuning of their structural and physical properties.[99] In large part the processing technology associated with traditional magnets has already been optimised, yet, as technology advances, engineers continue to seek further miniaturisation which is rapidly approaching the limits of 'top down' technology.[100] The magnetic properties of conventional materials rely on the energy stored in domain wall boundaries with domains typically on the micron scale. Further miniaturization to sub-domain particle size leads to a loss of hysteresis (magnetic memory) and formation of a superparamagnetic material. Consequently the domain size provides a lower limit to how small the material can be to exhibit a conventional magnetic response. In many cases the (non-uniform) distribution of particle sizes at/near the

domain-limit, renders them unsuitable for mass distribution and electronic applications.[101]

In contrast to traditional magnets, molecular or molecule-based magnets are materials assembled from discrete molecules, typically organic radicals and/or paramagnetic metal complexes, *via* a 'bottom-up' strategy. In these systems, elements are positioned in discrete molecular building blocks by employing modern organic and coordination chemistry methodologies that in part gives more control over their structural and physical properties. Within the large field of molecular magnetism, the family of 'single molecule magnets' are notable as (i) their size is typically in the nanometer dimension (substantially smaller than single domain particles) and (ii) their molecular nature means the particle sizes are mono-disperse.[102]

While the field of molecular magnetism not only provides a platform for theoreticians and physicists to test and refine models,[101] developments in the field of molecular magnetism have also led to significant achievements toward the realization of quantum computing leading to significant advancements in the fields of molecular spintronics[103] and molecular magnetic switches.[104] In order to address the current challenges in this field, it is important to first have a solid understanding of the general principles of magnetism, which are reviewed briefly in the next section.

1.2.2: Principles of Magnetism

Most of our theoretical understanding in the field of magnetism comes from research carried out over the past two centuries, particularly the electromagnetic studies of the 19th century and our understanding of the quantum origin of magnetism throughout the 20th century. Although one of the earliest recognized natural

phenomena, magnetism still remains a very complex field of research, where theoretical models are constantly being refined to account for new types of magnetic behaviour, that include for example slow relaxation of magnetisation within single discrete molecules.[105]

Origin of the Magnetic Phenomenon

Our current model of the atom suggests that a magnetic moment is produced by the motion of an unpaired electron traveling in a potential generated by the attractive forces between the electron and the nucleus, and the repulsive forces between the electrons. This potential acting on the electron gives rise to three quantum numbers, *n*, *l* and *m*, used to describe the wave-function of the electron in a given state. In this context, *n* is the principle quantum number, which determines the radial expansion of the wave function, such that, a greater *n* reflects a more extended wave function; *l* is the orbital quantum number, which determines the value of the kinetic orbital momentum, $\langle l^2 \rangle = l(l+1)$ and *m* describes the projection of the kinetic orbital moment. Each of these sets of numbers are quantized meaning they can only have integer values, where $n = 1, 2, 3\ldots$; $l = 0, \ldots, n\text{-}1$; $m = -l, \ldots, 0, \ldots, +l$.[106]

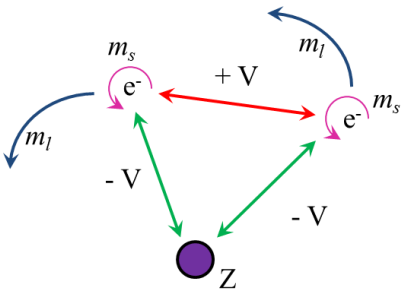

Figure 1.29: A representation of a helium-like atom. The constituent particles feel the attractive (green) and repulsive (red) forces between one another to generate a potential, *V* which may be repulsive (electron-electron repulsion) or attractive (electron-nuclear attraction). Electrons have two components to their spin: the intrinsic m_s (purple) spin and the orbital angular m_l spin (blue).

An electron in an atom not only travels around the nucleus, but it also spins on its own axis, analogous to the motion of Earth around the Sun. This generates two components to the magnetic moment, one from the orbital motion, m_l, and one from the intrinsic spin of the electron, m_s. The orbital magnetic moment relates to the kinetic orbital moment by $m_l = -\mu_B l$, and the intrinsic kinetic moment of the electron, *s*, relates to the spin magnetic moment by $m_s=-2\mu_B s$, where μ_B is a Bohr magneton and *s* has possible values of ± ½. Therefore, the total electronic magnetic moment, m_T, is simply a sum of these two contributions, $m_T = -\mu_B(l + 2s)$. Most elements in the Periodic Table have many electrons and in these cases the total magnetic moment of the atom or ion is the sum of the magnetic moments generated by each electron. This leads to two contributions again, one for the orbital moments $L = -\mu_B \sum m_l$ and one for the intrinsic spin moments $S = -2\mu_B \sum_i s_i$. In a filled shell, the magnetic moments cancel out leading to a nullification of these summations. Therefore, with respect to our earlier claim, the observed magnetic moment of an atom or ion is due to the

presence of unpaired electrons. Atoms or ions with no unpaired electrons are termed diamagnetic, whereas when species with unpaired electrons are classed as being paramagnetic.[106]

Temperature dependence of the dc-magnetic susceptibility

The magnetic properties of compounds are typically studied by measuring the magnetic response or susceptibility of the compound when magnetized in the presence of an applied magnetic field. In this context, the magnetic susceptibility, χ, is defined as the change in magnetisation, *M*, with a change in the external applied magnetic field, *H*, i.e. $\chi = \partial M/\partial H$. Provided *H* is small then the change in *M* with *H* is essentially linear and we can approximate $\chi \approx M/H$.

The magnetic susceptibility (χ) is typically measured using a **S**uperconducting **QU**antum **I**nterference **D**evice (SQUID); a very sensitive instrument that detects the magnetic response of a sample when subjected to a static dc-magnetic field.[107] The temperature dependence of χ provides important information about the magnetic properties of the sample. Magnetic susceptibility was first studied by Pierre Curie and his theories were later expanded on by Pierre Weiss. Curie and Weiss found that for many paramagnetic materials magnetic susceptibility follows the following law:

$$\chi = \frac{C}{T - \theta} \qquad \textit{Eq. 1.1}$$

where θ is the Weiss constant and *C* is the Curie constant which is defined as:

$$C = \frac{\mu_B^2}{3k_B} N g^2 J(J+1) \qquad \textit{Eq. 1.2}$$

In this equation, k_B is the Boltzmann distribution constant, *N* is Avogadro's number and g is the Landé g-factor, whose value depends on the environment of the unpaired

.electrons. A paramagnetic ion with a thermally well-isolated magnetic ground state typically obeys Curie behaviour (θ = 0 K). However any system which exhibits a distribution of magnetic states will also give rise to deviation from Curie Law ($\theta \neq 0$). There are several origins for non-zero θ:

Magnetic exchange interactions: The presence of significant magnetic exchange interactions (*vide infra*) which give rise to a distribution of different spin states (rather than a single configuration for an ideal Curie paramagnet). Each spin state, S_i, has its own unique susceptibility, χ_i. However on changing the temperature the population of the different S_i states changes and the resultant magnetic response changes with temperature. Deviations from ideal Curie behaviour are given by the Weiss constant θ. A negative θ indicates dominant antiferromagnetic interactions between spins whereas positive θ reflects local ferromagnetic interactions between neighbouring spins. The magnitude, $|\theta|$, reflects the strength of the magnetic exchange coupling (***J***) between spins.

Spin-Orbit coupling: The second phenomenon which can give rise to non-zero θ is spin-orbit coupling. For first row transition metal ions with residual orbital angular momentum (e.g. Co^{2+} with a ^4T spin ground term, coupling of S = 3/2 with an effective orbital contribution L_{eff} = 1) can give rise to a series of effective J states ranging from $|S + L_{eff}|$ to $|S - L_{eff}|$, separated by λJ_{eff}. Since each J_{eff} state has its own unique χ, we again expect a temperature dependence of χ due to depopulation of

excited J_{eff} states. In this case θ correlates with the magnitude of the spin orbit coupling constant, λ ($10^1 - 10^2$ cm^{-1} for first row transition metal ions).

Zero-field splitting: The presence of magnetic anisotropy which can arise from unquenched orbital angular momentum (L), structural or crystalline anisotropy all contribute to a phenomenon known as zero field splitting, denoted by the term ***D***. The zero-field splitting term D splits the energy of the M_S states of the ground term S according to:

$$E(M_s) = g\beta H M_s + D M_s^2 \qquad \textit{Eq. 1.3}$$

The presence of this zero field splitting term leads to differing populations of the M_S states (in relation to $\boldsymbol{D} = 0$) and the magnetic susceptibility which depends upon the thermal population of these M_S states is consequently varied. Here $|\theta|$ reflects the magnitude of ***D*** (typically $10^1 - 10^{-2}$ cm^{-1}).

Crystal Field Splitting, D: For lanthanide ions the magnitude of the crystal field ($\Delta \sim 10^2$ cm^{-1}) is much smaller than the spin-orbit coupling constant ($\lambda \sim 10^3$ cm^{-1}). Using a perturbation approach the magnetism of lanthanides depends on the ground state $^{2S+1}L_J$ and follows Eq. 1.1 and Eq. 1.2 in the high temperature region. However at low temperature the presence of the small crystal field splits the degeneracy of the M_J states of the J ground term into a series of Stark sub-levels.(micro-states). Once again thermal depopulation effects within this set of sub-levels gives rise to deviation from ideal Curie behaviour.

It is evident that although many metal ions exhibit Curie-Weiss behaviour in the high temperature regime, interpretation of the Weiss constant, θ, must be treated carefully as there are multiple origins for such deviations from Curie behaviour and

may have more than one origin. Figure 1.30 depicts the characteristic susceptibility curves for an arbitrary sample with different values of θ.

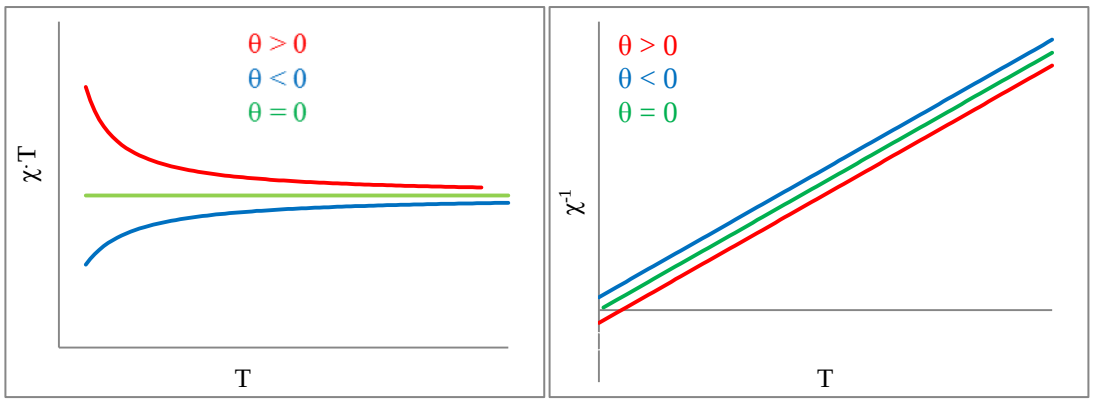

Figure 1.30: Illustration of the temperature dependence of χT (left) and $1/\chi$ *vs* T (right) for $\theta > 0$ (red), $\theta = 0$ (green) and $\theta < 0$ (blue).

Field dependence of the magnetisation.

To understand how the magnetisation changes with applied magnetic field, we consider the effect of a magnetic field on the energies of the M_S states. The spin ground state S comprises a series of M_S sub-levels which are quantized with values ranging from $+S \ldots -S$ e.g. for $S = 1$, M_S levels comprise $M_S = +1, 0, -1$. As described in Eq. 1.3 the energies of the M_S levels are affected by an applied field (since the energy of the electron aligning with or against the applied field are different). Ignoring zero field splitting then in zero field all three micro-states ($M_S = +1, 0, -1$) are degenerate and there are as many 'spin up' electrons as 'spin down' and no magnetisation is expected. However when a field is applied the degeneracy of these M_S states is lifted and the population of the $M_S = -1$ state is greater than the $M_S = +1$ state and a magnetisation is induced in the sample. The induced magnetisation

therefore depends upon the applied field which splits the states and the thermal energy *kT* which describes the Boltzman population of these states. In large applied fields and at low temperatures only the ground state is populated and the magnetization saturates. The saturation of the magnetization can be described by the Brillouin function (Eq. 1.4) and is shown in Figure 1.31.

$$B_J(x) = \frac{2J+1}{2J}coth\left(\frac{2J+1}{2J}x\right) - \frac{1}{2J}coth\left(\frac{1}{2J}x\right) \qquad \textit{Eq. 1.4}$$

$$where\, x = \frac{g\mu_B\mu_0 JH}{k_B T} \qquad \textit{Eq. 1.5}$$

$$and\, M = NgJ\mu_B B_j(x) \qquad \textit{Eq. 1.6}$$

Consistent with previous equations, g is the Landé g-factor, μ_B is the Bohr magneton, k_B is the Boltzmann constant, and μ_0 is the magnetic permeability of a vacuum. Note in a small applied field (or at high temperature) the ratio *M/H* is approximately constant so the susceptibility χ describes the linear dependence of *M vs H* in a small applied field well before saturation is achieved.

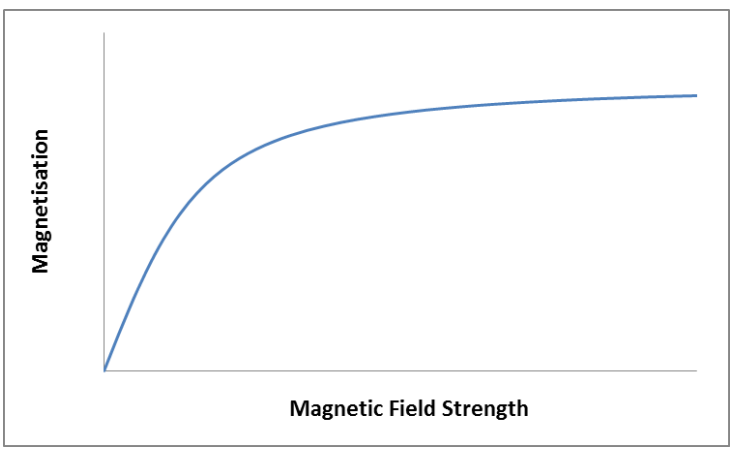

Figure 1.31: Plot showing the relationship between an increasing magnetic field strength, *H* and the magnetisation, *M*, of a sample according to the Brillouin function, Eq. 1.4.

In the presence of local ferromagnetic interactions the magnetisation rises more rapidly than that expected based on independent spins and in the superparamagnetic region (all spins interact ferromagnetically but particles are below domain size), the magnetisation rises dramatically and quickly saturates. When a field is applied in the opposite direction, the spins realign with the field and a magnetisation is induced in the opposite direction.

For long range ordered systems such as ferromagnets where particles are larger than the size of a single domain then hysteresis is often observed below the magnetic ordering temperature T_C. Now, when a magnetic field is applied to the sample, the sample magnetisation rises rapidly to saturation but when the magnetic field is switched off, the material remains magnetised. This arises because of energy stored in domain walls. Consider an ensemble of spins which are all ferromagnetically coupled. At 0 K they all align coparallel but at $T > 0$ K entropy can be maximised by taking macroscopic regions (domains) and re-orienting the spins with respect to other domains. Within each domain the spins align coparallel but domains point in different orientations. Energy is therefore stored in domain wall boundaries. When a large field is applied, work is put in to align the domains coparallel. When the field is switched off, entropy will work to randomise some of these domains but a net magnetisation is retained in the sample in zero field known as the remnant magnetisation, $\boldsymbol{M_{rem}}$. A field has to be applied in the opposite direction to realign the domain wall boundaries and the field required to reduce the magnetisation to zero is known as the coercive field, $\boldsymbol{H_{co}}$. The magnitude of the remnant magnetisation and the coercive field therefore define the *hysteresis loop* while the area bound by the loop relates to the energy stored

in the domain wall boundaries. Materials with large coercive fields are known as *hard* or *permanent* magnets and used for example as the magnets used to pin notes to a refrigerator. Conversely, if a small magnetic field is required to demagnetise the sample, then the loop is narrower and this material is termed a *soft* or *dynamic* magnet. The 'memory' of soft magnets is easily switched/lost and soft magnetic materials are used in data storage, credit cards etc.

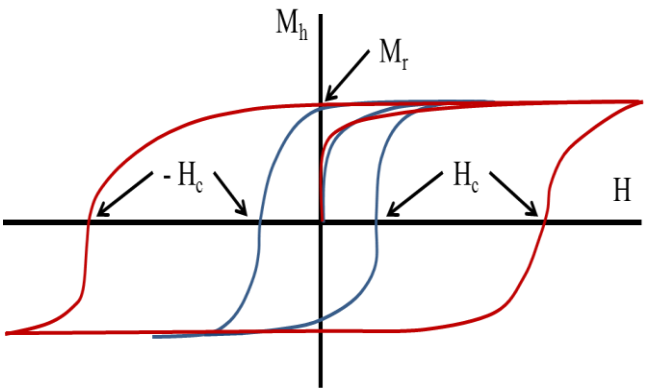

Figure 1.32: Depiction of hysteresis loops for both a hard (red) and soft (blue) magnet.

Over the past two decades, a new family of compounds have been discovered within the field of magnetism known as single molecule magnets or SMMs. These compounds are typically coordination complexes of paramagnetic transition metal and/or lanthanide ions. They display a unique type of hysteresis in which the nature of the hysteresis is of molecular origin rather than arising through the movement of domain walls. [108] The research objectives of Project 2 of this thesis are to develop new strategies for the design, synthesis and study of Ln-based SMMs, and so a brief introduction to the field of SMMs is presented.

1.2.3: Single-Molecule Magnets (SMMs)

SMMs are molecular compounds where the presence of magnetic hysteresis does not arise from ferro- or ferri-magnetic particles greater than the size of a magnetic domain, but due to complex magnetism arising within individual molecules typically of nanometer dimensions.[108] The lower size limit for the observation of hysteresis in these systems is lifted offering exciting potential for data storage at the molecular level.[103]

Transition metal SMMs:

A large number of polynuclear transition metal complexes have been reported, and in a number of cases, the combination of ferromagnetic (and antiferromagnetic) interactions within the molecule leads to a non-zero spin ground state, S_T.[109] The energies of the M_S levels associated with this 'total spin' ground state S_T are given by Eq. 1.3. In the presence of zero-field splitting, the energies of the $\pm M_S$ states are not degenerate in zero-field.[109] When $\boldsymbol{D} < 0$ (a so-called Ising spin system) the $\pm M_{S(T)}$ states lie lower in energy than the $M_S = 0$ state by an energy term $|\boldsymbol{D}|S_T^2$ (for integer values of S_T). The ground state is described as a Kramers doublet (KD) since it is associated with the two configurations, $+M_{S(T)}$ and $-M_{S(T)}$.[110] At low temperature, in zero field, both of these states are initially equally populated. As a field is applied the $+M_{S(T)}$ microstate is destabilised and the $-M_{S(T)}$ state is stabilised. In a large field the $-M_{S(T)}$ state is fully populated and the magnetisation is saturated. When the field is switched off, the $\pm M_{S(T)}$ states become degenerate once more but the population is initially 100% $-M_{S(T)}$. Classical thermal relaxation requires depopulation of the $-M_{S(T)}$

state and population of the $+M_{S(T)}$ state via the intermediate M_S states, i.e. over the energy barrier $U = |\boldsymbol{D}|S_T^2$.[110]

For example slow relaxation of magnetization in a single molecule was first observed by Christou *et al.* in 1993. The polynuclear cluster commonly known as Mn_{12}, $[Mn_{12}O_{12}(O_2CCH_3)_{16}(H_2O)_4]\cdot 4H_2O\cdot 2CH_3CO_2H$ (**1.25**) is comprised of eight Mn^{III} and four Mn^{IV} ions, giving rise to a total spin ground state of $S_T = 10$.[111] The complex exhibited strong uniaxial anisotropy, which split the $S_T = 10$ spin ground state into 21 M_S microstates, where M_S takes values from -10 to +10. The zero-field splitting parameter, $\boldsymbol{D}$, was found to be -0.50 cm^{-1} such that the energy barrier for thermal relaxation, $DS_T^2 \approx 50$ cm^{-1}. Impressively, at 1.5 K the relaxation of the magnetisation is so slow that it is hardly measureable and is predicted to take months, making Mn_{12} one of the most extensively studied compounds in the field of molecular magnetism to date.

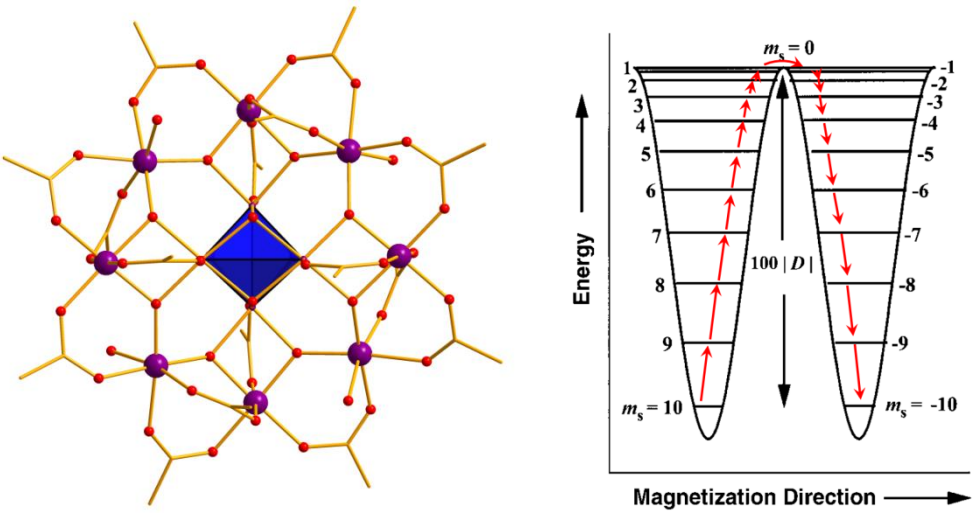

Figure1.33: Left: Molecular structure of Mn_{12} (**1.25**).[111] The central Mn^{4+} core is shown as a blue polyhedron. The outer Mn^{3+} ions are plotted as purple spheres. Diagram showing the slow relaxation of magnetisation of Mn_{12} *via* intermediate spin states adapted from ref 108. The spin states are plotted as energy *vs* magnetic moment and the red arrows show the thermal relaxation path of magnetisation over the anisotropy barrier.

For large spin ground states and/or zero field splitting then this energy barrier can be considerable and thermal relaxation can be quenched. The rate of relaxation follows the Arrhenius Law (*vide infra*). This slow relaxation of magnetisation is a characteristic feature of SMMs and leads to the observation of magnetic hysteresis at low temperatures, Figure 1.32. At low temperature the lifetime is long and the sample is expected to stay magnetized and hysteresis can be detected in SMMs below a *blocking temperature*, T_B.[108]

A second relaxation process known as quantum tunnelling can also occur even if $kT << U$. Here relaxation occurs by tunnelling between degenerate energy levels through the energy barrier. The ability to tunnel through the energy barrier also depends upon the transverse component of the zero-field splitting, ***E***, i.e. the energy

variation in the *xy* plane perpendicular to the magnetization axis (*z*). As the energies of the different spin states vary as a function of applied field, then the rate of quantum-tunneling is a function of the applied field with rapid relaxation occurring when microstates are degenerate. This leads to characteristic steps in the experimental hysteresis loop.

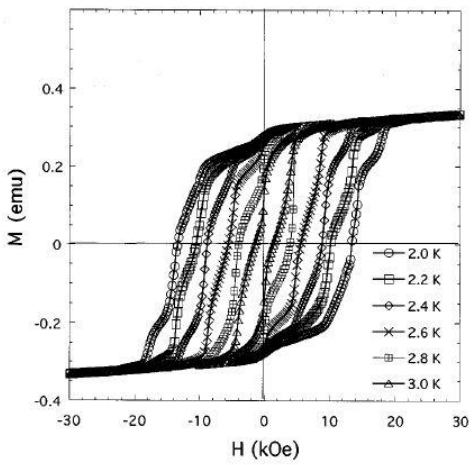

Figure 1.34: A hysteresis plot of the Mn_{12} complex showing the periodic steps due to the resonant tunnelling of the spin. Reproduced with permission from reference 112.

Following the success of Mn_{12}, researchers focused their attention on preparing high nuclearity transition metal clusters with large spin ground states in order to increase their anisotropy barriers for practical applications. From these early endeavours researchers discovered an octanuclear Fe^{3+} cluster, $[Fe_8O_2(OH)_{12}(tacn)_6]Br_8$,[113] (**1.26**) which, like Mn_{12}, also has a spin ground state of $S = 10$ arising from the alignment of its Fe^{3+} spins.[114] The magnetic properties however are quite different since the Fe^{3+} atoms form several triangles which lead to spin frustration.

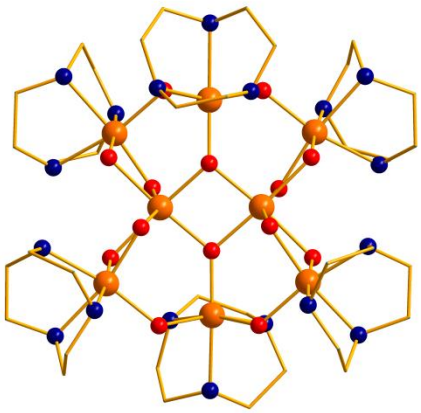

Figure 1.35: Molecular structure of the Fe_8 cluster **1.26** with the Fe^{3+} ions plotted as orange spheres.[113]

These two examples show the success of maximising *S* to obtain an appreciable anisotropy barrier, however, it has been shown that this is not always the case since for many of the larger clusters, the anisotropy barrier is substantially diminished. This drawback is prominently observed in the mixed-valence manganese cluster, $[Mn^{3+}_{12}Mn^{2+}_{7}(\mu_4\text{-}O)_8(\mu_3,\eta^1\text{-}N_3)_8(HL)_{12}(MeCN)_6]Cl_2\cdot 10MeOH\cdot MeCN$ (**1.27**) (H_3L = 2,6-bis(hydroxymethyl)-4-methylphenol) by Powel *et al.*[115] The ferromagnetic interactions between the twelve Mn^{3+} ions and the seven Mn^{2+} ions results in a spin ground state of 82/2, however, a small anisotropy barrier of 4 cm^{-1} is observed.

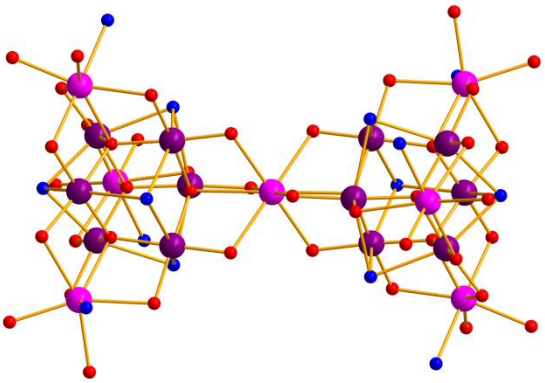

Figure 1.36: Core structure of **1.27** where the seven Mn^{2+} ions are pink and the twelve Mn^{3+} ions are purple.[115]

To account for this deviation in expectations, the total magnetic anisotropy of the molecule needs to be considered. In transition metals, the local crystal field of the individual ions affects the projections of the anisotropy axes, leading to some non-commuting anisotropy axes. In larger polynuclear clusters, there is a wider range of deviations in the crystal field which leads to a larger number of these non-commuting anisotropy terms. Therefore, since the total anisotropy term is a summation of all the anisotropy projections in the molecule, there is an inevitable decrease in the axial anisotropy as the transverse (non-commuting) anisotropy term, *E* increases for each paramagnetic ion in the molecule.[116]

Despite this drawback, there are now many polynuclear transition metal clusters with SMM properties reported in the chemical literature, several families of which are extensively studied, remaining among the most promising candidates for applications in new technologies, such as, high density data storage and molecular spintronics.[117] However, in response to addressing the magnetic anisotropy, some

researchers have looked beyond transition metal polynuclear clusters to lanthanide ions, which due to their unique electronic properties has afforded a new class of SMMs (*vide infra*).

Lanthanide SMMs

Nearly ten years after the first SMM was published, researchers began to investigate Ln^{3+} ions as alternatives to transition metal ions due to their unusually high intrinsic anisotropy and high spin ground states.[118] In addition to the strong spin orbit coupling, the 4*f* wave-functions are radially contracted such that the 4*f* orbitals have little to no effect on chemical bonding and as a result, the crystal field induces only slight perturbations to the magnetic spin states.[119] In this context, the strong spin-orbit coupling in Ln^{3+} ions is considered first to identify the $^{2S+1}L_J$ ground state of the lanthanide ion and then the effect of the crystal field is considered which splits the degeneracy of the $2J+1$ degenerate m_J states with values ranging from $-J$ to $+J$. If J is a half integer number then it is found that the $2J+1$ states will reduce to a series of doublets, termed *Kramers* doublets after the Dutch physicist, Hans Kramers. Each Kramers doublet (KD) consists of states with equal but opposite magnetic moments ($\pm M_J$) which typically exhibit strong uniaxial anisotropy, affording Ising-like states. When J is an integer number, the $2J+1$ microstates reduce to a series of KD plus a unique singlet $M_J = 0$ microstate. These new states that arise from the application of a crystal field are termed *microstates* or *Stark sublevels*. From a mathematical point of view the wavefunctions of these microstates are described as linear combinations of the m_J states unless the molecule has $C_{\infty v}$, $D_{\infty h}$ or D_{4d} symmetry, in which case there is

no microstate mixing and the Stark sublevels reduce to pure M_J states.[123] The separation of these KD depends upon both the symmetry and magnitude of the crystal field. The first lanthanide SMMs were reported by Ishikawa *et al.*[120] in 2003, comprising of a single Ln^{3+} ion sandwiched between two dianionic phthalcyanine (Pc) ligands. In these complexes the geometry of the Ln^{3+} ion is square antiprismatic, giving rise to a crystal field with D_{4h} symmetry, Figure 1.40. In their preliminary investigation, the Dy^{3+} and Tb^{3+} complexes not only displayed hysteresis but were also the first single ion magnets exhibiting large effective energy barriers. Numerous derivatives of the diphthalocyanine complex, $Ln(Pc)_2^-$, have since been reported resulting in an anisotropy barrier of 651 cm^{-1} for a *p*-terbutylphenoxide substituted Pc derivative.[121]

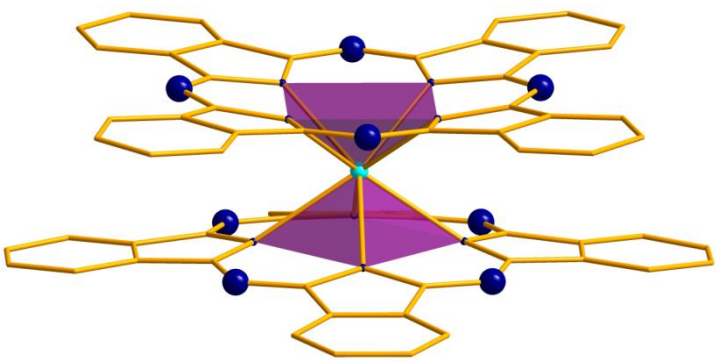

Figure 1.37: Molecular structure of Ishikawa's $[Ln(Pc)_2]^-$ complex.[120] Hydrogen atoms are omitted for clarity. The nitrogen atoms are represented as blue spheres with the central lanthanide ion is coloured teal where Ln^{3+} = Dy, Tb. A purple polyhedron is used to emphasise the coordination sphere of the Dy^{3+} ion.

Recent *ab initio* studies suggest that the magnetisation relaxes predominantly by the first excited KD, which suggests that the size of the barrier should reflect the magnitude of ZFS between the ground and first excited doublet.[122] This is only true if quantum tunneling mechanisms are supressed in the ground state which for Kramers ions occurs when the transversal anisotropy of the ground state is suppressed and the axial anisotropy approaches the Ising limit of $g_x=g_y < 0.5$ and $g_z=20$.[122]

There are three main relaxation mechanisms by which an SMM can return to its equilibrium state: (i) direct relaxation, (ii) Raman processes and (iii) Orbach processes. In direct relaxation, a transition occurs exclusively between microstates *via* thermal energy exchange within the lattice.[123] Raman processes are a type of spin-lattice relaxation mechanism where a phonon from the lattice excites an electron to a new microstate and the spin relaxes by a virtual state of the lattice to the opposite ground microstate.[123] Orbach processes are akin to Raman processes except that thermal energy from the lattice incites a spin transition, followed by a relaxation to the ground state.[123]

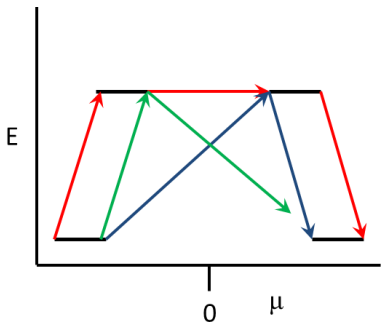

Figure 1.38: Plot of microstates (black) as energy *vs* magnetic moment. The arrows show the different relaxation processes where red is direct relaxation, green is Raman and Blue is Orbach.

Dy^{3+}-based SMMs:

Of the 14 elements in the lanthanide series, the vast majority of Ln-based SMMs are assembled from Dy^{3+}ions. The choice of Dy^{3+} is based on the fact that the $^{2S+1}L_J$ ground term for lanthanides uses the largest *J* ground term for lanthanides with a greater than half-filled shells which affords a large ground state magnetisation. In addition ions with integer *J* exhibit a singlet configuration $M_J = 0$ amongst their KD which can facilitate rapid relaxation. Therefore later lanthanides with large half-integer *I* values are the most favoured Ln^{3+} ions for forming SMMs. For Dy^{3+} the crystal field will split the degeneracy of the $^6H_{15/2}$ multiplet[124] to generate eight KD. Research towards the discovery of Dy^{3+} SMMs with high energy barriers for practical applications has in recent years, as one might expect been extensively geared towards optimising the ligand field of these complexes.

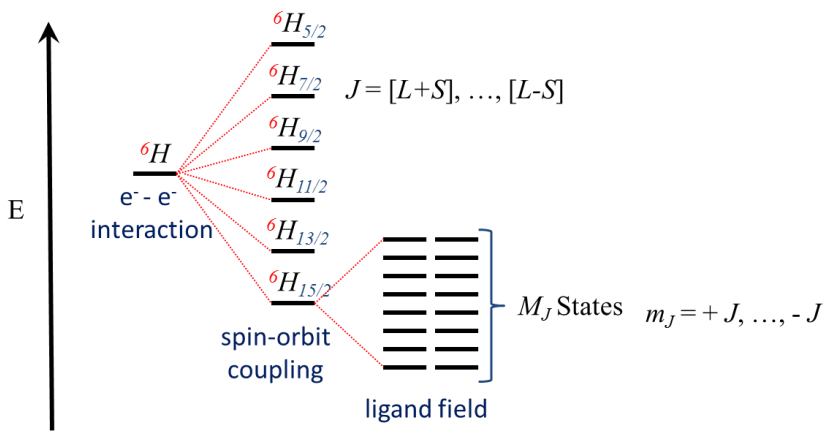

Figure 1.39: Truncated electronic structure diagram for a Dy^{3+} ion.

One of the most important conclusions to come out of detailed studies on Ishikawa's $Ln(Pc)_2^-$ complexes is the effect of symmetry on the anisotropy barrier.

Furthermore, it has since been determined that there is also relationship between the symmetry of the coordination environment and the orientation of the easy axis of magnetization. This relationship was first investigated by Sessoli *et al*. studying $Na[Dy(DOTA)(H_2O)]\cdot 4H_2O$ (**1.24**), Figure 1.40.[125] In this complex, the Dy^{3+} ion has nine-coordinate capped square anti-prismatic geometry with the coordinated water lying along the C_4 axis. To probe the direction of the easy axis of magnetisation, single crystal magnetic susceptibility measurements were carried out which revealed that the main magnetic axis of the ground state resides along the principle axis of the ligand field symmetry. *Ab initio* calculations of the multi-configurational type arrived at the same conclusions; thus, further supporting this claim that the axis of highest symmetry will be the direction of the main magnetic axis in the ground state.

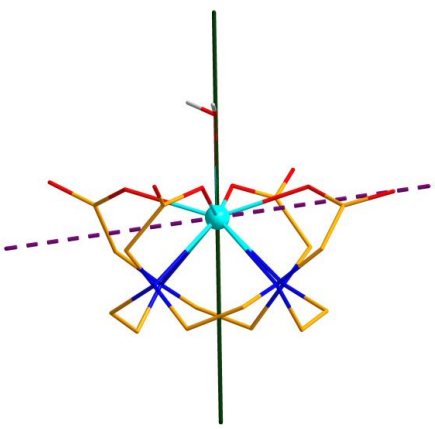

Figure 1.40: Crystal structure of $Na[Dy(DOTA)(H_2O)]\cdot 4H_2O$ (**1.24**). H-atoms, Na^+ ions and non-coordinating H_2O molecules are omitted. The C_4 axis is shown in dark green and the ground state magnetic axis is shown as a dashed purple line. A coordinated H_2O molecule is shown lying along the C_4 axis of the capped square antiprismatic geometry.[125]

Recently, the group of Winpenny *et al*.,[126,127] have exploited this symmetry relationship to prepare mononuclear Dy-based SMMs with remarkably high

anisotropy barriers. An impressive example is the recently published, bis(methanediide)-Dy^{3+} complex (**1.25**), Figure 1.41.[128] The unique feature of this system is the C=Dy=C linkage along the principle C_4 axis of this molecule which leads to an appreciable charge accumulation along this axis. As a result, the complex 'mimics' the electronic arrangement of a high symmetry linear, two-coordinate Dy^{3+} ion. Consequently, this complex has one of the largest anisotropy barriers reported to date (U_{eff} = 565 cm^{-1}) for a monometallic Dy^{3+} complex, which is consistent with previously reported calculations involving linear systems.[129]

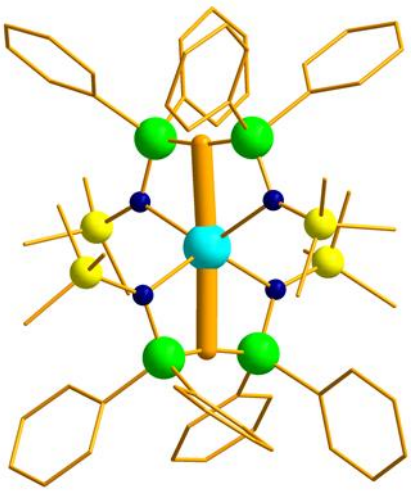

Figure 1.41: Molecular structure of (**1.25**) showing the C=Dy=C axis. P- and Si-atoms are coloured green and yellow, respectively. H-atoms are omitted for clarity.[128]

Unfortunately, synthesising linear Dy^3 complexes is inherently challenging due to the preference of Ln^{3+} ions for higher coordinate geometries, as previously explained. Additionally, many of the low coordinate Dy^{3+} SMMs are organometallic or air sensitive, which adds an extra element of difficulty for manufacturing and use in practical applications. In contrast, other low coordinate geometries are now under

critical examination, specifically the D_{5h} pentagonal bipyramidal geometry. It has been shown that by employing this local D_{5h} symmetry with negatively charged axially coordinating ligands, QTM can be suppressed which subsequently enhances the anisotropy barrier for high performance SMMs.

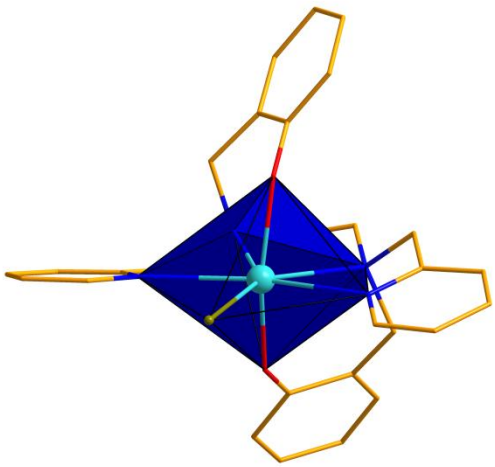

Figure 1.42: Crystal structure of (**1.26**). The distorted pentagonal bipyramidal geometry is highlighted by the blue polyhedron. The Br^- ion is shown as a brown sphere. The hydrogen atoms are omitted.

By exploiting this symmetry, Tong *et al.* was able to synthesis a SMM with a record high anisotropy barrier of over 1000 K. In their complex [Dy(bbpen)Br] (**1.26**) where bbpen = N,N′ - bis(2-hydroxybenzyl) - N,N′ - bis(2-methylpyridyl)ethylenediamine),[130] a five-coordinate equatorial plane is formed by the four weakly donating N-atoms of bbpen and a bromine atom, whereas the two axial positions are occupied by the negatively charged phenyl O-atoms of the bbpen ligand, Figure 1.42. The reason that this is such a desirable arrangement of donor atoms is because of the shape of the electron density of Dy^{3+} ions. In Dy^{3+}, the *f*-

electron density adopts a disk-like orientation that expands out equatorially, termed oblate (Figure 1.43). For this reason it is beneficial to have electron-withdrawing donor atoms in the equatorial plane and charged electron-rich donor atoms in the axial positions in order to reduce the electron-electron repulsion between the *f*-electrons of the Dy^{3+} ions and the electrons of the donor atoms. The result is an enhanced oblate electron density and therefore an enhanced axial anisotropy.

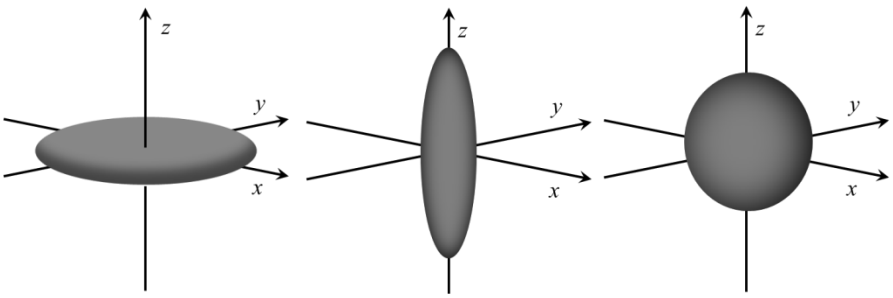

Figure 1.43: Electron density of Ln^{3+} ions. Left: oblate, middle: prolate, right: spherical.

Another successful example of this geometry applied to SMMs is the Fe(II)-Dy^{3+} (**1.27**) complex synthesised by Tong, *et al*.[131] which displays a high effective energy barrier of 319 cm^{-1}. In this complex, the origin of the SMM behaviour is single-ion with respect to the lanthanide, but in addition to the pentagonal bipyramidal geometry, the anisotropy barrier is enhanced by the presence of nearby transition metals, Figure 1.44. The effects of the transition metals are two-fold. Firstly, the electron withdrawing effects of the Lewis acidic transition metal can enhance the anisotropy of an oblate lanthanide if located in the equatorial plane. This occurs by pulling the electron density of the equatorial donor atoms away from the *xy*-elongated *f*-electron density; thus, causing a greater *xy*-expansion and increased directional dependence of the magnetic anisotropy. The second effect is due to the dipolar

alignment. Similar to transition metal clusters, the cooperative alignment of neighbouring dipole moments increases the single ion-anisotropy of the Ln^{3+} ion.

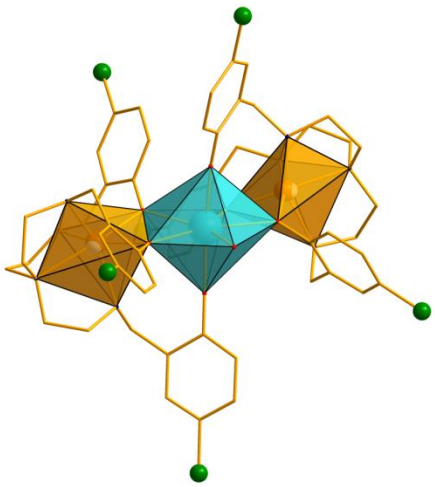

Figure 1.44: Molecular structure of Tong's $Fe^{2+}Dy^{3+}$ trinuclear mixed 3*d*-4*f* complex. The pentagonal bipyramidal geometry of the Dy^{3+} ion is depicted as a teal polyhedron and the Fe^{2+} coordination sphere is depicted in orange.[131]

Oblate electron density is observed for other lanthanide elements, such as, Ce^{3+}, Pr^{3+}, Nd^{3+}, Tb^{3+} and Ho^{3+}, whereas, some Ln^{3+} ions adopt an axially elongated electron density, termed prolate, which is observed for Pm^{3+}, Sm^{3+}, Er^{3+}, Tm^{3+} and Yb^{3+}. For these ions the opposite donor atom situation is desirable, where the equatorial atoms are electron rich and the axial donor atoms are electron withdrawing. Gd^{3+} is unique by adopting a spherical electron density, thus making it isotropic. Although not interesting from a SIM point of view, Gd^{3+} complexes are useful as MRI contrast agents.

Characterising SMMs

In the last few sections we have examined the ideas of Kramers doublet ground states, energy barriers to relaxation via thermal and quantum tunnelling relaxation mechanisms in both transition metal and lanthanide SMMs. In this section we examine in more detail the physical studies necessary to probe these relaxation processes.

For transition metal complexes the presence of exchange coupling (ferro- or antiferro-magnetic) between metal ions can lead to a complex evolution of χT upon cooling. In favourable (higher symmetry systems), detailed modelling of the exchange interactions can be used to estimate the spin ground state and determine the energy of low-lying excited states. In addition M *vs* H measurements at low temperature can provide information on the likely magnetic ground state and |D|. For lanthanide complexes computational studies can evaluate the relative energies of the different M_J states and their g-values from which both M *vs* H and χ(T) *vs* T data can be modelled. All of these studies give information on the energetics of the system, but do not directly probe the kinetics or mechanisms of relaxation.

In favourable cases of very slow magnetic relaxation such as was observed for Mn_{12}, a plot of M *vs* time at low temperature can be used to probe the relaxation pathway according to:

$$M = M_0 e^{\frac{U_{eff}}{kT}} \qquad \textit{Eq. 1.7}$$

However, in many cases the relaxation is too rapid to be measured in this fashion. In such instances ac susceptibility is used. In a typical ac-susceptibility experiment, the sample is placed in a zero dc-field with a small ac field (typically *ca.* 3 – 5 *Oe*)

applied of frequency ω. This oscillating applied field produces a time dependent magnetisation in the sample. In the high temperature region the system acts as a simple paramagnet and the magnetisation is entirely in phase with the applied field. In this case the in-phase susceptibility χ' is equivalent to the dc susceptibility, χ and the out-of-phase susceptibility, χ'', is zero. For SMMs, at low temperature slow relaxation of the magnetisation occurs and the sample magnetisation is no longer able to follow the alternating field and an out-of-phase response becomes evident at low temperature heralding the onset of slow relaxation of the magnetisation. At lower ac frequencies, the induced moment is able to perfectly follow the oscillations in the applied field and the out-of-phase component is only observed at low temperature. Conversely at higher frequencies, the induced magnetic moment lags behind the drive frequency due to the dynamics in the sample resulting in a phase shift with respect that field, with high frequency ac fields revealing out of phase components at elevated temperatures. The onset of an out-of-phase signal and a frequency dependence of the ac data are therefore diagnostic of SMM behaviour. For systems with very rapid quantum tunnelling a small dc field (typically < 1000 Oe) can be applied to remove the degeneracy of the $M_{S(T)}$ (transition metal based SMMs) or M_J states (lanthanides) to reduce quantum tunneling mechanisms.

The ac-susceptibility yields two pieces of information, the magnitude of the in-phase and out of phase components of the magnetic susceptibility, χ' and χ'' where:

$$\chi' = \chi cos\varphi \text{ where } \chi = \sqrt{\chi'^2 + \chi''^2} \quad \text{Eq. 1.8}$$

$$\chi'' = \chi sin\varphi \qquad \varphi = \arctan\left(\frac{\chi''}{\chi'}\right) \quad \text{Eq. 1.9}$$

From the ac-susceptibility measurements, the dynamics of the magnetisation can be investigated by constructing a Cole-Cole plot, i.e. by plotting the values of χ'' *vs.* χ'. The complexity of the Cole-Cole analysis is directly proportional to the complexity of the relaxation mechanisms in the compound under investigation.[124] For a single relaxation process at a single temperature, *T*, and constant magnetic field, *H*, the ac susceptibility, χ_{AC}, at a given oscillation frequency, ω, follows the Debye function:

$$\chi_{AC}(\omega) = \chi_s + \frac{\chi_T - \chi_s}{1 + i\omega\tau} \quad \text{Eq. 1.10}$$

where χ_S is the adiabatic susceptibility, χ_T is the isothermal susceptibility and τ is a time constant describing the relaxation time at a specific temperature.[132] During an ac-experiment, the frequency of the oscillating magnetic field is varied at each temperature where the low frequencies ($\omega < \tau^{-1}$) allow the complex to thermally equilibrate and the high frequencies ($\omega > \tau^{-1}$) result in a net lag of the magnetisation. Consequently this experiment yields semicircles in the Cole-Cole plot whose maxima on the χ' axis correspond to a frequency ω such that $\omega^{-1} = \tau_c$, where τ_c is the temperature specific relaxation time, Figure 1.45.[124]

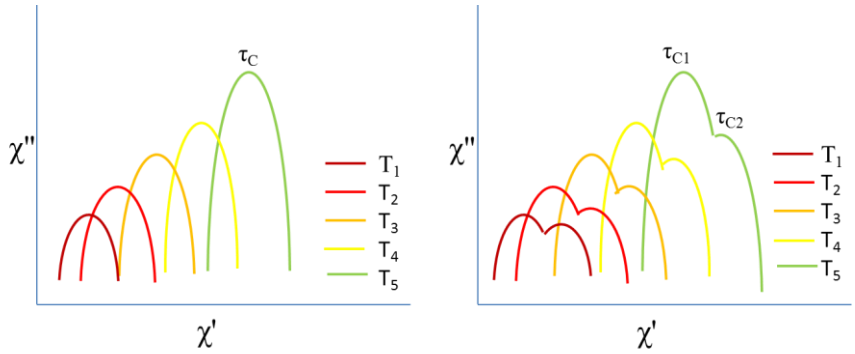

Figure 1.45: Left, Cole-Cole plot of a compound having one prominent relaxation mechanism. Right, Cole-Cole plot of a compound having two dominant anisotropy barriers.[124]

Many materials, however, do not have a single relaxation time constant and therefore the Debye function is modified to the Cole-Cole expression to compensate for the multiple τ values at a given temperature:

$$\chi_{AC}(\omega) = \chi_S + \frac{\chi_T - \chi_S}{1 + i\omega\tau^{(1-\alpha)}} \qquad \text{Eq. 1.11}$$

In the Cole-Cole expression, α is the Cole-Cole parameter having values of $0 < \alpha < 1$.[133] When α is zero then there is a single relaxation time constant and the equation reduces back to the Debye function. Alternatively, when α is 1 then this represents an infinite number of relaxation time constants. Thus, α is a reflection of the distribution of relaxation times in the system. A more complex situation arises when the complex relaxes *via* multiple relaxation mechanisms, but this is beyond the scope of this thesis.[134]

The significance of the Cole-Cole plot as applied to SMMs is that it offers a series of values for the relaxation times, τ_c, of a particular magnetic relaxation mechanism associated with an energy barrier, U_{eff}. This relationship between the relaxation times and the energy barrier is described by the Arrhenius equation:

$$\tau_c = \tau_o e^{\frac{U_{eff}}{kT}} \qquad \textit{Eq. 1.12}$$

Where τ_o is the relaxation time associated with a specific U_{eff} and k is the Boltzman constant. This equation can be converted the equation of a straight line ($y = mx + b$) by taking the natural logarithm of this equation:

$$ln(\tau_C) = \frac{U_{eff}}{k} \cdot \frac{1}{T} + ln(\tau_0) \qquad \textit{Eq. 1.13}$$

where the y-intercept is $\ln(\tau_0)$ and the slope is the energy barrier U_{eff}/k (in K) , when a plot of $\ln(\tau_C)$ versus T^{-1} is constructed. These ac studies can therefore provide a detailed insight into the relaxation processes operative in the system and the rates of relaxation associated with each process.

An important advancement in Ln-based SMM chemistry is the integration of powerful computational methods. The groups of Chibotaru, Sessoli and Ruiz in particular have made remarkable advancements towards understanding the complicated relaxation mechanisms found in Ln-SMMs by implementing a theoretical approach.[135] Unfortunately, due to the intricate electronic nature of these elements, it is not possible to analyse these systems with single-determinant methods. Instead, researchers have employed the computationally heavy *multiconfigurational theory*.[136] To perform these calculations, many groups use the quantum chemistry software package, MOLCAS.[137] A brief review of the software and the theory will be provided in the final section of this chapter.

1.3: Introduction to MOLCAS and Post Hartree-Fock Methods

1.3.1: MOLCAS

MOLCAS is an *ab initio* software package developed at Lund University for the treatment of general electronic structure problems, dealing with both the ground and excited states of molecules.[137] The appeal of MOLCAS is that it is capable of treating highly degenerate states that include excited states, transition states, and other complicated systems, with a high degree of accuracy. These systems in particular are challenging to work with because a single-reference approach (MP2, CC, CPF, DFT *etc*.) is not able to treat them with the precision required to reliably elucidate the system. For this reason MOLCAS is optimised to use the multi-configurational (MC) approach where it not only includes code for self-consistent field (SCF) calculations at the complete active space (CASSCF) level, but also includes procedures for restricted multiconfigurational SCF (MCSCF) wave functions (RASSCF). To treat dynamic correlation effects in multi-configurational calculations, MOLCAS is equipped with the CASPT2 procedure which uses second order perturbation theory to apply a correction to the MCSCF wave functions for these effects. MOLCAS is also capable of calculating molecular properties using the MCSCF wave functions in a state interaction procedure (RASSI) which can take into account obscure effects such as strong spin orbit coupling. The treatment of scalar relativistic contractions is easily adhered to by using the Douglas-Kroll-Hess (DKH) transformations of one-electron integrals. The basis set library ANO-RCC (atomic natural orbitals with relativistic contractions) is included in the MOLCAS package which includes basis sets that are optimised for DKH transformed integrals and also includes the correlation of semi-

core orbitals. Unfortunately, the type of problems that MOLCAS is optimised for cannot be solved using black box methods and thus, MOLCAS is not a black box program making it inherently challenging to use for the novice chemist. Even though one does not need to know the gritty details of the calculations, one does need to be familiar with the types of calculations performed and the physical meaning of the wave functions. A chemist should be able to use their chemical intuition to guide them through the calculations in order to produce physically meaningful results. In the next section, an overview of the calculation methods used in this thesis will be presented.

1.3.2: Introduction to Hartree-Fock Calculations

Self-Consistent-Field Procedure

At the turn of the 20th century three experiments yielded insight into the quantised nature of elementary particles and their wave nature: black-body radiation, the photoelectric effect, and the hydrogen emission spectrum.[138] The latter experiment revealed the quantised nature of an electron existing in an atom following the theoretical work of Bohr.[139] Schrödinger and Heisenberg separately developed a differential wave function formulation and matrix formulation for this observation, respectively, both of which agreed very well with experimental observations for simple systems.[140,141] Since Heisenberg's matrix formulation used mathematical objects that contemporary physicists were unfamiliar with, Schrödinger's equation was preferred and is shown here in its familiar form:

$$\hat{H}\Psi = E\Psi \qquad \textit{Eq. 1.14}$$

Here, $\hat{H}$, is the Hamiltonian operator indicated by the circumflex above the 'H', E is the average energy value of an electron existing in a specific state and Ψ is an eigenfunction of the Hamiltonian operator that represents the total overall wave function of the atom. An eigenfunction is any function that satisfies the above equation for a specific operator; it is a 'characteristic' function of an operator. Not all functions for a given operator are eigenfunctions. It is understood from this equation that if the electronic wave function, Ψ, is an eigenfunction of $\hat{H}$, then $\hat{H}$ operating on Ψ is equal to a constant multiplied by Ψ such that the constant is equal to the total average energy of Ψ. For this reason, $\hat{H}$ is actually the energy operator.

Schrödinger's and Heisenberg's theories, however, completely fall apart when considering more than one electron in an atom or molecule which includes nearly all materials of interest. The problem arises due to the fact that the Hamiltonian operator includes an electron-electron repulsion term as a function of the distance between two electrons. It is impossible to know the relative positions of the electrons to one another and therefore it is impossible to solve the equation using this operator. As an example, consider the Schrödinger equation of the He atom:

$$\left[-\frac{h^2}{8\pi^2 m}(\nabla_1^2 + \nabla_2^2) - \frac{Ze^2}{4\pi\varepsilon_0 r_1} - \frac{Ze^2}{4\pi\varepsilon_0 r_2} + \frac{e^2}{4\pi\varepsilon_0 r_{12}}\right]\Psi = E\Psi \qquad \textit{Eq. 1.15}$$

where h is Plank's constant, m is the mass of an electron, Z is the atomic number of the atom, e is the charge in Coulombs, ε_0 is the permittivity of free space, r_n is the distance between the nucleus and electron n and r_{12} is the distance between electrons 1 and 2. The symbol, ∇^2, is the Laplacian operator baring the namesake of Pierre-

Simon Laplace and is read as, *del squared*. ∇^2 is the partial second derivative operator in three dimensions:

$$\nabla^2 = \frac{\delta^2}{\delta x^2} + \frac{\delta^2}{\delta y^2} + \frac{\delta^2}{\delta z^2} \qquad \textit{Eq. 1.16}$$

In the Hamiltonian of the He atom, there are five terms when we exclude relativistic effects and magnetic effects. The first two terms correspond to the kinetic energies of electron 1 and electron 2, the third term is the attraction term between electron 1 and the nucleus, the forth term is the attraction between the electron 2 and the nucleus and the fifth term is the repulsion between electron 1 and electron 2 corresponding to the diagram of a He atom in Figure 1.46.

One might expect that the nuclear-electronic attraction terms would make this problem unsolvable, but this can be treated with the Born-Oppenheimer approximation due to the thousand-fold difference in the velocity of the two particles. It is the fifth term of the Hamiltonian that causes all of our problems since it is impossible to determine the relative positions of the electrons to one another at any given time and therefore the equation cannot be split into two one-electron systems like the Hydrogen atom which can be solved exactly. This *many-body problem* is not particularly new and even Isaac Newton acknowledged this problem in his *Philosophiæ Naturalis Principia Mathematica* when trying to treat celestial objects with classical mechanics.[142]

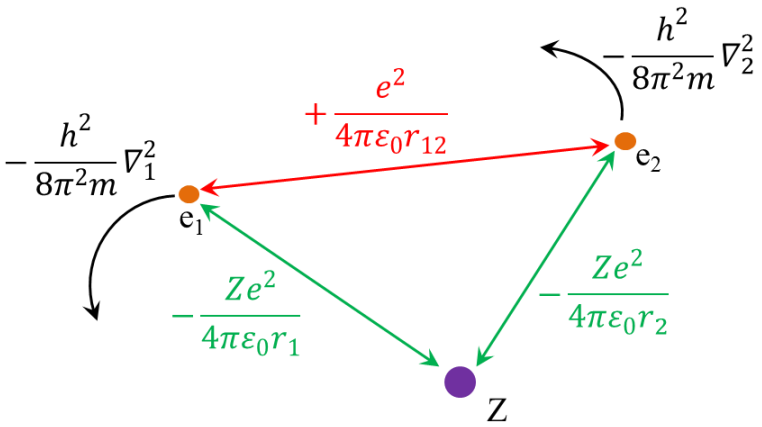

Figure 1.46: Depiction of a He-like atom, *Z*, showing the origin of the Hamiltonian describing the state of the system. Each of the arrows represents a contribution to the total energy of this atom where green is the attractive force between each electron and the nucleus, red is the repulsive force between the two electrons and black is the kinetic energy of each electron. The Hamiltonian terms are found next to each arrow and are colour-coded accordingly.

In order to solve this problem, Hartree devised a method to predict the true total polyelectronic wave function, Ψ as a product of one electron functions known now as the *Hartree product*.[143] The one-electron wave functions are atomic (or molecular) orbitals where $\psi_n(1)$ is the wave function of electron 1, $\psi_n(2)$ is a wave function of electron 2 and so on. To apply the Hartree process, an initial guess, Ψ_0, of the real wave function is made:

$$\Psi_0 = \psi_0(1)\psi_0(2)\psi_0(3)\ldots\psi_0(n) \qquad \textit{Eq. 1.17}$$

The zeroth order approximation, $\psi_0(1)$ is used to solve a one-electron Schrödinger equation for electron 1. where the electron-electron repulsion term is approximated as a static energetic potential due to electron 1 moving in an electrostatic field of smeared out electron density from all other electrons in the atom or molecule. Solving this equation, $\psi_1(1)$ is obtained as an improvement over $\psi_0(1)$ which is then

used as part of the electrostatic field for a calculation of electron 2. Continuing this procedure for all the electrons in the system yields the first refined total wave function Ψ_1:

$$\Psi_1 = \psi_1(1)\psi_1(2)\psi_1(3) \ldots \psi_1(n) \qquad \textit{Eq. 1.18}$$

Performing this cycle again will give an even more refined wave function Ψ_2. After *k* cycles, the energy calculated from Ψ_k is essentially the same as Ψ_{k-1}, which indicates that the electrostatic field used to account for electron-electron repulsion terms has ceased to change from one cycle to the next, that is, it is "consistent with" the field of the previous cycle and thus this is called the *self-consistent-field* (*SCF*) *procedure*.

Slater Determinants

An obvious problem with Hartree's procedure is that electrons have a spin which leads to the fact that a maximum of two electrons can occupy an orbital (Pauli Exclusion Principle). In the Hartree procedure, this is treated in an *ad hoc* fashion by simply not putting more than two electrons in an orbital. Another problem arises from the fact that electrons are indistinguishable which means that if two electrons switch positions then their wave function must either remain the same or change sign, that is, they are either symmetric or antisymmetric with respect to exchange, respectively. Based on experimental evidence, the electronic wave functions are antisymmetric and such particles are referred to as Fermions, baring the namesake of Enrico Fermi (1901-1954). Therefore, any theoretical treatment of electrons should use antisymmetric wave functions, but the Hartree product is a symmetric wave function with respect to the spatial coordinates (termed, spatial orbital).

To combat these shortcomings, Slater developed a function for *spin orbitals*.[144] Spin orbitals are described as the product of a spatial orbital and a spin function α or β, which have a spin coordinate denoted as ξ. α and β are both eigenfunctions of the $\widehat{S_z}$ operator and only have one eigenvalue each, as shown in the following equations:

$$\widehat{S_z}\alpha = \frac{1}{2}\cdot\frac{h}{2\pi}\alpha \; and \; \widehat{S_z}\beta = -\frac{1}{2}\cdot\frac{h}{2\pi}\beta \qquad \textit{Eq. 1.19}$$

In these equations, the spin function is zero unless $\xi = \pm 1/2$(spin function). The spin of an electron is more ubiquitously referred to by its spin quantum number m_s which, as previously shown, can only have possible values of ± ½ where an electron is said to have up-spin if m_s = + ½ and down-spin if m_s = – ½. This is sometimes denoted by representing electrons as arrows, ↑ and ↓ for up-spin and down-spin, respectively.

In addition to using spin orbitals, the Slater wave function also uses a mathematical object known as a determinant to solve the systems of equations instead of using the Hartree product. For example, we will consider a four electron closed-shell molecule. In this four electron system, we require two spatial orbitals since each spatial orbital can hold up to two electrons. From these two spatial orbitals, four spin orbitals exist, such that, there is an α and β spin orbital generated from each of the two spatial functions. Since the Hartree-Fock method does not restrict the electrons to specific orbitals, our determinant must include terms for each electron existing in each spin orbital. Figure 1.47 shows the construction of a Slater determinant for a four electron system.

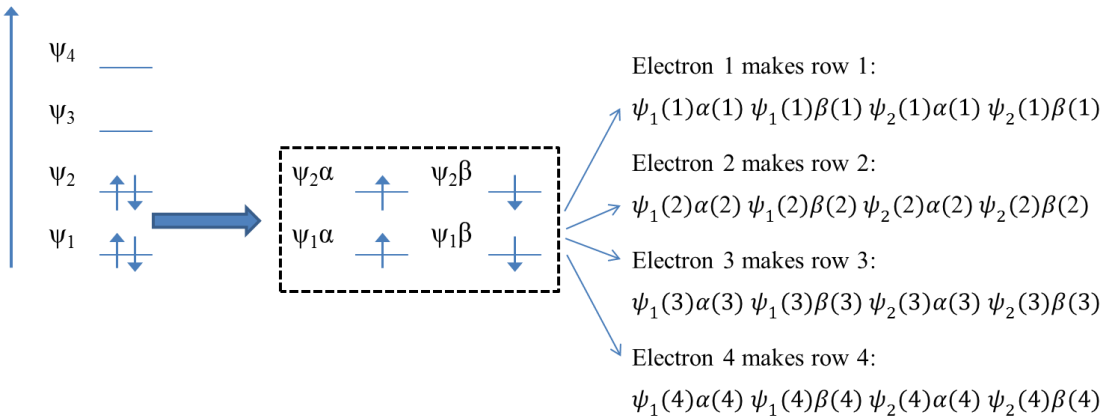

Figure 1.47: Construction of Slater determinant for a four electron closed-shell molecule. The first row of the determinant has four terms: one for the occupation of each spin orbital by electron one. Rows two to four follow the same methodology for their construction except that instead of using electron 1 they are constructed using electrons 2 to 4, respectively.

Our Slater determinant for this four electron system is then:

$$\Psi = \frac{1}{\sqrt{4!}}\begin{vmatrix} \psi_1(1)\alpha(1) & \psi_1(1)\beta(1) & \psi_2(1)\alpha(1) & \psi_2(1)\beta(1) \\ \psi_1(2)\alpha(2) & \psi_1(2)\beta(2) & \psi_2(2)\alpha(2) & \psi_2(2)\beta(2) \\ \psi_1(3)\alpha(3) & \psi_1(3)\beta(3) & \psi_2(3)\alpha(3) & \psi_2(3)\beta(3) \\ \psi_1(4)\alpha(4) & \psi_1(4)\beta(4) & \psi_2(4)\alpha(4) & \psi_2(4)\beta(4) \end{vmatrix} \qquad \textit{Eq. 1.20}$$

The $\frac{1}{\sqrt{4!}}$ term is a *normalisation* factor used to ensure that the wave-function squared integrates to 1 over all space.

The antisymmetric nature of the Slater determinant enforces the Pauli Exclusion Principle which states that two particles in the same quantum system cannot be described by identical quantum numbers. If two particles had the same quantum numbers then two rows would be identical, and the determinant would vanish to zero; thus upholding the Pauli Exclusion Principle. For any closed-shell system, the general Slater determinant would be:

$$\Psi_{2n} = \frac{1}{\sqrt{2n}} \cdot \begin{vmatrix} \psi_1(1)\alpha(1) & \psi_1(1)\beta(1) & \psi_2(1)\alpha(1) & \psi_2(1)\beta(1) & \dots & \psi_n(1)\beta(1) \\ \psi_1(2)\alpha(2) & \psi_1(2)\beta(2) & \psi_2(2)\alpha(2) & \psi_2(2)\beta(2) & \dots & \psi_n(2)\beta(2) \\ \vdots & \vdots & \vdots & \vdots & & \vdots \\ \psi_1(2n)\alpha(2n) & \psi_1(2n)\beta(2n) & \psi_2(2n)\alpha(2n) & \psi_2(2n)\beta(2n) & \dots & \psi_n(2n)\beta(2n) \end{vmatrix}$$

In this equation Ψ describes the total molecular wave-function and each spatial function ψ represent a region of space for two electrons to occupy. The spatial function may represent two electrons in a bond or a lone pair of electrons, but in many cases the spatial function describes a region of space that may extend over parts of the molecule. We call the spatial function a molecular orbital (MO).

Calculating the Energy of a System

Once we have a reasonable approximation of Ψ, the energy of a system is given by:

$$E = \frac{\int \Psi^* \hat{H} \Psi d\tau}{\int \Psi^* \Psi} \qquad \textit{Eq. 1.21}$$

The energy that is calculated from this equation is the *expectation value* of the Hamiltonian operator. For a given operator, an expectation value is the quantum mechanical average value of the physical quantity that is represented by the operator. This is only true if the wave function and the operator are exact descriptors of the system. It is postulated that there is a quantum mechanical operator for every measureable property.

At this point, we do not have an exact wave function but we have the Slater determinant described in the previous section. The Slater determinant is an appropriate approximation of the true wavefunction. As a wave function it is possible that Ψ is a complex function which is allowed by using its *complex conjugate*, Ψ^*, where every i in Ψ is $-i$ in Ψ^* ($i = \sqrt{-1}$). By using the complex conjugate, it is

ensured that the energy, *E*, of the system is a real number. In this equation the functions are integrated with respect to three spatial coordinates and one spin coordinate symbolised as the infinitesimal of τ where $d\tau = dxdydzd\xi$. If the wave functions are normalised then the denominator is unity and the equation reduces to:

$$E = \int \Psi^* \hat{H} \Psi d\tau \qquad \textit{Eq. 1.22}$$

For an arbitrary molecule with 2*n* electrons and *m* atomic nuclei, we can substitute in a generalized expression for the Hamiltonian which is simply an extension of the Helium Hamiltonian (Eq. 1.23)

$$\hat{H} = \sum_{i=1}^{2n} -\frac{1}{2}\nabla_i^2 - \sum_{all\ m,i} \frac{Z_m}{r_{mi}} + \sum_{all\ i,j} \frac{1}{r_{ij}} \qquad \textit{Eq. 1.23}$$

An experienced quantum chemist would realise that this is actually an expression for the electronic Hamiltonian. The nuclear-nuclear repulsion terms have been omitted by the Born-Oppenheimer approximation. This is simply accounted for by adding a correction potential at the end of the calculation using the following expression:

$$V_{NN} = \sum_{all\ \mu,\nu} \frac{Z_\mu Z_\nu}{r_{\mu\nu}} \qquad \textit{Eq. 1.24}$$

When the appropriate Hamiltonian and Slater determinant are substituted into the expression for energy and after much algebraic manipulation, the expression for the energy of a system can be described as:

$$E = 2\sum_{i=1}^{n} H_{ii} + \sum_{i=1}^{n}\sum_{j=1}^{n} (2J_{ij} - K_{ij}) \qquad \textit{Eq. 1.25}$$

For the sake of brevity, the derivation of this function will not be presented here but can be found in reference 145. In this new expression for energy, there are three distinct terms: H_{ii}, J_{ij} and K_{ij}. The H_{ii} term calculates the attractive forces between a

single electron moving through the molecule and the nuclei with all other electrons omitted. For electron 1, it is therefore expressed as:

$$H_{ii} = \int \psi_i^*(1)\hat{H}_{core}(1)\psi_i(1)dv \qquad \textit{Eq. 1.26}$$

With all the other electrons stripped away, the Hamiltonian represents the attractive force between the *core* (nuclei) of the molecule and a single electron plus the kinetic energy of the electron moving against the nuclear potential. Hence, $\hat{H}_{core}$ is expressed as:

$$\hat{H}_{core}(1) = -\frac{1}{2}\nabla_1^2 - \sum_{all\ \mu}\frac{Z_\mu}{r_{\mu 1}} \qquad \textit{Eq. 1.27}$$

For the rest of the electrons in the molecule, the terms are constructed similarly. The next term is the J_{ij} term. This term calculates the electrostatic repulsion between an electron in ψ_i and an electron in ψ_j or rather the repulsion between the respective charge clouds. An expression for the J_{ij} is such:

$$J_{ij} = \int \psi_i^*(1)\psi_i\left(\frac{1}{r_{12}}\right)\psi_j^*(2)\psi_j(2)dv_1 dv_2 \qquad \textit{Eq. 1.28}$$

The K_{ij} term arises naturally from the Slater determinant expansion terms and takes into account the exchange of electrons. A physical description of the *K* integrals can be quite challenging, but it is often speculated that the *K* integrals represent an *exchange force*. However, it is clear from Eq. 1.29 that the *K* integrals provide a correction to the *J* term by reducing the charge cloud repulsion. With antisymmetric wave functions, two particles can occupy the same orbital if they have opposite spins, but if they have the same spin then they cannot. The strictly coulombic integrals of *J* do not take these factors into account and so we may consider the *K* terms as correcting for Pauli Exclusion Effects. *K* integrals are expressed as:

$$K_{ij} = \int \psi_i^*(1)\psi_j^*(2)\left(\frac{1}{r_{12}}\right)\psi_i(2)\psi_j(1)dv_1 dv_2 \qquad \textit{Eq. 1.29}$$

Following on from the Hartree product method, the *J* and *K* integrals allow for the electron moving in a molecule to feel the smeared out electron density of the other electrons in the molecule. This, however, leads to a major deficiency of the Hartree-Fock method because the electron-electron repulsion terms of the actual point charges are overestimated by electron-electron cloud repulsion terms. Several endeavours have been made since the introduction of the Hartree-Fock procedure and we classify these enhanced methods as *Post Hartree-Fock* (HF) methods.[146]

1.3.3: Post-Hartree-Fock Calculations

Electron Correlation

To approach the electron-electron repulsion term the way Hartree did was revolutionary, although it still makes predictions that are too far from the actual physical observations. The problem of electron-electron repulsion is referred to as *electron correlation*.[147] This follows from the fact that the motion of electrons depends on one another; they are *correlated*.

The difference in energy between the calculated value and the true value is referred to as the *correlation energy*.[147] Correlation energy is typically divided into two types: *dynamic* correlation and *static* correlation energy.[148] Dynamic correlation arises from not allowing the electrons to be sufficiently separated. Generally, dynamic correlation is what we consider for the correlation energy. Static correlation energy is a consequence of using a single determinant method, such as, the HF method.

Variational Theorem

For the real picture of a molecule, the electrons are able to avoid one another better than an electron moving in an electric field; therefore, this means that the true energy of a molecule is lower than the predicted energy from HF calculations. In fact, any method that uses this type of function will yield an energy that is greater than the real energy since every function of this type is an approximation of the real wave function. Methods of this nature are said to be *variational* and the preceding logic has been compiled into what is known as the *Variational Theorem.*[149] It should be noted that not all quantum mechanical methods are variational and some may give energies that are lower than the true value.

By applying the Variational Theorem, it is easy to test the quality of a method by comparing the magnitudes of the energies that they provide. The lower the energy, the closer it is to the experimentally measured energy.[146] It is possible to minimize the energy calculated from the HF method by MOs that are constructed from the linear combination of a very large number of atomic functions (basis functions), but there exists a limit where the energy levels off. We call this the HF limit.[146] The energy is also minimized using *Lagrangian Multipliers*, but this method too only minimizes the energy to a certain extent. Therefore, there have been methods that extend beyond the limitations of the HF method that focus on treating the electron correlation problem. We call these methods the *Post*-HF methods. There are two main treatments of electron correlation for the *ab initio* HF method; these are Møller-Plesset (MP) theory[150] and Configuration Interaction (CI) methods.[151]

Møller-Plesset Theory

MP theory was first described in 1934 by the Danish physicist Møller and the American physicist Plesset.[150] It was later improved upon by Binkley and Pople.[152] The fundamental philosophy behind MP theory is that a complicated realistic system can be treated the same way, mathematically, as a simple idealised system by applying a small perturbation to the treatment of the simple system. This type of mathematical treatment is called perturbation theory.

There are different degrees of perturbations in MP theory; each successive perturbation further improves on the calculation.[146] These perturbations are symbolised as MP0, MP1, MP2, *etc.* The starting point of this theory is MP0 which describes the energy obtained by summing the one-electron integrals. MP1 is the first correction to the MP0 treatment by including the *J* and *K* integrals to treat the coulombic and exchange interactions between the moving electron and the smeared out electrostatic field.[149] At this point it should be clear that MP1 is just the HF treatment of the electronic energy and MP2 (second order perturbation) is the first treatment to go beyond the HF method. MP2 is often considered the first level of MP theory and is expressed as:

$$E_{MP2} = E_{HF}^{total} + E^{(2)} \qquad \textit{Eq. 1.30}$$

With respect to this equation, the $E^{(2)}$ term is the perturbation to the HF energy.

The MP2 level includes a correction term that is purely electronic as opposed to the HF term which has internuclear repulsions. This correction term treats the electron correlation problem by allowing the electrons to be sufficiently separated; thus, reducing the energy of the system. MP2 correction is achieved by summing a

series of terms that model the *double excitations* of pairs of electrons into higher energy virtual orbitals.[153] Allowing the occupation of empty orbitals by electrons of the HF system means the electrons have more room and are better able to avoid each other. Higher level MP corrections are also possible by allowing the excited states to interact with one another (MP3) and even by allowing the singly, doubly, triply and quadruply excited state states into the calculation (MP4).[146] When discussing post-HF methods, it is important to mention MP theory, however, the calculations included in this thesis make use of *configuration interaction methods*.

Configuration Interaction and the Multiconfigurational Methods

Between MP and CI methods, the principle for treating electron correlation is same in that electrons can avoid each other better if they are allowed to partially occupy virtual excited orbitals.[146] The difference between these two methods is the mathematical approach to such a philosophy. In the CI method, the idea is simple in that the HF wave function can be improved upon by the addition of terms that represent promoted electrons.

To explain the principles behind CI methods, the four electron closed-shell example from section 1.3.2 will be used. The Slater determinant for the ground state is constructed from two spatial orbitals which when multiplied by spin functions yields four spin orbitals as in the determinant of Eq. 1.33.[144] What was omitted in our discussion before is that the spatial component of the MO, ψ, is actually a linear combination of functions, ϕ, called basis functions where m basis functions generate m MOs.[144] There are many different types of basis functions that can be used, but for the most part these functions represent some form of atomic orbital. There is also no

limit to the number of basis functions that can be used for each spatial MO as mentioned when discussing the HF limit. The spatial component of the MO is then constructed as:

$$\psi_i = \sum_{s=1}^{m} c_{si}\phi_s \;\; i = 1,2,3,\ldots,m \qquad \textit{Eq. 1.31}$$

As the equation suggests, each basis function contributes to the description of the component MO. The degree to which a function contributes to the spatial MO is represented by a constant, c_{si}, which is the constant multiplied by the s^{th} basis function of the i^{th} MO. Therefore, the idea here is that larger basis sets should give better representations of the component MOs, but in the HF method there exists a limit where the number of basis functions no longer reduces the energy of the system (HF limit).

To move beyond this limit of the HF method, the CI method extends the total electronic wave function to include excited virtual MOs.[154] Since the electronic wave function includes excited MOs, this means that the electrons may partially occupy these states. The total electronic wave function can then be expressed as a linear combination of Slater determinants; one for each ground or excited electronic configuration:

$$\Psi = c_1 D_1 + c_2 D_2 + c_3 D_3 + \cdots + c_i D_i \qquad \textit{Eq. 1.32}$$

Similar to the construction of MOs, each Slater determinant contributes a finite amount to the description of the total electronic wave function which is represented by the constant, c. To understand how the excited Slater determinants are constructed, consider Figure 1.48.

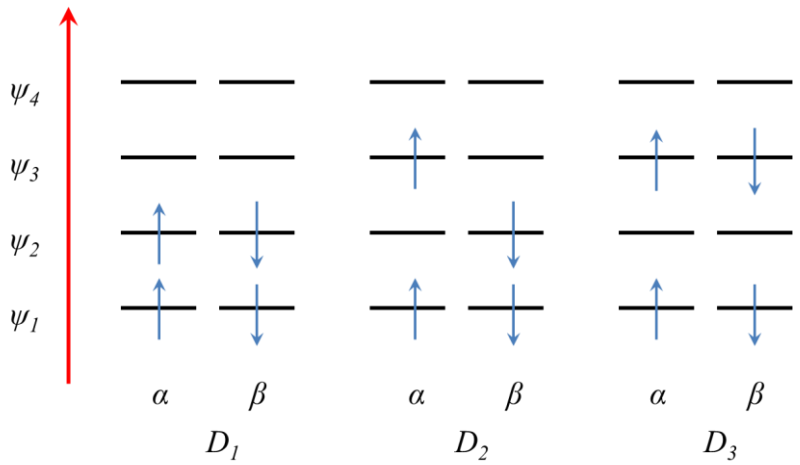

Figure 1.48: The construction of excited state determinants for a four electron system. D_1 corresponds to the regular HF Slater determinant with D_2 and D_3 Slater determinants representing the excited determinants.

The singly excited D_2 Slater determinant would then be:

$$D_2 = \frac{1}{\sqrt{4!}}\begin{vmatrix} \psi_1(1)\alpha(1) & \psi_1(1)\beta(1) & \psi_3(1)\alpha(1) & \psi_2(1)\beta(1) \\ \psi_1(2)\alpha(2) & \psi_1(2)\beta(2) & \psi_3(2)\alpha(2) & \psi_2(2)\beta(2) \\ \psi_1(3)\alpha(3) & \psi_1(3)\beta(3) & \psi_3(3)\alpha(3) & \psi_2(3)\beta(3) \\ \psi_1(4)\alpha(4) & \psi_1(4)\beta(4) & \psi_3(4)\alpha(4) & \psi_2(4)\beta(4) \end{vmatrix} \qquad \textit{Eq. 1.33}$$

Further, the doubly excited D_3 Slater determinant would be expressed as:

$$D_3 = \frac{1}{\sqrt{4!}}\begin{vmatrix} \psi_1(1)\alpha(1) & \psi_1(1)\beta(1) & \psi_3(1)\alpha(1) & \psi_3(1)\beta(1) \\ \psi_1(2)\alpha(2) & \psi_1(2)\beta(2) & \psi_3(2)\alpha(2) & \psi_3(2)\beta(2) \\ \psi_1(3)\alpha(3) & \psi_1(3)\beta(3) & \psi_3(3)\alpha(3) & \psi_3(3)\beta(3) \\ \psi_1(4)\alpha(4) & \psi_1(4)\beta(4) & \psi_3(4)\alpha(4) & \psi_3(4)\beta(4) \end{vmatrix} \qquad \textit{Eq. 1.34}$$

Much like how the MOs are expanded in terms of *m* basis functions to generate *m* MOs, the total electronic wave function is expanded in terms of *i* determinants leading to the generation of *i* total electronic wave functions:

$$\Psi_1 = c_{11}D_1 + c_{21}D_2 + c_{31}D_3 + \cdots + c_{i1}D_i \qquad \textit{Eq. 1.35}$$

$$\Psi_2 = c_{12}D_1 + c_{22}D_2 + c_{32}D_3 + \cdots + c_{i2}D_i \qquad \textit{Eq. 1.36}$$

$$\vdots$$

$$\Psi_i = c_{13}D_1 + c_{23}D_2 + c_{33}D_3 + \cdots + c_{i3}D_i \qquad \textit{Eq. 1.37}$$

This series of equations represent the ground electronic state, Ψ_1, and the electronic excited states. For the electronic ground state we would expect a larger contribution from the D_1 term since this is our ground HF Slater determinant. For the excited wave functions, there should be less contribution from the D_1 term and more contributions from the higher order D_i terms. Each Slater determinant in the electronic wave function represents an idealised electronic configuration and so we call these *configuration state functions (CSF).*[146] The most important point to take from this is that no single CSF represents the state of a system.

Theoretically, it is possible to consider a total wave function that takes into account all possible configurations and this is called a *full* CI treatment of the wave function. Although this will give a precise description of the wave function, from a computational perspective this is really only possible for very small molecules because the number of determinants required would be very large.[155] To emphasise this point, calculations with more than five billion CSFs have been performed for the molecule C_2H_2. Such a calculation is only useful for testing the strength of the theory and has no application in common computational practices.[155]

To compensate for the inevitable truncation of the CI wave function, *multiconfigurational SCF* (MCSCF) calculations have gained popularity.[136] In the single-determinant HF procedure, the coefficients of the basis functions are optimised. However, when this procedure is applied to the CI wave function, only the

coefficients of the determinants are optimized by the Fock matrix. MCSCF provides a method to optimise both the coefficients of the determinants and the coefficients of the basis functions that are used to construct the MOs in the determinants.

For many molecules, the MCSCF procedure is still too computationally expensive for practical applications and so it is more common to use a variation of the MCSCF procedure; the *complete active space SCF* (CASSCF) method.[156] The CASSCF procedure still retains the optimisation of the coefficients in both the CI expansion and the MO expansion within the determinants of the CI expansion, but CASSCF functions differ in that the calculation is performed on a select few MOs that are of interest to the researcher. The collection of selected MOs is called the *active space* of the calculation.

Recently, the CASSCF procedure has been used as a powerful tool to investigate the physical properties of highly degenerate excited states such as those found in lanthanide-based SMMs. The group of Chibotaru *et al.* have developed a MOLCAS module for calculating the *g*-tensors, direction vectors of the main magnetic axes, transition moments between states, and average magnetic moment of each of the excited states in Kramers ions.[157] Computational investigations of SMMs have led to a dramatic increase in our understanding of the relaxation pathways in these systems and are quickly becoming a necessity in this field. Despite the advantages of these calculations there are only a small handful of labs worldwide who have successfully applied the MOLCAS program to elucidate the relaxation dynamics of Ln-SMMs to date.

Chapter 2 : Project 1 - Synthesis and Characterization of a "Breathing" MOF with a Novel Topology

Working towards the design and study of SPCs, Chapter 2 of this thesis describes the synthetic strategy devised for the discovery of a novel Cu^{2+} MOF, followed by a series of detailed studies that shed light on its structural and physical properties.

2.1: Preparation of the organic linker H_4L_2

Over the last decade, research in the Pilkington group has focused on ligand design, targeting the discovery of new coordination complexes that display desirable structural topologies with interesting magnetic, electronic and/or optical properties. Throughout the past several years this has included the synthesis of polydentate ligands, that include the 2,2′- and 4,4′-bipyridine derivatives, shown in Scheme 2.1 and Figure 2.1.[158,159] The general approach involves functionalising selected positions of the bipyridine rings in order to introduce additional donor atoms and then exploring their coordination chemistry together with first row paramagnetic transition metal and/or lanthanide ions.

In order to achieve these goals, we have typically employed imine and amide linkers since they have additional nitrogen donors for coordination to metal ions and their synthetic chemistry is well-established.[158,159] Following this strategy, the first ligand targeted was the *bis*-imine (**2.1**). Not surprisingly, early research efforts established that its Schiff-base linkages are very reactive to both hydrolysis and nucleophilic addition that is enhanced in the presence of Lewis acidic metal ions, thus

providing an opportunity for the chemical transformation of the ligand. In earlier studies, a potential rearrangement pathway was proposed for (**2.1**) in the presence of Co^{2+} ions, supported by X-ray crystallographic studies of the reactive intermediates, Scheme 2.1.[158a]

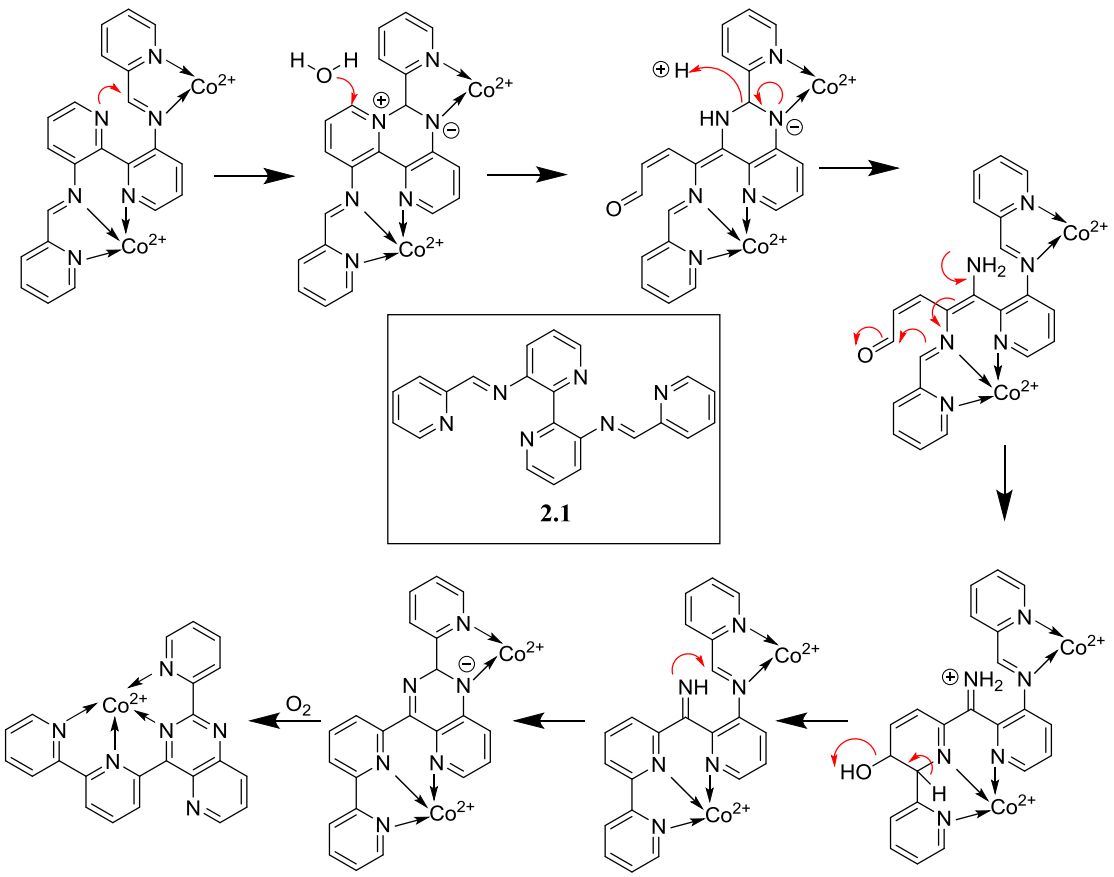

Scheme 2.1: The proposed rearrangement process for the *bis*-imine functionalised 2,2'-bipyridine ligand (**2.1**).[158a]

Although this study afforded a quaterpyridine complex in a simple one pot reaction, the unpredictability of the ligand's coordination mode makes imine linkages less desirable for the rational synthesis of coordination compounds; however, they

have been successfully employed previously in serendipitous approaches to the assembly of large polynuclear transition metal clusters.[160] Amide linkages, on the other hand, have a well-established chemical and thermal robustness that is prominently featured in biology.[161] In this regard, the Pilkington group has synthesised and investigated the coordination chemistry of several polydentate amide ligands, such as compound (**2.2**) in Figure 2.1. Detailed coordination chemistry studies of these ligands have revealed that as expected, they remain intact on coordination to transition metal ions and their polydentate nature means that they can accommodate a range of structural topologies with different nuclearities.[158c] For example, (**2.2)** coordinates Ni^{2+} and Zn^{2+} cations in a tridentate manner through its amide, pyridyl and bipyridine N-atoms to yield trinuclear and tetranuclear complexes (**2.2a)** and (**2.2b)** respectively. Interestingly, when the two pendant pyridine heterocycles are replaced with pyrazine substituents, its coordination chemistry with Cu^{2+} affords the 1-D chain (**2.2c)**, highlighting the suitability of these ligands for employment in rational design strategies.[158c]

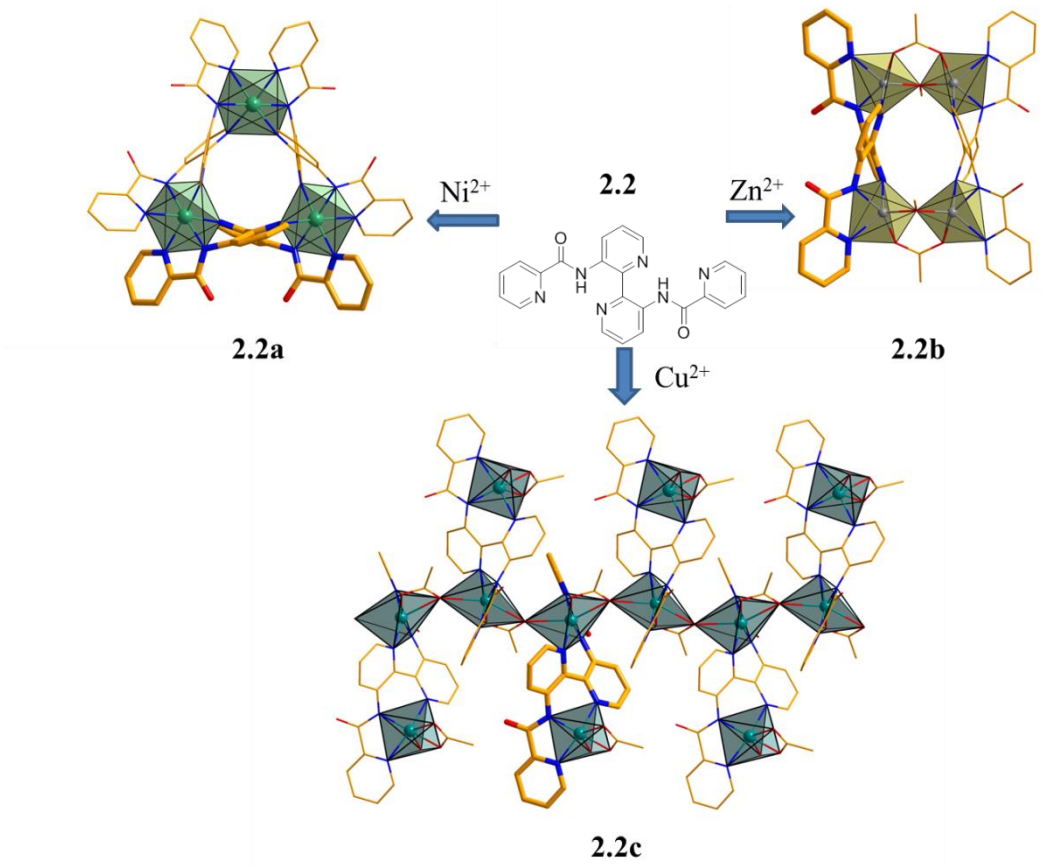

Figure 2.1: The coordination versatility of the amide-functionalised bipyridine ligand (**2.2)** with first row TM ions for the preparation of (**2.2a)**, (**2.2b)** and (**2.2c)**.[158c]

Following the success of functionalizing 2,2'-bipyridine ligands, the synthetic strategy was then extended to 4,4'-bipyridine derivatives.[159b] Within this research, a new tetrapyrrole ligand (**2.3**) was synthesised and characterized and its coordination chemistry with $Cu_2(OAc)_4$ afforded a unique Cu_8 cluster (**2.4**) that crystallizes with an interesting saddle -like topology, Figure 2.2.

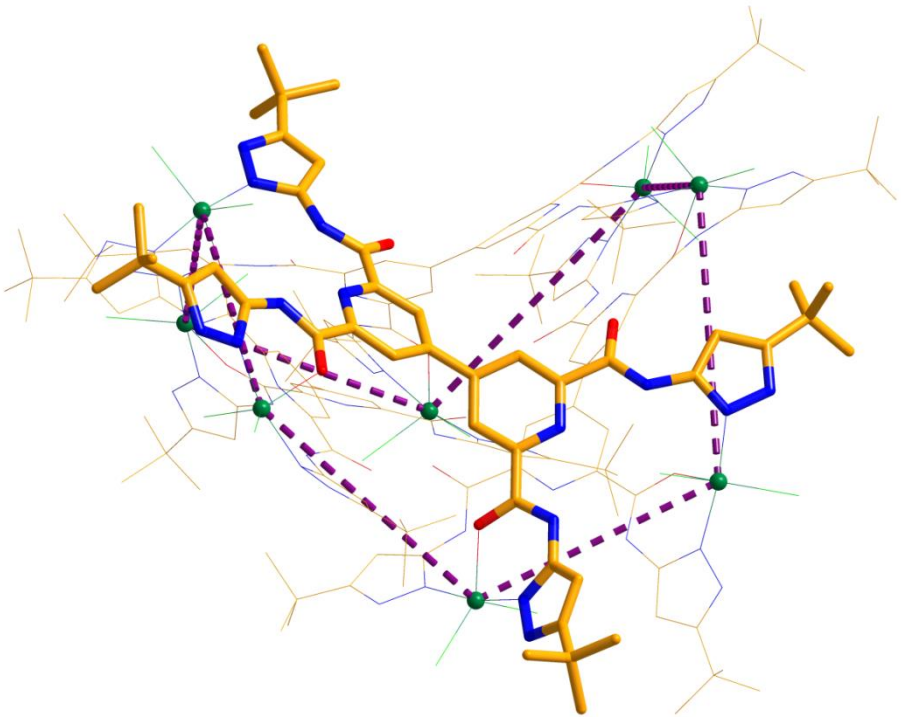

Figure 2.2: Molecular structure of the Cu_8 cluster. Cu^{2+} ions are presented as green spheres and a single 4,4'-bipyridine ligand (**2.3**) is highlighted for emphasis. The purple dotted line shows the saddle configuration of the Cu^{2+} ions. Hydrogen atoms are omitted for clarity. [159b]

The Cu_8 cluster comprises of eight 5-coordinate Cu^{2+} ions with square pyramidal geometries coordinated to four **(2.3)** linkers. Interestingly, all of the amide nitrogen atoms remain protonated since no additional base was added during the reaction. This effectively prevents the ligand from coordinating via its N_3-tridentate pocket and as a consequence, the amide-carbonyl O-donors and the pyrazole N-donors are the only coordination sites available to the Cu^{2+} ions.

Following on from the above study, the first objectives of my research project were to synthesise and characterize the closely related, flexible 4,4'-bipyridine polydentate ligand, (H_4**L**$_2$**)**. In contrast to the previously described ligand, this compound has pyridine rings that are appended *via* amide linkers onto the *ortho*

positions of the 4,4'-bipyridine rings. Given the rotational freedom that exists along the single bond connecting the two 4,4'-bipyridine heterocycles, we proposed to exploit this for the synthesis of an SPC, ultimately targeting the synthesis of a cluster, or framework type topology.

This ligand was successfully synthesised from the known tetracarboxy derivative (**2.7**) following the procedure presented in Scheme 2.2.[162] In this synthesis, a one-electron reduction of 2,6-lutidine (**2.5**) was carried out with elemental sodium. The resulting solution was reacted with an excess of sulphur dioxide in order to increase the acidity of the *p*-H atom. After basifying the solution, the crude product precipitated out as a white powder that was subsequently recrystallized from hot water to afford the tetramethyl derivative (**2.6)**. Jones oxidation of (**2.6**) via reaction with CrO_3 and conc. H_2SO_4 afforded the tetracarboxy ligand (**2.7**) in 80 % yield. The NMR data and m.p. for this ligand are consistent with the values reported in the literature.[162]

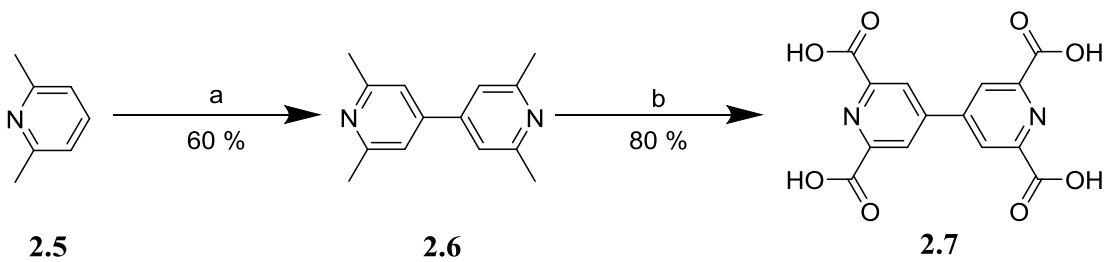

2.5 **2.6** **2.7**

Scheme 2.2: Synthesis of 2,2′,6,6′-tetracarboxy-4,4′-bipyridine (**2.7**). a) $Na_{(s)}$, SO_2, NaOH, THF, room temperature, 5 d. b) H_2SO_4, CrO_3, 70 °C.[162]

In order to synthesise the target ligand (**H_4L_2)**, the tetra-acid was first converted to the tetra-acyl chloride intermediate (**2.8)** by treatment with an excess of thionyl chloride. The tetra-acyl chloride intermediate was then reacted with four

equivalents of 3-aminopyridine in the presence of four equivalents of trimethylamine. After recrystallization from hot DMSO, the new ligand, (**H_4L_2**), was obtained as a white powder in 78 % yield, Scheme 2.3.

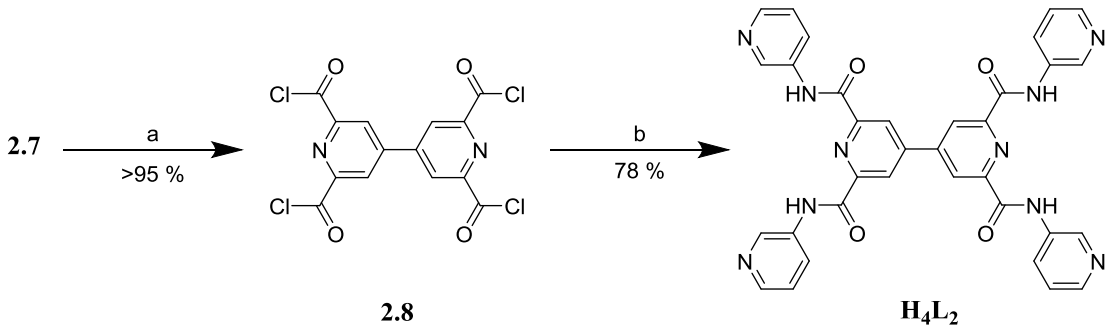

Scheme 2.3: Synthesis of (**H_4L_2**). a) $SOCl_2$, DMF, reflux, 5 h. b) 3-aminopyridine, Et_3N, DCM, reflux.

2.2: Characterization of the organic linker (H_4L_2)

(**H_4L_2**) was characterised by ^{1}H-NMR, FT-IR, FAB mass spectrometry and CHN elemental analysis. The melting point was determined to be above 300 °C. The poor solubility of the ligand in common NMR solvents at room temperature meant that we were not able to record its ^{13}C-NMR spectrum. Nevertheless, the ^{1}H-NMR data in DMSO-d6 confirmed the molecular structure of the ligand as shown in Figure 2.3.

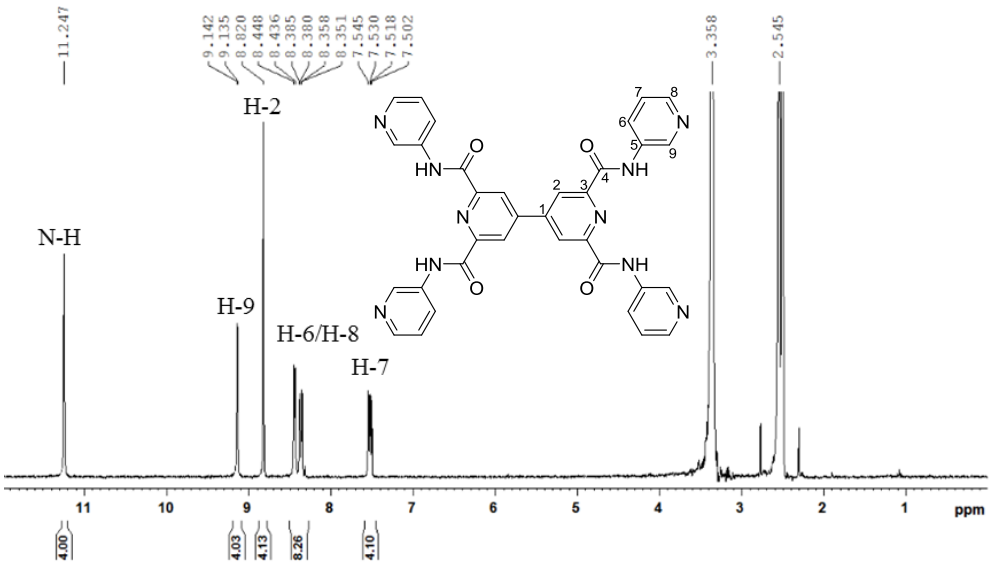

Figure 2.3: 300 MHz ^{1}H-NMR spectrum of (**H_4L_2**) in DMSO-d_6 at room temperature.

Examining the ^{1}H NMR spectrum of (**H_4L_2**), the NH proton of the amide is present as a singlet at 11.25 ppm. The doublet at 9.14 ppm is assigned to H-9, the *ortho* proton of the pyridine ring and the singlet at 8.82 ppm to H-2, the meta proton of the 4,4'-bipyridine. Finally, based on coupling constants, the three sets of doublet of doublets at 9.14, 8.37 and 7.52 ppm are assigned to H-6, H-8 and H-7, respectively.

The IR spectrum of (**H_4L_2**) has a moderately strong, broad band at 3387 cm^{-1} assigned to the N-H *str* of the amide, an sp^2 C-H str at 3275 cm^{-1} and a C=O *str* for the amide functionality at 1675 cm^{-1}. The FAB-mass spectrum shows a peak at *m/z* = 637 (10%) for the parent ion $[M]^{\cdot+}$and the CHN elemental analysis data is within the ±0.4% margin of error for $C_{34}H_{24}N_{10}O_4 \cdot 2(CH_3)_2SO$. Unfortunately, due to its poor solubility in organic solvents, suitable conditions for the growth of single crystals of (**H_4L_2**) for X-ray diffraction studies have eluded us to-date.

2.3: Synthesis of a flexible Cu^{2+} MOF-1

The coordination chemistry of (**H_4L_2**) with first row transition metal ions was inherently challenging due to its poor solubility in almost all common organic solvents. Finally, after many unsuccessful attempts, reaction of one equivalent of (**H_4L_2**) with two equivalents of copper acetate in a 2:1:1 mixture of DMF, water and pyridine gave a blue/green solution after heating in DMF for 2 hours. Diffusion of acetonitrile into this solution afforded single crystals suitable for X-ray diffraction studies, which revealed that the complex possessed a metal organic framework topology (MOF-1), *vide infra*. We found that any significant deviation from the above mixture of solvents resulted in the isolation of only amorphous, insoluble powders. Therefore, we propose that the above mixture of solvents likely affords a partially solvated suspension of the ligand which then in turn reacts slowly to yield a solution containing the SBUs of the MOF. Once the stoichiometry of the final product was determined, the synthetic procedure was optimised which involved reacting two equivalents of $Cu_2(OAc)_4$ with 1.5 equivalents of ligand (**H_4L_2**) in the presence of 2 equivalents of pyridine, **Equation 2.1**. Following this strategy, the reaction mixture was heated to 120 °C in DMF for 12 hours and then as previously described, acetonitrile solution was slowly diffused into the reaction mixture. Once the crystals formed we found it impossible to re-dissolve the product in organic solvents and also noted that the crystals lost crystallinity upon standing.

$2Cu_2(OAc)_4.2H_2O + 1.5\mathbf{L_2} + 2py \rightarrow [Cu_4(\mathbf{L_2})_{1.5}(OAc)_2(py)_2(OH_2)]_n + 6CH_3COOH + H_2O$

Equation 2.1: Reaction for the preparation of MOF-1.

2.4: Characterisation of MOF-1

MOF-1 was characterised by FT-IR, MS (MALDI), CHN elemental analysis, and X-ray diffraction. The IR spectrum shows a broad peak at ν = 3367 cm^{-1} consistent with the presence of both coordinated and lattice water molecules. A C=O *str* for the amide is still present at ν = 1655 cm^{-1}, slightly red-shifted when compared to the free ligand. This is consistent with a deprotonated amide where the greater electron density is polarised due to the carbonyl group, effectively weakening the double bond.[163] Furthermore, a C-O str is present at 1260 cm^{-1} consistent with the presence of bridging acetate ligands in the complex. The MALDI-TOF mass spectrum of the complex contains an intense peak for the $[Cu(\mathbf{L_2})]^+$ ion at *m/z* = 700. Elemental analysis data for the complex is within the ± 0.4% margin of error for $C_{30}H_{21.5}N_8O_{5.5}Cu_2{\cdot}4H_2O$, which is consistent with the molecular formula for the asymmetric unit elucidated from the X-ray diffraction studies described below.

As previously mentioned, dark-green-blue blocks of sufficient size and quality for single crystal X-ray diffraction studies (SCXRD) were grown via the slow diffusion of acetonitrile into the reaction solution, Figure 2.4.

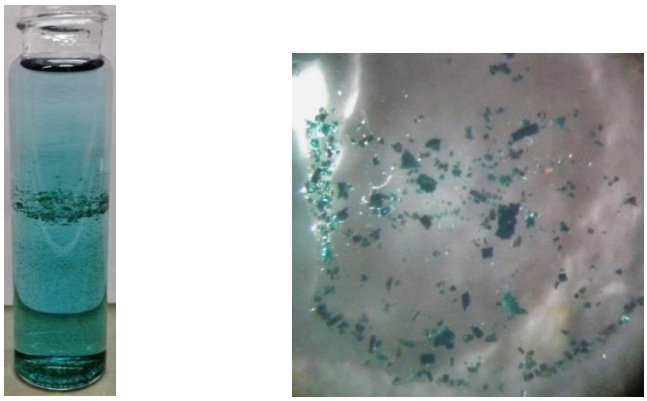

Figure 2.4: Single crystals of MOF-1.

The X-ray data was collected at Brock University and solved and refined using the Bruker SHELXTL software. During the refinement process, the X-ray data contained residual electron density peaks consistent with disordered water and acetonitrile molecules. Since this solvent could not be adequately modeled, the electron density was removed from the crystallographic model using the SQUEEZE routine within PLATON.[164] From the SQUEEZE routine, 1161 electrons were removed, which was attributed to 43 acetonitrile and 21.5 water molecules. The void volume was also calculated using the SQUEEZE routine and was determined to be 4943 $Å^3$.The crystallographic parameters for the complex are summarized in the Table 5.1 of the Appendix. The complex crystallises in the orthorhombic space group *Pban*. Analysis of the structural topology revealed that it crystallized as a 3-D porous network, or MOF, with stoichiometry $[Cu_8(\mathbf{L_2})_3(OAc)_4(py)_2(H_2O)_2]_n$ (MOF-1),Figure 2.5.

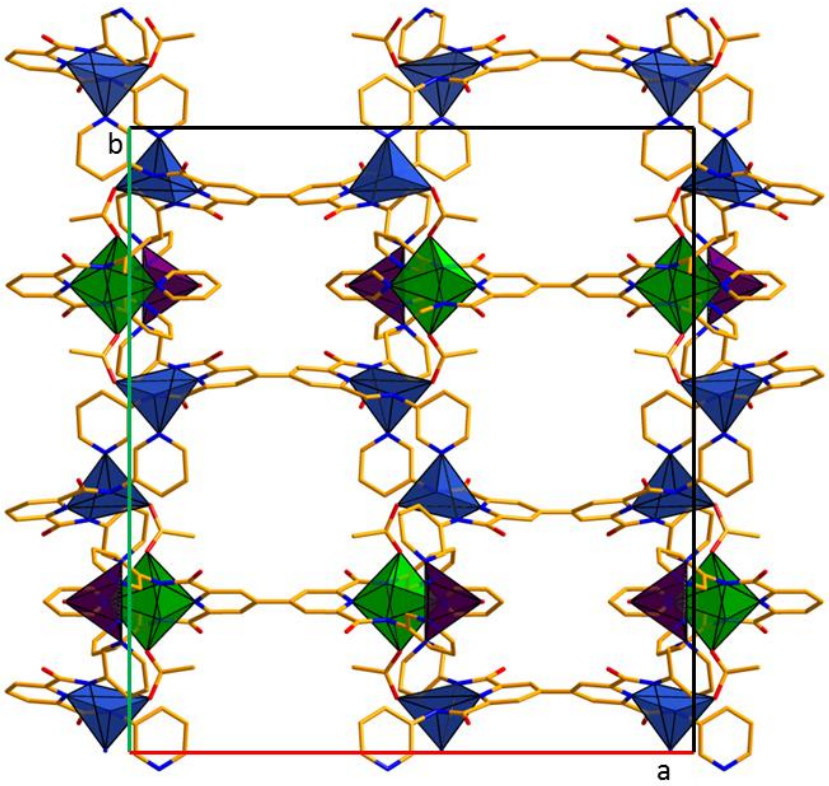

Figure 2.5: Crystal packing of MOF-1, viewed down the *c*-axis of the unit cell. H-atoms are omitted for clarity. Disordered solvent is removed from the crystallographic model using the SQUEEZE routine in PLATON.[164] The three crystallographically unique Cu^{2+} coordination spheres are represented as blue, purple and green polyhedral for Cu1 to Cu3 respectively.

The asymmetric unit comprises three crystallographically unique Cu^{2+} centres Cu1, to Cu3, two of which (Cu2 and Cu3) occupy crystallographic special positions together with 3/4 of an $\mathbf{L_2}^{4-}$ ligand, half a coordinated pyridine, an acetate ligand and a half a water molecule, Figure 2.6.

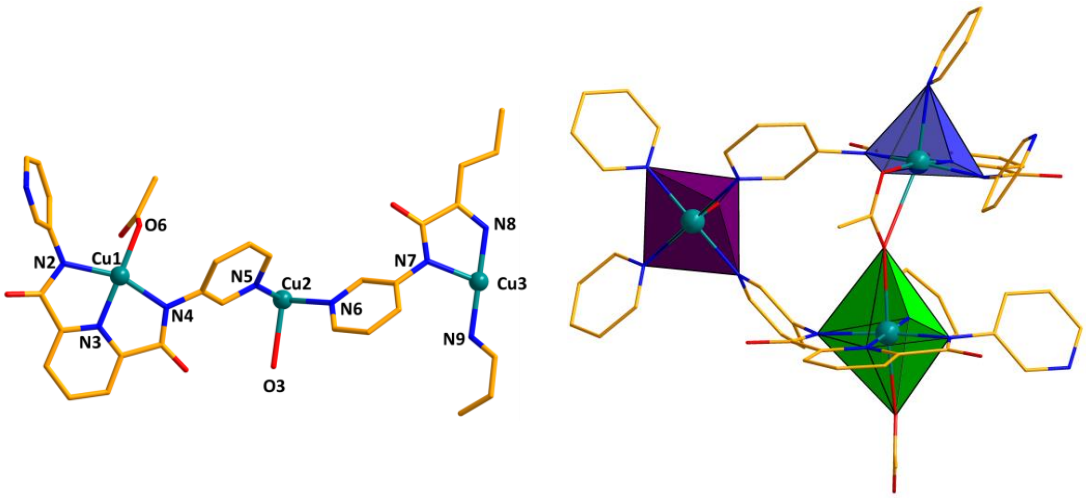

Figure 2.6. The asymmetric unit $[Cu_2(\mathbf{L_2})_{0.75}(pyr)_{0.5}(OH_2)_{0.5}]$ of MOF-1; Left, showing the crystallographically unique atoms with appropriate labelling scheme; Right, highlighting the coordination geometry of the Cu^{2+} ions, represented as blue, purple and green polyhedra for Cu1 to Cu3 respectively. H-atoms are omitted for clarity. In the left figure, ligand $\mathbf{L_2}^{4-}$ is truncated for clarity.

The first crystallographically unique Cu^{2+} centre, Cu1, adopted a distorted square pyramidal geometry (τ = 0.21), with the equatorial positions filled by three nitrogen donors, N2, N3 and N4 of $\mathbf{L_2}^{4-}$, together with an oxygen donor, O6 from a bridging acetate. The fifth axial position was occupied by a pyridyl nitrogen donor N1 from a neighbouring $\mathbf{L_2}^{4-}$ ligand, Figure 2.7.

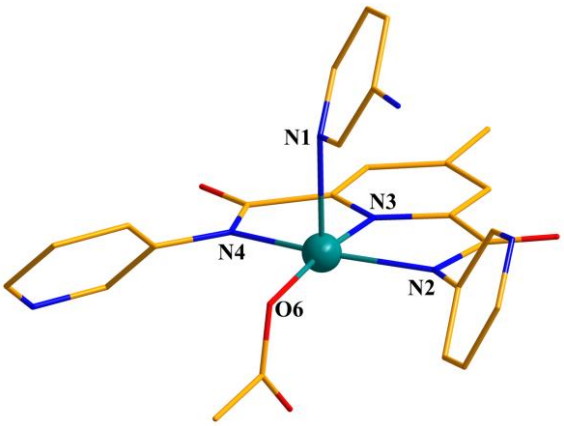

Figure 2.7: Part of the molecular structure of MOF-1 showing the coordination geometry of Cu1 represented as a teal sphere. H-atoms are omitted for clarity.

The second copper centre, Cu2 sits on a two-fold axis and had a distorted square pyramidal geometry (τ = 0.11). The equatorial positions were occupied by pyridine heterocycles from four symmetry related $\mathbf{L_2}^{4-}$ ligands, N5, N5i and N6 and N6i and a coordinating axial water molecule O3 which also sits on a crystallographic C_2 axis, Figure 2.8.

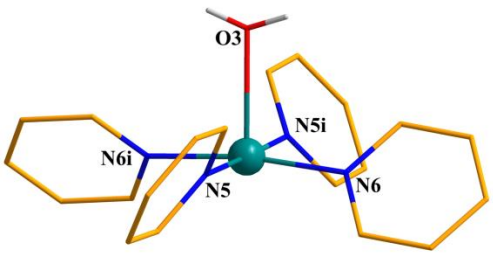

Figure 2.8: Part of the molecular structure of MOF-1 showing the coordination geometry of Cu2 (teal). The definition of '*i*' is given in Table 2.1.

.

The third copper centre, Cu3 also sits on a crystallographic 2-fold axis and had a Jahn-Teller distorted octahedral geometry with axial Cu3-O5 bond lengths of 2.475(7) Å and shorter equatorial Cu3-N bond lengths in the range of 1.930(5) to

2.031(4) Å, Figure 2.9. Regarding the types of donor atoms, the equatorial positions were occupied by three nitrogen donors of the tridentate pocket of one $\mathbf{L_2}^{4-}$ (N7, N8 and N7ii), and a coordinating pyridine (N9), whereas the axial sites were filled by two symmetry related oxygen donors (O5 and O5i) from two bridging acetate ligands. Selected bond lengths and angles for MOF-1 are presented in Table 2.1.

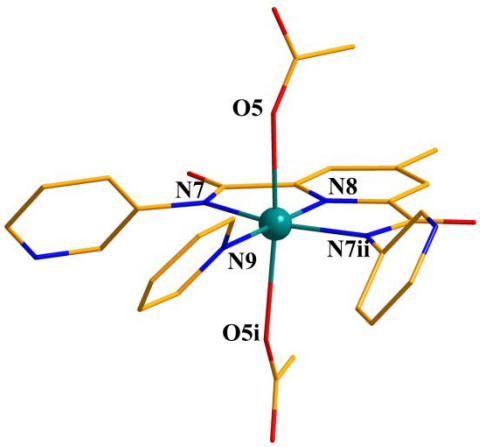

Figure 2.9: Part of the molecular structure of MOF-1 showing the coordination geometry of Cu2 represented as a teal sphere. The definition of 'ii' is given in Table 2.1. H-atoms are omitted for clarity.

The shortest Cu···Cu distances within the MOF ranged from 5.008 Å for Cu1-Cu3, 6.969 Å for Cu1-Cu2 and 6.977 Å for Cu2-Cu3, Figure 2.10.

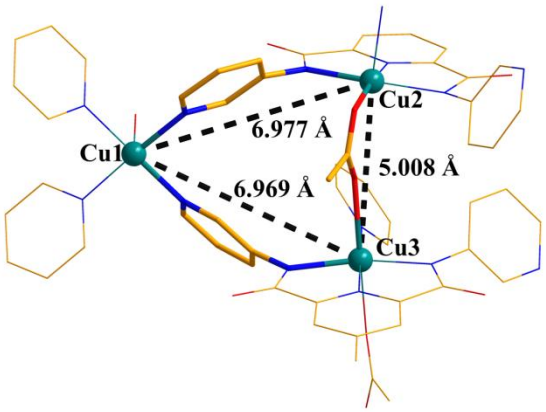

Figure 2.10: Fragment of MOF-1 showing the shortest $Cu^{2+}\cdots Cu^{2+}$ distances.

Table 2.1: Selected bong lengths (Å) and angles (°) for $[Cu_8(\mathbf{L_2})_3(OAc)_4(py)_2(H_2O)_2]_n$ (MOF-1).

Bond	**Length(Å)**	**Bond**	**Length (Å)**
N5—Cu2	1.9874 (19)	Cu2—N5i	1.9875 (19)
N6—Cu2	2.0289 (17)	Cu2—N6i	2.0289 (17)
Cu1—N3	1.934 (4)	Cu2—O3	2.398 (6)
Cu1—O6	1.947 (4)	Cu3—N8	1.930 (5)
Cu1—N4	2.035 (4)	Cu3—N9	1.996 (5)
Cu1—N2	2.053 (4)	Cu3—N7ii	2.031 (4)
Cu1—N1	2.308 (5)	Cu3—N7	2.031 (4)
Cu3—O5	2.475 (7)	Cu3—O5i	2.475 (7)
Bond	**Angle (°)**	**Bond**	**Angle (°)**
N3—Cu1—O6	170.78 (17)	N5—Cu2—N6	89.08 (7)
N3—Cu1—N4	79.07 (18)	N5i—Cu2—N6	91.02 (7)
O6—Cu1—N4	99.97 (18)	N6i—Cu2—N6	178.6 (2)
N3—Cu1—N2	79.96 (17)	N5—Cu2—O3	94.11 (6)
O6—Cu1—N2	99.86 (16)	N5i—Cu2—O3	94.11 (6)
N4—Cu1—N2	158.37 (17)	N6i—Cu2—O3	89.31 (16)
N3—Cu1—N1	97.29 (18)	N6—Cu2—O3	89.31 (6)
O6—Cu1—N1	91.92 (16)	N8—Cu3—N9	180.0

N4—Cu1—N1	97.06 (17)	N8—Cu3—N7ii	79.08 (10)
N2—Cu1—N1	90.82 (16)	N9—Cu3—N7ii	100.92 (10)
N5—Cu2—N5i	171.79 (13)	N8—Cu3—N7	79.08 (10)
N5—Cu2—N6i	91.02 (10)	N9—Cu3—N7	100.92 (10)
N5i—Cu2—N6i	89.08 (10)	N7ii—Cu3—N7	158.2 (2)

Symmetry codes: i) x, ½-y, 1-z. ii) x, ½-y, 2-z

One interesting feature of this framework is that the two copper centres Cu1 and Cu2 are both coordinatively unsaturated with vacant sites facing the inner surface of the pores in the MOF. In this context, it has been shown previously that when metal sites are accessible by guest substrates, they can function as catalysts for a range of organic reactions.[165] In the literature, there are several reported examples of Cu^{2+}-MOFs with available coordination sites that have been investigated as catalysts for Friedel-Crafts acylation,[166] Diels-Alder condensation,[167] epoxide ring-opening,[168] the Henry reaction,[169] as well as for the hydrogenation of CO_2.[170]

Given that the coordination chemistry was carried out in the presence of base, then as expected, all of the amide ligands are fully deprotonated and available for coordination to the Cu^{2+} ions, in sharp contrast to the amide N-atoms of the previously reported Cu_8 cluster (**2.4**). This is evident in the crystal structure of the framework where the Cu^{2+} ions coordinate in the N_3^{2-} tridentate pocket formed by two amide and one pyridy N-atom. Interestingly, $\mathbf{L_2}^{4-}$ serves exclusively as a linker between two Cu^{2+} ions of the same type. This leads to two distinct SBUs: the first constructed from $\mathbf{L_2}^{4-}$ and two Cu1 ions coordinated within each tridentate N_3^{2-} pocket, (SBU1) depicted in green in Figure 2.11, and the second constructed from $\mathbf{L_2}$ and two Cu3

ions within each N_3 pocket (SBU2), depicted in purple in Figure 2.11. SBU1 links to other SBU1 building blocks via the pyridyl N-donors which coordinate in the axial positions of Cu1. Linking between the SBU1 building blocks is oriented around an inversion centre which results in 1D arrays of SBU1. These SBU1 chains are linked together in a cooperative manner by acetate anions shown in blue and SBU2 building blocks, Figure 2.11. This structural topology is profoundly different from MOFs assembled from the unsubstituted 4,4'-bipyridine linker, which affords a grid-like topology.[171]

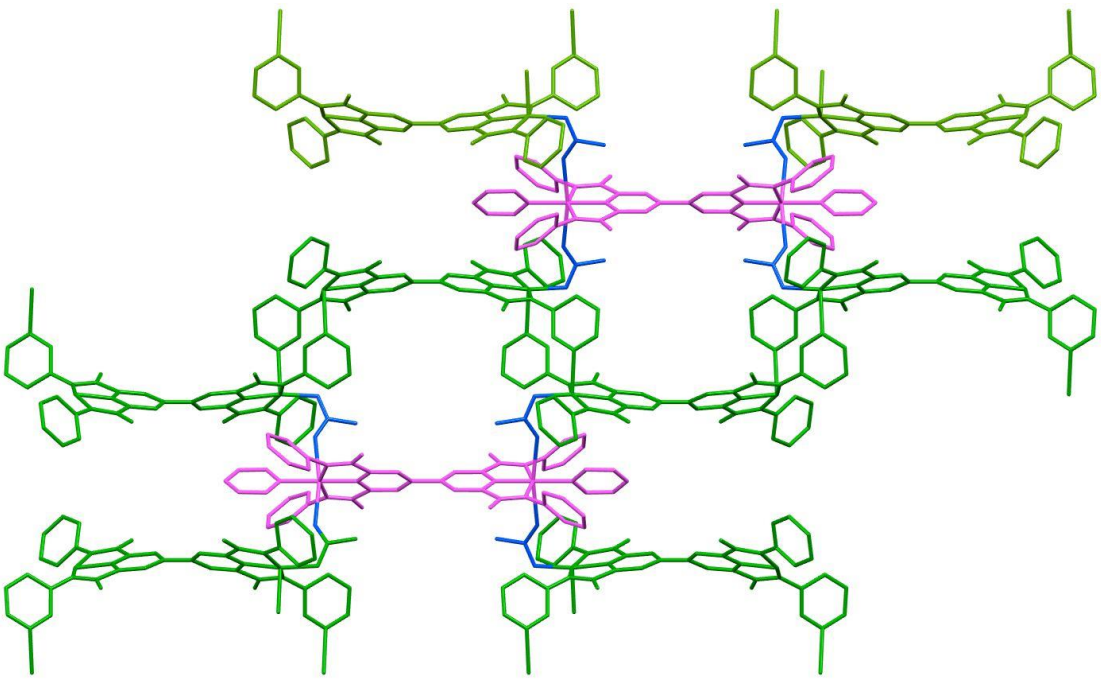

Figure 2.11: One individual sheet of MOF-1. The discrete SBUs are highlighted in green and purple for SBU1 and SBU2, respectively. The acetate linkers are shown in blue and the Cu2 inter-plane linking unit is omitted for clarity.

3.2.2: Topological Analysis Using TOPOS Software

A computational investigation of the topology of the MOF was carried out using the TOPOS software.[172] For the preliminary investigation, each copper center and both organic linkers ($\mathbf{L_2}^{4-}$ and OAc^-) were considered as nodes, Figure 2.12. Applying this criterion, MOF-1 can be characterized as a 5-nodal 3,3,4,6,6-net where each of the numbers represents the shortest loops around each node. The point symbol of this net is $(4.5.6)_4(4.5^2.7^2.8)_2(4^2.5^2.6.7^4.8^4.10^2)_2$-$(4^2.5^4.6.7^4.8^4)(5^2.8)_2$ where the information about each node are isolated by brackets and the number $A^a.B^b...$ is read as the number of *a* angles of *A*-size loops and the number of *b* angles of *B*-size loops of a given node. The subscript denotes the simplest ratio of nodes relative to one another.

Another way to view the MOFs is by following the Reticular Chemistry Structural Resource (RCSR) rules.[35] Following these conditions, the MOF is considered to have three nodes at each of the Cu(II) ions and is classified as a trinodal 4,4,5-c net with stoichiometry $(4\text{-c})_2(4\text{-c})(5\text{-c})$ and point symbol $(3.6^3.7^2)_2(3^2.6.7^2.8)(3^2.6^5.7^2.8)$. The computational analysis of MOF-1 reveals that it is the first framework to exhibit this topology and thus particularly interesting since novel MOF topologies are no longer common in the chemical literature.

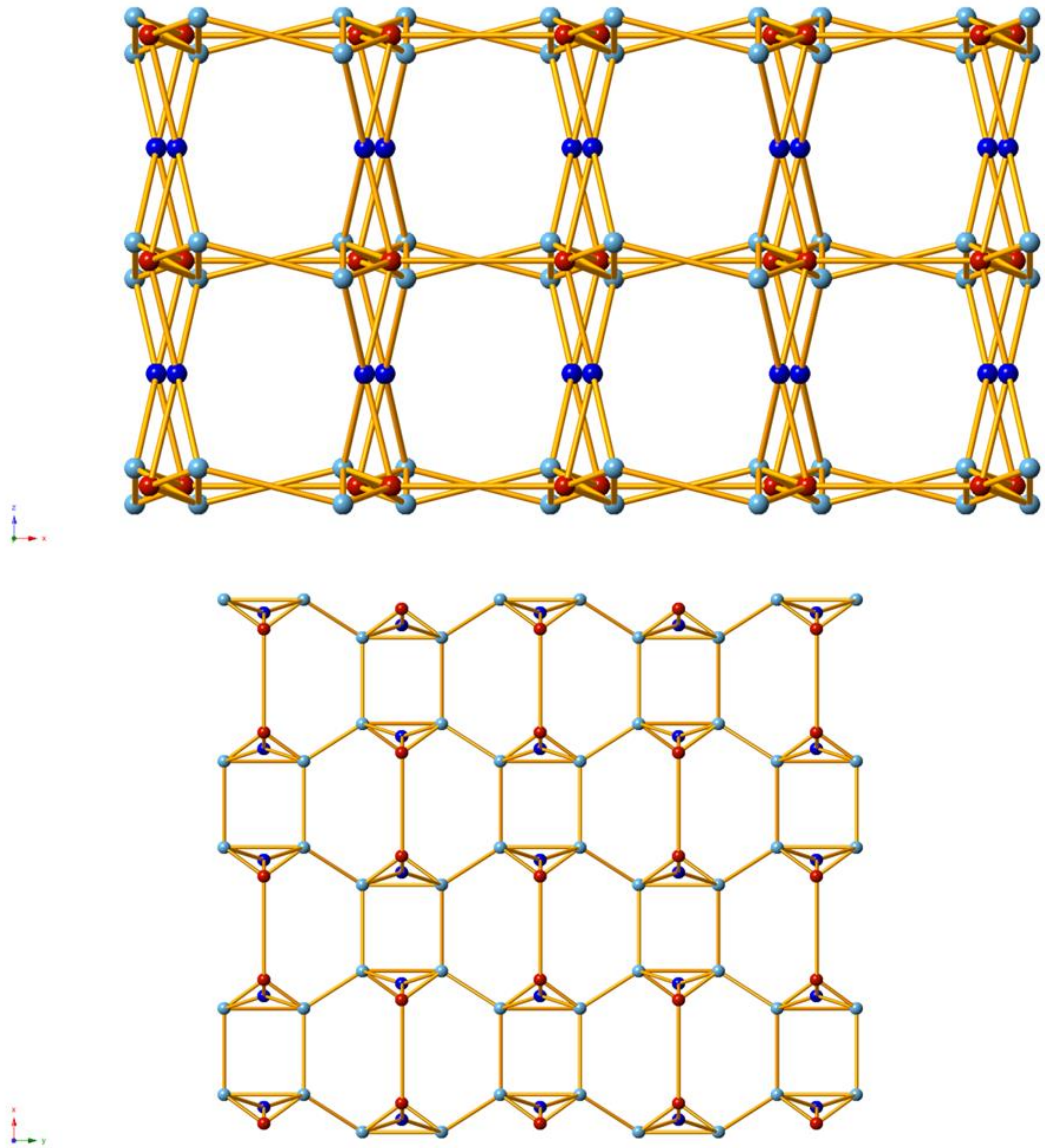

Figure 2.12: Computational representation of MOF-1 using the TOPOS software.[172] Top: view of the MOF-down the *y*-axis. Bottom: view of the MOF down the *z*-axis. $\mathbf{L_2}^{4-}$ and OAc^- are represented as gold sticks and the Cu^{2+} ions are represented as light-blue, dark-blue and red for Cu1, Cu2 and Cu3, respectively.

Powder X-ray Diffraction Studies

As mentioned previously, during our single crystal X-ray diffraction measurements we observed that the crystals readily lose their crystallinity,

presumably as a result of the loss of solvent from the crystal lattice. Unfortunately this meant that we were not able to use variable temperature single-crystal X-ray diffraction to investigate any structural changes taking place upon desolvation of the MOF. In light of these challenges, we carried out a series of variable temperature powder X-ray diffraction (PXRD) studies on crushed single crystals of MOF-1 to investigate in more detail its structural properties as a function of temperature. The fundamental principle of any XRD technique is that if a sample is crystalline then the ordered array of atoms will act as a diffraction grating and will deflect the X-rays at various angles determined by Bragg's law.[173] Even though they follow the same basic principles, PXRD differs from SCXRD by the degree of *texturing* in the sample. Texturing refers to the distribution of crystal orientations in a given sample; in SCXRD there is only one possible crystal orientation within the sample at any given time; thus, the sample is said to have maximal texture and is therefore anisotropic. Conversely, for a microcrystalline powder where the crystallinity is visible only through microscopic examination, the distribution of crystal orientations approaches infinity and the sample is said to have minimal texture and is isotropic. Therefore, in PXRD, the sharp diffraction spots observed for SCXRD are averaged out yielding diffraction rings at discrete angles and of unique intensity. This series of diffraction rings are characteristic of the sample and are referred to as the *powder pattern* which is depicted a plot of an intensity *vs.* angle. The first step in our analysis was to experimentally determine the powder pattern of microcrystalline sample of MOF-1 to make sure it remained intact after grinding the single crystals. To ensure that these conditions were met, we compared the experimentally measured powder pattern of

pristine MOF to a simulated powder pattern from the SCXRD data using the Mercury software.[174] The results of this study are shown in Figure 2.13.

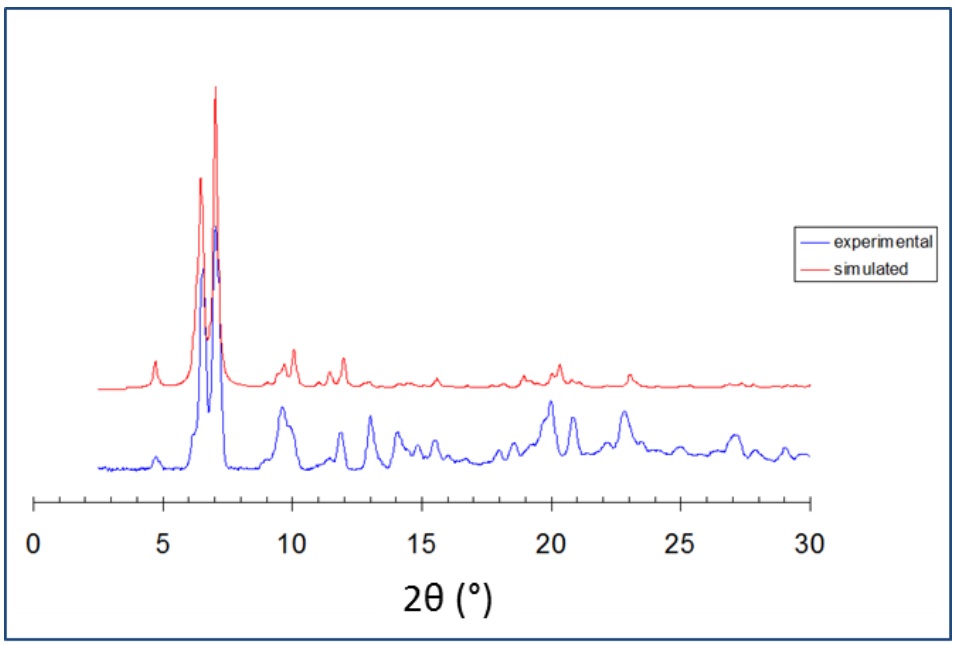

Figure 2.13: Experimentally determined (blue) and simulated (red) powder X-ray diffraction pattern for MOF-1.

From this data we conclude that the powder pattern acquired at room temperature agrees very well with the simulated pattern from the single crystal data. It should be noted the minor differences between the two patterns can be attributed to: (i) the fact that residual solvent was removed from the experimental model of the single crystal data and (ii) the single crystal data was collected at 150 K, whereas the powder data was acquired at room temperature. At this point we were interested in studying the effect of temperature on the crystallinity of the MOF. In the next experiment, a polycrystalline sample of MOF-1 was heated from 25 to 126 °C and the powder pattern was measured semi-intermittently throughout the heating process as

shown in Figure 2.14. Examining the resulting powder data we observed that MOF-1 retains its structural integrity until 75 °C after which point the intensity of the powder pattern rapidly decreases until the pattern is lost above 125 °C. Interestingly, cooling the sample back down to room temperature did not restore the powder pattern. The absence of a powder pattern is indicative of a loss of crystallinity which is most likely a consequence of structural changes to the topology of the MOF due to desolvation on heating.

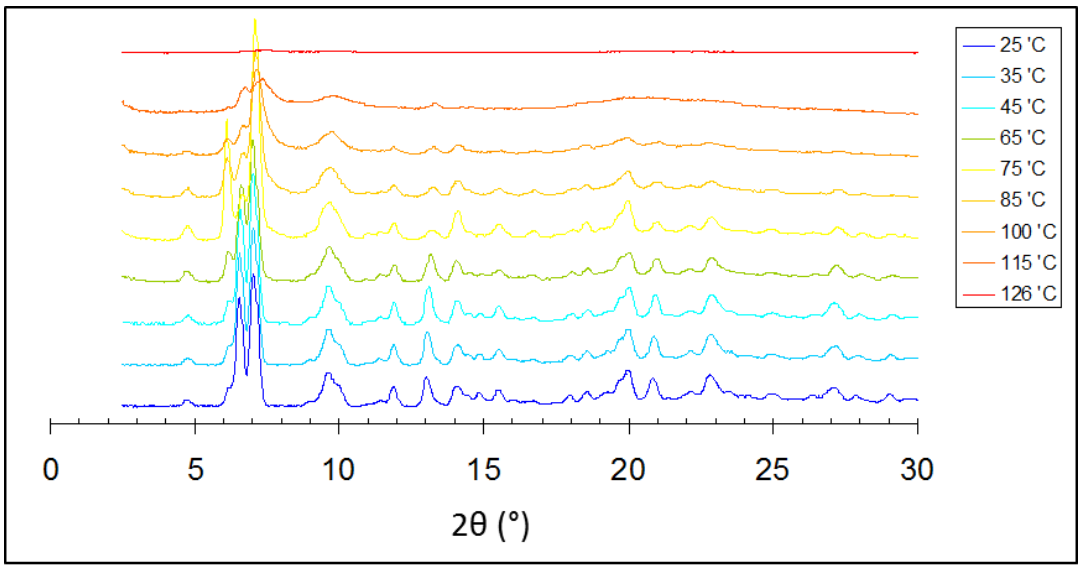

Figure 2.14: Variable temperature X-ray diffraction data for a polycrystalline sample of MOF-1 collected between 25 and 126 °C.

In order to determine whether or not the loss of crystallinity of the MOF after desolvation was a reversible process we re-introduced solvent into the pores of the framework by soaking the amorphous powder in a solution of acetonitrile for 12 hrs at room temperature and pressure. To our surprise, the powder pattern of the re-solvated sample was completely restored indicating that resolvation restores the MOF back to its initial crystalline state. To further substantiate this hypothesis, MOF-1 was first

heated to 125 °C under vacuum for 12 h. PXRD once again revealed the presence of an amorphous powder. The resulting powder was then resolvated by soaking it in acetonitrile for 12 hrs, and as expected, the MOF returned to its original crystalline state as shown in by the powder data in Figure 2.15. This significant reversible change in porosity is characteristic of a breathing MOF. As a consequence, due to the presence of solvent-filled pores in the initial crystalline state, we can classify MOF-1 as an SPC. To shed more light on these observations we subsequently carried out a thermogravimetric analysis (TGA) of MOF-1.

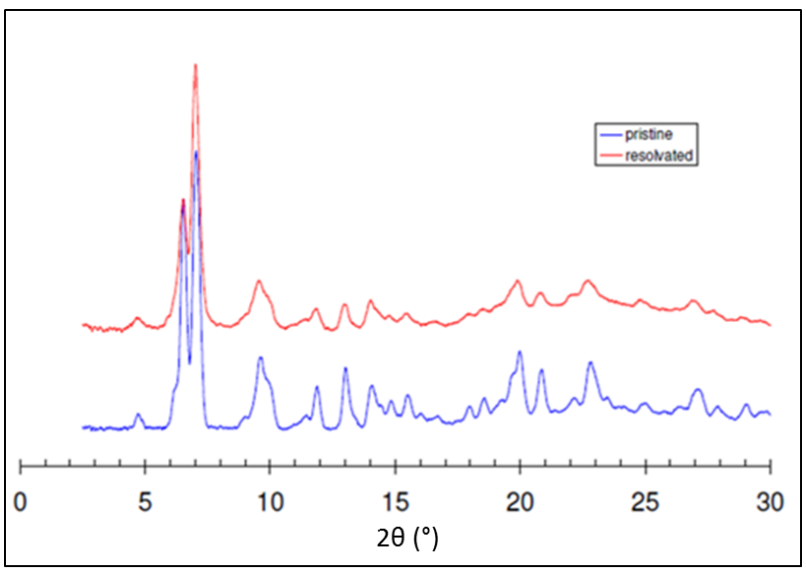

Figure 2.15: PXRD patterns of MOF-1; regular sample measured at RT (blue line) and then after desolvation by heating the sample to 125 °C under vacuum for 12 h. and subsequent resolvation by soaking in acetonitrile for 12 h. (red line).

Thermo-Gravimetric Analysis Studies of MOF-1

Thermo-gravimetric analysis (TGA) is an instrumental technique by which a sample is heated and the change in mass is measured.[175] We were interested in using

TGA to quantify the amount of solvent in the pores of MOF-1 as well as to identify the type of solvent molecules present. The experiment was carried out using a Mettler Toledo TGA/SDTA851 coupled to a mass spectrometer. In the experiment, helium was used to purge the system at a flow rate of 50 mL/min and the samples were heated in an opened crucible from 25 °C to 150 °C at a rate of 2 °C/min. When the temperature reached 150 °C, it was left at this temperature for 10 minutes. The results of this experiment are presented in Figure 2.16.

The TGA and TGA-MS curves indicate that the overall weight loss of the sample is about 19.86%. The first loss commences at room temperature and reaches a maximum around 80°C, consistent with the loss of crystallinity observed in the PXRD studies. This loss represents 14.67 % of the total weight and is attributed to the loss of both weakly bound water and acetonitrile molecules ($[CH_3CN]^+$ = 41 and $[H_2O]^+$ = 18) in the crystal lattice. Further weight loss commences at higher temperatures (100-150°C) resulting in an additional 5.19 % decrease in sample weight. In this region the loss of $CH_3C{=}O$ ions at *m/z* = 43 are attributed to the decomposition of coordinated acetate ligands, as well as the loss of water molecules that are more tightly bound within the cavity of the MOF.

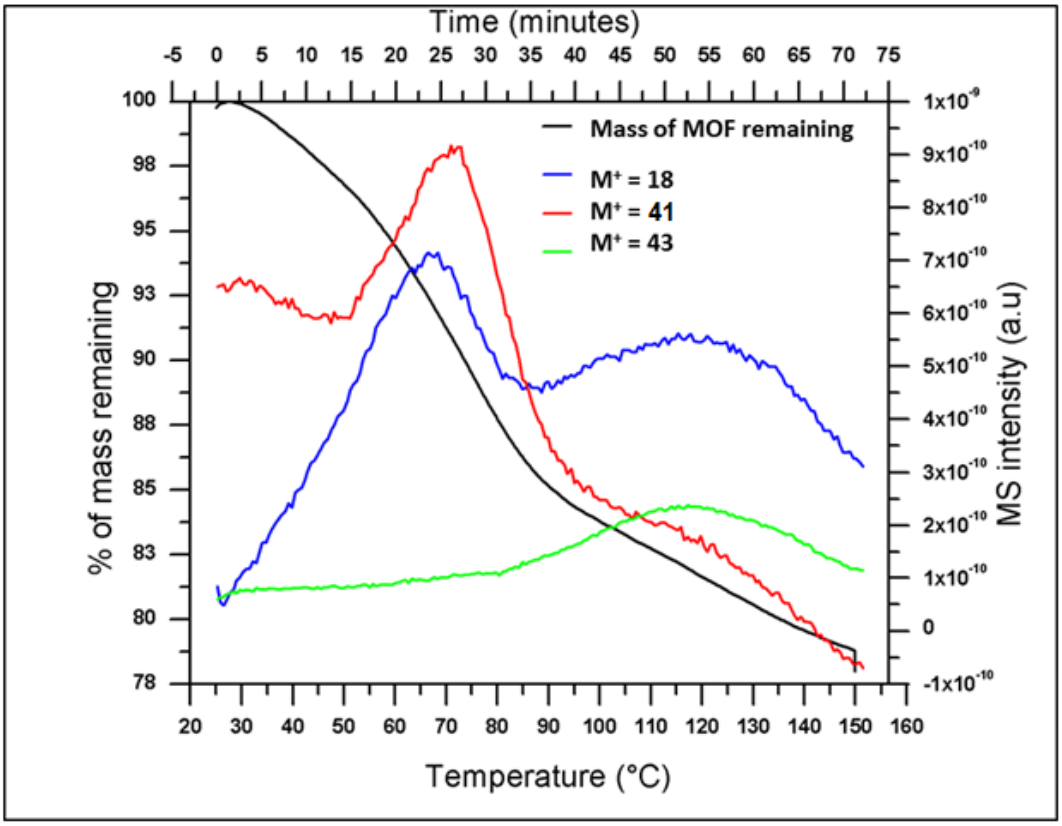

Figure 2.16: Thermo-gravimetric analysis coupled to mass spectrometry for MOF-1. The black line represents the percentage of mass remaining as a function of temperature. The blue line represents the loss of water at *m/z* = 18, the red line represents loss of acetonitrile at *m/z* = 41 and the green line represents the loss of a $[CH_3C{=}O]^+$ ion, most coming from the decomposition of the coordinated acetate ligands within the framework.

EPR Measurements of MOF-1

Since the MOF contains paramagnetic Cu^{2+} ions (S = ½), EPR studies were carried out on a crystalline sample at room temperature between 0 and 8000 G (ν = 9.851 GHz with a modulation amplitude of 4 Gpp). A simulation of the data was generated by PIP 24 *via* a windows interface, PIP for Windows v1.2. The data is presented in Figure 2.17.

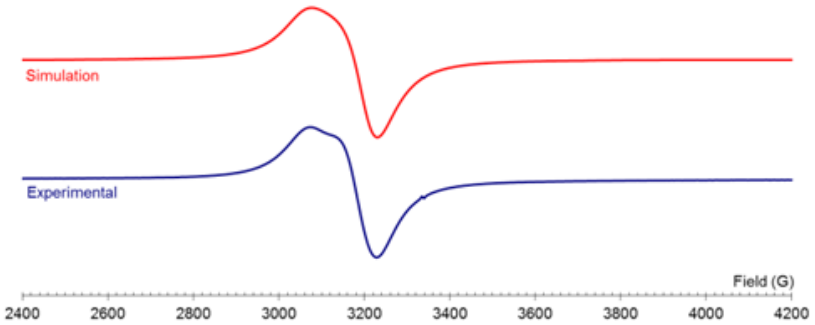

Figure 2.17: Solid-state EPR spectrum of MOF-1 at room temperature, the experimental data is plotted in blue and the simulated data is shown in red.

As shown above, solid state EPR spectroscopy revealed a broad singlet centered at g = 2.115. It is possible that this broadening is due to an overlapping of the individual singlets produced by each of the crystallographically unique three copper centers; however, broadening may also be evidence of weak dipole-dipole interactions. The EPR spectrum is consistent with the crystal structure of the MOF which shows that the paramagnetic Cu^{2+} ions are well separated (> 5 Å) and therefore any magnetic coupling between neighbouring Cu^{2+} centers is expected to be extremely weak.

DC-Magnetic Susceptibility Measurements

In order to further study the magnetic behaviour of the framework, dc-magnetic susceptibility measurements were carried out on a polycrystalline sample of MOF-1. The $1/\chi$ *vs* temperature plot (Figure 2.18, inset) is linear and follows Curie-Weiss behavior with a Curie constant C of 1.671 emu·K·mol^{-1} and a Weiss constant θ of −4.85 K, indicative of weak antiferromagnetic interactions between Cu^{2+} ions at low temperature. The plot of χT *vs* T is essentially a linear with a value close to C in

the high temperature region, followed by a steep decrease in magnetic susceptibility below 50 K. This steep decrease at low temperature is due to weak antiferromagnetic interactions, consistent with the negative Weiss constant, θ. Given that the shortest intermolecular Cu···Cu distances in the MOF are 5.007 Å, we conclude that the spins on the copper centres are essentially magnetically isolated and as a consequence, the magnetic susceptibility data was modelled as a linear trimer of S = ½ spins, applying the Heisenberg spin Hamiltonian shown in Eq. 2.2. The value of J was determined to be 5.98 cm^{-1}.

$$H = -2J\left(\hat{S}_1\hat{S}_2 + \hat{S}_2\hat{S}_3\right) \qquad \textit{Eq. 2.2}$$

To investigate whether or not the desolvation of the MOF has a significant effect on its magnetic properties, we evacuated the sample and heated it to 120°C overnight and then measured the dc susceptibility. Interestingly, no change in the χT *vs* T plot was observed confirming that even though the crystallinity of the sample is lost on desolvation, the Cu^{2+} ions remain magnetically isolated in the amorphous phase and that any structural changes that result in a loss of crystallinity do not have an observable effect on the magnetic properties of the framework.

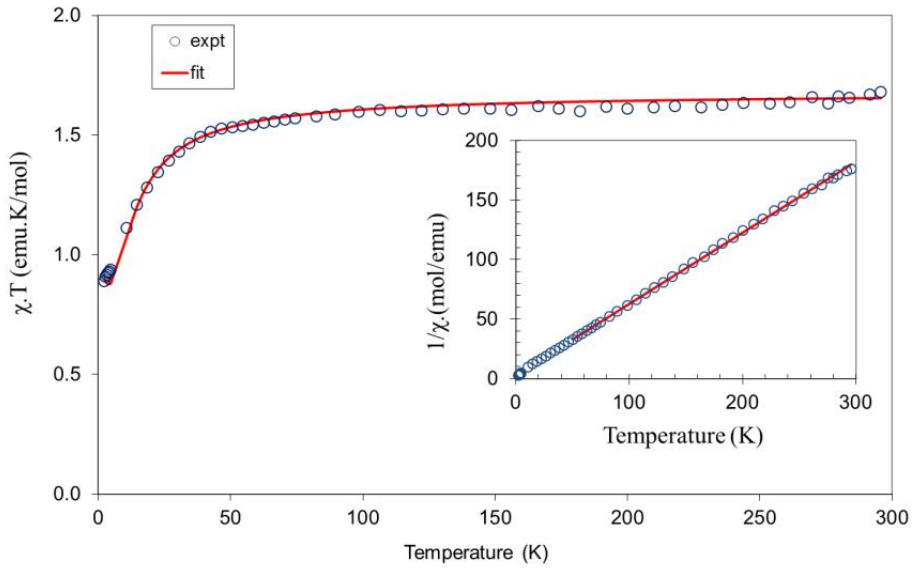

Figure 2.18: χT *vs* temperature plot for MOF-1, (inset) 1/χ *vs* temperature plot for MOF-1. The red lines are the modelled data, treating MOF-1 as a linear trimer of non-interacting Cu^{2+} ions.

Adsorption Studies

In MOF chemistry, it is common practice to quantify the pore volume by gas adsorption studies. This involves removing the solvent from the pores of the framework by either heating the substance or reducing the pressure. In some systems when a pressurised gas in applied to the sample, some of the gas is absorbed and this quantity is determined, yielding information about the pore volume. When this procedure was attempted, the dynamic nature of MOF-1 prevented any absorption from occurring and no surface area or pore volume could be determined.

This led us to investigate a supercritical drying technique where the solvent in the pores of the MOF is removed as a supercritical fluid and subsequently replaced by a known volume of gas. Attempts were made to try this approach in collaboration

with the MacLachlan group at the University of British Columbia. In this investigation the acetonitrile solvated MOF-1 was first soaked in a solution of absolute ethanol. The soaking solution was replaced 5 times over a 24 hours period to exchange all of the acetonitrile solvent molecules for ethanol. The absolute ethanol solvated MOF was then placed inside a critical point dryer and the ethanol was exchanged with $CO_{2(l)}$ over a period of 1 h. Nitrogen adsorption measurements were then performed however, these measurements yielded no appreciable surface area or pore volume which leads us to conclude that the inner surface of the MOF is most likely inaccessible when the MOF is desolvated.

In addition to gas adsorption studies, free-radicals were also explored as potential guest molecules for MOF-1. As part of these efforts the radical, 4-(4'-cyano-tetrafluorophenyl)-1,2,3,5-dithiadiazolyl (**2.9**) was exploited for inclusion studies due to its small size and well-known magnetic properties in the solid state.[176] To include the radical MOF-1 was purged with dry acetonitrile under argon three times to remove any oxygen and water. At this point the radical was introduced into the flask in acetonitrile under N_2 and the mixture was stirred for 2 hours.

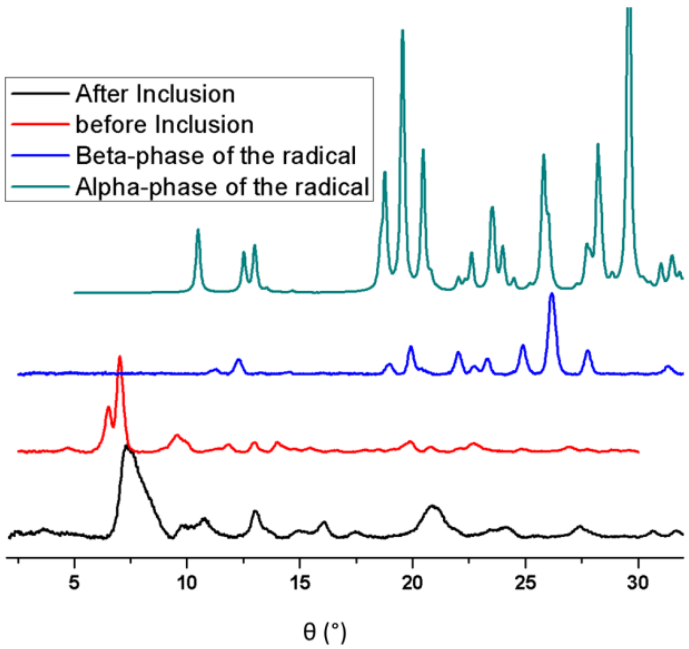

Figure 2.19: Powder patterns of the alpha and beta phases of NC-C_6F_4DTDA, pristine MOF, and MOF after the inclusion procedure.

Powder X-ray diffraction (Figure 2.19) and solid-state EPR (Figure 2.20) were used to probe the treated MOF for evidence of inclusion of the radical. In the PXRD studies, the powder patterns of the pristine MOF and radical were determined prior to inclusion and a final measurement after the inclusion attempt was performed. Between the pristine MOF and the treated MOF, there are some minor differences, such as, at 7.5° and 21°, however, these peaks are present in the partially collapsed spectrum of the MOF, and the absence of any new prominent peaks suggests no radical adsorption.

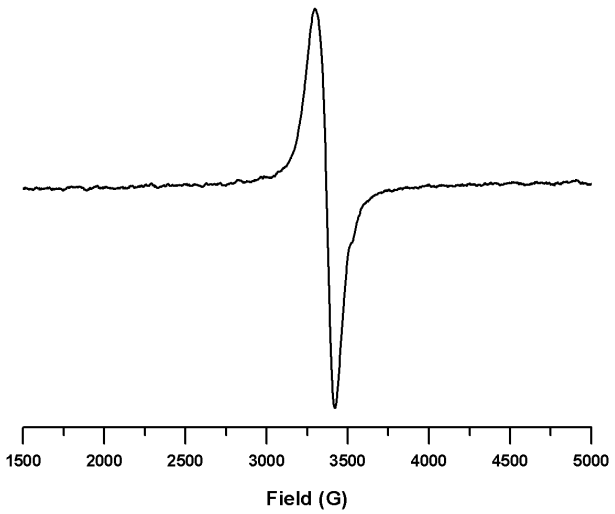

Figure 2.20: Solid-state EPR spectrum at room temperature of MOF-1 after being treated with the radical solution.

Solid-state EPR studies didn't reveal conclusive evidence for inclusion either. In the spectrum, a singlet was observed at *ca.* 3300 G similar to the singlet of the pristine MOF. No radical signal was observed which is likely due to the Cu^{2+} singlet masking the radical singlet. Unfortunately without a crystal structure, it is difficult to properly elucidate the inclusion affinity of this radical into MOF-1. Future experiments to determine whether or not MOF-1 could act as a catalyst for some of the reactions mentioned earlier would also be worth investigating.

Analysis of the breathing mechanism

Without a crystal structure of both phases of the MOF, it is difficult to accurately classify the dimension of breathing and the mechanism by which the MOF transforms. Nevertheless, the MOF can be analysed empirically by carefully analysing

the crystal structure. In this case we can consider the cross-linking 1D-pillars as one dimension and the 2D-sheets as the remaining two dimensions. Taking into consideration the pillars only, each Cu2 centre is coordinated to two sheets by two pyridyl substituents from each sheet, Figure 2.21. These pyridyl substituents have a considerable amount of rotational freedom which could induce an expansion or contraction of the structure along this dimension of the MOF. Therefore, the 1D-pillars should be considered as flexible dimensions.

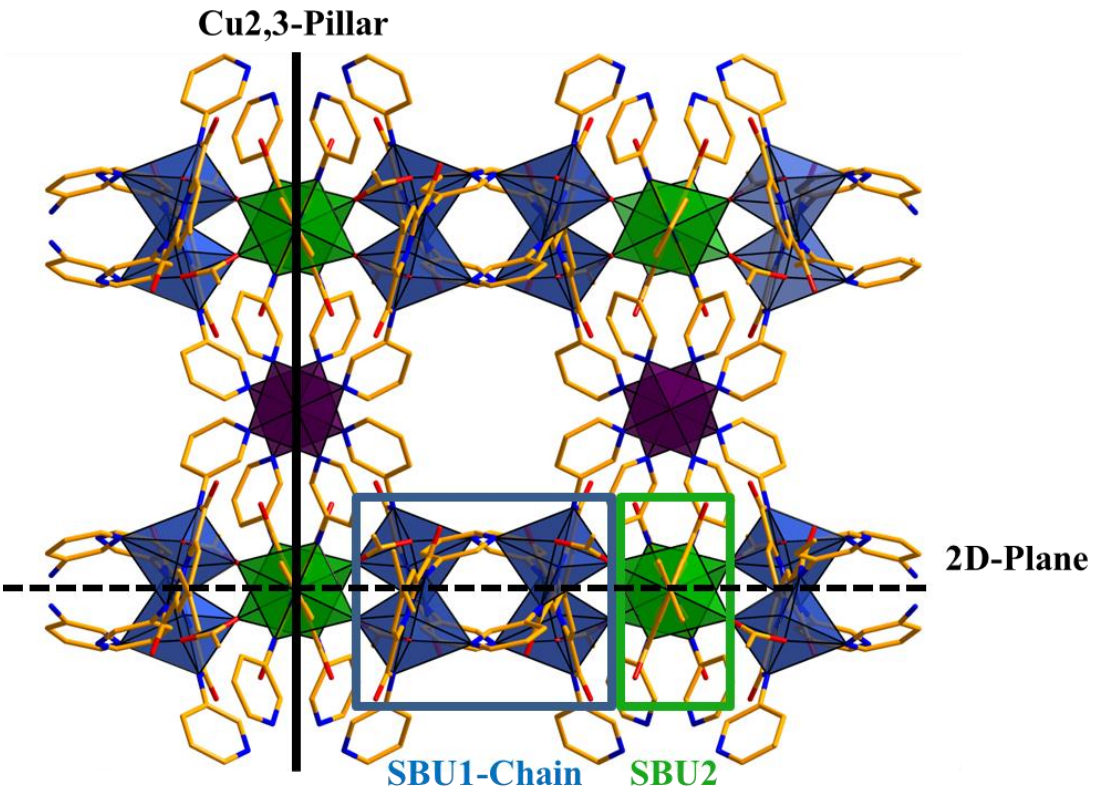

Figure 2.21: A truncated fragment of MOF-1 viewed down the *a*-axis. The blue, purple and green polyhedra correspond to the coordination environments of Cu1, Cu2 and Cu3, respectively. For perspective, the SBU1-chain is viewed along its length.

Concerning the 2D-sheets, the two dimensions can be analysed separately by considering the 1D-chains of SBU1 independently of the the SBU2 and the acetate units that link the 1D-chains together. Similar to the Cu2 pillar, the SBU1 units are linked together by the pyridyl substituents, leading to a reduced rigidity in this dimension. For the remaining dimension, both the acetate and SBU2 linkers have rotational freedom, Figure 2.22 along the O-Cu^{2+} coordination bond and within the bipyridine unit. From this empirical analysis, we therefore characterize MOF-1 as a 0DB-SPC that most likely undergoes structural transitions *via* a flexible-linker twisting mechanism that can potentially operate in all three dimensions of crystallographic space in a non-uniform manner, resulting in a collapse to an amorphous powder.

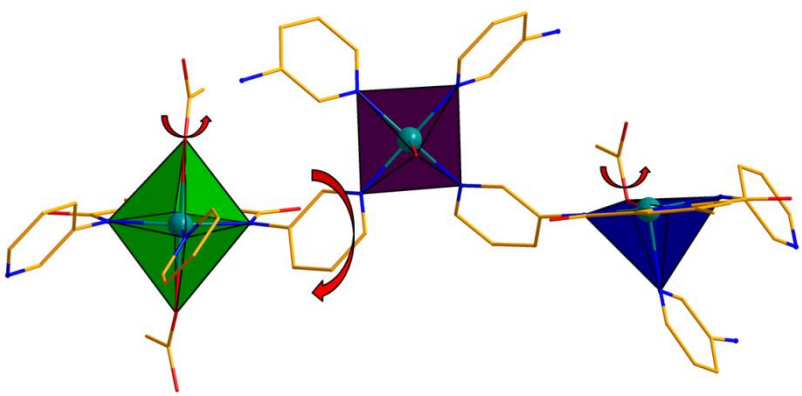

Figure 2.22: Asymmetric unit of MOF-1 showing the possible linker rotations (red arrows). The Cu^{2+} ion coordination spheres are colour-coded as green (Cu3), purple (Cu2) and blue (Cu1) polyhedra. H-atoms are omitted for clarity.

2.4: Summary and Conclusions for Project 1

A 2,2′,6,6′-tetracarbamide-4,4′-bipyridine ligand ($H_4\mathbf{L_2}$) with stable, amide appended pyridyl substituents was synthesised and characterised. Despite the limited

solubility of the ligand, reaction conditions were found with copper acetate for the growth of single crystals of the first transition metal complex of this ligand. X-ray diffraction studies reveal that the structural flexibility and polydentate nature of the ligand together afforded a porous 3D metal organic framework with a completely novel topology. Interestingly, the MOF was found to undergo a reversible structural transformation between a porous crystalline state and a collapsed amorphous state in response to the removal and the re-introduction of acetonitrile solvent into the pores. This transformation was studied by temperature-variable PXRD and TGA-MS which confirmed the breathing behaviour of the MOF. Gas-adsorption studies were performed using a supercritical drying method, but yielded no appreciable results due to the dynamic behaviour of the MOF.

Ongoing research is now in progress to investigate further the coordination chemistry of (H_4**L**$_2$**)** employing different metal ions and diverse reaction conditions that include solvothermal methods. To date, conditions for synthesising MOFs by solvothermal methods in our group have not been determined. The Pilkington research program has in more recent years shifted towards the discovery of Ln-based single molecule magnets. In this context, project 2 described in the next chapter of this thesis details my work towards the rational design and synthesis of a new family of Ln(III)-single molecule magnets.

Chapter 3 : Project 2 – Synthesis, Magnetostructural and Theoretical Studies of Ln^{3+} complexes of a Dual Compartmental Macrocycle

3.1: Synthetic Strategy

In the Pilkington group, research efforts have recently focused on the discovery of Ln^{3+}-based SMMs with pseudo D_{5h} geometries imparted on the metal ions *via* the employment of a suitable macrocyclic ligand. As discussed previously, the ligand field is an important factor to consider when working toward the discovery of high energy barrier SMMs since high symmetries can serve to increase the magnetic anisotropy of lanthanide ions and thus the energy barrier of the resulting complexes.[110] Regarding the coordination sphere of the Dy^{3+} ion, it is well-established that Dy^{3+} complexes tend to prefer 8- and 9-coordinate geometries which often crystallize in high symmetry, 8-coordinate square antiprismatic and 9-coordinate monocapped square antiprismatic geometries.[177] Despite these observations, with the right choice of ligand system Dy^{3+} ions can also crystallize in lower, 7-coordinate, pentagonal bipyramidal, face-capped octahedral and trigonal prismatic geometries. Out of these geometries, the most promising for the development of SMMs is pentagonal bipyramidal as has been elegantly demonstrated by Tong *et al.* for complexes (**1.26)** and (**1.27)** reviewed in Chapter 1 of this thesis.

With an interest in further understanding the effect of pentagonal bipyramidal geometry on the magnetic properties of transition metal and lanthanide complexes, we turned our attention to employing N_3O_2 and N_5 Schiff-base macrocyclic ligands that

are known to confer pseudo D_{5h} geometry on first row transition metal ions.[178,179,180] Along these lines, previous work in the Pilkington group involved the preparation of chiral Fe^{2+} N_3O_2 complexes with spin crossover properties[179] as well as developing Mn^{2+} and Gd^{3+} macrocycles as potential contrast agents for magnetic resonance imaging (MRI).[180] In these complexes the macrocycle typically coordinates the metal ion in the equatorial plane with two axial ligands completing the pseudo pentagonal bipyramidal geometry shown in Figure 3.1.

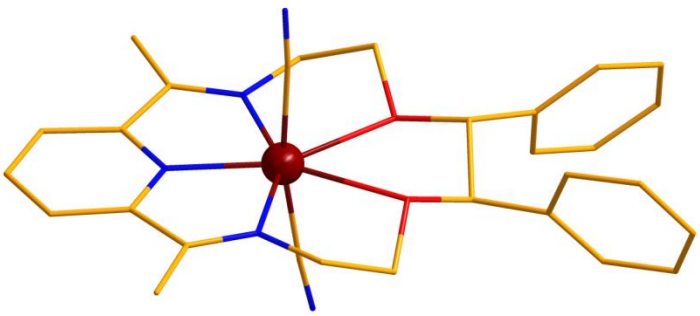

Figure 3.1: Crystal structure of the chiral $[Fe^{2+}(N_3O_2)(CN)_2]$ complex (**3.4)** showing the preference for pentagonal bipyramidal geometry with a chiral penta-coordinate N_3O_2 macrocycle.[179]

Although transition metal complexes of these macrocycles have been known since Nelson and Drew's work in the 1970s,[181] prior to our work their lanthanide complexes had not been structurally or magnetically characterised. Our group therefore set out to establish whether or not it would be possible to template these Schiff-base macrocycles around *f*-block ions, and then to characterize the magnetic properties of the resulting complexes.[182,183] Following this approach, Pilkington *et al.* successfully synthesised and characterized a range of Dy^{3+} complexes of Schiff-base macrocycles that included the N_3O_2 and N_5 systems described above.[183] Although

pentagonal bipyramidal geometry was conferred by a number of characterization methods, no single crystals of these complexes could be grown for X-ray diffraction studies and powder measurements revealed that all of this family of complexes were amorphous. Nevertheless, ac magnetic susceptibility studies showed that the Dy^{3+} complexes of both the N_5 and N_3O_2 macrocycles displayed slow relaxation of the magnetisation consistent with SMM behaviour. Given their amorphous nature we were unable to proceed further to carry out magnetostructural studies thus rendering this family of complexes unsuitable for future research. We therefore set out to find an alternative system that would both confer the desired pentagonal bipyramidal geometry on select metal ions and afford suitable single crystals of the resulting complexes for structural elucidation by X-ray diffraction. Employing this strategy, a detailed search of the Cambridge Crystallographic Database (CSD) uncovered Ln^{3+} complexes of a dual compartmental macrocyclic ligand **H_2L_3Me** (**3.5**) which were first reported in the late 1990s[184,185] as Ln-shift reagents for NMR spectroscopy (Figure 3.2). Closer examination of the structures of these complexes revealed that in almost all of the cases the Ln^{3+} ions are coordinated in the $N_3O_2^{2-}$ pocket of the macrocycle with pentagonal bipyramidal geometry.[184,185] We were particularly interested in this $N_3O_2^{2-}$ pocket, over the $O_3O_2^{2-}$ pocket since the nitrogen atoms are softer and so should interfere with the oblate 4*f*-electron density in the equatorial plane to a much lesser extent than their harder, oxygen counterparts.

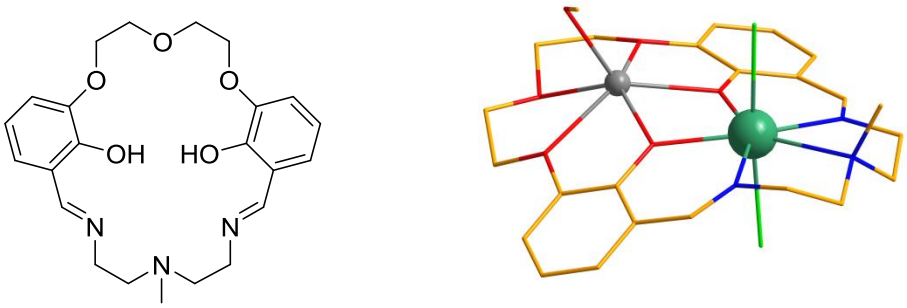

Figure 3.2: Left: Structure of the $H_2\mathbf{L_3}$Me macrocycle (**3.5)**. Right: Crystal structure of (**3.6**), the Eu^{3+} complex of (**3.5)**.[184] The Eu^{3+} ion (green sphere) is coordinated in the N_3O_2 equatorial plane of the macrocycle with two axial Cl^- ligands completing the pseudo pentagonal bipyramidal geometry. A Na^+ ion (grey sphere) is located in the O_5^{2-} binding pocket. H atoms and counterions are omitted for clarity.

Aside from facilitating a pentagonal bipyramidal geometry, the two coordination domains of **3.5** are asymmetric with respect to each other which may also, in the longer term, allow us synthetically access novel hetero-bimetallic systems (M_1^{n+},M_2^{m+}) that could provide insight into the influence of neighbouring metal ions on the magnetic anisotropy of Ln^{3+} ions in D_{5h} geometries. These bimetallic systems are not only interesting from a molecular magnetism point of view, but have also received attention for their correlation to the active sites of metalloproteins which serve as useful models for studying and mimicking the reversible binding of oxygen.[186]

The synthetic strategy for this project therefore involves targeting the novel H-derivative, $H_2\mathbf{L_3}$, where the methyl group on the amine of previously reported **3.5** is replaced with a hydrogen atom. We chose to target this derivative since its diethylenetriamine (dien) precursor is commercially available, whereas 1,5-diamino-

3-azamethylpentane (DAP) (**3.7**) the precursor to **3.5** is not and requires the additional synthetic steps shown below following ether Scheme 3.1[179] or Scheme **3.2**.[187]

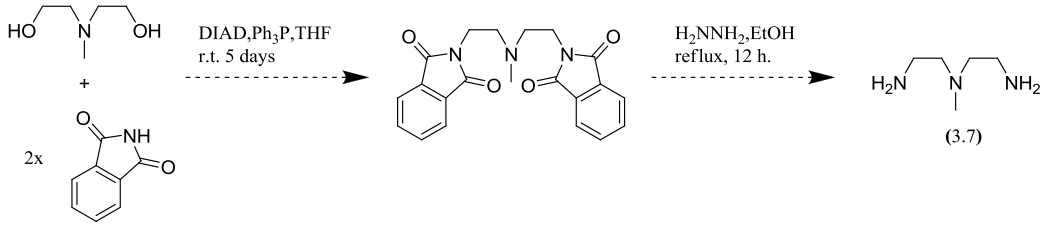

Scheme 3.1: Synthetic strategy for the synthesis of the methyl substituted dien precursor **3.7** using the modified Mitsunobu synthetic conditions reported in reference 179.

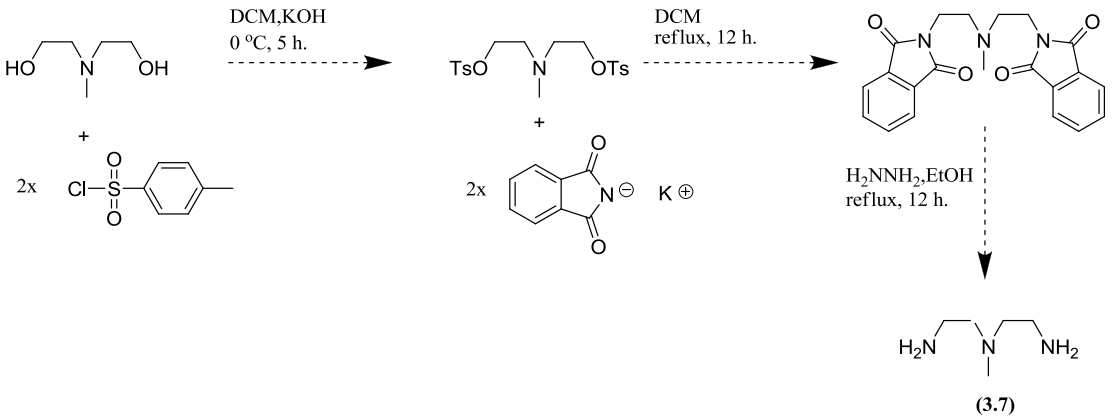

Scheme 3.2: Proposed synthesis of the methyl substituted dien precursor **(3.7)** using the modified procedure from reference 187.

Although we attempted to prepare this precursor, we found that the reaction conditions of Scheme 3.1 yielded a mixture of products which were not elucidated and were difficult to separate by column chromatography. Following the conditions outlined in Scheme 3.2, the reaction did not afford the desired product. Therefore, we subsequently made the decision to focus our efforts on targeting the preparation of the

new derivative (**H_2L_3**), whose coordination chemistry had not been explored previously.

3.2: Preliminary Computational Investigation of a Dy^{3+}-L_3 Complex

Prior to carrying out any synthetic work, a preliminary computational investigation was performed using the CASSCF/RASSI/SINGLE_ANISO approach in the MOLCAS[188] platform to determine whether or not the target complex would likely exhibit any SMM behaviour as well as to compute a theoretical energy barrier towards the reversal of magnetisation. As mentioned in the introduction, the CASSCF/RASSI wave functions can be used to calculate the physical observables of the Stark sublevels for Ln^{3+} complexes which reveal an insight into both the relaxation mechanism and the magnitude of the anisotropy barrier of Ln-SMMs.

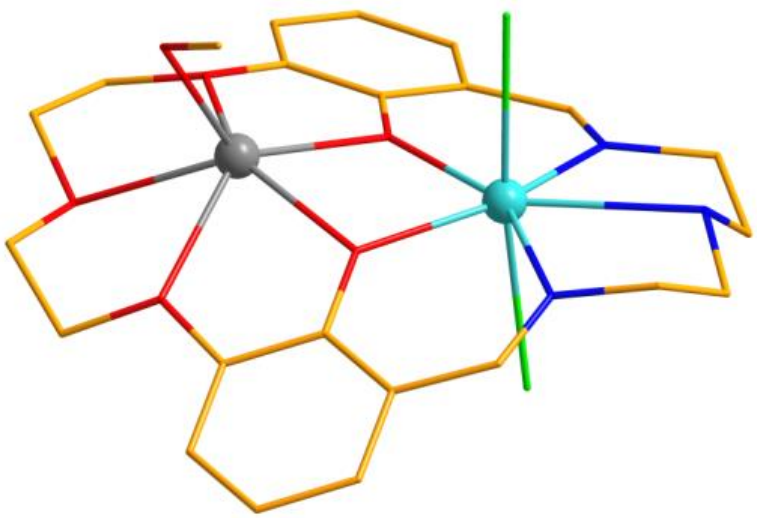

Figure 3.3: Crystallographic model used to predict the magnetic behaviour of the targeted Dy^{3+} complex. Dy^{3+} and Na^{+} ions are represented as blue and grey spheres respectively.

Fortunately, the crystal structure of the Er^{3+} complex of the methyl derivative, **3.6**, proved very useful here; since by simply exchanging the Me group for H and the Er^{3+} for Dy^{3+}, we were able to use this as the theoretical model for the *ab initio* calculations as shown in Figure 3.3. As previously mentioned, the crystal structure of this complex reveals the Ln^{3+} ion is coordinated in the $N_3O_2^{2-}$ pocket, adopting a distorted pentagonal bipyramidal coordination geometry that is completed by two axially coordinated chloride ligands. In this complex a Na^{+} ion (grey sphere) is coordinated in the O_5^{2-} cavity of the macrocycle, *vide infra*.

For the calculations, relativistic basis-sets of the atomic natural orbital type were used from the MOLCAS library.[188] Various truncations of the basis sets were considered in order to determine whether or not there is a basis set dependence on the calculations. It was found that different basis set models deviated very little from one another and so the results from only the most extensive basis set model is shown here with the following truncations for each element in the complex: Dy (9s8p6d4f3g2h), O-coordinating (4s3p2d1f), N (4s3p2d1f), O-distant (3s2p), C (3s2p), H (2s), and Na (5s4p2d1f). From the SINGLE_ANISO module, we acquired the g-tensors and direction of the main magnetic axis for each set of Kramers doublets in the $^6H_{15/2}$ multiplet. The results of the *ab initio* calculations are summarised in Table 3.1.

Table 3.1: Summary of computational results from the MOLCAS calculations on our target complex affording the energy levels, values of the g tensors and angle (°) between the eight Kramers doublets (KDs) of the $^6H_{15/2}$ multiplet.

KD	ΔE (cm^{-1})	g_x	g_y	g_z	Angle (°)
1	0.00	0.14	0.37	18.63	0.00
2	76.83	0.93	1.40	14.15	6.20
3	146.47	0.08	2.02	12.57	17.90
4	243.58	2.66	4.76	12.10	67.90
5	286.81	0.87	3.91	12.29	21.70
6	350.82	0.95	4.95	12.25	3.90
7	421.72	0.19	5.28	9.88	90.60
8	450.14	0.77	5.78	13.27	32.10

For the model complex **3.6**, the *ab initio* calculations reveal a large separation ΔE_1 = 76.83 cm^{-1} between the ground KD1± and first excited KD2± and that the g-tensors of KD1± are closer to Ising (g_x=g_y=0, g_z = 20) with small transverse components (g_x = 0.14, g_y = 0.37), whereas for the second excited state Kramers doublets, KD±2 the transverse components are considerably larger (g_x = 0.93, g_y = 1.40). From these studies it is apparent that for this complex, the magnetic relaxation should predominantly take place *via* the first excited state which has an energy barrier of 77 cm^{-1} and is therefore magnetically isolated; hence we would expect to observe SMM behaviour in this complex. Additionally, the angle between the main magnetic axes of the ground and first excited states is small (6°) which should reduce Orbach and/or Raman spin-lattice relaxation processes, as well as supress quantum tunnelling.

However, we also note that the small non-coincidence angle between the two magnetic axes does not completely eliminate two phonon spin-lattice relaxation processes.[189] In light of this data, we concluded that the results of this initial investigation were promising enough to move forward with the project and synthesise the target (**H_2L_3**), macrocycle and investigate its coordination chemistry together with appropriate Ln^{3+} ions.

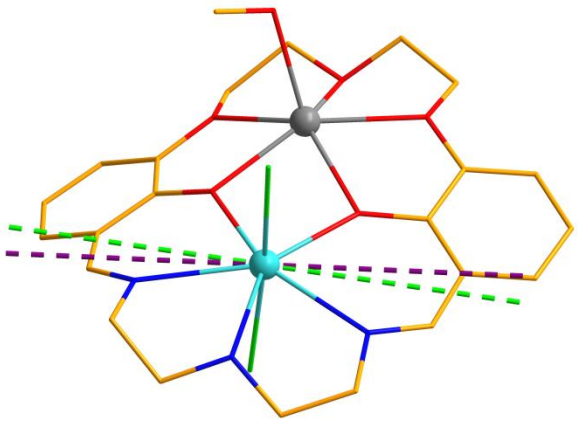

Figure 3.4: Structure of the Dy^{3+} macrocycle model with the computed main magnetic axes of the ground and first excited KD shown as purple and green dashed lines, respectively. The Dy^{3+} ion is plotted as a blue sphere.

3.3: Synthesis and Characterisation of the macrocycle H_2L_3

The synthesis of (**H_2L_3**), was achieved in two steps following the methodology previously reported by Reinhoudt[190] and Caselleto as outlined in Scheme 3.3.[184] First, the dialdehyde precursor, **L_3'** was prepared via the deprotonation of 2,3-dihydroxybenzaldehyde (H_2DHB) by treatment with NaH which then reacts with the tosylated diethylene glycol in an S_N2 manner. In this reaction, the hydroxyl group *ortho* to the aldehyde is the most acidic because the anion of the conjugate base is

stabilised *via* conjugation with the aldehyde. Both hydroxyl groups are initially deprotonated with the expectation that the conjugate base of the *meta* hydroxide is more basic and will react first. During the workup, the product is treated with acid to protonate the unreacted phenolate group and the resulting dialdehyde **L_3'** is isolated as yellow oil in 88 % yield which crystallises upon standing. The melting point and ^{1}H NMR spectrum of this compound were found to be consistent with the data reported in the chemical literature.[184]

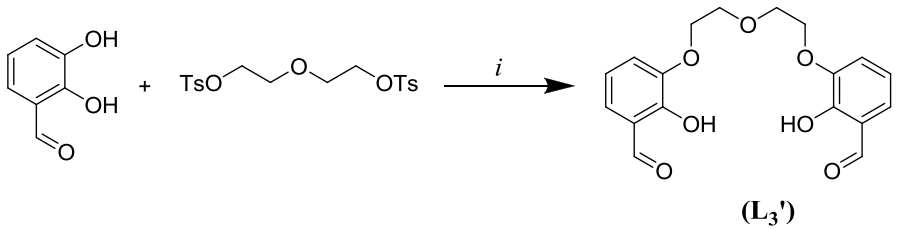

(L_3')

Scheme 3.3: Preparation of the dialdehyde (**L_3'**).[184] Reaction conditions: i) NaH, DMSO, r.t., 12 h, 88 % yield.

The second step in the synthetic strategy involves the Schiff-base condensation of dialdehyde (**L_3'**) together with the ethylenediamine (en) in a (1:3:300) mixture of methanol, chloroform and diethyl ether. The macrocycle (**H_2L_3**) was obtained as a yellow solid in 90% yield (Scheme 3.4). Due to its hygroscopic nature, it was quickly transferred to a sealed flask and placed under vacuum for 1 hour, after which time it was stored under N_2 until needed.

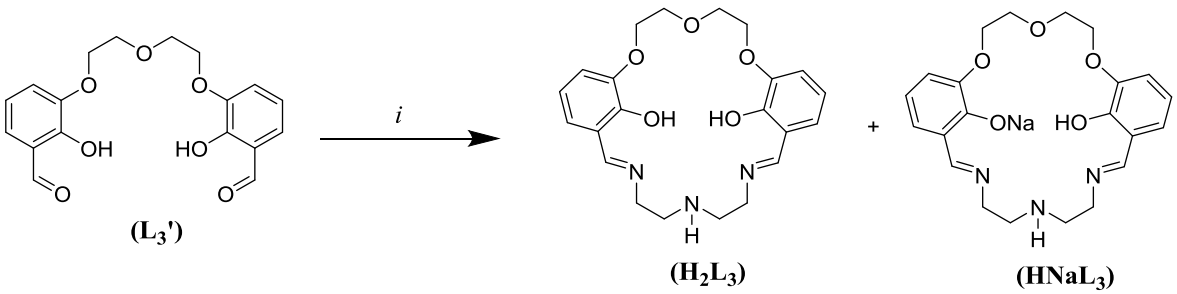

(L_3') (H_2L_3) ($HNaL_3$)

Scheme 3.4: Synthesis of (**H_2L_3**). Reaction conditions: en, MeOH/$CHCl_3$/Et_2O (1:3:300), r.t., 20 mins, 90 % yield.

The novel dual compartmental macrocycle (**H_2L_3**) was characterized by NMR, IR and MS spectrometry. Broad peaks in the ^{1}H NMR spectrum were observed and are attributed to the presence of a mixture both the fully protonated (**H_2L_3**) and the monosodic (**$HNaL_3$**) where the Na^+ ion from the NaH in the first step is coordinated to the macrocycle. This is consistent with what has been reported previously in the chemical literature for the methyl derivative (**3.5**).[184] These products were found in an approximate ratio of 2:1 (**H_2L_3**:**$HNaL_3$**) as observed in the NMR spectra. Removal of the monosodic derivative was deemed unnecessary since (**H_2L_3**) is deprotonated in the next step. Purification of the (**H_2L_3**) derivative can be achieved by recrystallization from $CHCl_3$.

The ^{1}H-NMR spectrum of (**H_2L_3**) is shown in Figure 3.5. A broad singlet is clearly visible at 8 ppm for the imine proton. A broad multiplet between 6.91 and 6.59 ppm is observed for the six aryl hydrogen atoms H4-H6 and H4'-H6'. The broadened ethylene resonances are found at 4.17, 3.93, 3.62 and 2.91 ppm, corresponding to H2, H3, H10 and H11 respectively. No N-H and O-H resonances could be observed, most likely since they are too broad to be detected. Even after drying under vacuum, a trace

amount of diethyl ether was still present in the compound which can be seen as a triplet at 1.17 ppm and a quartet at 3.44 ppm.

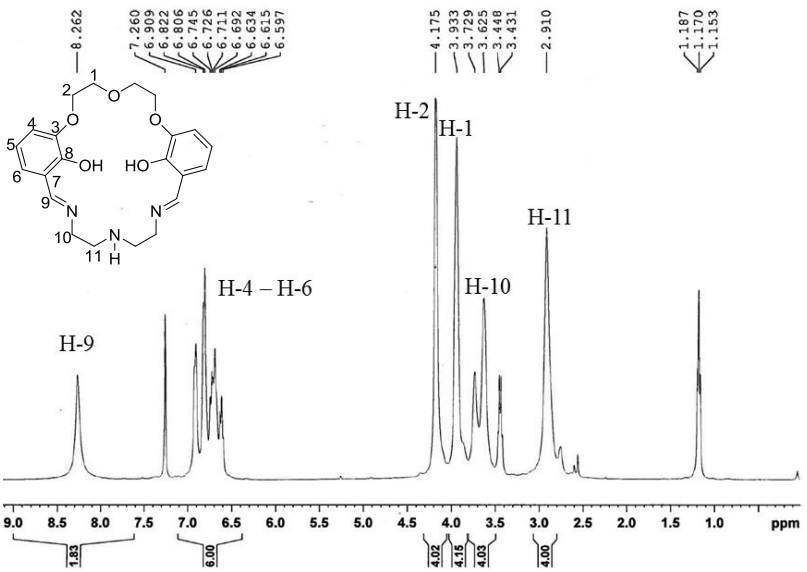

Figure 3.5: 300 MHz ^{1}H-NMR spectrum of (**H_2L_3**) in $CDCl_3$.

The ^{13}C NMR spectrum shows resonances consistent with all eleven unique carbon centers of the macrocycle. As previously observed for the methyl derivative, two resonances can be found for many of the carbon atoms of the macrocycle which are again attributed to a mixture of both the H_2L_3 and $HNaL_3$. The imine-C resonance appears furthest down-field at 166.17 ppm. Resonances for the C-O aryl carbon atoms are observed at 153.52 ppm and 147.55 ppm and are assigned to C3 and C8, respectively. The remainder of the aryl resonances are found at 123 ppm, 118 ppm, 117 ppm and 116 ppm, attributed to C7, C6, C5 and C4, respectively. Finally, four ethylene ^{13}C resonances are found upfield at 68 and 69 ppm and are assigned to the ethoxy carbon atoms, C2 and C1, and at 58 and 49 ppm for C10 and C11, Figure 3.6.

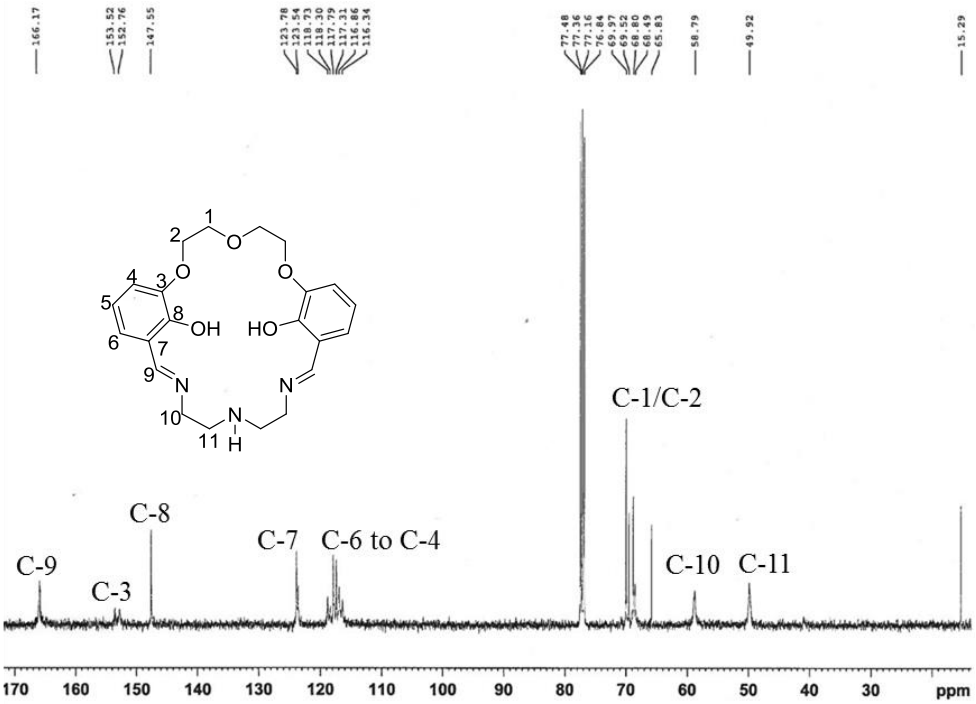

Figure 3.6:100 MHz ^{13}C-NMR spectrum of (**H_2L_3**) in $CDCl_3$.

The IR spectrum of (**H_2L_3**) contains a C=N str at 1629 cm^{-1} consistent with the presence of the Schiff-base imine linkage. In the ESI mass spectrum, two prominent peaks were observed corresponding to the protonated parent ion $[MH]^+$ at *m/z* = 414 and the monosodium ion $[MNaH]^+$ at *m/z* = 436. The UV-Vis spectrum in chloroform shows two absorption maxima at λ = 264 nm (ε = 21 000 $cm^{-1}M^{-1}$) and 328 nm (ε = 4800 $cm^{-1}M^{-1}$) assigned to the $\pi \rightarrow \pi^*$ transitions of the imine and the $n \rightarrow \pi^*$ transitions of a nitrogen lone-pair into the anti-bonding orbital of the imine respectively. Unfortunately, since (**H_2L_3**) is only soluble in either chloroform or DCM, absorption bands below 245 nm could not be adequately evaluated.

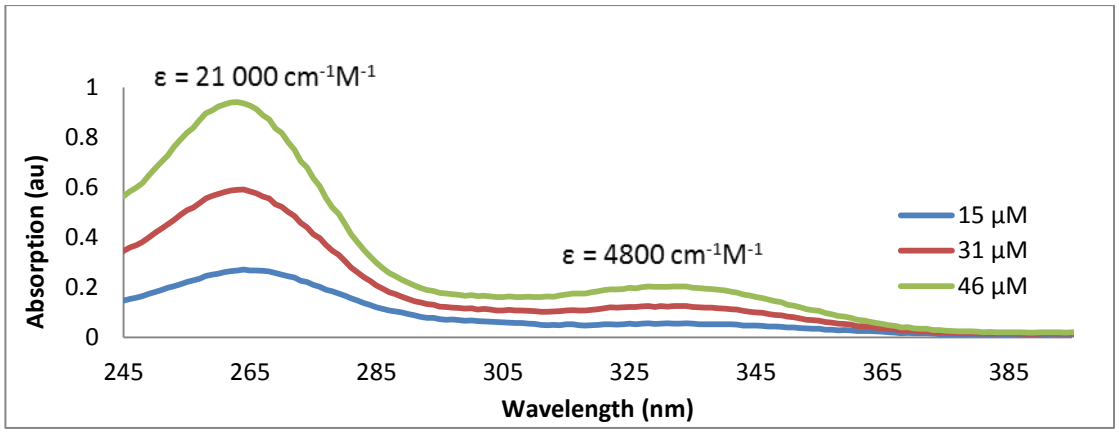

Figure 3.7: UV-Vis spectrum of (**H_2L_3**) in chloroform at room temperature.

3.4 Coordination Chemistry of H_2L_3

Once we had successfully prepared the macrocycle our next objectives were to study its coordination chemistry with Ln^{3+} ions. Dy^{3+} was initially chosen for its desirable electronic properties and magnetic anisotropy and subsequently, the coordination chemistry together with Tb^{3+} and Er^{3+} were also investigated. When employed with the correct choice of ligands, Tb^{3+} ions have afforded SMMs with some of the largest energy barriers reported to-date. However, Tb^{3+} has a spin ground state with $S = 3$ which typically leads to non-degenerate Stark sub-levels which means that an axial crystal field is necessary for the observation of a bistable ground state and thus SMM properties. Fortunately it has been shown that forTb^{3+} complexes with certain coordination geometries, the lowest Stark sublevels can be manipulated to yield a set of well isolated doublets and therefore SMM behaviour.[191] In contrast, Er^{3+} is a Kramers ion that has a ground multiplet of $^4I_{15/2}$ and as a result, in recent years researchers have successfully exploited Er^{3+} for the synthesis of SMMs.[192] It is noteworthy to mention that Er^{3+} differs significantly from Dy^{3+} and Tb^{3+} in that it has

prolate *f*-electron density and for this reason we were interested to explore the effects of a pentagonal bipyramidal crystal field imposed by the (**H_2L_3**) macrocycle on the magnetic anisotropy of a prolate Ln^{3+} ion.

3.4.1. General Synthesis of Complexes 3.1 – 3.3

All three complexes were synthesised by the reaction of one equivalent of $LnCl_3 \cdot 6H_2O$ together with one equivalent of (**H_2L_3**) under slightly basic conditions under nitrogen. Firstly, one equivalent of (**H_2L_3**) was deprotonated via the addition of two equivalents of NaOH at room temperature in a 1:1 mixture of MeOH and $CHCl_3$. This affords the disodium derivative **Na_2L_3** where the Na^+ ions are coordinated in the $O_3O_2^{2-}$ cavity making the N_3O_2 cavity available for the Ln^{3+} ion.[184] At this point a methanol solution of one equivalent of the lanthanide salt, $LnCl_3 \cdot 6H_2O$ was added, where Ln^{3+} = Dy (**3.1**), Tb (**3.2**) and Er (**3.3**). The resulting solution was then heated overnight and on cooling, the complexes were isolated as crystalline solids in 80, 95, and 95 % yields by mass for (**3.1**) to (**3.3**), respectively. For each complex the resulting solid was dissolved in methanol and single crystals were grown via the slow diffusion of diethyl ether into the resulting solution.

3.4.2 Structural Studies of Complexes 3.1 – 3.3

X-ray quality single crystals of all three Ln^{3+} complexes were obtained after 3 days. In contrast to the previously reported crystal structure of the methyl analogue (**3.5**), X-ray diffraction studies reveal that these complexes crystallize as dimers of stiochiometry $[Ln_2Na_2(\mathbf{L_3})_2(Cl)_4(MeOH)] \cdot xH_2O$ in the monoclinic space group $P2_1$. The asymmetric unit contains one crystallographically unique dimer and the unit cell

is comprised of two symmetry related dimers. The unit cell parameters for the three complexes are presented in Table 3.2.

Table 3.2: Summary of selected crystallographic parameters for complexes (**3.1**)-(**3.3**).

	Complex 3.1	**Complex 3.2**	**Complex 3.3**
Mol. Formula	$C_{45}H_{51}Cl_4Dy_2N_6Na_2O_{13}$	$C_{45}H_{52}Cl_4Tb_2N_6Na_2O_{11}$	$C_{45}H_{51}Cl_4Er_2N_6Na_2O_{12}$
Unit Cell	a = 9.4342, b = 20.316, c = 13.5275, β = 97.960	a = 9.426, b = 20.183, c = 13.547, β = 97.893	a = 9.4325, b = 20.239, c = 13.5590, β = 97.904
Volume (Å^3)	2567.77	2552.83	2563.88
Crystal System	monoclinic	monoclinic	monoclinic
Space Group	$P2_1$	$P2_1$	$P2_1$

For the Dy^{3+} analogue, some disorder was observed in the C atoms of the ethylene bridges which have also been observed in coordination complexes of similar ligand systems.[184,185] Each monomer of (**3.1**) is comprised of two crystallographically unique Dy^{3+} and Na^+ ions, Figure 3.8. The Dy^{3+} ions within the dimer are well separated by a distance of 6.966 Å. Both Dy^{3+} ions adopt pentagonal bipyramidal coordination geometries and reside within the $N_3O_2^{2-}$ pockets of their respective macrocycles. The Na^+ ions occupy the $O_3O_2^{2-}$ pockets and have trigonal prismatic coordination geometries. For each Dy^{3+} ion, $\mathbf{L_3^{2-}}$ coordinates in an equatorial fashion with two axial chloride ions completing a pseudo D_{5h} coordination geometry. Although the coordination spheres are the same for both Dy^{3+} ions, they differ slightly in their axially coordinated chloride ligands since the Cl2 ion coordinated to Dy1 is bridging and is therefore also coordinated to the Na^+ ion of the second macrocycle of the dimer. In contrast, the remaining three Cl1, Cl3 and Cl4 ions are all coordinated to a single Dy^{3+} ion in a monodentate fashion. It is noteworthy that the Cl-Dy-Cl angles for both crystallographically independent Dy^{3+} ions deviate from 180° as summarised in Table 3.3.

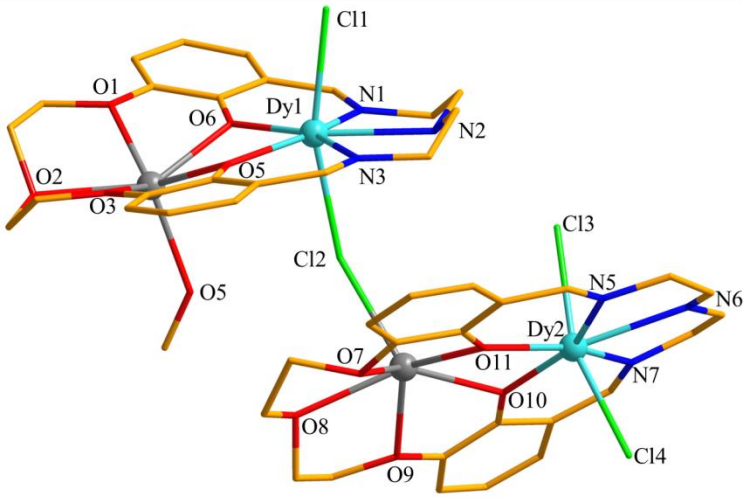

Figure 3.8: Crystal structure of the Dy^{3+} dimer, complex (**3.1**) with appropriate labelling scheme. H-atoms and water molecules are omitted for clarity.

Selected bond lengths for complex (**3.1**) are presented in Table 3.3. For both Dy^{3+} ions, the non-bridging Dy-Cl bond lengths range from 2.644 (7) to 2.660 (8) Å, while the bridging Dy1-Cl2 bond is slightly longer at 2.686(7) Å. Concerning the equatorial bond lengths, the respective Dy^{3+} ion is displaced from the center of the pentagonal plane towards the negatively charged O^{-} donor atoms. This is evident in the shorter Dy-O bond lengths that range from 2.228(19) Å to 2.26(2) Å and the considerably longer Dy-N bond lengths that range from 2.47(3) Å to 2.54(3) Å. For both Dy^{3+} ions, the O-Dy1-N angles vary from 72.3(7)° for O11-Dy1-N11 to 73.8(9)° for O21-Dy2-N21, which are close to the 72° angle expected for ideal pentagonal bipyramidal geometry. In contrast, the ∠ N-Dy1-N are less than ideal, and take values between 69.2(7)° for N11-Dy1-N12 to 67.0(10)° for N22-Dy2-N21. The largest deviation from 72° occurs for the ∠ O-Dy-O which have values of 78.1(8)° for O25-Dy2-O21 to 70.0(7) for O11-Dy1-O15, Table 3.3.

Table 3.3: Selected bond lengths and angles for $[Dy_2Na_2(\mathbf{L_3})_2(Cl)_4(MeOH)]\cdot 2H_2O$ (**3.1**).

Bond	Length (Å)	Bond	Length (Å)
Dy1—O11	2.228 (19)	Dy2—O25	2.23 (2)
Dy1—O15	2.248 (18)	Dy2—O21	2.26 (2)
Dy1—N11	2.51 (2)	Dy2—N22	2.47 (3)
Dy1—N13	2.51 (2)	Dy2—N23	2.54 (3)
Dy1—N12	2.51 (2)	Dy2—N21	2.54 (3)
Dy1—Cl1	2.644 (7)	Dy2—Cl3	2.656 (9)
Dy1—Cl2	2.686 (7)	Dy2—Cl4	2.660 (8)
Dy1—Na1	3.537 (13)	Dy2—Na2	3.596 (12)

Bond	Angle (°)	Bond	Angle (°)
O11—Dy1—O15	77.0 (7)	O25—Dy2—O21	78.1 (8)
O11—Dy1—N11	72.3 (7)	O25—Dy2—N22	141.1 (10)
O15—Dy1—N11	148.3 (7)	O21—Dy2—N22	140.6 (9)
O11—Dy1—N13	150.6 (7)	O25—Dy2—N23	72.7 (10)
O15—Dy1—N13	73.7 (8)	O21—Dy2—N23	150.4 (9)
N11—Dy1—N13	136.8 (8)	N22—Dy2—N23	68.4 (11)
O11—Dy1—N12	141.5 (7)	O25—Dy2—N21	151.9 (10)
O15—Dy1—N12	140.7 (8)	O21—Dy2—N21	73.8 (9)
N11—Dy1—N12	69.2 (7)	N22—Dy2—N21	67.0 (10)
N13—Dy1—N12	67.7 (8)	N23—Dy2—N21	135.4 (10)
O11—Dy1—Cl2	97.9 (6)	O25—Dy2—Cl3	95.8 (6)

O15—Dy1—Cl2	103.4 (6)	O21—Dy2—Cl3	95.3 (6)
N11—Dy1—Cl2	88.9 (6)	N22—Dy2—Cl3	79.9 (8)
N13—Dy1—Cl2	87.8 (6)	N23—Dy2—Cl3	83.3 (8)
N12—Dy1—Cl2	82.7 (6)	N21—Dy2—Cl3	87.9 (9)
O11—Dy1—Cl1	95.1 (5)	O25—Dy2—Cl4	97.0 (6)
O15—Dy1—Cl1	90.7 (6)	O21—Dy2—Cl4	100.0 (6)
N11—Dy1—Cl1	84.1 (6)	N22—Dy2—Cl4	82.0 (8)
N13—Dy1—Cl1	86.5 (5)	N23—Dy2—Cl4	88.1 (8)
N12—Dy1—Cl1	80.0 (6)	N21—Dy2—Cl4	87.0 (9)
Cl2—Dy1—Cl1	162.7 (2)	Cl3—Dy2—Cl4	161.7 (3)

The coordination sphere of Na1 comprises the five donor atoms of the $O_3O_2^{2-}$ pocket which are coordinated in a non-planar fashion and the fifth site is occupied by a methanol molecule giving rise to a trigonal prismatic geometry. Na2 adopts the same coordination geometry however, for this ion the fifth site is occupied by a bridging chloride ion.

Examining the crystal packing of complex (**3.1**), it is likely that the formation of the dimer is at least in part stabilized by the presence of hydrogen bonding interactions between the N-bound H12 atom of one macrocycle and the Cl3 ion of the other monomer with a N12-H12···Cl3 distance of 2.474(7) Å. This conclusion is further supported if we compare this structure to the Er^{3+} complex (**3.6**) of the methyl analogue (**3.5**) that contains no such H-bond and crystallizes as a discrete macrocycle.[184] Additionally, a search of the chemical literature reveals that when

other substituents are located at the N12 and N22 positions, no such dimerization is observed in the crystal structures of these compounds.[185] Two water molecules are present in the crystal lattice and an intermolecular H-bonding interaction is also present between the dimer and one of the water molecules such that O(14)-H···Cl1 = 2.558 Å. The dimers pack so that they are fairly isolated from one another with the shortest intermolecular $Dy^{3+}\cdots Dy^{3+}$ distances being 7.766 Å.

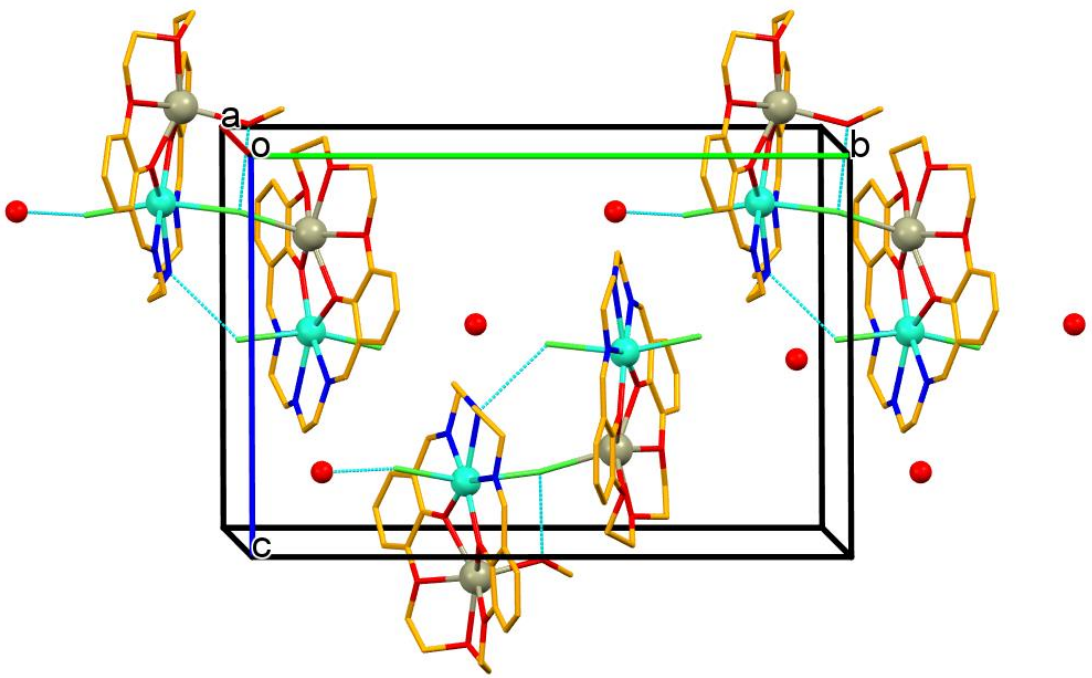

Figure 3.9: Packing diagram for (**3.1**) viewed down the *a*-axis. H-atoms are omitted for clarity and hydrogen bonding interactions are shown as blue dashed lines.

X-ray quality single crystals of the Tb^{3+} complex (**3.2**) were obtained as pale yellow plates. The molecular structure of the Tb^{3+} dimer is isostructural with that of the Dy^{3+} derivative with the stoichiometry $[Na_2Tb_2(\mathbf{L_3})Cl_4(MeOH)]$. Both of the

crystallographically unique Tb^{3+} ions are coordinated in a pentagonal bipyramidal manner and reside within the $N_3O_2^{2-}$ pockets of their respective macrocycles, Figure 3.10. For each Tb^{3+} ion, the macrocycle coordinates equatorially in a pentadentate fashion with two axially coordinated chloride ions completing the pseudo D_{5h} geometry. Selected bond lengths and angles for this complex are presented in Table 3.5.

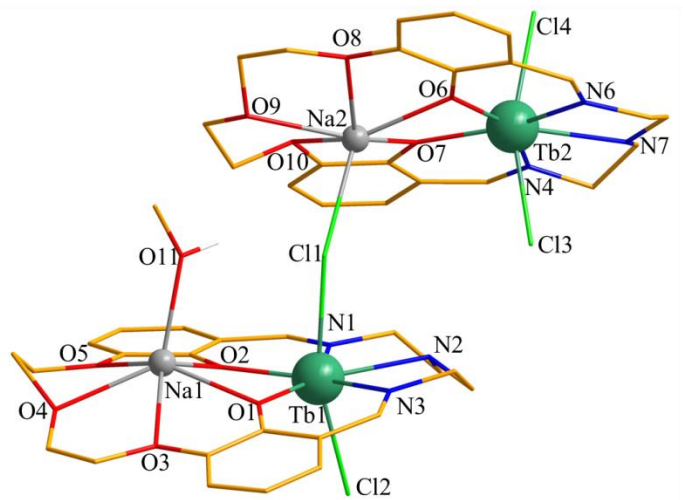

Figure 3.10: Molecular structure of the Tb^{3+} dimer (**3.2**). H-atoms are omitted for clarity.

The dimer (**3.2**) crystallizes in the monoclinic space group $P2_1$ with a similar unit cell to the previously described Dy^{3+} analogue, Table 3.2. Once again the unit cell is comprised of two dimers symmetry related by a 2_1 screw axis. In contrast to (**3.1**), there are no water molecules present in the crystal lattice of this complex. This results in the dimers being packed slightly tighter together then the Dy^{3+} analogue with the closest intermolecular $Tb^{3+}\cdots Tb^{3+}$ distance being 7.730 Å. This is also evident by the reduced unit cell volume of 2552.83 $Å^3$ in comparison to complexes (**3.1**) and (**3.3**), Table 3.2.

Table 3.4: Selected bond lengths and angles for $[Na_2Tb_2(\mathbf{L_3})_2Cl_4(MeOH)]$ (**3.2**)

Bond	**Length (Å)**	**Bond**	**Length (Å)**
Tb1—O2	2.243 (5)	Tb2—O6	2.238 (5)
Tb1—O1	2.244 (5)	Tb2—O7	2.250 (5)
Tb1—N2	2.495 (6)	Tb2—N4	2.529 (7)
Tb1—N1	2.503 (6)	Tb2—N6	2.532 (7)
Tb1—N3	2.518 (6)	Tb2—N5	2.533 (7)
Tb1—Cl2	2.658 (2)	Tb2—Cl4	2.648 (2)
Tb1—Cl1	2.699 (2)	Tb2—Cl3	2.661 (3)
Tb1—Na1	3.571 (3)	Tb2—Na2	3.556 (3)

Bond	**Angle (°)**	**Bond**	**Angle (°)**
O2—Tb1—O1	77.3 (2)	O6—Tb2—O7	78.45 (18)
O2—Tb1—N2	140.9 (2)	O6—Tb2—N4	152.2 (2)
O1—Tb1—N2	140.94 (19)	O7—Tb2—N4	73.7 (2)
O2—Tb1—N1	73.7 (2)	O6—Tb2—N6	73.0 (2)
O1—Tb1—N1	151.0 (2)	O7—Tb2—N6	151.1 (2)
N2—Tb1—N1	67.8 (2)	N4—Tb2—N6	134.7 (2)
O2—Tb1—N3	149.0 (2)	O6—Tb2—N5	140.4 (2)
O1—Tb1—N3	72.58 (19)	O7—Tb2—N5	140.9 (2)
N2—Tb1—N3	68.4 (2)	N4—Tb2—N5	67.4 (2)
N1—Tb1—N3	136.1 (2)	N6—Tb2—N5	67.4 (2)
O2—Tb1—Cl2	102.8 (2)	O6—Tb2—Cl4	97.08 (17)

O1—Tb1—Cl2	98.34 (18)	O7—Tb2—Cl4	99.04 (17)
N2—Tb1—Cl2	82.70 (15)	N4—Tb2—Cl4	87.0 (2)
N1—Tb1—Cl2	88.03 (15)	N6—Tb2—Cl4	89.19 (19)
N3—Tb1—Cl2	89.05 (15)	N5—Tb2—Cl4	82.6 (2)
O2—Tb1—Cl1	91.2 (2)	O6—Tb2—Cl3	96.93 (17)
O1—Tb1—Cl1	94.78 (18)	O7—Tb2—Cl3	96.20 (17)
N2—Tb1—Cl1	79.91 (15)	N4—Tb2—Cl3	86.6 (2)
N1—Tb1—Cl1	85.98 (15)	N6—Tb2—Cl3	82.80 (19)
N3—Tb1—Cl1	84.02 (15)	N5—Tb2—Cl3	78.5 (2)
Cl2—Tb1—Cl1	162.60 (6)	Cl4—Tb2—Cl3	161.06 (6)

Single crystals of the Er^{3+} analogue were obtained as pale brown blocks and the molecular structure of the complex is isostructural with the previously described Dy^{3+} and Tb^{3+} analogues. The stoichiometry of the complex is $[Na_2Er_2(\mathbf{L_3})Cl_3(MeOH)]\cdot H_2O$ (**3.3**) with an intramolecular $Er^{3+}\cdots Er^{3+}$ distance of 6.935 Å. Similar to **3.1** and **3.2**, the dimers pack along a 2_1 screw axis with the closest intermolecular $Er^{3+}\cdots Er^{3+}$ distance being 7.730 Å. A view of the molecular structure of the complex is presented in Figure 3.11 and selected bond lengths and angles are presented in Table 3.5.

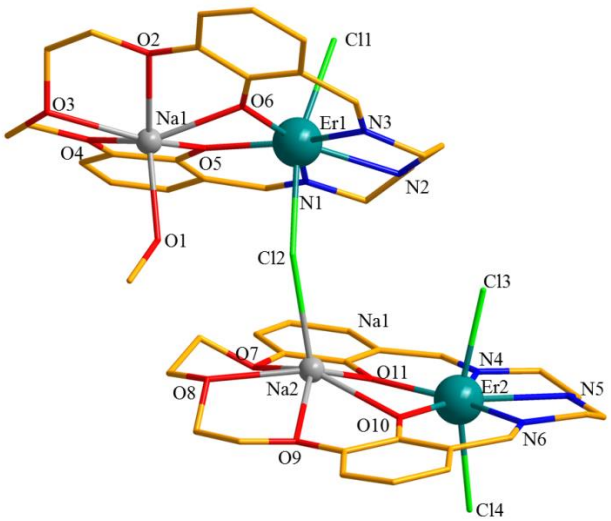

Figure 3.11: Crystal structure of the Er^{3+} dimer (**3.3**). H-atoms are omitted for clarity.

Table 3.5: Selected bond lengths and angles for $[Na_2Er_2(\mathbf{L_3})_2Cl_4(MeOH)]\cdot H_2O$ (**3.3**).

Bond	**Length (Å)**	**Bond**	**Length (Å)**
Er1—O6	2.223 (15)	Er2—O10	2.203 (15)
Er1—O5	2.249 (15)	Er2—O11	2.234 (15)
Er1—N2	2.469 (18)	Er2—N4	2.52 (2)
Er1—N3	2.47 (2)	Er2—N6	2.52 (2)
Er1—N1	2.493 (18)	Er2—N5	2.53 (2)
Er1—Cl1	2.619 (7)	Er2—Cl4	2.612 (8)
Er1—Cl2	2.669 (7)	Er2—Cl3	2.612 (9)
Er1—Na1	3.574 (10)	Er2—Na2	3.563 (8)

Bond	**Angle (°)**	**Bond**	**Angle (°)**
O6—Er1—O5	75.8 (5)	O10—Er2—O11	78.8 (6)
O6—Er1—N2	142.4 (6)	O10—Er2—N4	152.0 (6)

O5—Er1—N2	141.1 (6)	O11—Er2—N4	73.2 (6)
O6—Er1—N3	74.3 (6)	O10—Er2—N6	72.4 (6)
O5—Er1—N3	148.8 (6)	O11—Er2—N6	150.7 (6)
N2—Er1—N3	68.1 (7)	N4—Er2—N6	135.6 (6)
O6—Er1—N1	149.6 (6)	O10—Er2—N5	139.9 (6)
O5—Er1—N1	73.9 (6)	O11—Er2—N5	141.0 (6)
N2—Er1—N1	67.9 (7)	N4—Er2—N5	68.1 (7)
N3—Er1—N1	136.0 (7)	N6—Er2—N5	67.5 (6)
O6—Er1—Cl1	96.7 (5)	O10—Er2—Cl4	96.3 (5)
O5—Er1—Cl1	102.6 (5)	O11—Er2—Cl4	99.7 (5)
N2—Er1—Cl1	83.4 (5)	N4—Er2—Cl4	87.0 (7)
N3—Er1—Cl1	89.6 (5)	N6—Er2—Cl4	89.1 (6)
N1—Er1—Cl1	87.6 (5)	N5—Er2—Cl4	83.2 (8)
O6—Er1—Cl2	95.9 (5)	O10—Er2—Cl3	96.8 (5)
O5—Er1—Cl2	91.0 (5)	O11—Er2—Cl3	94.7 (5)
N2—Er1—Cl2	80.0 (5)	N4—Er2—Cl3	87.1 (7)
N3—Er1—Cl2	83.4 (5)	N6—Er2—Cl3	83.4 (6)
N1—Er1—Cl2	87.1 (5)	N5—Er2—Cl3	78.9 (8)
Cl1—Er1—Cl2	163.39 (18)	Cl4—Er2—Cl3	162.09 (19)

The complex packs in a similar manner to the previously described Dy^{3+} and Tb^{3+} analogues with one water molecule per formula unit.

3.4.3 Spectroscopic studies

The molecular structures of all three complexes were further elucidated by CHN elemental analysis, as well as a series of spectroscopic studies whose data is summarized in Table 3.6

Table 3.6: Summary of characterization data for complexes (3.1)-(3.3).

	Complex (3.1) $[Dy_2Cl_4(\mathbf{L_3})_2Na_2MeOH]\cdot 2H_2O$	**Complex (3.2)** $[Tb_2Cl_4(\mathbf{L_3})_2Na_2MeOH]$	**Complex (3.3)** $[Er_2Cl_4(\mathbf{L_3})_2Na_2MeOH]\cdot H_2O$
EI-MS (*m/z*)	1403 $[M+H]^+$ (5 %) 643 $[DyCl_2(H_2L)]^+$ (100 %)	1328 $[M+H]^+$ (1 %) 638 $[TbCl_2(H_2L)]^+$ (100 %)	1459 $[M+H]^+$ (2 %) 647 $[ErCl_2(H_2L)]^+$ (100 %)
IR (cm^{-1})	ν_{amine} = 3405 ν_{imine} = 1624	ν_{amine} = 3404 ν_{imine} = 1623	ν_{amine} = 3410 ν_{imine} = 1626
UV-Vis (nm)	202 (ε = 72 000 $cm^{-1}M^{-1}$) 231 (ε = 110 000 $cm^{-1}M^{-1}$) 272 (ε = 36 000 $cm^{-1}M^{-1}$) 356 (ε = 16 000 $cm^{-1}M^{-1}$)	202 (ε = 78 000 $cm^{-1}M^{-1}$) 232(ε = 110 000 $cm^{-1}M^{-1}$) 271 (ε = 40 000 $cm^{-1}M^{-1}$) 353 (ε = 15 000 $cm^{-1}M^{-1}$)	201 (ε = 74 000 $cm^{-1}M^{-1}$) 231 (ε = 110 000 $cm^{-1}M^{-1}$) 271 (ε = 37 000 $cm^{-1}M^{-1}$) 351 (ε = 16 000 $cm^{-1}M^{-1}$)
CHN Analysis (%)	Calculated C = 38.50 H = 4.16 N = 5.99 $[Dy_2Cl_4(\mathbf{L_3})_2Na_2MeOH]\cdot 2H_2O$ Found C = 38.53 H = 3.94 N = 5.87	Calculated C = 38.70 H = 3.90 N = 6.02 $[Tb_2Cl_4(\mathbf{L_3})_2Na_2MeOH]$ Found C = 38.90 H = 3.78 N = 5.91	Calculated C = 37.18 H = 3.88 N = 5.78 $[Er_2Cl_4(\mathbf{L_3})_2Na_2MeOH]\cdot H_2O$ Found C = 37.29 H = 3.80 N = 5.57

EI mass spectrometry studies of (**3.1**) shows a peak at *m/z* = 1403 that is consistent with the presence of the protonated dimer $[M+H]^+$ (5 %). In addition, a fragment ion (100 %) corresponding to $[DyCl_2(H_2\mathbf{L_3})]^+$ is observed at *m/z* = 643. The IR spectrum of (**3.1**) contains an N-H stretch at 3405 cm^{-1} and an imine stretch at 1624 cm^{-1}, which is slightly red-shifted when compared the C=N str at 1629 cm^{-1} in the uncoordinated macrocycle. In the UV-Vis spectrum two absorption bands are found at 272 nm (ε = 36 000 $cm^{-1}M^{-1}$) and 356 nm (ε = 16 000 $cm^{-1}M^{-1}$) that are red-shifted when compared to the bands at 245 nm and 328 nm in the uncoordinated macrocycle. In addition, two additional bands are observed, the first at 231 nm (ε = 110 000 $cm^{-1}M^{-1}$) assigned to high energy $\pi \rightarrow \pi^*$ transitions of the aryl-ring, that was absent from the electronic spectrum of the free ligand and a second band at 202 nm (72 000 $cm^{-1}M^{-1}$) assigned as a LMCT band. This latter transition is electric-dipole allowed and occurs because the Ar-O^- substituent is able to act as an electron donor and the partially-filled *f*-shell of the Dy^{3+} ions are able to accept electron density.[193]

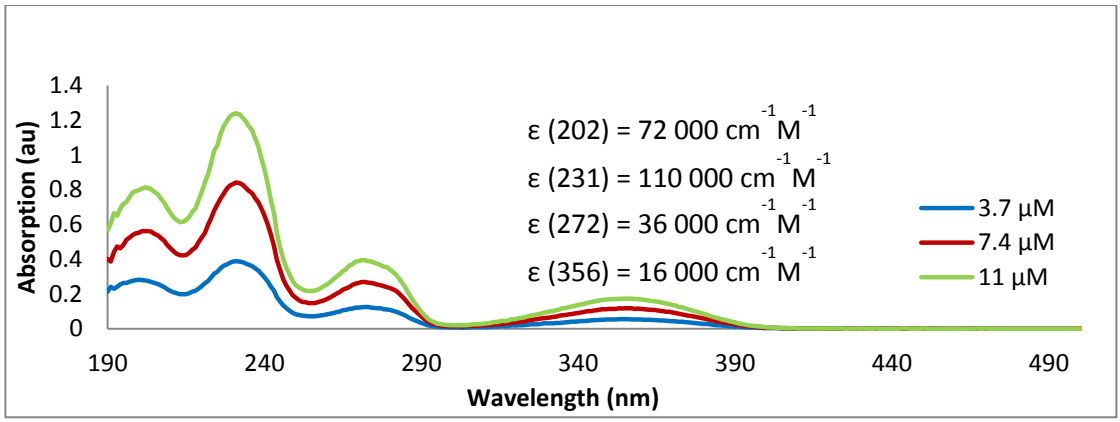

Figure 3.12 UV-Vis spectrum of complex (**3.1**) in CH_3CN at room temperature.

The EI mass spectrum of the Tb^{3+} derivative, (**3.2**) has a peak at *m/z* = 1328, assigned to the protonated dimer $[M+H]^+$. A second more intense peak at *m/z* = 638 is assigned to $[TbCl_2(\mathbf{H_2L_3})]^+$. The fingerprint region of the IR spectrum is superimposable with that of the Dy^{3+} complex (**3.1**). In addition, an N-H stretch is observed at 3404 cm^{-1} and an imine stretch is clearly visible at 1623 cm^{-1}. The absorption spectrum of the (**3.2**) contains the same 3 bands at 202, 231 and 271 nm as previously discussed for the Dy^{3+} analogue. When compared to (**3.1**), the LMCT band at 350 nm is less intense for this complex since there are fewer electrons in the Tb^{3+} 4*f*-orbitals when compared to Dy^{3+}.

The spectroscopic data for the Er^{3+} complex is presented in Table 3.6 and once again support the assignment of the molecular structure. A protonated molecular ion is found in the EI mass spectrum at *m/z* = 1459 and C=N and N-H str's are present in the IR spectrum at 1626 and 3410 cm^{-1} respectively. The UV-Vis spectrum of (**3.3**) contains the same four absorption bands as were previously observed in complexes (**3.1**) and **(3.2**).

3.4.4 Magnetic Studies

DC Susceptibility

The magnetic properties of all three complexes were first studied by dc-susceptibility experiments. Although variable temperature dc measurements do not provide information about relaxation dynamics, they do reveal insight into the depopulation of the Stark sublevels and/or any significant dipolar interactions present in the complex. For the three complexes, the dc data were measured in an applied field of 0.2 T, over a temperature range of 5 to 300 K.

Complex (**3.1**) follows Curie-Weiss behaviour as shown in Figure 3.13. The Curie constant, *C*, was determined to be 29.0 $cm^3 \cdot K \cdot mol^{-1}$ which is consistent with the theoretical value of 28.34 (g = 1.243, J = 15/2) for two non-interacting Dy^{3+} ions. The Weiss constant, θ is −5.8 K, most likely attributed to zero field splitting. In the χT *vs* T plot, the value of χT above 100 K is consistent with the theoretical value of 28.34 $cm^3 \cdot K \cdot mol^{-1}$ for two non-interacting Dy^{III} ions. Below 50 K, the χT value decreases rapidly to 19.5 $cm^3 \cdot K \cdot mol^{-1}$ at 5 K which can be attributed to a thermal depopulation of the m_J sublevels in the $H_{15/2}$ multiplet. To support this claim, the data was modelled using *ab initio* methods in MOLCAS.[188] The data was calculated with no dipolar coupling (red line, Figure 3.13) and is in excellent agreement with the low temperature experimental data; hence, the Dy^{3+} dimers can be considered to be magnetically isolated within the crystal lattice.

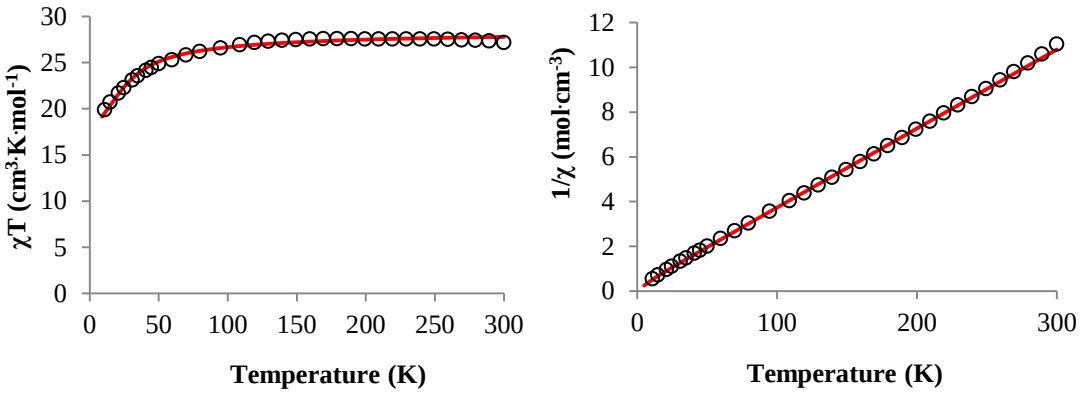

Figure 3.13: DC-magnetic susceptibility data for a microcrystalline sample of (**3.1**). Left: χT vs T plot collected in a 0.2 T static field from 5 to 300 K. Right: $1/\chi$ vs T plot with observed Curie-Weiss behaviour (C = 29.0 $cm^3 \cdot K \cdot mol^{-1}$, θ = −5.8 K). The black circles are the experimental data points and the red line represnts the *ab initio* calculated data.

The Tb^{3+} complex also follows Curie Weiss behaviour with a Curie constant of 23.041 $cm^3 \cdot K \cdot mol^{-1}$ as expected for an isolated Tb^{3+} ion (J = 6, g = 1.326) and a Weiss constant of −4.189 K. The χT vs. T plot for (**3.2**) is shown in Figure 3.14 (left), the magnetic susceptibility is constant until 50 K where it drops rapidly, most likely due to a depopulation of the Stark sublevels. The experimental value of χT at 300 K is 22.680 $cm^3 \cdot K \cdot mol^{-1}$ consistent with the Curie constant. As previously described, the dc data was simulated for this complex using the MOLCAS quantum chemistry software package and fits well with the experimental data for non-interacting Tb^{3+} ions. The calculation was performed by approximating the singlet states as Kramers doublets. For this reason, a slight deviation between the modelled data and the experimental data occurs between 2 K and 50 K due to the presence of quantum tunneling which we cannot account for in the calculation.

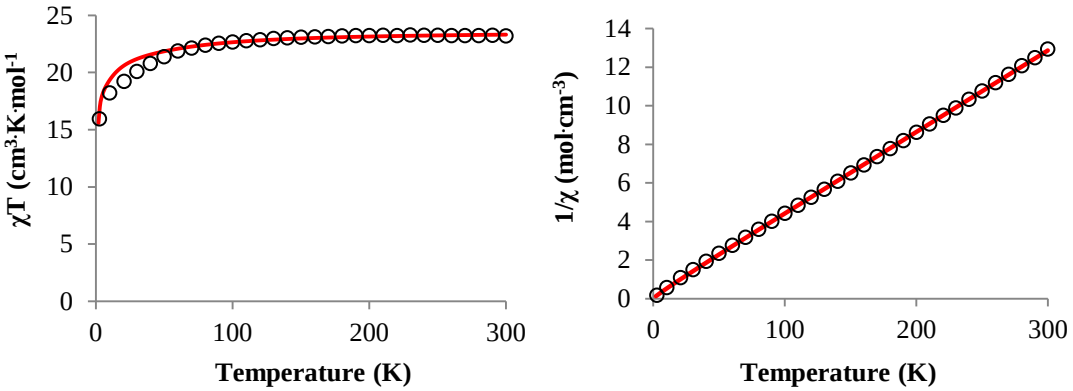

Figure 3.14: DC-susceptibility data for complex (**3.2**). Left: plot of χ^{-1} *vs. T*. Right: plot of $\underline{\chi T}$ *vs*. *T*. The *ab initio* modelled data is shown as a red line and the experimental data is shown as black circles.

Above 200K, the χT value of 22.5 $cm^3 \cdot K \cdot mol^{-1}$ for complex (**3.3**) is consistent with 22.9 $cm^3 \cdot K \cdot mol^{-1}$ reported in the literature for other Er^{3+} complexes with isolated magnetic centers.[194] Complex (**3.3**) displays Curie Weiss behaviour with C = 22.904 $cm^3 \cdot K \cdot mol^{-1}$ which is expected for two non-interacting Er^{3+} ions (J = 15/2, g = 2.996, C = 22.96 $cm^3 \cdot K \cdot mol^{-1}$). As expected from the crystal structure, a small value of −3.58 K was calculated for the Weiss constant of **3.3** which is attributed predominantly to zero field splitting. In the plot of χT *vs. T* (Figure 3.15, left), a steep decrease in the magnetic susceptibility is observed for the temperature region below 50 K which we attribute to the depopulation of the Stark sublevels for each Er^{3+} ion. A simulation of the dc susceptibility curve was carried out using the MOLCAS 8.0 quantum chemistry package.[188] The simulation of the data (red line) was performed by considering the Er^{3+} ions as non-interacting and shows an excellent fit to the experimental magnetic susceptibility, consistent with the crystal structure.

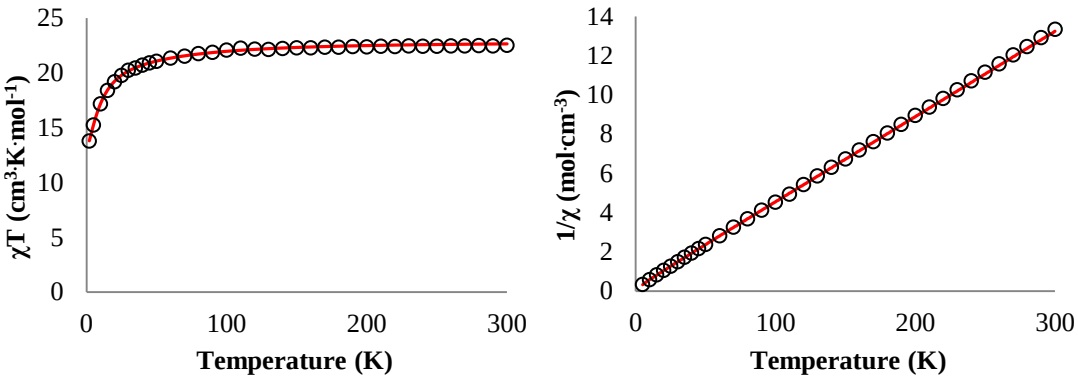

Figure 3.15: DC-susceptibility data for complex (**3.3**). Left: plot of χ^{-1} *vs*. *T*. Right: plot of χT *vs*. *T*. The *ab initio* calculated data is shown as a red line and the experimental data is shown as black circles.

AC susceptibility

In order to study the dynamic magnetic behaviour of all three complexes ac magnetic susceptibility studies were carried out in an oscillating field of 3.5 Oe in static dc fields ranging from 0 – 5000 Oe. Ac susceptibility data were measured from 2-15 K using frequencies between 50 and 10000 Hz. For complex **3.1** in zero dc field, there is a frequency dependence to the imaginary component of the ac susceptibility χ'', consistent with SMM behaviour, Figure 3.16, but due to fast quantum tunnelling, a maximum could not be resolved in the Cole-Cole plot to determine the relaxation parameters.

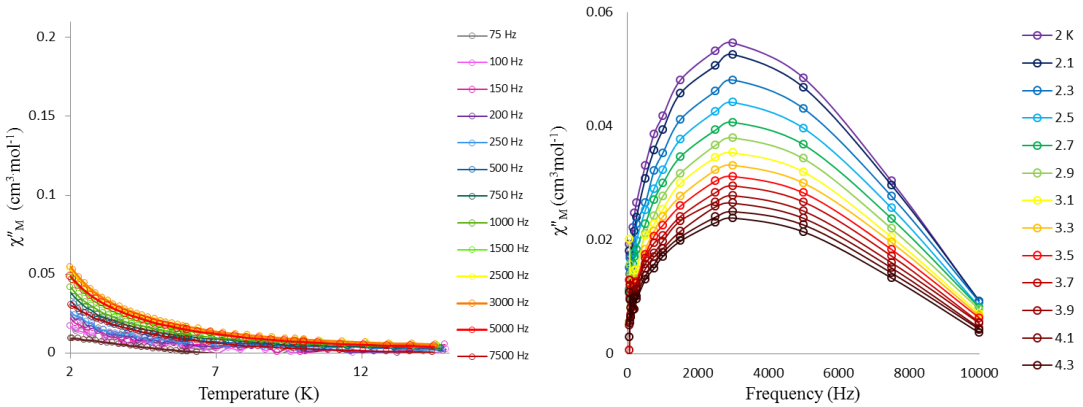

Figure 3.16: Left: Plots of χ'' *vs T* for (**3.1**) measured in the absence of a static field. Right: plots of χ'' *vs* ν for (**3.1**) measured in the absence of a static field.

When a small static dc field of 0.3 T was applied, the degeneracy of the m_J states was lifted, which in turn, suppresses quantum tunnelling processes, affording a single well resolved maxima shown in the two plots of Figure 3.17.

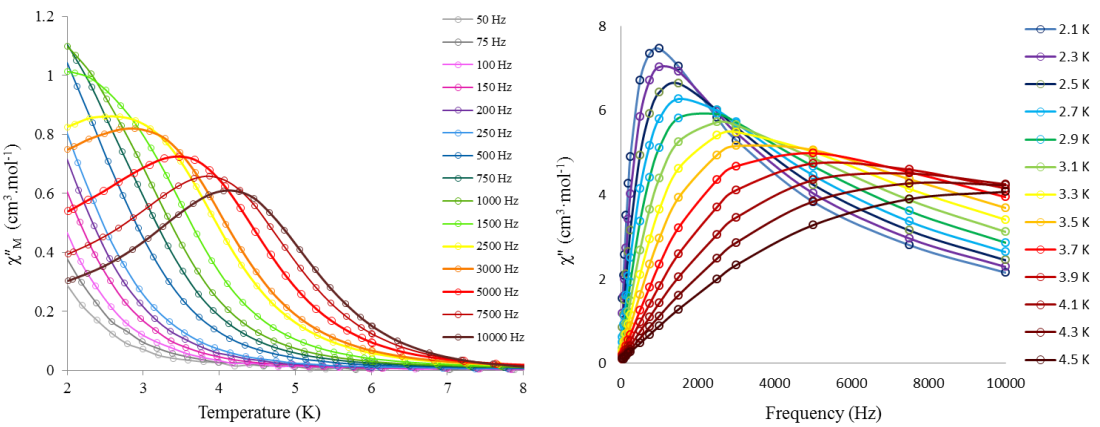

Figure 3.17. Left: Plots of χ'' *vs T* for (**3.1**) in a 0.3 T field. Right: plots of χ'' *vs* ν measured for (**3.1**) in a 0.3 T field.

The frequency specific relaxation times, τ_c, were then determined from the Cole-Cole plot of χ' vs χ'' by modelling the data to the single component Debye function described below:

$$\chi_{AC}(\omega) = \chi_S + \frac{\chi_T - \chi_S}{1 + (i\omega\tau_c)^{1-\alpha}} \qquad \textit{Eq. 3.1}$$

The Cole-Cole parameter, α, ranges from 0.07 to 0.09 which indicates that there is most likely just a single relaxation process for this complex. The resulting τ_c values were subsequently fit to the Arrhenius equation (Figure 3.18) which afforded an effective energy barrier U_{eff} of 12.6 cm^{-1} and relaxation rate of τ_0, of 2.91 x 10^{-7} s that is close to the U_{eff} of 16.4 cm^{-1} obtained for our first N_5 Schiff-base Dy^{3+} macrocycle, which displays a slightly slower relaxation time τ_0 of 6.4 x 10^{-6} s.[182]

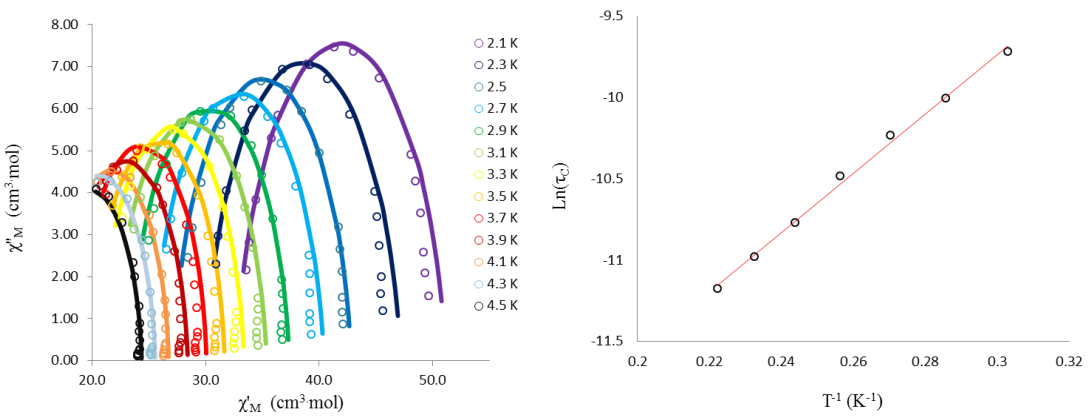

Figure 3.18: Left, Cole-Cole plot; Right, Arrhenius plot for complex (**3.1**). Black circles represent ln(τ_c) values extracted from the modelled experimental data between 2.1 and 4.5 K; the red line represents a linear regression of the data.

Unfortunately in contrast to the Dy^{3+} complex, the ac susceptibility studies for the Tb^{3+} and Er^{3+} complexes reveal no frequency dependence to the out of phase component of the ac susceptibility in either zero or in the presence of applied static dc fields, Figure 3.19 and Figure **3.20**, which means that neither of these complexes

displays any slow relaxation of magnetisation and cannot be thus classified as an SMM.

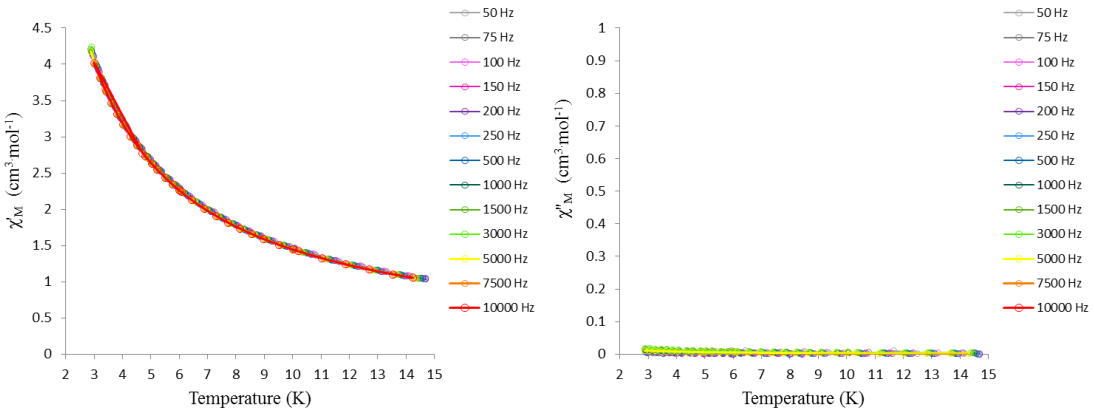

Figure 3.19: Left, Plot of χ' vs. T; right, plot of χ'' *vs.* T for (**3.2**) in a zero applied dc field.

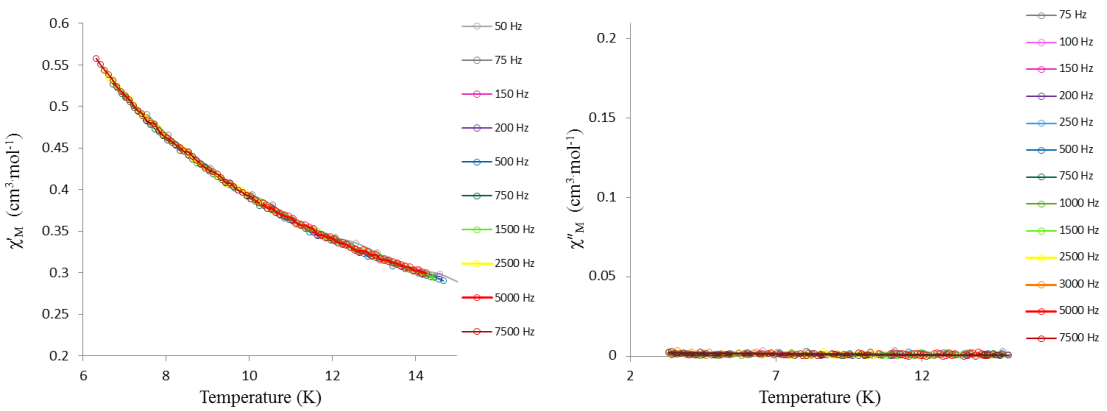

Figure 3.20: Left, Plot of χ' vs. T; right, plot of χ'' *vs.* T for (**3.3**) in a zero applied dc field.

3.4.5 *Ab initio* studies

In order to shed more light on the relaxation dynamics for all three complexes *ab initio* calculations were carried out using the CASSCF/RASSI/SINGLE_ANISO method in the MOLCAS 8 software.[188] The calculations were performed using the coordinates determined from single crystal X-ray diffraction studies of the three

complexes which were used without any geometry optimisation. Each crystallographically unique Ln^{3+} ion was calculated separately by employing two structural models, Figure 3.21. Each model includes only one half of the dimer to ensure that only one Ln^{3+} ion is included in the calculation to reduce the size of the calculation in order to minimize the computational time and to ensure that the calculation falls within the hardware limitations.

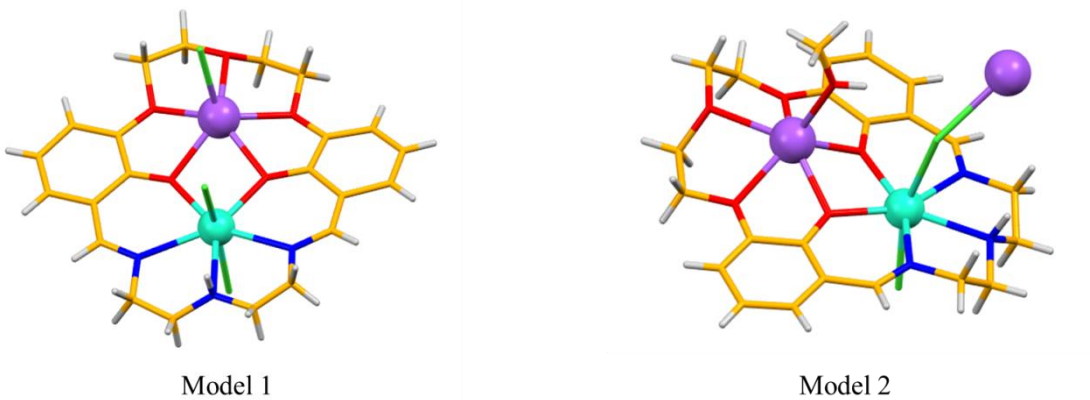

Figure 3.21: Models 1 and 2 used for the *ab initio* calculations of Ln1 (left) and Ln2 (right) represented as teal spheres.

From the theoretical calculations, there are three main pieces of data that are used to elucidate the magnetic relaxation mechanism(s): (i) the energies of the Kramers doublets, (ii) the g-tensors and (iii) the angles between the main magnetic axes. Since the magnetisation typically relaxes via the first excited state in Ln^{3+} complexes, the energy difference ΔE_1 between the ground and first excited KD is typically considered to be the theoretically determined energy barrier.

For complex (**3.1**) the energies and magnetic orientations of the eight Kramers doublets in the $^6H_{15/2}$ ground multiplet of the Dy^{3+} ion were calculated and the results are presented in Table 3.7 and Table 3.8. The seven 4*f* orbitals of the Dy^{3+} ion were

used as the active space with mixing of 21 sextet (^{6}H, ^{6}F and ^{6}P) and 128 quartet (^{4}I, ^{4}F, ^{4}M, ^{4}G, ^{4}K, ^{4}L, ^{4}D, ^{4}H, ^{4}P ^{4}G, ^{4}F, and ^{4}I) states.

Table 3.7: Eight Kramers doublets of the $^6H_{15/2}$ multiplet within Dy1 of complex (**3.1**).

KD	Energy (cm^{-1})	g_x	g_y	g_z	Zm (°)	Sign of g-product
1	0.00	0.15	0.43	18.46	0.00	+
2	69.95	1.11	1.87	13.33	11.17	+
3	132.87	0.39	2.17	12.06	0.54	−
4	231.70	2.85	4.03	14.03	86.21	+
5	274.56	10.38	6.15	0.75	90.98	+
6	344.68	9.57	6.67	1.13	7.12	+
7	394.52	2.02	3.50	15.60	64.24	+
8	443.56	0.47	0.57	17.87	109.57	−

Table 3.8: Eight Kramers doublets of the $^6H_{15/2}$ multiplet within Dy2 of complex (**3.1**).

KD	Energy (cm^{-1})	g_x	g_y	g_z	Zm (°)	Sign of g-product
1	0.00	0.44	1.67	17.31	0.00	+
2	57.54	1.62	1.89	12.20	6.29	+
3	144.08	0.69	3.84	10.89	3.23	+
4	277.40	7.47	6.76	4.71	92.63	+
5	405.16	0.95	2.16	11.56	86.92	+
6	527.06	0.04	0.75	16.94	15.66	+
7	544.93	0.52	0.65	17.40	17.08	+
8	630.99	0.13	0.22	18.39	158.38	+

Since the complex is a dimer comprising of two crystallographically independent Dy^{3+} ions in slightly different geometries, two energy barriers ΔE_1 of 70 and 58 cm^{-1} were obtained for Dy1 and Dy2 respectively. These values are higher than the experimentally determined U_{eff} of 12.6 cm^{-1}, but such a discrepancy is not unusual in such systems and can be attributed to the presence of QTM and/or a slight change in the energy levels of the m_J states due to the application of a small static dc field, neither of which the calculations can take into consideration.

Although the g-tensors show axial anisotropy in the ground states of both Dy^{3+} ions, considerable transverse components are also present with $g_x = 0.15$, $g_y = 0.43$ for Dy1 and $g_x = 0.44$, $g_y = 1.67$ for Dy2. This suggests that non-direct relaxation pathways such as spin-lattice and QTM are operative in this complex. Increased transverse magnetic anisotropy in the ground Kramers doublet is likely also caused by the lower ligand field symmetry of the ions due to the bent conformation of the axial chloride ligands. In addition to the reduced symmetry, there are phenolate O^- ligands in the equatorial plane which are strong electron donors that greatly impact the direction of the main magnetic axes of the ground states of the two Dy^{3+} ions as shown in Figure 3.22. This donor effect is also evident in the UV-Vis spectrum which shows a strong LMCT band and therefore this macrocyclic ligand has electron density in the equatorial plane that interacts with the oblate *f*-electron density of the Dy^{3+} ion. The effects of these strong oxygen donor atoms have also been observed previously by Tong *et al.* for other Dy^{3+} pentagonal bipyramidal complexes where they are located axially along the five-fold symmetry axis in order to enhance the axial anisotropy of the complex.

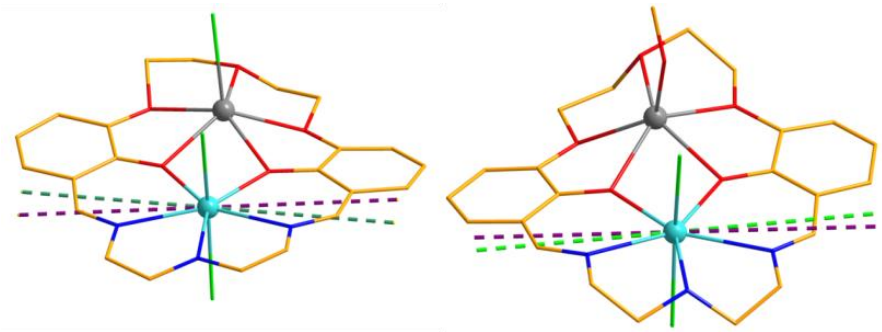

Figure 3.22: Molecular structures of the two halves of the macrocyclic dimer of **3.1** showing the magnetic axes of the ground (purple) and first excited (green) KD for Dy1 (left) and Dy2 (right).

For both Dy^{3+} ions, the angle between the main magnetic axes of the ground and first excited states shows a deviation from zero degrees which support the presence of spin-lattice relaxation that include Raman and Orbach processes. The preference for spin lattice relaxation is further confirmed in the values of the matrix elements between the microstates given that when the matrix elements are greater than 0.1, then that particular relaxation pathway is operative. The results are summarised in a plot of energy versus magnetic moment for each KD of the two ions, Figure 3.23.[195]

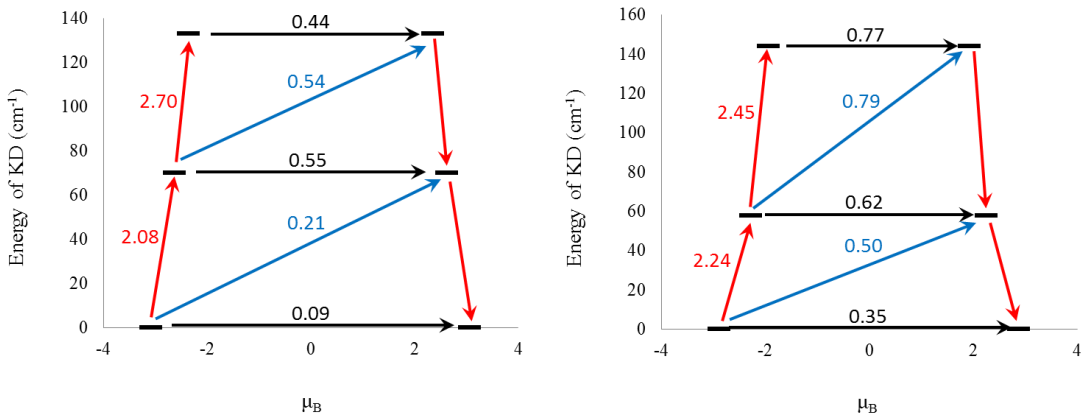

Figure 3.23: Plots of the energy vs. the average magnetic moment of the KD for Dy1 (left) and Dy2 (right). Possible magnetic relaxation pathways are shown by the arrows where red indicates a single phonon state-to-state thermal transition; blue indicates an Orbach spin-lattice transition and black indicates a QTM pathway between states of equal energy, but opposite magnetic moment. The values of the matrix elements of the transition moments are shown next to their respective arrows.

For Dy1, the plot reveals that the ground state quantum tunnelling is slightly below 0.1 and so does not dominate, but can still contribute to the relaxation of magnetisation. The thermal and spin-lattice transition moments are substantially larger at 2.08 and 0.21, respectively. Given these values, we would expect a thermal relaxation pathway to dominate, but the spin-lattice relaxation mechanism is a kinetic process and therefore this process dominates at low temperature which is consistent with our experimental observations.

Dy2 shows a dramatically different plot of energy versus average magnetic moment. This is solid evidence that even small differences in the coordination sphere of these complexes can result in large changes in the electronic structure of their respective lanthanide ions. For Dy2, we would expect no observable SMM behaviour because of the presence of an active ground state quantum tunnelling mechanism, as

evidenced by a transition moment matrix element of 0.35. The spin-lattice mechanism is also active, but ground state quantum tunnelling is a low energy kinetic process and therefore likely takes precedence over any other relaxation process.

Another empirical method for analysing the magnetic properties of an SMM is to consider the spin-free states i.e. states without strong SOC before the RASSI module is applied. Applying this strategy, Ruiz, *et al*. found that strongly anisotropic ground states occur in systems where the ground doublet arises predominantly due to the exclusive mixing of ground and first excited spin flop (SF) states.[195] For this situation to occur, the second excited SF state must be energetically isolated from the first excited SF-state. The degree of isolation can then be approximated by considering the ratio between the relative energies. Ruiz devised the following simple algorithm for this approximation:

$$R_{SF} = \frac{(\Delta E_2 - \Delta E_1)}{\Delta E_1} \qquad \textit{Eq. 3.2}$$

In this equation, R_{SF} is a Ruiz parameter for the first three SF-states, ΔE_1 and ΔE_2 are the relative energies of the first and second excited SF-states. Applying this equation, a larger Ruiz parameter corresponds to a more isolated second excited state and thus a better SMM. Using this approximation to analyze the complex (**3.1)**, affords a RSF value of 4.81 for Dy1 and 3.09 for Dy2 which is consistent with literature values for the observation of SMM behaviour for Dy1 and no slow relaxation of the magnetization for Dy2.

For the Tb^{3+} analogue **3.2**, the theoretical values of the total energy and physical properties of the $^7F_6$ ground multiplet were calculated using the CASSCF/ RASSI/ SINGLE_ANISO method. Each crystallographically unique Tb^{3+} ion was

calculated separately using the coordinates obtained from the crystal structure to prepare two models following the previously described methodology for the Dy^{3+} analogue. The seven 4*f* orbitals were used as the active space with mixing of 7 septet (^{7}F) and 140 quintet (^{5}D, ^{5}G and ^{5}L) states. The results from this calculation are presented in Table 3.9 and Table **3.10**.

Table 3.9: Computed Energies (cm^{-1}) of the ground ^{7}F Multiplet for the Tb1 ion in (**3.2**).

$^7\mathbf{F_6}$	$^7\mathbf{F_5}$	$^7\mathbf{F_4}$	$^7\mathbf{F_3}$	$^7\mathbf{F_2}$	$^7\mathbf{F_1}$	$^7\mathbf{F_0}$
0.00	2100.031	3492.887	4605.171	5309.761	5868.983	6322.275
0.443	2109.228	3539.973	4625.059	5424.109	5934.978	
67.082	2143.43	3550.006	4632.932	5458.162	6256.18	
82.903	2175.458	3632.603	4672.064	5497.084		
90.619	2226.137	3656.17	4726.134	5571.998		
110.462	2276.969	3719.504	4760.839			
146.203	2339.963	3744.881	4804.286			
167.526	2433.336	3772.46				
175.451	2442.484	3847.282				
294.796	2496.572					
299.405	2506.347					
746.319						
746.566						

Table 3.10: Computed Energies (cm^{-1}) of the ground ^7F Multiplet for the Tb2 ion in complex (**3.2**).

$^7F_6$	$^7F_5$	$^7F_4$	$^7F_3$	$^7F_2$	$^7F_1$	$^7F_0$
0.00	2097.98	3459.45	4554.14	5289.53	5791.96	6178.47
1.97	2102.33	3514.43	4584.77	5338.97	5897.94	
35.99	2144.15	3516.16	4588.80	5418.52	6052.40	
44.72	2180.69	3556.23	4635.69	5448.42		
95.42	2220.54	3561.54	4644.02	5554.50		
142.21	2253.24	3642.54	4720.72			
154.39	2297.61	3684.66	4727.48			
191.22	2316.56	3756.38				
193.98	2346.66	3818.05				
210.57	2385.93					
220.61	2402.90					
505.53						
506.46						

As previously mentioned, since Tb^{3+} does not have an odd number of electrons, it is not a Kramers ion which means that unless the correct crystal field is applied its electronic structure comprises of a series of $2J+1$ singlet states. In complex (**3.2)**, the pentagonal bipyramidal ligand field is distorted away from perfect D_{5h} symmetry. As we see from the $^7F_6$ multiplet energies, there is a small energy gap of 0.44 cm^{-1} for Tb1 and 1.97 cm^{-1} for Tb2 between the ground and first excited

states. As described in the quantum tunnelling section, this is the tunnel splitting, ΔE_t. The magnitude of this energy difference reflects the strength of the QTM pathways and the uniaxial anisotropy of the spin ground state in the complex. To put this tunnel splitting into perspective, if we consider Brooker's [$Cu_3Tb(\mathbf{L}^{Pr})$] and [$Cu_3Tb(\mathbf{L}^{Bu})$] complexes[196] where **L** is the O_6^{6-} macrocyclic ligand shown in Figure 3.24. In the propyl derivative, ΔE_t is 4.248 cm^{-1} and this complex does not display any appreciable SMM behaviour. However in contrast, the butyl derivative has a ΔE_t of 0.174 cm^{-1} and therefore displays a small anisotropy barrier of 12 cm^{-1}. In our Tb^{3+} derivative (**3.2**), the values of ΔE_t are between those reported for Brooker's two complexes, but the calculations also reveal dominant QTM and thus no SMM behaviour is observed for either Tb^{3+} ion.

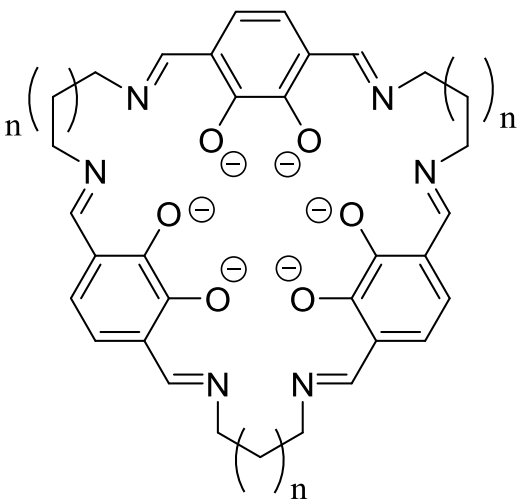

n = 1 for L^{Pr}
n = 2 for L^{Bu}

Figure 3.24: Molecular structure of Brooker's L^{Pr} and L^{Bu} macrocycles.[196]

By considering a series of average states, we were able to probe the anisotropy of the ground state of (**3.2**). For Tb1, this approach revealed a g_z value of 17.7 which is considerably large and leads to a reduced tunnel splitting of 0.44 cm^{-1}. Still, in

order to obtain a substantial anisotropy barrier, the tunnel splitting should be on the scale of 10^{-7} cm^{-1} and as a consequence, no appreciable effective anisotropy barrier should be observed. These theoretical findings support our experimental observations and are consistent with the published findings of both Brooker and Chibotaru.[196] The results of this calculation are summarised in **Table 3.11**.

Table 3.11: Summary of the physical parameters calculated for averaged pairs of singlet states within the $^7F_6$ multiplet of the Tb1 ion in (**3.2**).

Energy (cm^{-1})	**g_z**	**Angle (°)**
0.22	17.69	0.00
74.99	11.90	10.40
100.54	12.21	69.96
156.86	9.06	61.34
235.12	6.30	54.30
522.86	4.42	71.69

Table 3.12: Summary of the physical parameters calculated for averaged pairs of singlet states within the $^7F_6$ multiplet of the Tb2 ion in (**3.2**).

Energy (cm^{-1})	**g_z**	**Angle (°)**
0.98	16.82	0.00
40.35	13.37	15.92
118.81	8.17	80.29
172.80	14.02	32.86
202.27	14.62	43.83
363.06	17.81	84.28

Using the same methodology for the Tb2 ion reveals it has a pseudo-ground doublet that is less anisotropic as indicated by the lower g_z value of 16.82, Table 3.12. As a result, we would expect a larger quantum tunnelling contribution and therefore a greater tunnel splitting for this ion. This is also consistent with our experimental results for this complex which shows no SMM behaviour.

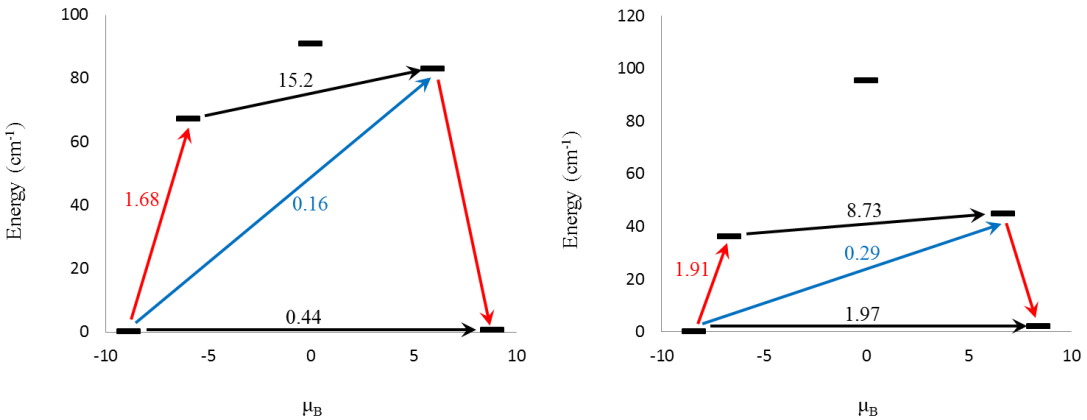

Figure 3.25: Plot of the exchange states for Tb1 and Tb2 in (**3.2)**. The states are plotted as energy *vs* the magnetic moment of the state with arrows showing the potential relaxation pathways (blue and green) and the tunnel splitting (black). The number beside each arrow is the matrix element of the transition moment (blue and green) and the value of the tunnel splitting (black).

For complex (**3.3**), the active space was chosen as the 11 electrons in the seven 4*f* orbitals and the atomic coordinates from the crystal structure were used as the nuclear coordinates without any additional geometry optimisation. For the calculation of the spin-free states, 35 quartet CSFs and 112 doublet CSFs were calculated. In the RASSI procedure, all 35 quartet and 112 doublet states were used. The results of the calculations are summarised in Table 3.13 and Table 3.14.

Table 3.13: Summary of the results for the $^4I_{15/2}$ multiplet of Er1 within complex (**3.3)**.

KD	Energy	g_x	g_y	g_z	Zm (°)
1	0.00	0.41	2.16	14.14	0.00
2	18.11	8.36	6.50	3.44	86.52
3	33.33	1.83	2.95	12.35	2.82
4	57.29	1.14	3.50	12.65	93.03
5	112.66	2.30	2.87	11.23	3.25
6	141.91	1.04	4.73	12.28	90.36
7	261.72	0.38	1.08	15.53	64.87
8	283.76	0.26	1.52	16.12	132.57

Table 3.14: Summary of the results for the $^4I_{15/2}$ multiplet of Er2 within complex **3.3**.

KD	Energy	g_x	g_y	g_z	Zm (°)
1	0.00	0.67	1.74	15.45	0.00
2	26.81	0.43	0.80	12.48	20.50
3	45.13	1.08	2.69	10.92	157.38
4	56.04	0.58	2.07	12.86	30.22
5	81.21	3.72	5.34	9.46	78.04
6	192.82	0.26	1.28	15.09	70.77
7	304.51	1.10	3.78	11.77	90.21
8	329.57	0.67	5.25	13.15	1.88

From the *ab initio*, there is a reversal of the trends when compared to the oblate ions in complexes (**3.1**) and (**3.2**). For example, in the first two complexes, the Dy1 and Tb1 ions are more anisotropic with g_x, g_y and g_z values closer to 0 0 20 when compared to their Dy2 and Tb2 counterparts. This is due to the less distorted ligand field around these ions. In contrast to the previously reported complexes, the Er1 ion of (**3.3**) is the least anisotropic which is due to the differences in the shape of the electron density around Ln^{3+} ions. In this context, the Dy^{3+} and Tb^{3+} ions have an electron density shaped like a disk extending out from the equatorial plane (oblate), whereas the Er^{3+} ions have an electron density that is stretched along the *z*-axis (prolate). For prolate ions, the hard donor atoms should be in the equatorial plane in order to avoid repulsion between the electrons on the donor atom and the electrons in the *f*-orbitals. Since the ligand field of the Er2 ion has the chloride ions distorted away from the *z*-axis, this reduces the electron-electron repulsion and enhances the axial anisotropy. Despite this, both Er^{3+} ions in (**3.3**) are considerably less anisotropic than the Dy^{3+} and Tb^{3+} ions of complexes (**3.1**) and (**3.2**), which hold particularly true for Er1, where there is an appreciable *xy*-transverse component to the anisotropy. Based on the energy difference between the ground and first excited states, each Er^{3+} ion would have a potential anisotropy barrier of 18.1 and 26.8 cm^{-1} respectively; although, the strong transverse anisotropy promotes rapid quantum tunneling in the ground state and thus no SMM behaviour is observed. To investigate the relaxation mechanism further, a plot of the average energy versus the average magnetic moment of each state has been constructed for both Er^{3+} ions, Figure 3.26.

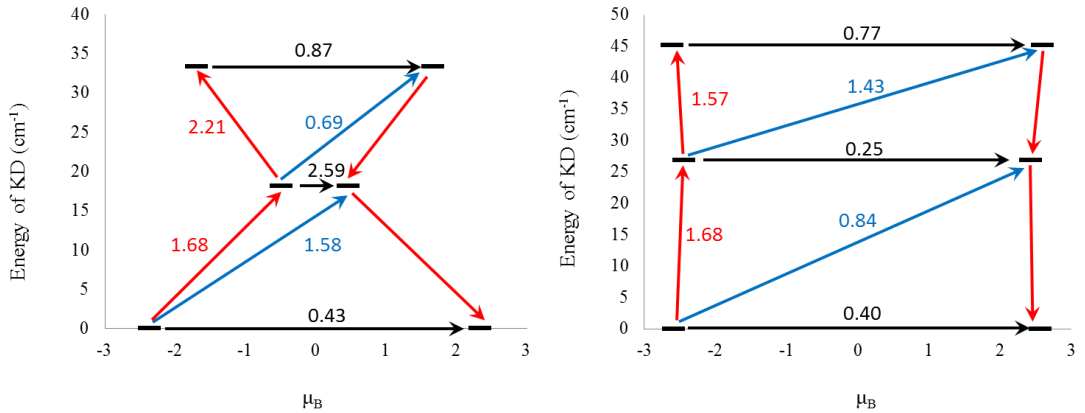

Figure 3.26: Energy *vs*. average magnetic moment plots of the first three KD within the $^4I_{15/2}$ ground multiplet of Er1 (left) and Er2 (right) within complex **3.3**. The possible magnetic relaxation pathways are shown as arrows. Empirical values for the average matrix elements of the transition moment between each state are included on the plot and are colour-coded to their respective transitions. Red arrows are thermal relaxation processes, blue arrows are spin-lattice relaxation processes and the black arrows are ground and excited QTM processes.

The plot of the m_J states for the Er1 ion reveals an unusual first excited doublet which is far more isotropic when compared to the other doublets. There is also a strong spin-lattice contribution to the relaxation pathway of the first excited doublet due to the large angle between the main magnetic axes of the ground and first excited state (86.5°). Even though the thermal pathway has a strong transition moment, the kinetic ground state quantum tunnelling process is allowed (> 0.1) and will be the dominant relaxation pathway. Therefore, no experimental energy barrier is anticipated for this ion in full agreement with the experimental ac susceptibility data.

For the second Er2 ion, all of the KDs are fairly consistent with regards to their magnetic anisotropy. The smaller angle between the main magnetic axes of the ground and first excited doublets (20.5°) results in a suppressed spin-lattice pathway and the largest transition moment occurs for the thermal relaxation pathway. In

addition, the ground state quantum tunneling pathway is accessible (> 0.1) and as a consequence, this kinetic relaxation pathway dominates. Therefore, no experimental anisotropy barrier is predicted for this complex again in complete agreement with our experimental data.

3.5: Conclusions and Future Perspectives

In this project a novel dual compartmental macrocyclic ligand, **H_2L_3** has been synthesized and its coordination chemistry was investigated with Dy^{3+}, Tb^{3+} and Er^{3+} ions. Under the right synthetic conditions the Ln^{3+} ions are coordinated in the N_3O_2 cavity that together with two axial ligands give rise to pentagonal bipyramidal geometry. This geometry was initially targeted because little is known in the literature about how subtle changes in a D_{5h} crystal field can affect the electronic nature of both oblate and prolate Ln^{3+} ions. The molecular structures of all three macrocyclic complexes were elucidated by single crystal X-ray diffraction which reveals they are isostructural, crystallizing in the monoclinic space group $P2_1$. In contrast to the previously reported methyl analogue these complexes all crystallize as dimers with two crystallographically independent Ln^{3+} ions in the asymmetric unit. Magnetic susceptibility studies reveal that the Dy^{3+} complex exhibits SMM behavior with a U_{eff} of 12.6 cm^{-1}, whereas the presence of fast quantum tunnelling processes due to a significant deviation from ideal D_{5h} geometry afford no such behaviour for the Tb^{3+} and Er^{3+} derivatives. Detailed *ab initio* studies performed on all three complexes reveal that the Dy1 ion in (**3.1**) relaxes via spin-lattice relaxation mechanism consistent with field induced SMM behaviour, whereas rapid QTM are present for Dy2. For complex (**3.2**), the ligand field is such that the Tb^{3+} ions do not have doubly

degenerate ground states and as a result the complex exhibits no SMM behaviour. Although complex (**3.3**) contains a Kramers ion which affords a doubly degenerate ground state, like the Tb^{3+} complex the ground state contains a large transverse anisotropy which facilitates rapid QTM in the ground state, thus supporting our experimental observations of no slow relaxation of the magnetisation and no SMM behaviour.

To the best of our knowledge this is the first joint experimental and theoretical study carried out on a series of Ln-based coordination complexes with pseudo D_{5h} geometry. Future work will involve modifying the reaction conditions to investigate the coordination chemistry of the second O_5^{2-} pocket, as well as optimizing the axial anisotropy of the Ln^{3+} complexes by exchanging the axial ligands. There is also ongoing research focused on substituting the axial ligands with organic radicals to study whether or not they can also enhance the axial anisotropy of the system.

Attempts to modify the framework of the macrocyclic ligand are also currently under investigation with an interest in studying trinuclear complexes for applications in molecular magnetism and as luminescence probes that includes the development of fluorescent tags for biological applications.[197] The proposed synthetic strategy for the preparation of these complexes is presented in Scheme 3.5.

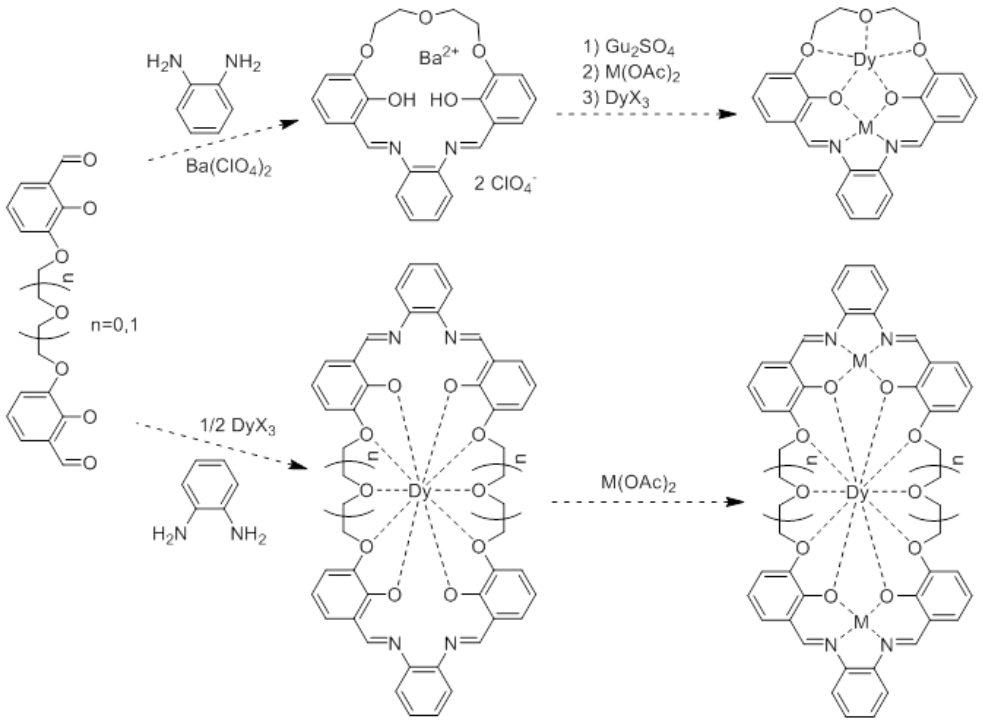

Scheme 3.5: Proposed reaction conditions for the synthesis of novel dinuclear and trinuclear complexes. Reaction conditions are proposed from references 198 and 199.

Chapter 4 Experimental

4.1: General Considerations

Unless otherwise stated, all starting materials were purchased from Sigma-Aldrich, Oakwood Chemicals and Alfa Aesar without any further purification. Anhydrous solvents were acquired using a Puresolve PS MD-4 solvent purification system and stored over 4 Å molecular sieves for no longer than two weeks under N_2 in a Schlenk flask.

4.2: Instrumentation

4.2.1: NMR Spectroscopy:

In Project 1, the ^{1}H-NMR spectra were collected on a 300 MHz Bruker Avance AV 300 Digital NMR spectrometer with a 7.05 Tesla Ultrashield magnet in d_5-DMSO. For all ligands and intermediates synthesised in Project 2, the ^{1}H-NMR spectra were measured in deuterated chloroform and the experiments were performed on a Bruker Avance III HD 400 Digital NMR spectrometer. ^{13}C-NMR data were collected at 100 MHz on a Bruker Avance III HD 400 Digital NMR spectrometer.

4.2.2: UV-Vis Spectroscopy:

UV-Vis absorption spectra were collected using a Beckman Coulter DU 720 General-Purpose UV-Vis spectrophotometer. Data were collected for wavelengths between 190 nm and 1100 nm at increments of 1 nm. For each compound, three successive measurements were carried out at three different concentrations for the construction of a calibration plot to determine the molar extinction coefficient, ε.

4.2.3: IR Spectroscopy

IR spectroscopy was performed using a Bruker ALPHA Platinum ATR system on dry powders.

4.2.4: Mass Spectrometry

MS data were recorded on a Carlo Erba/Kratos EC/ms acquisition system and processed on a SPARC workstation. Samples were introduced through a direct inlet system, with tris(perflouroheptyl-S-triazine) as the internal standard.

4.2.5: Elemental Analysis

Elemental analysis was performed for carbon, nitrogen and hydrogen at Atlantic Microlab Inc.

4.2.6: Thermo-Gravimetric Analysis

Thermogravimetric analysis (TGA) coupled to mass spectroscopy (MS) studies were performed on a Mettler Toledo TGA/SDTA851. Helium was used to purge the system at a flow rate of 50 mL/min. Samples were run at opened crucible from 25°C to 150°C at a rate of 2°C/min and then heated to 150°C for 10 minutes.

4.2.7: Single Crystal X-ray Diffraction Measurements

X-ray crystallographic data were collected on a Bruker Apex II CCD diffractometer equipped with an Oxford low temperature device at 150 K unless otherwise stated. A graphite-monochromated Mo-Kα (λ = 0.71073 Å) radiation source was used for the diffraction experiment and the data was analysed using Bruker Apex II software.[200] A multi-scan absorption correction was applied to the data using the Bruker-SADABS program.[201] The crystal structures were solved by direct methods and refined by full-

matrix least-squares on F^2 within the SHELXL platform.[200,201,202] Hydrogen atoms were assigned to calculated positions and refined as riding atoms using default parameters. Reflection data for the MOF-1 framework contained residual electron density peaks consistent with disordered water and acetonitrile molecules residing within the porous cavities of the MOF. Since this electron density could not be adequately modeled it was removed using the SQUEEZE routine within PLATON.[202] The three macrocyclic complexes described in Chapter 3 all crystallize in the monoclinic, chiral space group $P2_1$, but were all refined as racemic twins. A summary of the crystallographic parameters for all of the crystal structures discussed in the thesis can be found in the Appendix section.

4.2.8: Powder X-ray Diffraction

Variable temperature powder data was collected at the University of Windsor by the Rawson group on a Bruker D8 Discovery powder X-ray diffractometer fitted with a variable temperature device using a Cu-Kα radiation source.

4.2.9: Electron Paramagnetic Resonance

Solid state EPR spectra of MOF-1 were collected using a Bruker EMX plus X-band EPR spectrometer at the University of Windsor. The experiment was run at room temperature between 0 and 8000 G (ν = 9.851 GHz with a modulation amplitude of 4 Gpp).

4.2.10: Magnetic Susceptibility

DC susceptibility measurements were performed using a Quantum Design MPMS SQUID magnetometer. Temperature scans were performed in an applied field of 0.2

T, from 2 – 300 K. AC susceptibility measurements were carried out using a Quantum Design PPMS, with an oscillating field of 3.5 Oe over multiples frequencies between 25 and 1500 MHz. Static fields ranging from 0 to 0.5 T were applied from 2 – 15 K. Diamagnetic corrections were applied to all samples.

4.2.11: MOLCAS Quantum Chemical Calculations

All energies and physical observables for complexes **3.1** to **3.3** were calculated using the MOLCAS 8.0 quantum chemistry package.[188] The calculations performed were of the CASSCF/RASSI/SINGLE_ANISO type, where the active space was chosen as the seven *4f* orbitals of the Ln^{III} ions. Molecular coordinates were determined from single crystal X-ray diffraction experiments and were used without further optimisation. Relativistic contractions were accounted for by utilising the ANO-RCC basis set library as well as the Douglas-Kroll-Hess Hamiltonian. Strong spin-orbit coupling was included in the RASSI procedure where 21 sextet states were mixed with 128 quartet states for Dy^{3+}, 7 septet and 140 quintet states were mixed for Tb^{3+} and 35 quartet states were mixed with 112 doublet states for Er^{3+}. Results of the calculations are found in the *ab initio* section of Chapter 3 and the Appendix.

4.3: Synthetic Procedures

4.3.1: Synthesis of 2,2′,6,6′-tetramethyl-4,4′-bipyridine (2.6)

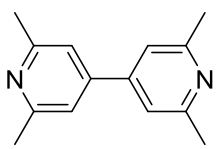

2.6

The precursor, **2.6**, was prepared following a procedure from the literature.[162] Recrystallization of the crude product from hot water afforded long needles of **2.6** (5.2 g, 49 % yield). ^{1}H-NMR ($CDCl_3$, 300 MHz), δ (ppm): 7.19 (4H, s, py-H), 2.62 (12H, s, CH_3). ^{13}C-NMR ($CDCl_3$, 75 MHz), δ (ppm): 158.5 (2-C), 146.8 (4-C), 118.2 (3-C), 24.5 (1-C). IR, ν (cm^{-1}): 3010, 2955, 2915, 1434, 1383, 1099, 1030, 989, 485, 455. M.p.: 152 ˚C, Lit. [152˚C].[162] FAB-MS: *m/z* = 212 $[M]^+$, 50 %

4.3.2: Synthesis of 2,2′,6,6′-tetracarboxy-4,4′-bipyridine (2.7)

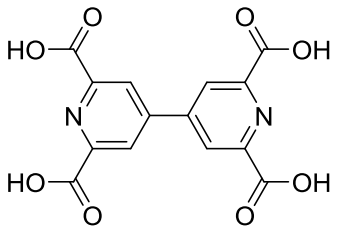

2.7

$L_{2.4}$ was synthesised from a modified procedure in the literature to afford the crude product as a white solid.[162] The product was recrystallized from 35 % HNO_3 to yield **$L_{2.4}$** as a white crystalline powder (5.71, 91 % yield). ^{1}H-NMR (DMSO-d_6, 300 MHz), δ (ppm): 13.62 (4H, s, OH), 8.61 (4H, s, py-H). ^{13}C-NMR (DMSO-d_6, 75 MHz), δ (ppm): 165.8 (1-C), 150.1 (2-C), 146.7 (4-C), 125.8 (3-C). IR (KBr), ν (cm^{-1}): 3200 (br, O-H), 3040 (md, C-H), 2551, 1732 (st, C=O), 1704, 1601, 1372, 1304, 1255, 1232, 1161, 1084, 911, 785, 768, 686, 644. M.p.: 272 ˚C. Lit. [270 ˚C].[162] FAB-MS: m/z = 332 $[M]^+$, 70%.

4.3.3: Synthesis of [4,4']bipyridinyl-2,6,2',6'-tetracarboxylic acid pyridin-3-ylamide (H_4L_2)

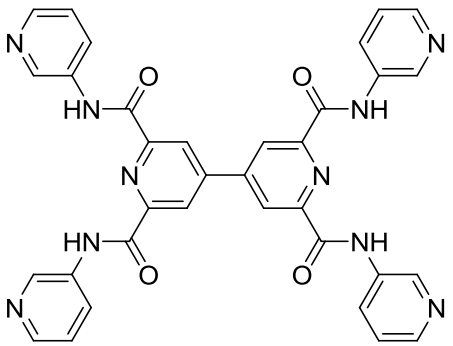

H_4L_2

Distilled thionyl chloride (15 mL, excess) and dry DMF (2 drops, *cat.*) were added to 2,2′,6,6′-tetracarboxy-4,4′-bipyridine (1.00 g, 3 mmol) in a 100 mL two-necked flask equipped with a reflux condenser. The resulting mixture was then heated under nitrogen to 95 °C for 5 h with continuous stirring. The thionyl chloride was then removed by mild heating to 30 °C under a gentle vacuum to afford the tetracarbonyl chloride intermediate (**2.8**) as a deep purple solid which was used *in situ*. A solution of 3-aminopyridine (12 mmol, 4 equiv.) and triethylamine (10 mL, excess) was prepared in dry THF (25 mL) under nitrogen and immediately added to the above solution of (**2.8**). The reaction mixture was refluxed for two days, after which time crude **H_4L_2** was filtered and washed subsequently with DCM (50 mL), H_2O (50 mL) and Et_2O (50 mL). Recrystallization of the crude product from hot DMSO afforded **H_4L_2** as a microcrystalline powder (1.52 g, 78 % yield). ^{1}H-NMR ($CDCl_3$, 300 MHz) δ (ppm): 11.25 (4H, s, N-H), 9.14 (4H, d, *J* = 2.1 Hz, 9-H), 8.82 (4H, s, 2-H), 8.44 (4H, d, *J* = 3.6 Hz, 8-H), 8.37 (4H, dd, *J* = 6.9 Hz, 2.1 Hz, 6-H), 7.52 (4H, dd, *J* = 8.4 Hz, 4.8 Hz, 7-H). FT-IR *v* (cm^{-1}): 3215 (br, N-H), 3087, 1690 (st, C=O), 1591, 1546,

1484, 1426, 1337, 1277, 1231, 1067, 896, 801, 755, 700, 680, 637, 480. FAB-MS: *m*/*z* = 637 $[M]^+$, 10%. UV-Vis (DMF) λ (nm): 280 (ε = 140 $M^{-1}cm^{-1}$). CHN Elemental Analysis: Calcd. for $C_{34}H_{24}N_{10}O_4 \cdot 2(CH_3)_2SO$ C, 57.17, H, 4.49 N, 17.46 %; Found C, 57.56; H, 4.58; N, 17.67 %.

4.3.4: Synthesis of $[Cu_8(L_2)_3(OAc)_4(py)_2(H_2O)_2]_n$, MOF-1

In a two-necked flask, **H_4L_2** (100 mg, 126 μmol) was added together with DMF (20 mL), pyridine (5 mL) and H_2O (10 mL). The solution was heated to 120 °C for 12 h after which time a solution of $Cu(OAc)_2 \cdot 2H_2O$ (46 mg, 252 μmol) in water (1 mL) was added resulting in the formation of a blue-green solution. The solution was vigorously stirred at 120 °C for an additional hour and then cooled to room temperature. The deep green mixture was then further stirred at room temperature for an additional 24 h and then filtered to afford a clear, deep-green solution. 3mLportions of this solution were then transferred to 10 mL vials that were 8 cm in height. Each vial was placed in a jar that was subsequently half-filled with MeCN and sealed for gas-liquid diffusion. Dark-green-blue blocks suitable for single crystal X-ray diffraction were obtained after 2 weeks (53 mg, 54 % yield). FT-IR (KBr), ν (cm^{-1}): 3367 (br, Water O-H), 3078, 2928 (w, py C-H), 1655 (m, Amide C=O), 1561 (s, py), 1480, 1417, 1377, 1336, 1260 (w, C-O), 1192, 1104, 1083, 1059, 980, 892, 806, 783, 759, 686, 507, 418. MALDI-MS: *m*/*z* = 700.1 $[CuL^2]^-$ 16%. UV-Vis (DMF-H_2O-Pyridine; 2:1:1) λ (nm) 294 (ε = 954 $M^{-1}cm^{-1}$). CHN Elemental Analysis: Calcd. for $C_{30}H_{21.5}N_8O_{5.5}Cu_2 \cdot 4H_2O$: C, 46.12; H, 3.81; N, 14.34 %. Found C, 46.34; H, 3.50; N, 14.24 %.

4.3.5: Synthesis of L_3'

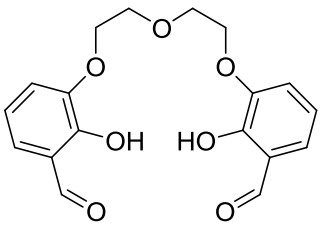

L_3'

L_3' was prepared using a modified procedure from the literature (yield: 1.20 g, yield 95 %). ^{1}HNMR ($CHCl_3$) δ (ppm): 10.94 (2H, s, OH), 9.93 (2H, s, CHO), 7.22-7.17 (4H, m, Ar-H), 6.95-6.90 (2H, m, Ar-H), 4.27-4.24 (4H, m, CH_2O), 4.00-3.97 (4H, m, CH_2O); ^{13}CNMR ($CHCl_3$) δ (ppm): 196.2, 152.2, 147.4, 125.2, 121.2, 120.9, 119.5, 69.9, 69.3; IR υ (cm^{-1}): 3566 (O-H), 2855 (C-H aldehyde), 1650 (C=O); m.p. = 96-97 °C. Lit. [96-97 °C].[184]

4.3.6: Synthesis of H_2L_3.

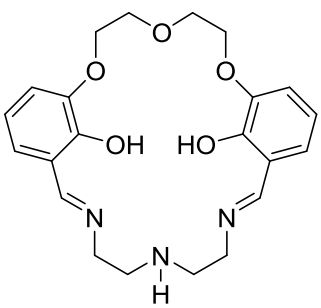

H_2L_3

A solution of L_3' (500 mg, 1.4 mmol) in $CHCl_3$ (3 mL) was added dropwise over a 1 h period to a solution of diethylenetriamine (0.15 mL, 1.4 mmol) in MeOH (1 mL) and Et_2O (300 mL) in a 500 mL round bottomed flask. The resulting thick yellow precipitate was stirred for 20 mins after which time it was filtered and washed with Et_2O to yield **H_2L_3** as a yellow powder. No further purification was required (yield

527 mg, 90 %). ^{1}HNMR ($CHCl_3$) δ (ppm): 8.33 (2H, s, CHN), 6.89-6.69 (6H, m, Ar-H), 4.21 (4H, m, CH_2O), 4.07 (4H, m, CH_2O), 3.97 (4H, m, $CNCH_2$), 3.79 (1H, m, N-H), 2.99 (4H, m, CH_2NH; ^{13}CNMR ($CHCl_3$) δ (ppm): 166.2 (C=N), 147.3 (Ar-OC), 144.7 (Ar-OH), 123.5 (Ar-CH_2N), 118.6 (*m*-Ar), 117.7 (*p*-Ar), 116.1 (*m*-Ar), 69.4 (C-*o*-Ar), 68.0 (CH_2O), 59.2 (C-NC), 49.8 (C-HN); IR υ (cm^{-1}): 2871 (sp^2 C-H), 1627 (C=N), 1459 (ethylene C-H), 1245 (C-O); MS *m/z*: $[MH]^+$ ion is found at 414 and the $[MNaH]^+$ ion is found at 436. m.p. = 60-61°C. CHN Elemental Analysis, calculated for $C_{22}H_{27}N_3O_5$: C 63.91, H 6.98, N 10.16 %; found C 63.82, H 6.87, N 10.25 %

4.3.7: General Procedure for the Synthesis of Complexes 3.1, 3.2 and 3.3

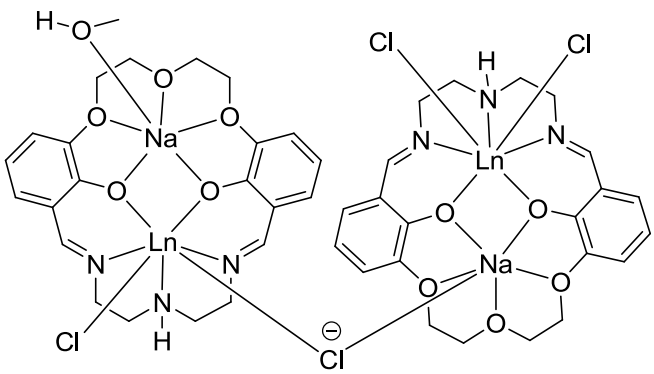

Ln^{3+} = Dy^{3+}, Tb^{3+} and Er^{3+} for Complexes (**3.1**), (**3.2**) and (**3.3**)

H_2L_3 (200 mg, 0.484 mmol) was added in one portion to a MeOH solution (5 mL) containing NaOH (39 mg, 0.968 mmol). The resulting mixture was stirred for 10 mins at room temperature yielding a yellow suspension, after which time, the appropriate $LnCl_3 \cdot 6H_2O$ was added (0.484 mmol, 1 equiv.). The resulting solution was then refluxed for 12 h and cooled to room temperature. Et_2O (100 mL) was then added affording the crude product as a solid which was collected by filtration and washed with $CHCl_3$ (50 mL) and Et_2O (50 mL). The resulting powder was dissolved

in MeOH (10 mL) and single crystals suitable for X-ray diffraction, were grown *via* the slow gas-liquid diffusion of Et_2O (10 mL) into the MeOH solution.

4.3.8: Synthesis of Complex (3.1)

Complex (**3.1)** was synthesised following the general procedure in section 4.9. The complex was isolated as pale yellow plates (yield 160 mg, 47 %). IR υ (cm^{-1}): 3405 (N-H), 2903 (C-H), 1624 (C=N), 1453 (C-H bend), 1213 (C-O); UV-Vis λ (nm): 202 (72 000 $cm^{-1}M^{-1}$), 231 (ε = 110 000 $cm^{-1}M^{-1}$), 272 (ε = 36 000 $cm^{-1}M^{-1}$), 356 (ε = 16 000 $cm^{-1}M^{-1}$); Elemental analysis, calculated for $[Na_2Dy_2(\mathbf{L_3})_2Cl_4(MeOH)]\cdot 2H_2O$, C = 38.50, H = 4.16, N = 5.99 %; found: C = 38.53, H = 3.94, N% = 5.87 % MS-EI (*m*/*z*): 1404 $[M+H]^+$ (10 %), 643 $[Dy(L_3)Cl_2+H]^+$ (100%); m.p. = > 200 °C.

4.3.9: Synthesis of Complex (3.2)

Complex (**3.2**) was synthesised following the general procedure in section 4.9 and collected as pale yellow plates (yield: 178 mg, 54 %). IR υ (cm^{-1}): 3404, 2900, 1623, 1453, 1213; UV-Vis λ (nm): 202 (78 000 $cm^{-1}M^{-1}$), 232 (ε = 110 000 $cm^{-1}M^{-1}$), 271 (ε = 40 000 $cm^{-1}M^{-1}$), 353 (ε = 15 000 $cm^{-1}M^{-1}$); Elemental analysis, Found: C% = 38.90, H% = 3.78, N% = 5.91, Calculated: C% = 38.70, H% = 3.90, N% = 6.02 for the following structure $[Tb_2Na_2(\mathbf{L_3})_2Cl_4(MeOH)]$; MS-EI (*m*/*z*): 1450 $[M+H]^+$ (10 %), 638 $[Tb(L_3)Cl_2+H]^+$ (100%); m.p. = > 200 °C.

4.3.10: Characterisation of Complex (3.3)

Complex (**3.3**) was synthesised following the general procedure in section 4.9 and collected as pale yellow plates (yield 190 mg, 56 %) IR υ (cm^{-1}): 3410 (N-H), 2903 (C-H), 1625 (C=N), 1454 (C-H bend), 1215 (C-O); UV-Vis λ (nm): 201 (74 000 cm^{-}

$^{1}M^{-1}$), 231 (ε = 114 000 $cm^{-1}M^{-1}$), 271 (ε = 37 000 $cm^{-1}M^{-1}$), 351 (ε = 16 000 $cm^{-1}M^{-1}$); Elemental analysis, Found: C% = 37.29, H% = 3.80, N% = 5.57, Calculated: C% = 37.18, H% = 3.88, N% = 5.78 for the following structure $[Er_2Na_2(L_3)_2Cl_4(MeOH)]\cdot H_2O$; MS-EI (*m*/*z*): 1459 $[M+H+NaCl]^+$ (10 %), 647 $[Er(L^2)Cl_2+H]^+$ (100%); m.p. = > 200 °C.

Chapter 5 Appendix

5.1: Crystallography Details

Table 5.1: Summary of the single-crystal X-ray diffraction data for MOF-1.

Crystal Data	
Chemical formula	$C_{30}H_{21.5}Cu_2N_8O_{5.5}$
M_f	709.13
Crystal system, space group	Orthorhombic, *Pban*
Temperature (K)	296(2)
a, b, c (Å)	25.1110 (16), 28.1060 (17), 13.6310 (9)
V (Å^3)	9620.3 (11)
Z	8
Radiation type	Mo K_α
μ (mm^{-1})	0.92
No. of measured, independent and observed [$I > 2\sigma(I)$] reflections	97559, 9843, 6999
R_{int}	0.066
$(\sin \theta/\lambda)_{max}$ (Å^{-1})	0.627
Refinement	
$R[F^2 > 2\sigma(F^2)]$, $wR(F^2)$, S	0.084, 0.232, 1.06
No. of parameters	385
No. of restraints	0

H-atom treatment	H-atom parameters constrained $w = 1/[\sigma 2(F_o^2) + (0.1123P)^2 + 31.5194P]$ where $P = (F_o^2 + 2F_c^2)/3$

Table 5.2: Summary of the single-crystal X-ray diffraction data for (**3.1**).

Crystal Data	
Chemical formula	$C_{45}H_{51}Cl_4Dy_2N_6Na_2O_{13}$
M_f	1396.70
Crystal system, space group	Monoclinic, $P2_1$
Temperature	150(2)
a, b, c (Å)	9.4342(9), 20.316(2), 13.5275(13)
β (°)	97.960(4)
V (Å^3)	2567.8(4)
Z	2
Radiation type	Mo $K\alpha$
μ (mm^{-1})	3.18
Data collection	
Diffractometer	Bruker *APEX*-II CCD Diffractometer
Absorption correction	Multi-scan Bruker *SADABS*
T_{min}, T_{max}	0.536, 0.746
No. of measured, independent and observed [$I>2\sigma(I)$]	53491, 11140, 10992
R_{int}	0.041
$(\sin\theta/\lambda)_{max}$ (Å^{-1})	0.639
Refinement	
$R[F^2 > 2\sigma(F^2)]$, $wR(F^2)$, S	0.073, 0.174, 1.23
No. of reflections	11140

No. of parameters	471
No. of restraints	1
H-atom treatment	H-atom parameters constrained
	$w = 1/[\sigma^2(F_o^2) + (0.0272P)^2 + 69.8514P]$
	where $P = (F_o^2 + 2F_c^2)/3$
$\Delta\rho_{max}$, $\Delta\rho_{min}$ (e Å^{-3})	7.17, -3.80
Absolute structure	Refined as an inversion twin
Absolute structure parameter	0.42 (3)

Table 5.3: Summary of the single-crystal X-ray diffraction data for (**3.2)**.

Crystal data	
Chemical formula	$C_{45}H_{52}Cl_4N_6Na_2O_{11}Tb_2$
M_r	1358.54
Crystal system, space group	Monoclinic, $P2_1$
Temperature (K)	100
a, *b*, *c* (Å)	9.426 (3), 20.183 (6), 13.547 (4)
β (°)	97.893 (10)
V (Å^3)	2552.7 (13)
Z	2
Radiation type	Mo *Kα*
μ (mm^{-1})	3.04
Crystal size (mm)	0.34 × 0.24 × 0.07
Data collection	
Diffractometer	Bruker *APEX*-II CCD diffractometer
Absorption correction	Multi-scan *SADABS*
T_{min}, T_{max}	0.615, 0.746
No. of measured, independent and observed [$I > 2\sigma(I)$] reflections	126948, 15626, 13949
R_{int}	0.073

$(\sin \theta/\lambda)_{max}$ ($Å^{-1}$)	0.716
Refinement	
$R[F^2 > 2\sigma(F^2)]$, $wR(F^2)$, S	0.042, 0.102, 1.09
No. of reflections	15626
No. of parameters	638
No. of restraints	1
H-atom treatment	H-atom parameters constrained
$\Delta\rho_{max}$, $\Delta\rho_{min}$ (e $Å^{-3}$)	1.69, −3.07
Absolute structure	Flack x determined using 6194 quotients [(I+)-(I-)]/[(I+)+(I-)] (Parsons and Flack (2004), Acta Cryst. A60, s61).
Absolute structure parameter	−0.019 (4)

Table 5.4: Summary of the single-crystal X-ray diffraction data for (**3.3**).

Crystal data	
Chemical formula	$C_{45}H_{51}Cl_4Er_2N_6Na_2O_{11}O$
M_r	1390.21
Crystal system, space group	Monoclinic, $P2_1$
Temperature (K)	151
a, *b*, *c* (Å)	9.4325 (12), 20.239 (3), 13.5590 (17)
β (°)	97.904 (6)
V (Å^3)	2563.9 (6)
Z	2
Radiation type	Mo *K*α
μ (mm^{-1})	3.54
Crystal size (mm)	× ×
Data collection	
Diffractometer	Bruker *APEX*-II CCD diffractometer
Absorption correction	Multi-scan Bruker *SADABS*
T_{min}, T_{max}	0.612, 0.746
No. of measured, independent and observed [$I > 2\sigma(I)$] reflections	48502, 10015, 9418
R_{int}	0.056

$(\sin \theta/\lambda)_{max}$ (Å^{-1})	0.617
F	
$R[F^2 > 2\sigma(F^2)]$, $wR(F^2)$, S	0.078, 0.174, 1.20
No. of reflections	10015
No. of parameters	475
No. of restraints	1
H-atom treatment	H-atom parameters constrained
	$w = 1/[\sigma^2(F_o^2) + (0.0151P)^2 + 75.8769P]$ where $P = (F_o^2 + 2F_c^2)/3$
$\Delta\rho_{max}$, $\Delta\rho_{min}$ (e Å^{-3})	6.43, −2.82
Absolute structure	Refined as an inversion twin.
Absolute structure parameter	0.24 (3)

5.2: Computational Details

Table 5.5: CASSCF/RASSI computed spin-free and spin-orbit energies for complex (**3.1**)**.**

Spin Free Energies (cm^{-1})				Spin-Orbit Energies (cm^{-1})			
Dy1		Dy2		Dy1		Dy2	
0.00	29809.14	0.00	29890.28	0.00	10962.75	0.00	11054.13
13.19	29822.26	22.20	29902.75	0.00	10962.75	0.00	11054.13
76.62	29833.91	90.82	29908.69	69.95	11029.63	57.54	11223.39
157.13	29835.26	172.35	29941.68	69.95	11029.63	57.54	11223.39
223.83	29840.56	254.03	29947.56	132.87	11509.76	144.08	11598.72
280.10	29849.42	379.12	29957.94	132.87	11509.76	144.08	11598.72
293.94	29867.35	550.72	29963.10	231.70	11550.51	277.40	11636.82
336.03	29883.20	594.61	29997.98	231.70	11550.51	277.40	11636.82
502.75	29890.89	606.74	30001.68	275.56	11560.95	405.16	11650.07
551.74	31154.46	731.53	31282.53	275.56	11560.95	405.16	11650.07
584.52	31156.62	742.17	31283.47	344.68	11585.57	527.06	11677.52
7559.24	31158.22	7632.56	31287.85	344.68	11585.57	527.06	11677.52
7650.37	31161.91	7740.71	31290.48	394.52	11592.03	544.93	11699.38
7682.18	31179.92	7804.66	31301.32	394.52	11592.03	544.93	11699.38
7724.58	31192.81	7855.39	31311.03	443.56	13390.62	630.99	13486.19
7752.09	31197.38	7872.89	31325.76	443.56	13390.62	630.99	13486.19
7828.64	31209.55	7938.99	31333.90	3557.72	13449.47	3567.42	13541.50
7891.06	31237.61	7993.67	31354.81	3557.72	13449.47	3567.42	13541.50
34794.17	31245.82	34807.45	31357.85	3605.36	13492.62	3619.14	13582.35

34994.82	31254.58	34940.89	31362.38	3605.36	13492.62	3619.14	13582.35
35226.81	31304.76	35586.82	31405.35	3698.16	13509.68	3702.34	13605.59
24841.05	31315.50	24896.99	31411.76	3698.16	13509.68	3702.34	13605.59
24842.99	31318.39	24904.00	31414.87	3744.91	14862.41	3798.63	14958.70
24882.67	31325.14	24934.58	31419.20	3744.91	14862.41	3798.63	14958.70
24900.86	31357.13	24962.95	31469.91	3783.18	14926.45	3892.32	15016.32
24970.38	31357.22	25032.19	31469.96	3783.18	14926.45	3892.32	15016.32
24974.54	32991.12	25049.94	33096.78	3801.36	14936.74	3979.42	15032.13
24976.27	33047.50	25063.45	33162.39	3801.36	14936.74	3979.42	15032.13
24986.60	33151.40	25159.88	33245.73	3829.84	15828.69	4064.36	15918.59
24996.26	33177.85	25181.70	33266.10	3829.84	15828.69	4064.36	15918.59
25091.47	33193.62	25202.00	33278.95	6143.58	15833.98	6162.59	15932.46
25101.44	34553.26	25209.43	34642.02	6143.58	15833.98	6162.59	15932.46
25118.43	34556.97	25215.27	34653.97	6167.18	16330.36	6206.49	16427.79
25136.57	34566.92	25250.04	34662.52	6167.18	16330.36	6206.49	16427.79
25181.32	34576.54	25277.56	34668.55	6226.13	25254.01	6252.85	25318.80
25199.76	34587.98	25306.30	34692.09	6226.13	25254.01	6252.85	25318.80
25224.92	34589.45	25337.20	34695.56	6255.49	25286.75	6340.27	25393.88
25283.52	34653.27	25352.29	34771.42	6255.49	25286.75	6340.27	25393.88
25298.48	34675.87	25369.40	34782.84	6297.05	25370.67	6427.13	25476.64
25301.44	34679.37	25414.12	34791.58	6297.05	25370.67	6427.13	25476.64
25309.38	34685.39	25428.87	34800.20	6378.80	25469.86	6593.63	25548.97
25313.48	34698.39	25431.27	34808.50	6378.80	25469.86	6593.63	25548.97

25318.59	37670.42	25457.43	37682.53	8111.84	25570.94	8139.60	25639.12
25326.33	37699.41	25461.01	37876.78	8111.84	25570.94	8139.60	25639.12
25366.97	37762.02	25465.28	37901.75	8121.25	27689.57	8178.92	27726.82
25381.77	37843.32	25476.70	37941.58	8121.25	27689.57	8178.92	27726.82
25393.27	37859.92	25484.70	37965.89	8170.73	27750.24	8223.58	27770.69
25432.83	37936.61	25556.89	37990.66	8170.73	27750.24	8223.58	27770.69
25436.65	37989.56	25561.10	38074.73	8227.88	27759.79	8332.04	27811.53
25468.32	38019.67	25576.20	38081.87	8227.88	27759.79	8332.04	27811.53
25528.66	38075.37	25591.33	38160.79	8317.80	27794.42	8508.63	27891.56
25531.81	38148.64	25602.52	38309.96	8317.80	27794.42	8508.63	27891.56
25547.91	38157.52	25637.35	38316.57	9639.92	27843.49	9666.67	27988.75
25552.47	38180.87	25669.78	38324.08	9639.92	27843.49	9666.67	27988.75
25561.31	43442.84	25688.64	43483.47	9675.18	27893.29	9725.64	28054.00
25599.83	43655.05	25693.98	43675.92	9675.18	27893.29	9725.64	28054.00
25621.23	43673.02	25708.91	43863.48	9715.51	28002.38	9816.03	28068.68
25624.11	43741.04	25720.26	43884.82	9715.51	28002.38	9816.03	28068.68
25657.33	43778.39	25761.61	43903.49	9850.93	28026.97	10006.59	28089.27
25659.52	43879.53	25765.07	43973.16	9850.93	28026.97	10006.59	28089.27
26374.84	43952.59	26436.66	44046.64	9967.06	28133.23	10029.81	28169.10
26389.93	45089.53	26438.71	45065.40	9967.06	28133.23	10029.81	28169.10
26421.55	45091.16	26474.58	45066.64	10027.19	28165.54	10146.60	28215.87
26439.15	45277.34	26500.58	45355.05	10027.19	28165.54	10146.60	28215.87
26447.62	45284.11	26514.52	45357.46	10050.05	28177.30	10160.89	28275.83

26474.85	45299.60	26620.48	45455.70	10050.05	28177.30	10160.89	28275.83
26547.28	45316.56	26710.44	45464.26	10089.27	28201.56	10179.60	28329.43
26557.04	45324.55	26737.83	45473.70	10089.27	28201.56	10179.60	28329.43
26569.25	45331.66	26746.74	45490.23	10127.20	28214.45	10223.41	28359.41
29703.86	45374.32	29783.68	45504.71	10127.20	28214.45	10223.41	28359.41
29708.46	45410.25	29793.57	45529.72	10153.84	28249.89	10244.17	28396.59
29736.42	45434.00	29807.95	45552.56	10153.84	28249.89	10244.17	28396.59
29748.88	45492.01	29827.00	45609.84	10789.28	28493.47	10792.16	28504.38
29749.96	45494.84	29837.90	45614.76	10789.28	28493.47	10792.16	28504.38
29762.62		29846.75					

Table 5.6: CASSCF/RASSI computed spin-free and spin-orbit energies for complex (**3.2**)**.**

Spin Free Energies (cm^{-1})				Spin-Orbit Energies (cm^{-1})			
Tb1		Tb2		Tb1		Tb2	
0.00	45899.52	0.00	45851.03	0.00	31325.02	0.00	31277.63
133.39	45908.01	135.30	45904.64	0.44	31339.76	1.97	31279.32
181.88	45914.98	252.41	45911.78	67.08	31342.74	35.99	31283.76
257.67	45939.96	379.85	45922.84	82.90	31363.06	44.72	31318.72
261.64	45952.25	441.76	45963.40	90.62	31415.80	95.42	31378.88
749.12	45974.27	547.96	45968.74	110.46	31442.95	142.21	31416.02
1072.09	45993.25	933.57	45978.21	146.20	31479.00	154.39	31429.53
25658.34	46104.69	25722.57	45996.25	167.53	31492.93	191.22	31450.25
25705.55	46105.93	25736.55	46038.07	175.45	31508.21	193.98	31468.14
25745.74	50015.17	25793.44	46042.23	294.80	31509.72	210.57	31469.43
25912.03	50047.60	25854.80	50099.87	299.41	31525.45	220.61	31488.32
25923.74	50090.72	25868.70	50116.42	746.32	31529.25	505.53	31493.40
29213.66	50163.67	29187.02	50172.82	746.57	32031.08	506.46	31989.74
29217.14	50204.11	29189.16	50207.45	2100.03	32033.11	2097.98	31991.10
29221.67	50282.98	29223.46	50230.81	2109.23	32045.76	2102.33	32008.09
29226.62	50314.37	29229.78	50262.11	2143.43	32049.66	2144.15	32012.70
29239.18	50331.60	29246.11	50266.06	2175.46	32117.64	2180.69	32027.07
29255.09	50343.09	29264.15	50294.38	2226.14	32121.78	2220.54	32029.45
29357.17	51568.93	29364.07	50340.67	2276.97	32126.87	2253.24	32078.25
29370.64	51929.69	29378.35	51620.63	2339.96	32135.75	2297.61	32092.27

29454.28	51986.98	29469.40	51879.73	2433.34	32167.37	2316.56	32131.32
29504.46	52019.68	29532.02	51957.59	2442.48	32195.72	2346.66	32149.90
29532.03	52172.78	29552.90	52065.71	2496.57	32211.46	2385.93	32156.72
29562.16	54409.93	29564.81	52090.95	2506.35	32261.73	2402.90	32204.96
29575.50	54773.55	29585.39	54550.54	3492.89	32271.54	3459.45	32228.31
29608.70	54846.25	29631.01	54693.00	3539.97	32295.92	3514.43	32244.75
29629.49	57689.93	29657.06	54798.10	3550.01	32304.85	3516.16	32261.97
29643.22	57705.13	29661.64	57690.79	3632.60	32334.55	3556.23	32285.66
29650.46	57717.56	29670.70	57701.77	3656.17	32343.63	3561.54	32290.42
30619.35	57738.96	30639.98	57712.25	3719.50	32344.85	3642.54	32295.19
30644.44	57760.89	30651.16	57732.94	3744.88	32348.96	3684.66	32306.94
30684.82	57781.67	30725.86	57785.67	3772.46	32941.18	3756.38	32901.95
30706.19	57864.71	30742.95	57796.45	3847.28	32947.31	3818.05	32905.28
30723.76	57869.47	30763.11	57844.55	4605.17	32952.00	4554.14	32915.17
30740.02	57880.02	30783.86	57879.74	4625.06	32955.12	4584.77	32918.34
30755.16	57908.67	30806.68	57905.79	4632.93	32996.23	4588.80	32945.17
30981.04	57918.05	30903.94	57915.01	4672.06	33026.93	4635.69	32979.99
30987.08	68501.84	30915.16	57926.73	4726.13	33029.56	4644.02	32982.31
35242.66	75018.24	35238.59	68508.60	4760.84	33050.10	4720.72	32991.79
35260.34	75034.49	35256.77	75029.57	4804.29	33058.53	4727.48	32995.24
35271.21	75085.40	35264.39	75060.34	5309.76	33063.94	5289.53	33015.25
35320.10	75096.63	35329.90	75078.07	5424.11	33078.87	5338.97	33019.18
35372.73	75101.21	35390.44	75087.33	5458.16	33079.14	5418.52	33035.56

35489.68	75135.06	35520.73	75099.48	5497.08	33092.53	5448.42	33044.43
35513.81	75193.71	35522.01	75122.05	5572.00	33108.68	5554.50	33058.95
35569.77	75201.01	35601.61	75193.81	5868.98	33125.83	5791.96	33070.69
35598.46	75231.38	35637.69	75202.22	5934.98	33139.22	5897.94	33079.90
35656.94	75237.82	35665.36	75234.32	6256.18	33158.61	6052.40	33090.17
35677.39	75316.78	35697.50	75255.83	6322.28	33161.05	6178.47	33134.24
40254.19	75346.84	40303.18	75321.61	24286.22	33173.22	24268.32	33156.18
40278.59	75360.83	40314.20	75365.35	24295.99	33183.45	24272.22	33162.60
40309.13	77357.67	40331.70	75370.86	24320.80	33209.46	24306.67	33174.17
40313.17	77414.07	40343.12	77449.73	24356.41	33217.90	24323.57	33184.24
40325.87	77666.39	40353.67	77508.01	24374.93	33222.82	24344.68	33193.29
40349.50	77671.48	40364.72	77590.24	24434.80	33228.64	24368.79	33199.79
40369.42	77724.82	40391.86	77648.63	24442.69	33240.18	24375.99	33205.43
40408.09	77767.18	40408.88	77699.03	24495.00	33244.32	24388.96	33229.40
40423.24	77792.61	40421.28	77726.49	24495.69	33267.98	24391.09	33234.96
40428.50	92826.23	40449.87	77822.43	29847.41	33284.27	29803.19	33248.25
40457.68	92847.47	40458.67	93130.68	29854.21	33292.77	29806.87	33258.25
40463.03	93247.74	40502.36	93170.28	29855.28	33303.81	29810.53	33261.76
40492.97	93290.08	40556.03	93321.51	29868.68	33307.63	29814.79	33268.74
40596.89	93526.97	40561.65	93344.13	29869.37	33316.20	29817.52	33279.89
40613.29	93581.27	40629.71	93439.25	29881.34	33321.88	29819.55	33285.77
40623.01	93728.97	40640.16	93561.31	29888.49	33323.19	29826.68	33291.12
40657.90	93870.98	40667.20	93605.97	31131.11	33340.12	31042.20	33300.43

40679.43	93887.96	40689.69	93773.90	31132.52	33343.34	31042.50	33307.94
40851.16	95043.04	40737.74	93778.72	31138.73	33345.53	31085.78	33315.59
40882.90	95068.76	40777.01	95155.57	31139.37	33479.15	31088.02	33352.46
45771.30	95526.38	45785.07	95203.10	31147.46	33489.86	31095.48	33356.06
45776.23	95597.37	45787.41	95370.01	31150.66	33511.31	31099.60	33378.52
45795.34	95783.75	45836.70	95487.48	31240.39	33514.92	31186.35	33387.16
45804.08	95783.75	45840.26	95553.03	31245.70	33627.13	31191.14	33610.39
45817.03		45846.02		31306.52	33636.82	31261.98	33615.18
45819.17					33219.08		33219.08

Table 5.7: CASSCF/RASSI computed spin-free and spin-orbit energies for complex **3.3.**

Spin Free Energies of Complex 3.3 (cm^{-1})				Spin-Orbit Energies of Complex 3.3 (cm^{-1})			
Er1		Er2		Er1		Er2	
0.00	33228.54	0.00	33297.79	0.00	23566.59	0.00	23556.08
13.01	33292.81	3.06	33364.48	0.00	23566.59	0.00	23556.08
18.11	33302.57	28.58	33377.44	18.11	23617.44	26.81	23652.65
67.25	43697.15	57.19	43565.71	18.11	23617.44	26.81	23652.65
89.54	43697.90	57.69	43566.30	33.34	25127.75	45.13	25101.63
132.85	43866.44	80.13	43776.48	33.34	25127.75	45.13	25101.63
177.18	43880.02	92.61	43786.85	57.29	25181.16	56.04	25156.58
181.28	43880.81	182.30	43883.54	57.29	25181.16	56.04	25156.58
210.56	43909.28	201.98	43924.81	112.66	25214.54	81.21	25239.70
313.88	43921.19	313.82	43927.73	112.66	25214.54	81.21	25239.70
328.25	43932.49	351.53	43940.55	141.91	25270.90	192.82	25334.76
339.79	43962.49	353.47	43946.08	141.91	25270.90	192.82	25334.76
350.89	44004.80	378.81	43979.32	261.72	27220.45	304.51	27212.65
18174.68	44012.70	18156.59	43991.20	261.72	27220.45	304.51	27212.65
18232.01	44084.86	18211.62	44063.99	283.76	27260.64	329.57	27251.66
18276.63	44088.00	18231.09	44072.09	283.76	27260.64	329.57	27251.66
18333.16	44518.38	18266.39	44120.61	6593.80	27296.94	6584.85	27324.33
18334.74	44518.62	18291.21	44128.40	6593.80	27296.94	6584.85	27324.33
18378.06	44614.80	18322.67	44363.85	6613.93	27525.89	6605.41	27491.53
18419.29	44616.26	18492.07	44366.43	6613.93	27525.89	6605.41	27491.53

18553.29	44732.46	18604.59	44635.78	6623.23	27626.44	6617.87	27700.66
28524.86	44738.67	28526.70	44638.69	6623.23	27626.44	6617.87	27700.66
28580.69	44819.22	28585.26	44870.58	6662.23	27759.49	6654.97	27773.89
28614.13	44850.91	28613.89	44879.56	6662.23	27759.49	6654.97	27773.89
28660.14	44881.83	28650.40	45037.92	6670.15	27808.80	6719.63	27807.40
28681.70	44935.93	28682.67	45051.49	6670.15	27808.80	6719.63	27807.40
28785.51	44943.82	28762.63	45136.84	6758.54	27834.23	6804.10	27835.37
28849.70	45008.51	28841.81	45184.06	6758.54	27834.23	6804.10	27835.37
28864.82	45010.13	28869.45	45216.04	6789.73	27872.06	6837.28	27886.90
28982.18	45075.94	28968.28	45268.04	6789.73	27872.06	6837.28	27886.90
46594.94	45076.62	46403.99	45275.38	10640.23	27892.03	10628.31	27924.21
46697.25	45218.46	46552.96	45377.03	10640.23	27892.03	10628.31	27924.21
46940.58	45218.47	47071.83	45377.24	10653.62	31919.90	10642.75	31809.75
47059.73	50092.30	47166.85	50034.18	10653.62	31919.90	10642.75	31809.75
47182.02	50095.96	47252.21	50034.41	10674.79	31969.48	10671.95	31874.33
18021.66	50153.32	17996.61	50134.09	10674.79	31969.48	10671.95	31874.33
18026.44	50172.54	18003.40	50140.75	10680.05	32016.83	10720.38	31922.35
18034.51	50176.34	18010.42	50182.72	10680.05	32016.83	10720.38	31922.35
18052.66	50177.13	18032.29	50201.30	10740.65	32072.96	10780.33	32051.89
18063.18	50182.14	18046.93	50201.96	10740.65	32072.96	10780.33	32051.89
18067.78	50191.57	18074.44	50222.00	10770.02	32111.94	10811.42	32195.41
18070.05	50195.59	18080.43	50222.74	10770.02	32111.94	10811.42	32195.41
18088.94	50258.03	18082.04	50260.98	13375.80	32211.14	13396.70	32322.42

18110.46	50261.99	18095.92	50265.13	13375.80	32211.14	13396.70	32322.42
18116.78	51318.12	18114.52	51168.91	13437.72	32325.61	13432.29	32446.81
18120.28	51355.28	18115.74	51201.97	13437.72	32325.61	13432.29	32446.81
23859.59	51452.08	23792.75	51532.77	13492.93	32410.36	13495.51	32516.82
23874.02	51575.23	23821.42	51613.93	13492.93	32410.36	13495.51	32516.82
23926.09	51641.62	23857.98	51762.21	13543.11	32680.12	13561.02	32703.40
23960.37	60611.34	23929.93	60547.95	13543.11	32680.12	13561.02	32703.40
23999.29	60696.22	23962.68	60619.91	13565.05	32698.32	13605.50	32720.84
24015.54	60720.55	24053.32	60730.56	13565.05	32698.32	13605.50	32720.84
24018.23	60729.99	24056.71	60748.49	18967.25	32739.80	18950.26	32758.27
24052.37	60752.23	24103.20	60769.01	18967.25	32739.80	18950.26	32758.27
24055.99	60771.70	24103.88	60789.15	18996.07	32816.95	18985.60	32835.10
26943.11	60784.37	26801.36	60816.57	18996.07	32816.95	18985.60	32835.10
26944.15	77070.07	26801.85	76928.52	19033.87	32871.98	19002.26	32895.11
26989.71	77075.88	26856.70	76928.87	19033.87	32871.98	19002.26	32895.11
26994.17	77135.82	26857.43	77100.35	19048.21	32884.45	19067.74	32901.52
27049.05	77169.69	26935.20	77139.43	19048.21	32884.45	19067.74	32901.52
27067.36	77193.60	26935.75	77242.39	19148.25	33205.35	19237.60	33211.61
27076.06	77249.59	27078.47	77271.42	19148.25	33205.35	19237.60	33211.61
27077.76	77262.21	27087.25	77336.96	22621.13	33222.58	22635.62	33227.93
27134.44	77327.56	27220.05	77387.05	22621.13	33222.58	22635.62	33227.93
27187.72	77330.10	27247.31	77404.79	22629.96	33239.14	22651.03	33266.44
27218.09	110240.59	27322.15	109941.63	22629.96	33239.14	22651.03	33266.44

27329.22	110270.19	27417.76	109971.62	22653.10	33251.51	22669.65	33288.19
27337.48	110615.23	27443.02	110650.89	22653.10	33251.51	22669.65	33288.19
27417.77	110652.44	27505.81	110732.30	22687.78	33925.46	22705.05	33930.15
27419.59	110697.59	27512.67	110876.13	22687.78	33925.46	22705.05	33930.15
32991.47	110861.08	32892.87	110976.77	22717.64	33934.74	22738.08	33960.42
33045.25	110879.93	32940.22	111004.43	22717.64	33934.74	22738.08	33960.42
33064.64		32947.29		22722.33	33954.04	22740.90	33975.95
33121.37		33076.15		22722.33	33954.04	22740.90	33975.95

Table 5.8: g-tensors and MMAs of the $^6H_{15/2}$ multiplet within Dy1 of complex **3.1**.

KD	g_x	g_y	g_z	Zm (˚)
1	0.15	0.43	18.46	0.00
2	1.11	1.87	13.33	11.17
3	0.39	2.17	12.06	0.54
4	2.85	4.03	14.03	86.21
5	10.38	6.15	0.75	90.98
6	9.57	6.67	1.13	7.12
7	2.02	3.50	15.60	64.24
8	0.47	0.57	17.87	109.57

Table 5.9: g-tensors and MMAs of the $^6H_{15/2}$ multiplet within Dy2 of complex (**3.1**).

KD	g_x	g_y	g_z	Zm (˚)
1	0.44	1.67	17.31	0.00
2	1.62	1.89	12.20	6.29
3	0.69	3.84	10.89	3.23
4	7.47	6.76	4.71	92.63
5	0.95	2.16	11.56	86.92
6	0.04	0.75	16.94	15.66
7	0.52	0.65	17.40	17.08
8	0.13	0.22	18.39	158.38

Table 5.10: Summary of the physical parameters calculated for averaged pairs of singlet states within the $^7F_6$ multiplet of the Tb1 ion within the (**3.2**) dimer.

KD	g_z	Angle (°)
1	17.69	0.00
2	11.90	10.40
3	12.21	69.96
4	9.06	61.34
5	6.30	54.30
6	4.42	71.69

Table 5.11: Summary of the physical parameters calculated for averaged pairs of singlet states within the $^7F_6$ multiplet of Tb2 within the **3.2** dimer.

KD	g_z	Angle (°)
1	16.82	0.00
2	13.37	15.92
3	8.17	80.29
4	14.02	32.86
5	14.62	43.83
6	17.81	84.28

Table 5.12: Summary of the results for the $^4I_{15/2}$ multiplet of Er1 within complex (**3.3**).

KD	g_x	g_y	g_z	Zm (˚)
1	0.41	2.16	14.14	0.00
2	8.36	6.50	3.44	86.52
3	1.83	2.95	12.35	2.82
4	1.14	3.50	12.65	93.03
5	2.30	2.87	11.23	3.25
6	1.04	4.73	12.28	90.36
7	0.38	1.08	15.53	64.87
8	0.26	1.52	16.12	132.57

Table 5.13: Summary of the results for the $^4I_{15/2}$ multiplet of Er2 within complex (**3.3**).

KD	g_x	g_y	g_z	Zm (˚)
1	0.67	1.74	15.45	0.00
2	0.43	0.80	12.48	20.50
3	1.08	2.69	10.92	157.38
4	0.58	2.07	12.86	30.22
5	3.72	5.34	9.46	78.04
6	0.26	1.28	15.09	70.77
7	1.10	3.78	11.77	90.21
8	0.67	5.25	13.15	1.88

Table 5.14: Computed crystal field parameters, B_q^k, for complexes (**3.1**) – (**3.3**) using the SINGLE_ANISO module of MOLCAS.

		Dy1	Dy2	Tb1	Tb2	Er1	Er2
k	q	B(k,q)	B(k,q)	B(k,q)	B(k,q)	B(k,q)	B(k,q)
2	-2	4.2E-01	-1.8E-01	-2.1E+00	6.6E-01	4.1E-01	-4.3E-01
2	-1	3.5E-01	9.6E-03	2.2E+00	8.1E-02	-4.3E-01	-2.7E-01
2	0	-1.5E+00	-2.2E+00	-2.6E+00	-3.6E+00	-3.9E-01	-9.2E-01
2	1	1.4E-01	-3.6E-01	-1.1E-01	4.5E+00	1.4E+00	-3.6E+00
2	2	1.7E+00	4.8E+00	-2.0E+00	7.3E+00	-9.3E-01	-9.3E-01
4	-4	3.5E-03	-1.1E-02	6.0E-02	4.2E-02	-2.8E-03	-9.3E-03
4	-3	-1.5E-02	-9.2E-03	-7.2E-02	5.9E-02	5.9E-02	3.2E-02
4	-2	-2.9E-03	-6.0E-04	3.6E-02	-1.0E-02	-3.7E-03	2.2E-03
4	-1	-1.2E-02	-3.9E-03	-4.0E-02	-2.4E-04	1.4E-04	9.9E-04
4	0	-1.6E-03	-9.6E-04	2.9E-03	3.2E-03	-2.5E-03	-1.0E-03
4	1	9.9E-04	4.9E-03	7.5E-03	-6.2E-02	-3.3E-03	1.9E-02
4	2	3.4E-02	3.2E-02	7.3E-02	-7.4E-02	7.8E-03	1.5E-02
4	3	3.8E-03	2.9E-03	5.1E-02	1.0E-01	-6.7E-02	4.8E-02
4	4	-3.2E-02	-2.8E-02	5.0E-02	6.2E-02	5.4E-03	8.9E-04
6	-6	1.1E-05	-1.1E-04	-1.7E-04	2.8E-04	-2.5E-04	2.7E-04
6	-5	-6.2E-05	-3.5E-05	-8.1E-05	2.2E-04	-1.1E-03	-8.3E-04
6	-4	3.3E-07	-4.2E-05	-1.3E-04	-6.1E-06	-9.5E-05	1.9E-04
6	-3	5.9E-05	4.7E-05	3.4E-04	-2.6E-04	-2.3E-04	-5.0E-04
6	-2	3.3E-05	-6.4E-05	-1.5E-04	1.0E-04	-1.2E-04	1.0E-04
6	-1	2.0E-04	6.8E-05	2.2E-04	5.3E-05	-1.2E-05	-7.0E-05

6	0	-2.0E-05	-1.9E-05	7.8E-06	-2.9E-06	2.2E-05	1.3E-05
6	1	2.9E-06	-3.5E-05	-1.0E-04	5.0E-04	2.2E-05	3.8E-05
6	2	-1.5E-04	-1.6E-04	-3.8E-04	3.5E-04	2.2E-04	3.3E-05
6	3	4.7E-05	-2.7E-05	-1.7E-04	-4.0E-04	2.8E-04	-2.2E-04
6	4	5.5E-05	6.6E-05	-3.5E-05	-1.8E-04	8.8E-05	-5.3E-05
6	5	6.0E-05	4.7E-05	-1.3E-04	2.1E-04	5.3E-04	2.5E-05
6	6	-6.5E-05	-7.6E-05	-2.5E-05	1.5E-04	1.2E-05	-6.8E-05

Table 5.15: Composition of the CASSCF/RASSI wavefunctions of the $^{6}H_{15/2}$ multiplet for Dy1 of complex (**3.1**).

JM >	w.f. 1	w.f. 2	w.f. 3	w.f. 4
-15/2	0.876292 -0.159287	-0.000000 0.000000	-0.009129 -0.060072	0.002248 0.014795
-13/2	-0.007451 0.023563	-0.009561 0.000955	0.131995 -0.029465	-0.649730 0.081500
-11/2	-0.386778 0.056303	-0.000137 -0.000488	-0.002229 -0.019325	-0.001278 -0.026450
-9/2	-0.012422 0.001924	0.013586 -0.001253	-0.126488 0.028874	0.598504 -0.076516
-7/2	0.208928 -0.037988	0.000501 -0.001803	0.011406 0.076231	-0.002644 -0.104193
-5/2	-0.003990 -0.040131	-0.015560 0.002525	0.066416 -0.017388	-0.334002 0.042970
-3/2	-0.069922 0.007973	0.000620 -0.002736	-0.008628 -0.095351	0.011274 0.083803
-1/2	-0.000001 0.008803	0.030227 -0.000648	-0.013006 0.001322	0.124764 -0.007262
1/2	0.029856 -0.004768	0.001575 0.008661	0.011565 0.124439	0.000647 0.013057
3/2	-0.001099 -0.002581	-0.070221 0.004661	-0.084545 0.001444	-0.095565 0.005796
5/2	-0.015760 0.000299	-0.003251 -0.040197	-0.007699 -0.336667	0.007212 -0.068274
7/2	-0.000816 -0.001684	0.212353 0.000011	0.103407 -0.013041	0.077080 -0.000177
9/2	0.013591 -0.001197	0.012566 -0.000329	0.014274 0.603206	-0.009542 0.129390
11/2	0.000048 -0.000505	-0.390612 0.013777	0.026342 -0.002711	-0.019441 0.000700
13/2	-0.009578 0.000770	0.011545 0.021850	-0.017044 -0.654600	0.009300 -0.134924
15/2	0.000000 0.000000	0.890652 0.000000	-0.014965 0.000000	-0.060761 0.000000
JM >	w.f. 5	w.f. 6	w.f. 7	w.f. 8
-15/2	0.022602 -0.001616	-0.410729 0.029360	0.017455 0.012305	0.052915 0.037302
-13/2	-0.115169 0.005051	0.015015 0.220788	-0.166484 0.150364	-0.145014 0.228309
-11/2	0.030308 -0.007208	-0.527338 0.020644	0.026473 -0.002704	0.127449 0.055411
-9/2	0.052355 -0.006027	0.010571 -0.040628	0.020464 0.064966	-0.063409 0.051566

-7/2	-0.036752 -0.010430	0.594210 -0.032054	-0.121699 -0.096765	-0.164463 -0.196601
-5/2	0.034873 0.000581	0.004116 -0.186965	0.464714 -0.149703	0.021271 -0.295195
-3/2	0.014664 0.042228	-0.269835 -0.002799	-0.185039 0.035518	-0.272887 -0.416339
-1/2	-0.121329 0.004438	-0.009794 0.047181	0.287684 0.003967	-0.241978 0.007521
1/2	-0.013133 -0.046363	0.121337 -0.004224	-0.193441 -0.145569	-0.237417 -0.162514
3/2	0.268949 -0.022031	0.011616 -0.043166	0.462922 -0.183054	-0.130773 -0.135645
5/2	0.017436 0.186196	-0.034743 0.003066	-0.152698 0.253527	-0.293568 -0.390113
7/2	-0.594983 0.010395	-0.035915 0.013024	0.247697 -0.065927	-0.155222 0.008969
9/2	0.013440 0.039771	-0.052652 -0.002279	-0.022115 -0.078681	-0.054158 0.041308
11/2	0.527468 -0.017007	0.030745 0.005029	-0.136094 -0.028144	0.020079 0.017463
13/2	-0.000765 -0.221297	0.115236 -0.003173	0.013022 -0.270156	0.049436 0.218820
15/2	0.411777 0.000000	0.022659 0.000000	-0.064741 0.000000	0.021356 -0.000000
JM >	w.f. 9	w.f. 10	w.f. 11	w.f. 12
-15/2	0.044402 0.091353	0.005089 0.010470	-0.013225 -0.119972	0.000308 0.002791
-13/2	-0.368237 0.176979	0.274886 -0.004153	-0.121031 -0.045715	-0.229585 0.067251
-11/2	0.161399 0.301497	-0.028374 0.041955	0.006205 -0.554854	0.039440 -0.008254
-9/2	-0.210449 0.086637	0.278752 0.018641	-0.297695 -0.035502	-0.340770 0.095632
-7/2	0.019888 0.087934	-0.045104 0.019662	0.010598 -0.374203	0.020028 -0.028629
-5/2	0.298083 -0.132790	0.065880 0.052946	0.004114 0.025423	0.013116 0.014448
-3/2	0.013483 0.235650	-0.043688 -0.006606	-0.023673 0.413941	-0.082394 -0.006623
-1/2	-0.161137 0.100127	0.528380 0.025851	0.034871 -0.033506	0.238147 -0.081101
1/2	0.254231 0.463918	-0.019613 0.188695	0.054518 -0.245600	-0.029483 0.038332
3/2	0.025040 0.036404	0.217835 -0.090888	-0.015611 -0.081172	-0.408855 0.068887

5/2	0.076418 0.036106	-0.010877 -0.326142	-0.015798 -0.011454	0.025721 0.001304
7/2	0.002034 0.049161	0.087781 -0.020553	-0.026262 0.023044	0.370789 -0.051537
9/2	0.138621 0.242557	0.014078 0.227149	-0.057717 0.349197	-0.067908 -0.292013
11/2	-0.025330 0.043860	0.341719 0.013361	-0.003883 0.040107	0.550834 -0.066965
13/2	0.116431 0.249045	0.001801 0.408554	-0.041689 0.235571	-0.058701 -0.115293
15/2	-0.011641 0.000000	0.101572 -0.000000	0.002808 0.000000	0.120698 0.000000
JM >	w.f. 13	w.f. 14	w.f. 15	w.f. 16
-15/2	-0.038070 -0.021956	0.005924 0.003417	-0.032955 0.003001	0.000851 -0.000077
-13/2	-0.011012 -0.127824	-0.058367 0.129419	-0.028180 -0.017787	-0.108588 -0.022002
-11/2	-0.238009 -0.115979	0.054733 -0.028200	-0.204230 -0.029916	0.028456 0.017382
-9/2	-0.005962 -0.192948	-0.128851 0.331000	-0.089106 0.025948	-0.262216 -0.130793
-7/2	-0.431398 -0.095254	0.084792 -0.065909	-0.316791 -0.181731	0.007934 0.024164
-5/2	0.026560 -0.133529	0.011476 0.466202	-0.131973 0.013170	-0.166006 -0.349317
-3/2	-0.310604 0.200234	-0.144101 -0.003888	0.012177 -0.461890	-0.002628 -0.115533
-1/2	-0.081280 0.143093	0.311320 0.003675	0.142290 0.020864	0.504640 -0.209607
1/2	0.271519 0.152353	-0.001080 0.164563	0.521570 0.162977	-0.139811 0.033682
3/2	0.126771 0.068625	-0.169025 -0.328632	-0.007861 -0.115295	0.054016 0.458882
5/2	0.242856 -0.398117	0.043704 -0.128939	-0.133642 0.362932	0.132624 0.001147
7/2	-0.040524 -0.099456	-0.421290 -0.133013	-0.005709 0.024784	-0.299005 0.209712
9/2	0.053750 -0.351105	0.101562 -0.164164	-0.249274 0.154034	0.091092 0.017760
11/2	-0.033324 -0.051773	-0.264119 -0.018443	-0.026762 0.019891	-0.200676 0.048314
13/2	0.014098 -0.141270	0.073401 -0.105226	-0.106145 0.031759	0.026451 -0.020269
15/2	-0.006839 0.000000	-0.043948 0.000000	-0.000854 0.000000	-0.033091 0.000000

Table 5.16: Composition of the CASSCF/RASSI wavefunctions of the $^{6}H_{15/2}$ multiplet for Dy2 of complex (**3.1**).

JM >	w.f. 1	w.f. 2	w.f. 3	w.f. 4
-15/2	-0.810073 -0.112436	0.000000 0.000000	-0.061052 0.113473	0.012128 -0.022542
-13/2	0.008076 -0.014232	-0.033699 -0.002807	-0.224895 -0.042358	-0.591405 -0.008803
-11/2	0.470137 0.021620	0.001028 0.000221	0.002787 -0.001914	0.014660 0.000944
-9/2	-0.007714 -0.001119	0.044015 0.004190	0.220683 0.040891	0.579789 0.011280
-7/2	-0.285544 -0.045466	-0.000351 -0.001909	0.027609 -0.065782	-0.005450 -0.021507
-5/2	-0.004828 0.017369	-0.045611 -0.006146	-0.128538 -0.039387	-0.354011 -0.043869
-3/2	0.124939 0.029079	-0.001498 -0.000075	-0.047326 0.098092	-0.003073 0.005250
-1/2	0.004136 -0.008033	0.060218 0.000118	0.045766 0.019021	0.166794 0.023895
1/2	-0.059663 -0.008162	0.002992 0.008525	0.057986 -0.158205	-0.004934 0.049315
3/2	-0.001494 -0.000132	-0.127751 0.011627	0.006079 -0.000219	-0.108806 -0.004800
5/2	0.046023 0.000183	-0.002394 -0.017868	-0.129100 0.332538	0.026216 -0.131856
7/2	-0.000610 0.001843	0.289083 -0.005778	-0.016358 -0.014989	0.071011 0.006854
9/2	-0.044173 -0.001901	-0.007795 0.000048	0.264774 -0.515924	-0.068551 0.213714
11/2	0.001049 -0.000077	-0.468645 -0.043220	-0.006114 0.013358	0.003006 -0.001547
13/2	0.033764 0.001853	0.006043 0.015207	-0.272458 0.524979	0.069255 -0.218119
15/2	0.000000 0.000000	0.817839 0.000000	-0.025598 0.000000	-0.128854 0.000000
JM >	w.f. 5	w.f. 6	w.f. 7	w.f. 8
-15/2	0.012255 0.006547	0.451879 0.241399	-0.106195 0.094675	-0.012693 0.011316
-13/2	-0.194871 0.005088	0.047609 -0.084554	-0.182246 -0.096281	0.556082 -0.053331
-11/2	0.013215 0.004262	0.385855 0.192541	-0.212048 0.224580	-0.025805 0.031384
-9/2	0.093560 -0.006609	-0.024072 0.024223	-0.041644 -0.033452	0.177739 0.014362

-7/2	-0.012665	-0.017862	-0.522166	-0.249135	0.080763	-0.101576	0.007533	0.024242
-5/2	0.052915	-0.006067	-0.029451	0.029508	0.152282	0.075669	-0.510999	0.037741
-3/2	0.011877	0.020424	0.297106	0.183073	0.146516	-0.144606	-0.017906	-0.063348
-1/2	-0.173255	0.011659	0.031942	-0.022608	-0.086295	-0.082368	0.351154	0.004149
1/2	-0.017521	-0.034992	-0.147322	-0.091919	-0.259352	0.236776	-0.009601	0.118908
3/2	0.348319	-0.021482	-0.020100	0.012419	0.028790	0.059201	-0.205594	-0.010438
5/2	0.012073	0.039904	0.043814	0.030284	0.406541	-0.311878	0.063313	-0.157819
7/2	-0.577957	-0.026295	0.019588	-0.009787	-0.010509	-0.023108	-0.127879	-0.022075
9/2	0.009819	0.032708	0.079408	0.049914	-0.123113	0.128998	-0.008824	0.052682
11/2	0.431060	0.011985	-0.013665	-0.002468	-0.040146	-0.006254	0.307729	0.026524
13/2	-0.002151	-0.097012	-0.169485	-0.096310	-0.450567	0.330243	-0.071963	0.193145
15/2	0.512317	0.000000	-0.013894	0.000000	-0.017005	0.000000	0.142270	0.000000
JM >	w.f. 9		w.f. 10		w.f. 11		w.f. 12	
-15/2	-0.133010	0.016219	-0.068401	0.008341	0.021066	-0.000870	0.051204	-0.002114
-13/2	-0.153646	0.006967	0.300702	0.008916	0.154335	0.094200	-0.030444	-0.051815
-11/2	-0.457715	0.128235	-0.232714	0.067545	0.118869	-0.039993	0.229049	-0.076552
-9/2	-0.170020	0.022313	0.345657	0.034400	0.345545	0.155357	-0.036719	-0.133772
-7/2	-0.189195	0.005282	-0.092718	0.024472	0.217542	0.019946	0.256658	-0.116045
-5/2	0.061220	-0.049382	-0.168725	0.000342	0.273972	0.150051	0.162537	-0.009628
-3/2	0.452269	-0.137750	0.208983	-0.063768	0.074462	0.365449	-0.040580	-0.105168
-1/2	0.179143	-0.034982	-0.209643	0.014373	-0.169443	0.065362	0.334309	0.419633
1/2	-0.209841	0.011109	-0.182061	-0.013041	-0.316712	0.433068	-0.171996	-0.058316
3/2	-0.215165	-0.038003	0.465618	0.081992	-0.036206	0.106753	-0.059322	0.368210

5/2	-0.167526 0.020084	-0.066747 -0.041609	-0.162796 -0.002914	0.267548 -0.161226
7/2	0.094999 0.013069	-0.188443 0.017658	0.261228 0.105358	-0.216534 0.028904
9/2	0.338951 -0.075987	0.171471 0.001569	0.031169 -0.135173	0.338842 -0.169480
11/2	0.239179 0.038880	-0.469871 -0.071888	0.232012 0.067037	-0.120418 -0.035055
13/2	0.297411 -0.045249	0.153359 -0.011682	0.028280 -0.053027	0.150317 -0.100487
15/2	0.068908 0.000000	-0.133995 0.000000	0.051248 -0.000000	-0.021084 0.000000
JM >	w.f. 13	w.f. 14	w.f. 15	w.f. 16
-15/2	0.044512 0.029106	0.018918 0.012370	-0.034038 -0.020430	-0.000296 -0.000177
-13/2	-0.069897 0.022627	0.156589 0.006457	0.019989 0.002714	-0.092938 -0.070310
-11/2	0.269609 0.068572	0.088310 0.036273	-0.222020 -0.023140	0.004821 0.000015
-9/2	-0.180710 0.009470	0.329791 -0.049179	0.072113 0.011694	-0.301046 -0.118217
-7/2	0.410344 0.118863	0.055277 -0.021801	-0.444781 0.033641	0.022288 0.023270
-5/2	-0.136227 -0.157749	0.282053 -0.133223	0.117591 0.006495	-0.486479 -0.078631
-3/2	0.190026 0.152704	-0.038753 -0.294538	-0.438454 0.195305	0.026977 0.026880
-1/2	0.215443 -0.399354	0.061105 -0.228401	0.059186 -0.034767	-0.298984 0.204911
1/2	-0.073858 0.224602	0.038245 -0.452147	0.150901 0.329559	0.032855 0.060269
3/2	0.193629 -0.225304	0.242614 -0.023808	0.036963 -0.009164	0.275428 0.393098
5/2	0.163153 0.265863	0.200348 -0.057473	0.457580 0.182935	0.104167 0.054946
7/2	-0.034333 -0.048498	0.408488 0.125091	0.031085 -0.008482	0.364049 0.257740
9/2	0.249103 0.221649	0.146063 0.106825	0.318959 0.053565	0.067849 0.027084
11/2	-0.093762 -0.017972	0.263176 0.090161	0.004141 0.002468	0.202271 0.094416
13/2	0.134591 0.080294	0.046117 0.057190	0.115870 -0.012456	0.018536 0.007960
15/2	-0.022603 0.000000	0.053183 0.000000	-0.000345 0.000000	0.039698 0.000000

Table 5.17: Composition of the CASSCF/RASSI wavefunctions of the $^7F_6$ multiplet for Tb1 of complex (**3.2**).

JM >	w.f. 1	w.f. 2	w.f. 3	w.f. 4
-6	-0.006452 -0.642066	0.011137 0.658677	-0.016256 -0.033957	-0.015936 -0.069909
-5	0.014406 -0.000768	-0.019991 -0.003507	0.590205 -0.041900	0.623987 0.030854
-4	-0.070930 0.264138	0.074023 -0.235390	0.002871 -0.103580	0.000727 -0.136586
-3	0.052730 0.031348	-0.048436 -0.026213	-0.292643 0.012359	-0.216084 -0.055849
-2	-0.048185 -0.027810	0.034217 -0.021871	-0.037312 0.122460	-0.027250 0.120679
-1	-0.040239 -0.011617	-0.003517 0.001964	-0.077326 -0.166003	-0.065740 -0.084485
0	0.063628 -0.064270	-0.004783 -0.004703	-0.053917 -0.033965	-0.085110 0.106694
1	-0.012021 -0.040120	-0.001905 0.003550	0.183119 -0.001936	-0.096983 -0.045319
2	0.028293 0.047903	-0.021289 0.034582	0.094343 -0.086534	-0.111604 0.053389
3	0.031876 0.052412	0.027028 0.047986	0.115217 0.269291	-0.102477 -0.198267
4	-0.263412 0.073580	-0.234105 0.077992	-0.092186 0.047316	0.133009 -0.031065
5	-0.000623 0.014413	0.003844 0.019929	-0.217062 -0.550438	0.168764 0.601524
6	0.642098 0.000000	0.658771 0.000000	-0.037647 0.000000	0.071703 0.000000
JM >	w.f. 5	w.f. 6	w.f. 7	w.f. 8
-6	-0.066233 -0.212138	0.018436 0.034154	0.101318 0.172237	0.004697 0.074417
-5	-0.173226 0.021660	0.296919 0.013863	0.087594 -0.081411	-0.021640 -0.202598
-4	-0.069054 -0.346464	-0.019238 0.076488	0.164923 0.530167	-0.182400 0.173794
-3	-0.014629 -0.002412	0.184083 -0.200655	0.020652 0.031065	0.196805 -0.437725
-2	0.136244 0.301572	0.060216 -0.170576	-0.122421 -0.264627	-0.128957 0.150027
-1	0.269085 0.068512	-0.084210 0.494817	-0.073771 -0.171886	-0.053458 -0.255578
0	-0.275978 0.375282	0.257960 0.153898	-0.155760 -0.089086	-0.220313 0.234656

1	0.145594 0.236438	-0.395430 0.309145	0.185557 -0.023566	-0.258438 -0.037253
2	-0.328472 -0.040175	-0.121501 0.134014	-0.290161 0.028655	-0.141607 0.138151
3	-0.006662 -0.013245	0.089132 -0.257302	-0.037247 -0.002050	-0.424460 0.223985
4	0.351299 -0.037340	0.058169 -0.053261	0.540587 -0.126658	-0.161959 0.192984
5	-0.030951 -0.171810	-0.153238 -0.254698	0.025758 -0.116777	-0.203559 -0.008836
6	0.222237 0.000000	0.038812 0.000000	0.199828 0.000000	-0.074565 0.000000
JM >	w.f. 9	w.f. 10	w.f. 11	w.f. 12
-6	-0.011755 0.148501	-0.075477 -0.130508	0.061548 -0.044011	-0.003336 -0.001506
-5	0.027207 -0.007739	-0.198829 -0.043106	0.199398 0.033471	0.019721 -0.022513
-4	-0.237631 0.243912	-0.095088 -0.346564	0.205439 -0.165045	0.031675 0.065927
-3	0.123947 -0.110356	-0.308320 -0.181271	0.500451 0.204648	-0.252788 0.140748
-2	-0.198993 0.517205	0.006991 -0.224973	0.272017 -0.084882	0.055663 -0.155730
-1	0.135095 0.070648	-0.256197 -0.181662	0.055267 0.029048	0.611826 -0.014288
0	0.053997 0.058440	0.121395 -0.210441	0.108750 -0.034881	-0.124760 -0.026855
1	-0.059767 -0.140248	-0.285519 -0.130831	-0.028060 0.055775	-0.551763 -0.264751
2	0.531295 -0.157560	0.191250 -0.118682	0.270640 -0.089175	-0.013341 0.164840
3	0.119792 -0.114853	-0.311275 -0.176148	-0.288048 0.457559	0.172491 0.232290
4	0.261903 -0.217643	0.347610 -0.091190	0.263111 0.014758	0.055995 -0.047056
5	0.009862 -0.026511	-0.136856 -0.150537	-0.142728 0.143208	-0.008712 -0.028633
6	0.148965 0.000000	0.150762 0.000000	0.075665 0.000000	-0.003660 0.000000
JM >	w.f. 13			
-6	0.008411 0.007521			
-5	-0.014300 0.012424			

-4	-0.060062 -0.092898
-3	0.141053 0.010139
-2	0.054074 0.477436
-1	-0.065444 -0.128206
0	0.234301 -0.613581
1	-0.134240 0.051955
2	-0.358535 0.319878
3	0.111910 0.086458
4	0.106694 -0.029221
5	-0.002379 -0.018794
6	-0.011283 0.000000

Table 5.18: Composition of the CASSCF/RASSI wavefunctions of the $^7F_6$ multiplet for Tb2 of complex (**3.2**).

JM >	w.f. 1	w.f. 2	w.f. 3	w.f. 4
-6	0.687738 0.119023	-0.690841 -0.118508	-0.003141 -0.009802	-0.006397 0.004982
-5	0.002093 -0.008838	-0.003212 0.006155	0.096599 0.533096	-0.633807 -0.261818
-4	0.044712 0.041592	-0.046106 -0.031039	-0.053586 -0.073480	0.128841 0.026268
-3	-0.047837 -0.028777	0.047027 0.022886	-0.171955 0.052378	0.044144 -0.049755
-2	-0.044603 -0.041531	0.026798 0.038924	0.154603 -0.155616	0.022276 0.056914
-1	0.035531 0.014594	-0.015050 -0.006864	0.181574 -0.190795	-0.034423 0.054133
0	0.038139 0.003276	0.002127 -0.024983	-0.183195 0.251068	-0.013965 0.004797
1	-0.037499 0.008321	-0.015994 0.004221	-0.126292 0.231133	0.060421 0.021555
2	-0.051032 0.033316	-0.032993 0.033833	0.101020 -0.194714	-0.017398 -0.058590

3	0.052044 -0.020198	0.050219 -0.014605	-0.002589 -0.179736	-0.065400 -0.012128
4	0.051150 -0.033358	0.050690 -0.022797	0.086326 0.028609	0.085506 -0.099894
5	-0.000555 -0.009066	-0.002125 -0.006609	0.537148 -0.070673	0.339151 -0.596017
6	0.697961 0.000000	0.700932 0.000000	0.010293 0.000000	-0.008108 0.000000
JM >	w.f. 5	w.f. 6	w.f. 7	w.f. 8
-6	0.097445 0.003963	-0.035423 -0.013954	0.077122 0.022184	0.035211 0.033813
-5	0.007621 0.018654	-0.284231 -0.296826	-0.118995 -0.096504	-0.076736 -0.079920
-4	-0.077012 -0.267050	0.063573 0.195868	-0.398667 -0.350251	-0.409756 -0.435636
-3	0.195993 0.072248	-0.128124 0.182196	0.236070 0.234019	0.114703 0.063059
-2	0.303192 0.112521	0.063413 -0.304496	0.166277 0.087842	-0.157574 0.130667
-1	-0.442396 -0.037022	0.087309 -0.228946	-0.090100 -0.185332	0.178901 0.059652
0	-0.367433 -0.007469	-0.075014 0.395092	-0.002436 0.017281	0.238558 0.095994
1	0.443535 -0.019013	-0.002679 0.245014	-0.137823 0.153202	-0.170356 -0.080887
2	0.307515 -0.100107	0.052603 -0.306548	-0.184080 0.038453	-0.023151 -0.203390
3	-0.198767 0.064223	-0.052430 -0.216477	0.291563 -0.159639	-0.126411 -0.033964
4	-0.087801 0.263700	-0.130937 0.158937	0.479956 -0.226392	-0.597289 0.030407
5	-0.008373 0.018329	-0.373244 0.171995	-0.141036 0.059848	0.110704 -0.004495
6	0.097526 0.000000	0.038072 0.000000	-0.080249 0.000000	0.048817 0.000000
JM >	w.f. 9	w.f. 10	w.f. 11	w.f. 12
-6	0.005654 0.015412	-0.019080 -0.019163	0.001481 0.016156	-0.006865 -0.007362
-5	-0.098633 -0.052824	-0.004303 -0.078830	-0.028467 0.085047	-0.020790 -0.049458
-4	-0.189896 0.041335	0.070035 -0.324729	-0.045146 0.166953	-0.030021 -0.088594
-3	-0.278457 0.463360	-0.075320 -0.144582	-0.298998 0.458058	0.009612 -0.304495

-2	0.249067 -0.211119	0.134542 -0.507545	0.151531 0.007458	-0.059359 -0.180856
-1	0.175291 -0.126490	-0.166734 0.229344	-0.180272 0.229974	0.166300 -0.568115
0	-0.072120 -0.050362	0.002233 0.000928	0.221848 -0.243121	-0.121787 -0.052951
1	0.058376 -0.208132	-0.044879 0.279973	0.212552 -0.200518	0.302052 -0.509092
2	-0.112417 0.306542	-0.264735 0.453452	-0.021263 -0.150217	-0.172748 0.079939
3	-0.339102 0.421012	0.155600 -0.048639	0.428842 -0.339575	0.216129 -0.214705
4	-0.026599 -0.192514	-0.180700 0.278750	-0.162133 0.060203	-0.085266 0.038469
5	0.083563 0.074404	0.058898 -0.052571	0.082092 -0.036114	0.050349 -0.018527
6	0.016417 0.000000	-0.027042 0.000000	-0.016224 0.000000	-0.010066 0.000000

JM >	w.f. 13
-6	0.009305 0.011697
-5	0.015794 0.033403
-4	0.014495 0.147256
-3	0.037310 0.155897
-2	-0.093664 0.461816
-1	0.078860 0.143071
0	-0.276185 0.572620
1	0.161059 -0.027354
2	-0.303100 0.360802
3	0.145230 -0.067855
4	-0.124264 0.080330
5	0.035973 -0.008435
6	-0.014947 0.000000

Table 5.19: Composition of the CASSCF/RASSI wavefunctions of the $^4I_{15/2}$ multiplet for Er1 of complex (**3.3**).

JM >	w.f. 1	w.f. 2	w.f. 3	w.f. 4
-15/2	-0.007856 0.002352	0.717526 -0.214780	0.004075 0.002706	-0.108063 -0.071762
-13/2	-0.056867 -0.021889	-0.030738 0.035142	-0.356560 -0.086102	0.428482 0.069753
-11/2	0.033597 -0.010860	-0.364034 0.350286	0.093165 -0.002619	0.088811 -0.027805
-9/2	0.011743 0.014315	0.027233 -0.050203	0.246305 -0.057367	-0.173212 0.030749
-7/2	-0.098829 0.062905	-0.063815 0.153945	-0.208938 0.090027	-0.029296 0.054653
-5/2	0.063108 -0.054735	-0.042875 0.322489	0.193614 -0.102922	-0.205340 0.166628
-3/2	0.005611 0.042543	0.011489 -0.086778	0.123003 -0.163183	-0.194108 0.291935
-1/2	-0.018813 0.070375	0.015144 0.060355	-0.151406 0.316453	-0.010360 0.293999
1/2	-0.002800 -0.062163	0.038204 0.062025	0.154010 -0.250646	-0.048935 0.347378
3/2	-0.035892 -0.079839	-0.006824 -0.042365	0.000202 0.350577	0.012194 0.203985
5/2	-0.133552 -0.296650	-0.076153 -0.034339	-0.078879 -0.252404	-0.104353 -0.192847
7/2	0.105281 0.129180	-0.112717 -0.031923	-0.005829 0.061735	-0.124252 -0.190582
9/2	0.040486 0.040285	-0.007145 0.017082	-0.127283 -0.121437	-0.173448 -0.184046
11/2	0.449194 0.231183	0.035300 0.000769	-0.058602 -0.072294	0.076162 0.053720
13/2	-0.039525 -0.024851	0.048202 -0.037277	0.395533 0.178930	0.344663 0.125523
15/2	-0.748982 0.000000	-0.008201 0.000000	0.129720 0.000000	0.004892 0.000000
JM >	w.f. 5	w.f. 6	w.f. 7	w.f. 8
-15/2	-0.027034 -0.156295	0.001866 0.010790	0.042698 0.265696	0.000578 0.003596
-13/2	-0.053673 -0.309842	0.086511 -0.074229	-0.109729 -0.398911	0.230293 -0.012690
-11/2	0.059893 0.152551	0.091687 -0.060638	0.100396 0.187379	-0.054563 -0.000023
-9/2	0.208500 0.201144	-0.118682 0.083064	-0.054697 -0.029758	0.199442 -0.087942

-7/2	-0.014797 -0.031886	-0.248033 0.248854	-0.216975 -0.132677	0.068493 -0.031388
-5/2	-0.084044 -0.042446	0.010255 0.037016	0.236658 0.093074	-0.073059 0.103533
-3/2	0.356048 0.035385	-0.005749 0.194675	-0.552002 -0.046985	0.078662 -0.150551
-1/2	-0.216020 0.027774	-0.025209 0.608223	0.100322 0.005124	-0.011471 0.326456
1/2	-0.595028 0.128503	-0.009449 -0.217593	-0.320501 0.063124	0.020977 0.098239
3/2	0.190847 -0.038844	-0.095551 -0.344808	-0.136163 0.101552	0.133973 0.537555
5/2	-0.038222 -0.003796	-0.056149 -0.075580	-0.090629 0.088560	0.129445 0.218892
7/2	0.202939 -0.286817	0.033942 0.009146	-0.020123 0.072606	0.165423 0.193175
9/2	-0.061621 0.131102	0.233737 0.171168	0.055184 -0.210869	-0.038059 -0.049283
11/2	-0.044124 0.100681	-0.160527 -0.033017	-0.008680 -0.053868	-0.200935 -0.069394
13/2	0.058398 -0.097897	-0.314457 -0.000080	-0.024010 -0.229389	-0.411268 -0.045046
15/2	0.010951 0.000000	0.158616 0.000000	0.003643 0.000000	-0.269105 0.000000
JM >	w.f. 9	w.f. 10	w.f. 11	w.f. 12
-15/2	-0.241776 0.006648	-0.039823 0.001095	-0.123652 -0.496183	-0.001697 -0.006810
-13/2	-0.167943 0.033361	0.439064 0.070766	-0.125548 -0.195425	0.121631 0.011515
-11/2	-0.141316 0.091630	-0.214387 0.021826	-0.366538 -0.428863	-0.057057 -0.008305
-9/2	-0.097911 0.054496	0.504396 -0.145566	0.014494 0.003221	0.146227 -0.026844
-7/2	0.006549 0.034205	-0.236784 0.120512	-0.363421 -0.140831	-0.145832 0.078523
-5/2	-0.096123 0.169612	0.327302 -0.298672	-0.216839 -0.014399	0.166093 -0.151542
-3/2	0.000718 -0.084311	-0.029614 0.024126	-0.192171 -0.004982	-0.043258 0.058460
-1/2	-0.020888 -0.119048	0.059040 -0.130542	0.042233 -0.038161	0.007839 -0.054750
1/2	-0.062606 -0.128870	-0.017608 0.119577	-0.051230 0.020846	0.026816 -0.050208
3/2	-0.030266 -0.023303	-0.003036 -0.084259	-0.046265 0.056110	-0.051303 -0.185263

5/2	-0.335388 -0.289563	-0.100748 -0.166906	-0.106882 0.197809	0.066405 0.206923
7/2	-0.240007 -0.113959	-0.005606 0.034372	-0.040929 0.160492	-0.224531 -0.318581
9/2	-0.508206 -0.131647	-0.099372 -0.051785	0.009312 0.148378	-0.006630 -0.013285
11/2	-0.214906 -0.015925	0.143781 0.087711	0.021855 0.053356	-0.504769 -0.251957
13/2	-0.436953 0.082808	-0.168796 -0.028732	0.040585 0.115237	0.219985 0.074567
15/2	-0.039839 0.000000	0.241867 -0.000000	0.007019 0.000000	-0.511359 0.000000
JM >	w.f. 13	w.f. 14	w.f. 15	w.f. 16
-15/2	0.001089 0.004963	-0.008870 -0.040409	-0.011712 0.028692	0.003299 -0.008081
-13/2	-0.031229 0.021499	-0.126354 -0.074595	-0.001271 0.116228	0.038766 -0.029826
-11/2	0.147268 0.013986	-0.197591 -0.235883	0.218315 0.200234	-0.194391 -0.023743
-9/2	0.284681 -0.097742	0.224356 -0.270236	0.154790 -0.194790	-0.366921 0.155586
-7/2	0.045257 -0.065968	0.526262 -0.061547	-0.314647 -0.249618	0.040714 0.081274
-5/2	-0.241220 0.173540	0.205372 0.197569	-0.265926 0.114630	0.200712 -0.228768
-3/2	0.031174 0.154373	-0.232395 0.273394	0.130768 0.115988	0.091895 -0.284163
-1/2	-0.028835 -0.114439	-0.109232 0.093282	0.395596 -0.010888	0.034147 0.112398
1/2	-0.067695 0.126691	-0.117960 -0.003630	-0.091156 -0.074093	-0.159591 0.362140
3/2	0.217213 -0.285605	-0.157467 0.002647	-0.297818 -0.022316	-0.057964 -0.164905
5/2	-0.237005 -0.158239	0.117789 -0.272816	0.287657 -0.099365	0.206631 -0.202880
7/2	0.052710 0.527220	0.054731 -0.058348	0.059859 0.068411	0.112187 0.385649
9/2	0.215852 -0.277076	-0.034436 0.299017	-0.282720 0.280905	-0.238843 0.069692
11/2	-0.272760 -0.142425	-0.045233 -0.140846	0.051486 -0.188947	-0.102874 -0.277799
13/2	0.099950 0.107423	0.014304 -0.035112	0.042265 -0.024618	0.108088 0.042750
15/2	-0.041371 0.000000	-0.005081 0.000000	-0.008728 0.000000	-0.030990 0.000000

Table 5.20: Composition of the CASSCF/RASSI wavefunctions of the $^4I_{15/2}$ multiplet for Er2 of complex (**3.3**).

JM >	w.f. 1	w.f. 2	w.f. 3	w.f. 4
-15/2	0.030067 -0.026662	0.582144 -0.516214	-0.309594 0.192334	-0.001218 0.000756
-13/2	-0.067537 0.010786	-0.179447 0.231392	-0.465201 0.408059	-0.353497 0.003745
-11/2	-0.008912 -0.002741	-0.375124 0.262884	-0.062512 0.033539	0.002758 -0.071903
-9/2	0.060104 -0.010241	-0.006069 0.166374	0.082908 -0.298708	0.223781 -0.061400
-7/2	0.057092 -0.007314	0.006992 -0.108477	0.122323 -0.238679	0.145389 -0.049740
-5/2	0.029383 0.017280	0.168375 0.029991	0.187619 0.026986	0.021900 0.009089
-3/2	-0.018646 -0.055379	0.073204 -0.076902	-0.014973 -0.033625	-0.152433 -0.103607
-1/2	-0.026528 0.017100	-0.001411 0.004573	-0.050540 0.117287	-0.118657 0.036762
1/2	-0.004090 -0.002485	0.031193 -0.004806	0.120190 -0.031389	-0.104823 -0.072957
3/2	-0.105794 -0.008970	0.022791 0.053806	-0.074808 0.168446	-0.005026 -0.036463
5/2	0.106081 -0.134151	-0.010520 0.032424	-0.013806 0.019277	0.145129 -0.121929
7/2	-0.077202 -0.076524	0.047569 -0.032406	0.149746 -0.034472	-0.229857 -0.138191
9/2	-0.114925 -0.120455	-0.051765 0.032214	-0.222487 0.065935	0.228054 0.209980
11/2	0.455085 -0.052192	-0.004849 0.007964	0.040287 0.059621	0.070798 -0.004499
13/2	-0.287784 -0.054071	0.057688 -0.036738	0.302247 -0.183361	-0.610489 -0.101129
15/2	-0.778055 0.000000	0.040186 0.000000	-0.001433 0.000000	0.364473 0.000000
JM >	w.f. 5	w.f. 6	w.f. 7	w.f. 8
-15/2	0.370132 -0.108092	-0.000132 0.000039	0.057132 -0.059662	-0.072066 0.075258
-13/2	0.252306 0.084339	0.180562 0.039038	-0.015235 0.146861	-0.221603 0.165215
-11/2	0.359928 -0.271982	0.073534 0.057266	0.063292 -0.026478	-0.010770 0.139787
-9/2	0.399652 -0.222055	-0.094835 0.077515	-0.001263 0.045382	0.011312 0.282514

-7/2	0.150466 -0.150146	-0.091849 0.142979	-0.180365 0.295291	-0.132914 0.283586
-5/2	-0.092035 0.002418	0.001182 0.228071	-0.145732 0.402574	-0.179106 0.246851
-3/2	-0.332897 -0.126993	0.022746 0.014694	-0.231997 0.168057	-0.287643 0.157720
-1/2	-0.172633 -0.056534	-0.029974 0.118510	-0.094174 0.286138	-0.053573 0.017904
1/2	-0.061994 -0.105356	0.149864 -0.102660	0.049984 -0.026311	-0.271799 -0.129882
3/2	-0.017715 0.020481	-0.283950 0.215221	-0.312855 0.098670	0.281835 -0.051330
5/2	-0.062799 -0.219258	0.089023 -0.023479	0.302164 0.041366	-0.391554 -0.173173
7/2	0.128247 0.111499	0.186523 0.101946	-0.296749 -0.100137	0.338021 0.073959
9/2	-0.112762 -0.047822	-0.445875 -0.101119	0.196225 0.203563	-0.033651 -0.030475
11/2	-0.054532 0.075584	0.421740 0.160180	-0.108411 -0.088901	-0.062898 0.027400
13/2	0.162380 -0.088089	-0.218547 0.151686	0.272594 -0.045789	-0.116609 -0.090569
15/2	0.000138 0.000000	0.385593 0.000000	-0.104198 0.000000	-0.082605 0.000000
JM >	w.f. 9	w.f. 10	w.f. 11	w.f. 12
-15/2	-0.092133 -0.117513	0.006575 0.008386	-0.245204 0.065657	-0.003762 0.001007
-13/2	-0.008867 0.219111	0.026106 -0.103084	0.341633 0.123746	-0.008956 -0.004499
-11/2	-0.184472 -0.310516	0.146668 0.043734	-0.471897 -0.248372	0.024740 0.017614
-9/2	-0.022466 -0.177298	-0.077363 -0.001799	0.233205 0.288142	-0.047682 0.017006
-7/2	-0.061923 0.282063	-0.055407 -0.174163	0.047824 -0.161180	-0.055145 -0.056822
-5/2	0.098712 0.120014	0.192960 0.138297	-0.034908 0.247013	0.075261 0.033227
-3/2	-0.106900 -0.167532	0.243392 -0.096837	0.007079 -0.424314	0.123769 0.012649
-1/2	0.375432 -0.442738	-0.198020 0.211652	-0.139873 0.232308	-0.024169 0.070190
1/2	0.044385 -0.286424	0.116778 -0.568621	0.041501 0.061550	-0.195200 -0.188224
3/2	-0.073966 -0.251289	-0.197799 0.019240	0.116286 -0.044231	-0.116587 -0.408044

5/2	0.227891 0.066523	-0.155352 -0.003635	-0.064106 0.051563	-0.097610 -0.229579
7/2	0.171246 -0.063855	0.183767 -0.222764	-0.038571 0.069152	-0.087886 -0.143325
9/2	-0.049149 -0.059772	0.153389 -0.091713	0.050458 0.004094	0.150741 -0.338655
11/2	-0.124911 -0.088438	-0.358184 0.046415	0.019342 -0.023414	0.391597 -0.361977
13/2	-0.065016 0.084147	-0.166962 0.142169	0.007487 -0.006662	0.298000 -0.207899
15/2	-0.010657 0.000000	-0.149324 0.000000	-0.003895 0.000000	0.253842 0.000000
JM >	w.f. 13	w.f. 14	w.f. 15	w.f. 16
-15/2	0.005831 -0.021670	0.012038 -0.044737	0.035939 -0.054834	0.000000 -0.000000
-13/2	-0.034883 -0.057637	0.010401 0.019880	0.017083 -0.011220	-0.017630 -0.035852
-11/2	0.265796 0.050156	-0.031301 0.021775	0.035335 0.093033	0.140034 -0.001221
-9/2	-0.353166 -0.034711	-0.164010 -0.048199	-0.352914 -0.194469	-0.130875 -0.005726
-7/2	-0.023448 -0.164197	0.393378 0.115199	0.362187 0.319522	-0.117693 -0.058848
-5/2	0.388018 0.368321	-0.140033 -0.171806	-0.063606 -0.061621	0.147991 0.285808
-3/2	-0.076453 -0.231120	-0.222098 0.033257	-0.085610 -0.384211	-0.203095 -0.151835
-1/2	-0.178840 -0.087904	-0.183242 0.220635	0.138735 0.370479	-0.064315 -0.206735
1/2	-0.260669 0.119620	-0.038416 -0.195538	0.137651 0.167117	0.233807 0.319119
3/2	0.089824 -0.205829	0.203317 0.133880	-0.015659 -0.253093	0.274413 0.282214
5/2	0.129519 0.179864	0.254851 0.470394	-0.157916 -0.280445	-0.016671 -0.086977
7/2	0.009030 0.409800	0.152465 0.065307	0.015298 -0.130693	-0.068698 -0.478074
9/2	0.003928 0.170901	0.058246 -0.350055	-0.066952 0.112598	0.030809 -0.401767
11/2	0.029160 -0.024568	0.020629 -0.269700	-0.077783 0.116451	-0.058440 -0.080551
13/2	-0.016494 -0.015209	-0.046594 -0.048661	0.020321 0.034398	-0.018749 0.008137
15/2	-0.046328 0.000000	0.022440 0.000000	-0.000000 0.000000	0.065562 0.000000

Chapter 6 References

[1] S. R. Batten, N. R. Champness, X.-M. Chen, J. Garcia-Martinez, S. Kitigawa, L. Öhrström, M. O'Keeffe, M. P. Suh and J. Reedijk, *Pure Appl. Chem.*, 2013, **85**, 1715-1724.

[2] A. Schneemann, V. Bon, I. Schwedler, I. Senkovska, S. Kaskel and R. A. Fischer, *Chem. Soc. Rev.*, 2014, **43**, 6062-6096.

[3] S. Kitagawa, R. Kitaura and S.-I. Noro, *Angew. Chem. Int. Ed.*, 2004, **43**, 2334-2375.

[4] X. Wang, A. Tian and X. Wang, *RSC Adv.*, 2015, **5**, 41155-41168.

[5] M. Eddaoudi, D. B. Moler, H. Li, B. Chen, T. M. Reineke, M. O'Keeffe and O. M. Yaghi, *Acc. Chem. Res.*, 2001, **34**, 319-330.

[6] **a)** A. R. Paital, J. Zhan, R. Kim, J. Kampf, P. Comllins, D. Coucouvanis, *Polyhedron*, 2013, **64**, 328-338. **b)** J.-R. Li, X.-H. Bu, J. Jiao, W.-P. Du, X.-H. Xu and R.-H. Zhang, *Dalton Trans.*, 2005, 464-474. **c)** Y. Zheng, M. Du, J.-R. Li, R.-H. Zheng and X.-H. Bu, *Dalton Trans.*, 2003, 1509-1514.

[7] S. L. James, *Chem. Soc. Rev.*, 2003, **32**, 276-288.

[8] S. Roy, A. Chakraborty, T. K. Maji, *Coord. Chem. Rev.*, 2014, **273**, 139-164.

[9] J.-R. Li, R. J. Kuppler and H.-C. Zhou, *Chem. Soc. Rev.*, 2009, **38**, 1477-1504.

[10] J. Y. Lee, O. K. Farha, J. Roberts and K. A. Scheidt, *Chem. Soc.Rev.*, 2009, **38**, 1450-1459.

[11] M. Kurmoo, *Chem. Soc. Rev.*, 2009, **38**, 1353-1379.

[12] C.-Y. Sun, C. Qin, X.-L. Wang and Z.-M. Su, *Expert Opin. Drug Deliv.*, 2013, **10**, 89-101.

[13] Z. Hu, B. J. Deibert and J. Li, *Chem. Soc. Rev.*, 2014, **43**, 5815-5840.

[14] M. P. Suh, H. J. Park, T. K. Prasad and D.-W. Lim, *Chem. Rev.*, 2012, **112**, 782–835.

[15] M.-L. Han, Y.-P. Wu, J. Zhao, D.-S. Li and Y.-Y. Wang, *J. Solid State Chem.*, 2015, **230**, 218-223.

[16] T. Sawano, N. C. Thacker, Z. Lin, A. R. McIsaac and W. Lin, *J. Am. Chem. Soc.*, 2015, **137**, 12241-12248.

[17] O. M. Yaghi, M. O`Keeffe, N. W. Ockwig, H. K. Chae, M. Eddaoudi and J. Kim, *Nature*, 2003, **423**, 705-714.

[18] F. Schwochow and L. Puppe, *Angew. Chem. Int. Ed.*, 1975, **14**, 620-628

[19] F. A. Mumpton, *Am. Mineral.*, 1973, **58**, 287-290.

[20] M. Ozekmekci, G. Salkic and M. F. Fellah, *Fuel Process. Technol.*, 2015, **139**, 49-60.

[21] A. Adatoz, A. K. Avci, S. Keskin, *Sep. Purif. Technol.*, 2015, **152**, 207-237.

[22] Y. Sugi and A. Vinu, *Catal. Surv. Asia*, 2015, **19**, 188-200.

[23] **a)** R. M. Barrer, *J. Chem. Soc.*, 1948, 127-132. **b)** R. M. Barrer, *J. Chem. Soc.*, 1948, 2158-2163. **c)** R. M. Barrer, L. Hinds, *Nature*, **166**, 562-562.

[24] F.-S. Xiao, S. Qiu,W. Pang and R. Xu, *Adv. Mater.*, 1999, **11**, 1091-1099.

[25] S. Oliver, A. Kuperman and G. A. Ozin, *Angew. Chem. Int. Ed.*, 1998, **37**, 46-62.

[26] S. Wang, Y. Peng, *Chem. Eng. J.*, 2010, **156**, 11-24.

[27] I. Shimada, K. Takizawa, H. Fukunaga, N. Takahashi and T. Takatsuka, *Fuel*, 2015, **161**, 207-214.

[28] X. Meng, Q. Wu, F. Chen and F.-S. Xiao, *Sci. China Chem.*, 2015, **58**, 6-13.

[29] a) B. F. Hoskins and R. Robson, *J. Am. Chem. Soc.*, 1989, **111** , 5962-5964. b) B. F. Hoskins and R. Robson, *J. Am. Chem. Soc.*, 1990, **112**, 1546-1554. c**)** B. F. Abrahams, B. F. Hoskins, D. M. Michail and R. Robson, *Nature*, 1994, **369**, 727-729.

[30] O. M. Yaghi, H. Li, C. Davis, D. Richardson and T. L. Groy, *Acc. Chem. Res.*, 1998, **31**, 474-484.

[31] D. Venkataraman, G. B. Gardner, S. Lee and J. S. Moore, *J. Am. Chem. Soc.*, 1995, **117**, 11600- 11601.

[32] S. Subramanian and M. J. Zaworotko, *Angew. Chem. Int. Ed.*, 1995, **34**, 2127-2129.

[33] C. Janiak, *Dalton Trans.*, 2003, 2781-2804.

[34] J. Gascon in *Metal organic frameworks as heterogeneous catalysts*, ed. F. X. Llabrés i Xamena and J. Gascon, RSC Pub., Cambridge, 2013, Ch. 7, pp. 238-239.

[35] M. O'Keeffe, M. A. Peskov, S. J. Ramsden and O. M. Yaghi, *Acc. Chem. Res.*, 2008, **41**, 1782-1789.

[36] G. B. Gardiner, D. Venkataraman, J. S. Moore, S. Lee, *Nature*, 1995, **374**, 792-795.

[37] R. H. Baughman and D. S. Galvão, *Nature*, 1993, **365**, 735-737.

[38] C. Zhengt and R. Hoffmann, *Inorg. Chem.*, **28**, 1074-1080.

[39] A. Mewis, *Z. Naturforsch. B*, 1978, **33**, 983-986.

[40] K. Klepp and E. Parthé, *Acta. Cryst. B.*, 1982, **38**, 1105-1108.

[41] M. Eddaoudi, J. Kim, J. B. Wachter, H. K. Chae, M. O'Keeffe and O. M. Yaghi, *J. Am. Chem. Soc.*, 2001, **123**, 4368-4369.

[42] H. Li, M. Eddaoudi, T. L. Groy and O. M. Yaghi, *J. Am. Chem. Soc.*, 1998, **120**, 8571-8572.

[43] M. Eddaoudi, J. Kim, M. O'Keeffe and O. M. Yaghi, *J. Am. Chem. Soc.*, 2002, **124**, 376-377.

[44] O. M. Yaghi, D. A. Richardson, G. Li, C. E. Davis and T. L. Groy, *Mat. Res. Soc. Symp. Proc.*, 1995, **371**, 15-19.

[45] O. M. Yaghi and H. Li, *J. Am. Chem. Soc.*, 1995, **117**, 10401-10402.

[46] S.-I. Noro, S. Kitagawa, M. Kondo and K. Seki, *Angew. Chem. Int. Ed.*, 2000, **39**, 2082–2084.

[47] J. J. Perry IV, J. A. Perman and M. J. Zaworotko, *Chem. Soc. Rev.*, 2009, **38**, 1400–1417.

[48] D. Banerjee, A. J. Cairns, J. Liu, R. K. Motkuri, S. K. Nune, C. A. Fernandez, R. Krishna, D. M. Strachan and P. K. Thallapally, *Acc. Chem. Res.*, 2015, **48**, 211−219.

[49] **a)** P. Silva, S. M. F. Vilela, J. P. C. Tomébc and F. A. Almeida Pazm, *Chem. Soc. Rev.*, 2015, **44**, 6774-6803. **b)** U. Mueller, M. Schubert, F. Teich, H. Puetter, K. Schierle-Arndt and J. Pastré, *J. Mater. Chem.*, 2006, **16**, 626–636.

[50] E. Barea, C. Montoro and J. A. R. Navarro, *Chem. Soc. Rev.*, 2014, **43**, 5419-5430.

[51] C. R. A. Daniel, N. M. Rodrigues, N. B. da Costa Jr. and R. O. Freire, *J. Phys. Chem. C*, 2015, **119**, 23398−23406.

[52] H. Furukawa, K. E. Cordova, M. O'Keeffe, O. M. Yaghi, *Science*, 2013, **341**, 974-997.

[53] a**)** D. S. Raja, W.-L. Liu, H.-Y. Huang and C.-H. Lin, *Comments Inorg. Chem.*, 2015, **35**, 332–350. b**)** P. Ling, J. Lei, H. Ju, *Biosens. Bioelectron*., 2015, **71**, 373-379.

[54] H. Li, M. Eddaoudi, M. O'Keeffe and O. M. Yaghi, *Natur*e, 1999, **402**, 276-279.

[55] M. Eddaoudi, J. Kim, N. Rosi, D. Vodak, J. Wachter, M. O'Keeffe, O. M. Yaghi, *Science*, 2002, **295**, 469-472.

[56] S. S.-Y. Chui, S. M.-F. Lo, J. P. H. Charmant, A. G. Orpen and I. D. Williams, *Science*, 1999, **283**, 1148-1150.

[57] D. J. Tranchemontagne, J. R. Hunt, O. M. Yaghi, *Tetrahedron*, 2008, **64** 8553–8557.

[58] S. Ma, D. Sun, J. M. Simmons, C. D. Collier, D. Yuan and H.-C. Zhou, *J. Am. Chem. Soc.*, 2008, **130**, 1012-1016.

[59] Z. Lu, L. Du, K. Tang and J. Bai, *Cryst. Growth Des.*, 2013, **13**, 2252−2255.

[60] J. M. Roberts, B. M. Fini, A. A. Sarjeant, O. K. Farha, J. T. Hupp and K. A. Scheidt, *J. Am. Chem. Soc.*, 2012, **134**, 3334−3337.

[61] X. Lin, I. Telepeni, A. J. Blake, A. Dailly, C. M. Brown, J. M. Simmons, M. Zoppi, G. S. Walker, K. M. Thomas, T. J. Mays, P. Hubberstey, N. R. Champness, and M. Schröder, *J. Am. Chem. Soc.*, 2009, **131**, 2159–2171.

[62] Z. Guo, H. Wu, G. Srinivas, Y. Zhou, S. Xiang, Z. Chen, Y. Yang, W. Zhou, M. O'Keeffe and B. Chen, *Angew. Chem. Int. Ed.*, 2011, **50**, 3178 –3181.

[63] Y. Peng, V. Krungleviciute, I. Eryazici, J. T. Hupp, O. K. Farha and T. Yildirim, *J. Am. Chem. Soc.*, 2013, **135**, 11887−11894.

[64] C. Song, Y. Ling, Y. Feng, W. Zhou, T. Yildirim and Y. He, *Chem. Commun.*, 2015, **51**, 8508-8511.

[65] O. K. Farha, A. Ö. Yazaydın, I. Eryazici, C. D. Malliakas, B. G. Hauser, M. G. Kanatzidis, S. T. Nguyen, R. Q. Snurr and J. T. Hupp, *Nat. Chem.*, 2010, **2**, 944-948.

[66] H. Furukawa, N. Ko, Y. B. Go, N. Aratani, S. B. Choi, E. Choi, A. Ö. Yazaydin, R. Q. Snurr, M. O'Keeffe, J. Kim, O. M. Yaghi, *Science*, 2010, **329**, 424-428.

[67] S. Li and F. Huo, *Nanoscale*, 2015, **7**, 7482–7501.

[68] a) A. Demessence, D. M. D'Alessandro, M. L. Foo and J. R. Long, *J. Am. Chem. Soc.*, 2009, **131**, 8784–8786. b) T. M. McDonald, D. M. D'Alessandro,R. Krishna and J. R. Long, *Chem. Sci.*, 2011, **2**, 2022–2028. c) T. M. McDonald, *J. Am. Chem. Soc.*, 2012, **134**, 7056–7065. d) C. S. Hong, *Energy Environ. Sci.*, 2014, **7**, 744–751.

[69] T. M. McDonald, J. A. Mason, X. Kong, E. D. Bloch, D. Gygi1, A. Dani, V. Crocellà, F. Giordanino, S. O. Odoh, W. S. Drisdell, B. Vlaisavljevich, A. L. Dzubak, R. Poloni, S. K. Schnell, N. Planas, K. Lee, T. Pascal, L. F. Wan, D. Prendergast, J. B. Neaton, B. Smit, J. B. Kortright, L. Gagliardi, S. Bordiga, J. A. Reimer and J. R. Long, *Nature*, 2015, **519**, 303-308.

[70] P. Silva, S. M. F. Vilela, J. P. C. Tomé and F. A. A. Paz, *Chem. Soc. Rev.*, 2015, **44**, 6774-6803.

[71] L. J. Murray, M. Dincă and J. R. Long, *Chem. Soc. Rev.*, 2009, **38**, 1294–1314.

[72] S. Kitagawa and M. Kondo, *Bull. Chem. Soc. Jpn.*, 1998, **71**, 1739-1753.

[73] G. Férey and C. Serre, *Chem. Soc. Rev.*, 2009, **38**, 1380–1399.

[74] S. Horike, S. Shimomura and S. Kitagawa, *Nat. Chem.*, 2009, **1**, 695-704.

[75] C. R. Murdock, B. C. Hughes, Z. Lu, D. M. Jenkins, *Coord. Chem. Rev.*, 2014, **258– 259**, 119– 136.

[76] D. Fairen-Jimenez, S. A. Moggach, M. T. Wharmby, P. A. Wright, S. Parsons, and T. Düren, *J. Am. Chem. Soc.*, 2011, **133**, 8900–8902.

[77] S. A. Moggach, T. D. Bennett and A. K. Cheetham, *Angew. Chem. Int. Ed.*, 2009, **48**, 7087 –7089.

[78] a) C. Serre, F. Millange, S. Surblé and G. Férey, *Angew. Chem. Int. Ed.*, 2004, **43**, 6286–6289. b) C. Serre, C. Mellot-Draznieks, S. Surblé, N. Audebrand, Y. Filinchuk and G. Férey, *Science*, 2007, **315**, 1828-1831. c) C. Mellot-Draznieks, C. Serre, S. Surblé, N. Audebrand and G. Férey, *J. Am. Chem. Soc.*, 2005, **127**, 16273-16278. d) S. Surblé, C. Serre, C. Mellot-Draznieks, F. Millange and G. Férey, *Chem. Commun.*, 2006, 284–286.

[79] M. Ohba, K. Yoneda, G. Agustí, M. C. Muñoz, A. B. Gaspar, J. A. Real, M. Yamasaki, H. Ando, Y. Nakao, S. Sakaki and S. Kitagawa, *Angew. Chem. Int. Ed.*, 2009, **48**, 4767 –4771.

[80] P. D. Southon, L. Liu, E. A. Fellows, D. J. Price, G. J. Halder, K. W. Chapman, B. Moubaraki, K. S. Murray, J.-F. Létard and C. J. Kepert, *J. Am. Chem. Soc.*, 2009, **131**, 10998–11009.

[81] C. Bartual-Murgui, N. A. Ortega-Villar, H. J. Shepherd, M. C. Muñoz, L. Salmon, G. Molnár, A. Bousseksou and J. A. Real, *J. Mater. Chem.*, 2011, **21**, 7217–7222.

[82] C. Serre, F. Millange, C. Thouvenot, M. Nogués, G. Marsolier, D. Louër and G. Férey, *J. Am. Chem. Soc.*, 2002, **124**, 13519-13526.

[83] D. N. Dybtsev, H. Chun and K. Kim, *Angew. Chem. Int. Ed.*, 2004, **43**, 5033 –5036.

[84] a) Z. Wang and S. M. Cohen, *J. Am. Chem. Soc.*, 2009, **131**, 16675–16677. b) S. Henke, R. Schmid, J.-D. Grunwaldt and R. A. Fischer, *Chem. Eur. J.*, 2010, **16**, 14296

– 14306. c) S. Henke, D. C. F. Wieland, M. Meilikhov, M. Paulus, C. Sternemann, K. Yusenko and R. A. Fischer, *CrystEngComm*, 2011, **13**, 6399–6404.

85 A. Demessence and J. R. Long, *Chem. Eur. J.*, 2010, **16**, 5902 – 5908.

86 M. Taddei, F. Costantino, A. Ienco, A. Comotti, P. V. Daud and S. M. Cohen, *Chem. Commun.*, 2013, **49**, 1315-1317.

87 G. Alberti, S. Murcia-Mascarós and R. Vivani, *J. Am. Chem. Soc.*, 1998, **120**, 9291-9295.

88 R. M. P. Colodrero, P. Olivera-Pastor, E. R. Losilla, M. A. G. Aranda, L. Leon-Reina, M. Papadaki, A. C. McKinlay, R. E. Morris, K. D. Demadis and A. Cabeza, *Dalton Trans.*, 2012, **41**, 4045–4051.

89 X.-L. Li, G.-Z. Liu, L.-Y. Xina and L.-Y. Wang, *CrystEngComm*, 2012, **14**, 5757–5760.

90 I.-H. Park, S. S. Lee and J. J. Vittal, *Chem. Eur. J.*, 2013, **19**, 2695 – 2702.

91 M.-H. Zeng, S. Hu, Q. Chen, G. Xie, Q. Shuai, S.-L. Gao and L.-Y. Tang, *Inorg. Chem.*, 2009, **48**, 7070-7079.

92 J.-H. Wang, M. Li and D. Li, *Chem. Sci.*, 2013, **4**, 1793-1801.

93 S. Yang, X. Lin, W. Lewis, M. Suyetin, E. Bichoutskaia, J. E. Parker, C. C. Tang, D. R. Allan, P. J. Rizkallah, P. Hubberstey, N. R. Champness, K. M. Thomas, A. J. Blake and M. Schröder, *Nat. Mater.*, 2012, **11**, 710-716.

[94] M. Wriedt, A. A. Yakovenko, G. J. Halder, A. V. Prosvirin, K. R. Dunbar and H.-C. Zhou, *J. Am. Chem. Soc.*, 2013, **135**, 4040−4050.

[95] C.-B. Tian, R.-P. Chen, C. He, W.-J. Li, Q. Wei, X.-D. Zhang and S.-W. Du, *Chem. Commun*., 2014, **50**, 1915-1917.

[96] A. Caneschi, D. Gatteschi and R. Sessoli, *Acc. Chem. Res.*, 1989, **22**, 392-398.

[97] Stöhr and H.C. Siegmann in *Magnetism From Fundamentals to Nanoscale Dynamics*, ed. M. Cardona, P. Fulde, K. von Klitzing, R. Merlin, H.-J. Queisser, H. Störmer, Springer, Berlin, 2006, Ch. 6, pp. 209.

[98] J. V. Yakhmi, *Bull. Mater. Sci.*, 2009, **32**, 217–225.

[99] J. S. Miller and A. J. Epstein, *Angew. Chem. Int. Ed.*, 1994, **33**, 385-415.

[100] P. C. E. Stamp, E. M. Chudnosvsky, B. Barbara, *Int. J. Mod. Phys.*, 1992, **B6**, 1355.

[101] S.M.J. Aubin, M.W. Wemple, D.M. Adams, H.-L. Tsai, G. Christou, and D.N. Hendrickson, *J. Am. Chem. Soc.*, 1996, **118**, 7746-7754.

[102] J. M. Manriquez, G. T. Yee, R. S. Mclean, A. J. Epstein, J. S. Miller, *Science*, 1991, **252**, 1415-1417.

[103] L. Bogani and W. Wernsdorfer, *Nat. Mater.*, 2008, **7**, 179-186.

[104] M. Castellano, R. Ruiz-García, J. Cano, J. Ferrando-Soria, E. Pardo, F. R. Fortea-Pérez, S.-E. Stiriba, M. Julve and F. Lloret, *Acc. Chem. Res.*, 2015, **48**, 510−520.

[105] J. Stöhr and H.C. Siegmann in *Magnetism From Fundamentals to Nanoscale Dynamics*, ed. M. Cardona, P. Fulde, K. von Klitzing, R. Merlin, H.-J. Queisser, H. Störmer, Springer, Berlin, 2006, Ch. 1, pp. 1.

[106] E. Beaurpaire, H. Bulou, F. Scheurer, J.-P. Kappler in *Magnetism: A Synchrotron Radiation Approach*, Springer, Berlin, 2006, Ch. 1.

[107] J. Bartolomé, F. Luis, J. F. Fernández, *Molecular Magnets*, P. Avouris, B. Bhushan, D. Bimberg, K. von Klitzing, H. Sakaki, R. Wiesendanger, Springer, Berlin, 2004, Ch. 2.

[108] G. Christou, D. Gatteschi, D. N. Hendrickson and R. Sessoli, *MRS Bull.*, 2000, **25**, 66-71.

[109] Y.-S. Meng, S.-D. Jiang, B.-W. Wang and S. Gao, *Acc. Chem. Res.*, 2016, **49**, 2381−2389.

[110] A. K. Bara, C. Pichon, J.-P. Sutter, *Coord. Chem. Rev.*, 2016 **308**, 346–380.

[111] R. Sessoli, D. Gatteschi, A. Caneschi, M. A. Novak, *Nature*, 1993, **365**, 141-143.

[112] J. M. Hernandez, X. Zhang, F. Luis, J. Tejada, J. R. Friedman, M. P. Sarachik and R. Ziolo, *Phys. Rev. B.*, 1997, **55**, 5858-5865.

[113] K. Wieghardt, K. Pohl, I. Jibril and G. Huttner, *Angew. Chem. Int. Ed. Eng.*, 1984, **23**, 77-78.

[114] C. Sangregorio, T. Ohm, C. Paulsen, R. Sessoli and D. Gatteschi, *Phys. Rev. Lett.*, 1997, **78**, 4645-4648.

[115] A. M. Ako, I. J. Hewitt, V. Mereacre, R. Clérac, W. Wernsdorfer, C. E. Anson and A. K. Powell, *Angew. Chem. Int. Ed.*, 2006, **45**, 4926 -4929.

[116] F. Neese and D. A. Pantazis, *Faraday Discuss.*, 2011, **148**, 229-238.

[117] G. A. Craig and M. Murrie, *Chem. Soc. Rev.*, 2015, **44**, 2135-2147.

[118] K. Bernot, J. Luzon, L. Bogani, M. Etienne, C. Sangregorio, M. Shanmugam, A. Caneschi, R. Sessoli and D. Gatteschi, *J. Am. Chem. Soc.*, 2009, **131**, 5573-5579.

[119] F. Habib and M. Murugesu, *Chem. Soc. Rev.*, 2013, **42**, 3278-3288.

[120] N. Ishikawa, M. Sugita, T. Ishikawa, S.-y. Koshihara and Y. Kaizu, *J. Am. Chem. Soc.*, 2003, **125**, 8694-8695.

[121] F. Branzoli, P. Carretta, M. Filibian, G. Zoppellaro, M. J. Graf, J. R. Galan-Mascaros, O. Fuhr, S. Brink and M. Ruben, *J. Am. Chem. Soc.*, 2009, **131**, 4387–4396.

[122] Y.-N. Guo, L. Ungur, G. E. Granroth, A. K. Powell, C. Wu, S. E. Nagler, J. Tang, L. F. Chibotaru and D. Cui, *Sci. Rep.*, 2014, **4**, 5471.

[123] S. T. Liddle and J. van Slageren, *Chem. Soc. Rev.*, 2015, **44**, 6655-6669.

[124] Y.-N. Guo, G.-F. Xu, Y. Guo and J. Tang, *Dalton Trans.*, 2011, **40**, 9953–9963.

[125] G. Cucinotta, M. Perfetti, J. Luzon, M. Etienne, P.-E. Car, A. Caneschi, G. Calvez, K. Bernot and R. Sessoli, *Angew. Chem. Int. Ed.*, 2012, **51**, 1606 –1610.

[126] a) T. Pugh, F. Tuna, L. Ungur, D. Collison, E. J. L. McInnes, L. F. Chibotaru and R. A. Layfield, *Nat. Commun.*, 2015, **6**, 7492. b) B. M. Day, N. F. Chilton and R. A.

Layfield, *Dalton Trans.*, 2015, **44**, 7109–7113. c) S. N. König, N. F. Chilton, C. Maichle-Mössmer, E. M. Pineda, T. Pugh, R. Anwander and R. A. Layfield, *Dalton Trans.*, 2014, **43**, 3035–3038.

[127] D. N. Woodruff, R. E. P. Winpenny and R. A. Layfield, *Chem. Rev.*, 2013, **113**, 5110−5148.

[128] M. Gregson, N. F. Chilton, A.-M. Ariciu, F. Tuna, I. F. Crowe, W. Lewis, A. J. Blake, D. Collison, E. J. L. McInnes, R. E. P. Winpenny and S. T. Liddle, *Chem. Sci.*, 2016, **7**, 155–165.

[129] L. Ungur and L. F. Chibotaru, *Phys. Chem. Chem. Phys.*, 2011, **13**, 20086-20090.

[130] J. Liu, Y.-C. Chen, J.-L. Liu, V. Vieru, L. Ungur, J.-H. Jia, L. F. Chibotaru, Y. Lan, W. Wernsdorfer, S. Gao, X.-M. Chen, and M.-L. Tong, *J. Am. Chem. Soc.*, 2016, **138**, 5441−5450.

[131] J.-L. Liu, J.-Y. Wu, Y.-C. Chen, V. Mereacre, A. K. Powell, L. Ungur, L. F. Chibotaru, X.-M. Chen and M.-L. Tong, *Angew. Chem. Int. Ed.*, 2014, **53**, 12966-12970.

[132] H. B. G. Casimir and F. K. Du Pre, *Physica*, 1938, **5**, 507-511.

[133] K. S. Cole and R. H. Cole, *J. Chem. Phys.*, 1941, **9**, 341-355.

[134] M. Grahl, J. Kotzler and I. Sessler, *J. Magn. Magn. Mater.*, 1990, **90-1**, 187-188.

[135] L. F. Chibotaru and L. Ungur, *J. Chem. Phys.*, 2012, **137**, 064112-064134.

[136] W. H. Adams, *Phys. Rev.*, 1967, **156**, 109-117.

[137] a) G. Karlström, R. Lindh, P.-Å. Malmqvist, B. O. Roos, U. Ryde, V. Veryazov, P.-O. Widmark, M. Cossi, B. Schimmelpfennig, P. Neogrady and L. Seijo, *Comput. Mater. Sci.*, 2003, **28**, 222-239. b) V. Veryazov, P. Widmark, L. Serrano-Andrés, R. Lindh and B. O. Roos, *Int. J. Quantum Chem.*, 2004, **100**, 626-635. c) F. Aquilante, L. De Vico, N. Ferré, G. Ghigo, P. Malmqvist, P. Neogrády, T. B. Pedersen, M. PitoňáK, M. Reiher, B. O. Roos, L. Serrano-Andrés, M. Urban, V. Veryazov and R. Lindh, *J. Comput. Chem.*, 2010, **31**, 224-247.

[138] I. N. Levine, *Quantum Chemistry*, 6th edn. Pearson Prentice Hall, Upper Saddle River, N.J, 2009, Ch. 1.

[139] N. Bohr, *Philosophical Magazine 26*, 1913, **153**, 476–502.

[140] W. Heisenberg, *Z. Phys.*, 1925, **33**, 879-893.

[141] E. Schrödinger, *Phys. Rev.*, 1926, **28**, 1049-1070.

[142] I. Newton, *Philosophiæ Naturalis Principia Mathematica*, 1687, Encyclopædia Britannica, London.

[143] D. R. Hartree, *Proc. Camb. Phil. Soc.*, 1928, **24**, 89-110.

[144] J. Slater and H. C. Verma, *Phys. Rev.*, 1929, **34**, 1293–1322.

[145] J. P. Lowe *Quantum chemistry*, 2nd edn. Academic Press, New York, 1993, Appendix 7.

[146] E. G. Lewars, *Computational Chemistry*, Springer, Berlin, 2004, Ch. 5., pp 255

[147] K. Raghavachari, J. B. Anderson, *J. Phys. Chem.*, 1996, **100,** 12960-12973.

[148] J. W. Hollett, H. Hosseini and C. Menzies, *J. Chem. Phys.*, 2016, **145**, 084106-084120.

[149] F. L. Pilar, *Elementary quantum chemistry*, 2nd edn. McGraw-Hill, New York, 1990, pp 286.

[150] C. Møller, M. S. Plesset, *Phys. Rev.*, 1934, **46**, 618-622.

[151] I. N. Levine, *Quantum chemistry*, 5th edn. Prentice Hall, Engelwood Cliffs, NJ, 2000, pp 256–259.

[152] J. S. Binkley, J. A. Pople, *Int. J. Quant. Chem.*, 1975, 9, 229-236.

[153] A. Szabo, N. S. Ostlund, *Modern quantum chemistry*. McGraw-Hill, New York, 1989, p 353

[154] I. N. Levine, *Quantum chemi*stry, 5th edn. Prentice Hall, Engelwood Cliffs, NJ, 2000, p 296

[155] N. Ben-Amor, S. Evangelisti, D. Maynau, E. P. S. Rossi, *Chem. Phys. Lett*., 1998, **288**, 348-355.

[156] B. Roos, P. R. Taylor, *Chem. Phys.*, 1980, **48**, 157-173.

[157] L. F. Chibotaru, L. Ungur and A. Soncini, *Angew. Chem. Int. Ed.*, 2008, **47**, 4126-4129. b) L. F. Chibotaru, L. Ungur, Ch. Aronica, H. Elmoll, G. Pillet and D. Luneau, *J. Am. Chem. Soc.*, 2008, **130**, 12445-12455. c) L. F. Chibotaru and L. Ungur, *J. Chem. Phys.*, 2012, **137**, 064112. d) L. Ungur, M. Thewissen, J.-P. Costes, W. Wernsdorfer and L. F. Chibotaru, *Inorg. Chem.*, 2013, **52**, 6328-6337.

[158] a) J. Wang, S. Onions, M. Pilkington, H. Stoeckli-Evans, J. C. Halfpenny and J. D. Wallis, *Chem. Commun*., 2007, 3628–3630. b) J. Wang, B. Djukic, J. Cao, A. Alberola, F. S. Razavi and M. Pilkington, *Inorg. Chem*., 2007, **46,** 8560-8568. c) N. J. Hurley, J. J. Hayward, J. M. Rawson, M. Murrie and M. Pilkington, *Inorg. Chem.*, 2014, **53**, 8610−8623. d) J. Wang, J. J. Hayward, R. Gumbau-Brisa, J. D. Wallis, H. Stoeckli-Evans and M. Pilkington, *CrystEngComm*, 2015, **17**, 1159–1167. e) N. J. Hurley, J. M. Rawson and M. Pilkington, *Dalton Trans.*, 2015, **44**, 1866–1874.

[159] a) R. T. Acha, E. L. Gavey, J. Wang, J. M. Rawson, M. Pilkington, *Polyhedron*, 2014, **76**,122–127. b) N. Zarrabi, J. J. Hayward, W. Clegg and M. Pilkington, *Dalton Trans.*, 2014, **43**, 2352–2355. c) J. Wang, B. Slater, A. Alberola, H. Stoeckli-Evans, F. S. Razavi and M. Pilkington, *Inorg. Chem.*, 2007, **46**, 4763-4765.

[160] P. S. Perlepe, L. Cunha-Silva, K. J. Gagnon, S. J. Teat, C. Lampropoulos, A. Escuer and T. C. Stamatatos, *Inorg. Chem.*, 2016, **55**, 1270-1277.

[161] P. E. Dawson, T. W. Muir, I. Clark-Lewis and S. B. H. Kent, *Science*, 1994, **266**, 776-779.

[162] S. Hüinig, I. Wehner, *Synthesis*, 1989, **7**, 552-554.

[163] C.R. Kemnitz, M.J. Loewen, *J. Am. Chem. Soc., 2007*, **129**, 2521-2528.

[164] A.L. Spek, *Acta Cryst.*, 2009, **D65**, 148-155.

[165] O. Daugulis, H.-Q. Do and D. Shabashov, *Acc. Chem. Res.*, 2009, **42**, 1074-1086.

[166] G. Calleja, R. Sanz, G. Orcajo, D. Briones, P. Leo, F. Martínez, *Catalysis Today*, 2014, **227**, 130-137.

[167] B. Gole, A. Kumar Bar, A. Mallick, R. Banerjee and P. S. Mukherjee, *Chem. Commun.*, 2013, **49**, 7439-7441.

[168] K. K. Tanabe and S. M. Cohen, *Inorg. Chem.*, 2010, **49**, 6766-6774.

[169] L.-X. Shi and C.-D. Wu, *Chem. Commun.*, 2011, **47**, 2928-2930.

[170] T. Maihom, S. Wannakao, B. Boekfa and J. Limtrakul, *J. Phys. Chem. C*, 2013, **117**, 17650-17658.

[171] H. Kajiro, A. Kondo, K. Kaneko and H. Kanoh, *Int. J. Mol. Sci.*, 2010, **11**, 3803-3845.

[172] V. A. Blatov, A. P. Shevchenko, V. N. Serezhkin, *J. Struc. Chem*., 1993, **34**, 820-822.

[173] W. H. Bragg, W. L. Bragg, *Proc R. Soc. Lond. A*, 1913, **605**, 428–438.

[174] C. F. Macrae, P. R. Edgington, P. McCabe, E. Pidcock, G. P. Shields, R. Taylor, M. Towler and J. van de Streek, *J. Appl. Cryst.*, 2006, **39**, 453-457.

[175] R. H. Muller, *Anal. Chem.*, 1953, **25**, 2A-3A.

[176] A. Alberola, C. M. Pask, J. M. Rawson, E. J. L. McInnes, J. Wolowska, H. El Mkami and G. Smith, *J. Phys. Chem. B*, 2003, **107**, 14158-14160.

[177] R. Sessoli and A. K. Powell, *Coord. Chem. Rev.*, 2009, **253**, 2328–2341.

[178] E.L. Gavey and M. Pilkington, *Coord. Chem. Rev.*, 2015, **296**, 125–152.

[179] Q. Wang, S. Venneri, N. Zarrabi, H. Wang, C. Desplanches, J.-F. Létard, T. Sedae and M. Pilkington, *Dalton Trans.*, 2015, **44**, 6711-6714.

[180] E.L. Gavey and M. Pilkington, U.S. Provisional Patent Application No. 62/174,752 filed on June 12, 2015.

[181] M.G.B. Drew, A.H. bin Othman, S.G. McFall, P.D.A. McIlroy and S.M. Nelson, *J. Chem.Soc. Dalton Trans.*, 1977, 1173–1180.

[182] E. L. Gavey, Y. Beldjoudi, J. M. Rawson, T. C. Stamatatos and M. Pilkington, *Chem. Commun.*, 2014, **50**, 3741−3743.

[183] E.L. Gavey and M. Pilkington, *Polyhedron*, 2016, **108**, 122–130.

[184] U. Casellato, S. Tamburini, P. Tomasin, P. A. Vigato, S. Aime and M. Botta, *Inorg. Chem.*, 1999, **38**, 2906-2916.

[185] U. Casellato, S. Tamburini, P. Tomasin, P. A. Vigato, *Inorganica Chimica Acta*, 2002, **341**, 118-126.

[186] P. Guerriero, S. Tamburini and P.A. Vigato, *Coord. Chem. Rev.*, 1995, **139,** 11-243.

[187] G. Riggio, W. H. Hopff, A. A. Hofmann and P. G. Waser, *Helv. Chim. Acta*, 1980, **63**, 488−497.

[188] F. Aquilante, J. Autschbach, R. K. Carlson, L. F. Chibotaru, M. G. Delcey, L. De Vico, I. Fdez. Galván, N. Ferré, L. M. Frutos, L. Gagliardi, M. Garavelli, A. Giussani,

C. E. Hoyer, G. Li Manni, H. Lischka, D. Ma, P. Å. Malmqvist, T. Müller, A. Nenov, M. Olivucci, T. B. Pedersen, D. Peng, F. Plasser, B. Pritchard, M. Reiher, I. Rivalta, I. Schapiro, J. Segarra-Martí, M. Stenrup, D. G. Truhlar, L. Ungur, A. Valentini, S. Vancoillie, V. Veryazov, V. P. Vysotskiy, O. Weingart, F. Zapata, R. Lindh, *J. Comp. Chem.*, 2016, **37**, 506−541.

[189] J. P. Costes, S. Titos-Padilla, I. Oyarzabal, T. Gupta, C. Duhayon, G. Rajaraman and E. Colacio, *Inorg. Chem.*, 2016, **55**, 4428−4440.

[190] F. C. J. M. van Veggel, M. Bos, S. Harkema, H. van de Bovenkamp, W. Verboom, J. Reedijk and D. N. Reinhoudt, *J. Org. Chem.*, 1991, **56**, 225-235.

[191] L. Ungur, M. Thewissen, J.-P. Costes, W. Wernsdorfer and L. F. Chibotaru, *Inorg. Chem.*, 2013, **52**, 6328−6337.

[192] A. J. Brown, D. Pinkowicz, M. R. Saber and K. R. Dunbar, *Angew. Chem. Int. Ed.*, 2015, **54**, 5864 –5868.

[193] Z. Asadi and M. R. Shorkaei, *Spectrochim. Acta Mol. Biomol. Spectrosc.*, 2013, **105**, 344–351.

[194] A. J. Brown, D. Pinkowicz, M. R. Saber and K. R. Dunbar, *Angew. Chem. Int. Ed.*, 2015, **54**, 5864 –5868.

[195] S. Gómez-Coca, D. Aravena, R. Morales, E. Ruiz, *Coor. Chem. Rev.*, 2015, **289–290**, 379-392.

[196] H. L. C. Feltham, R. Clérac, L. Ungur, L. F. Chibotaru, A. K. Powell and S. Brooker, *Inorg. Chem*., 2013, **52**, 3236−3240.

[197] S. V. Eliseeva and J.-C. G. Bünzli, *Chem. Soc. Rev.*, 2010, **39**, 189–227.

[198] F. C. J. M. van Veggel, M. Bos, S. Harkema, H. van de Bovenkamp, W. Verboom, J. Reedijk and D. N. Reinhoudt, *J. Org. Chem.*, 1992, **56**, 1992, 225-235.

[199] C. J. van Staveren, J. van Eerden, F. C. J. M. van Veggel, S. Harkema and D. N. Reinhoudt, *J. Am. Chem. Soc*., 1988, **110**, 4994-5008.

[200] Bruker-AXS (2014). APEX2. Version 2014.11-0. Madison, Wisconsin, USA.

[201] Krause, L., Herbst-Irmer, R., Sheldrick, G. M. and Stalke, D., *J. Appl. Crystallogr.*, 2015, **48**, 3-10.

[202] Spek, A. L. (1980-2014). PLATON. Version 191114. Utrecht University, Padualaan 8, 3584 CH Utrecht, The Netherlands.